



**Christopher M. Foley, PhD, PE; Baolin Wan, PhD; Carl Schneeman, MS;
Kristine Barnes, MS; Jordan Komp, MS; Junshan Liu, MS; Andrew Smith, MS**

Marquette University

Department of Civil & Environmental Engineering

June 2010

WHRP 10-09

Technical Report Documentation Page

1. Report No. WHRP 10-09	2. Government Accession No	3. Recipient's Catalog No	
4. Title and Subtitle In-Situ Monitoring and Testing of IBRC Bridges in Wisconsin		5. Report Date June 2010	6. Performing Organization Code Wisconsin Highway Research Program
7. Authors Christopher Foley, PhD, PE; Baolin Wan, PhD; Carl Schneeman, MS; Kristine Barnes, MS; Jordan Komp, MS; Junshan Liu, MS; Andrew Smith, MS		8. Performing Organization Report No.	
9. Performing Organization Name and Address Marquette University Department of Civil & Environmental Engineering Milwaukee, Wisconsin		10. Work Unit No. (TRAIS)	11. Contract or Grant No. WisDOT SPR# 0092-05-02
12. Sponsoring Agency Name and Address Wisconsin Department of Transportation Division of Business Services Research Coordination Section 4802 Sheboygan Ave. Rm 104 Madison, WI 53707		13. Type of Report and Period Covered Final Report, 2004-2010	
14. Sponsoring Agency Code			
15. Supplementary Notes			
16. Abstract This study examines two highway bridges constructed using novel fiber-reinforced polymer (FRP) composite stay-in-place formwork and an FRP grillage reinforcement system. Both bridge superstructures rely on the FRP components as bridge deck reinforcement. These bridges were monitored in-situ for a period of five years. The monitoring included a series of in-situ load test as well as non-destructive evaluation (NDE). Laboratory investigations accompanied and guided the load testing and NDE implemented. Finite element simulations were employed to evaluate the likely causes of premature deck cracking seen in the traditionally-constructed bridge and the FRP-component superstructures. The study identifies sources of potential deterioration, identifies aspects of the bridge superstructures likely to enhance durability, and quantifies the effectiveness and potential for deterioration of the load transfer mechanisms present in the FRP-component superstructures.			
17. Key Words		18. Distribution Statement No restriction. This document is available to the public through the National Technical Information Service 5285 Port Royal Road Springfield VA 22161	
19. Security Classif.(of this report) Unclassified	19. Security Classif. (of this page) Unclassified	20. No. of Pages 232	21. Price

Disclaimer

This research was funded through the Wisconsin Highway Research Program by the Wisconsin Department of Transportation and the Federal Highway Administration under Project 0092-05-02. The contents of this report reflect the views of the authors who are responsible for the facts and accuracy of the data presented herein. The contents do not necessarily reflect the official views of the Wisconsin Department of Transportation or the Federal Highway Administration at the time of publication.

This document is disseminated under the sponsorship of the Department of Transportation in the interest of information exchange. The United States Government assumes no liability for its contents or use thereof. This report does not constitute a standard, specification or regulation.

The United States Government does not endorse products or manufacturers. Trade and manufacturers' names appear in this report only because they are considered essential to the object of the document.

Table of Contents

Acknowledgements.....	iii
Executive Summary	vi
Chapter 1 – Introduction, Literature Review and Synthesis	1
1.1 Introduction.....	1
1.2 Motivations for Present Research Effort.....	2
1.3 Bridges B-20-133/134 – Waupun, Wisconsin	4
1.4 Bridges B-20-148/149 – Fond du Lac, Wisconsin.....	6
1.5 Literature Review.....	8
1.6 Literature Synthesis	22
1.7 Layout of Research Report	25
1.8 References.....	26
Chapter 2 – Sensor Development and Laboratory Studies	35
2.1 Introduction.....	35
2.2 Development of Portable Strain Sensors	35
2.3 Freeze Thaw Testing.....	46
2.4 Conclusions.....	52
2.5 References.....	53
Chapter 3 – In-Situ Monitoring and Non-Destructive Evaluation	67
3.1 Introduction.....	67
3.2 Benchmark Condition Evaluation of B-20-133/134	67
3.3 Benchmark Condition Evaluation of B-20-148/149	70
3.4 Evaluation of NDE Techniques	72
3.5 In-Situ Moisture Evaluation in Waupun Bridges.....	78
3.6 Conclusions.....	80

3.7 References	81
Chapter 4 – In-Situ Load Testing	117
4.1 Introduction	117
4.2 In-Situ Instrumentation.....	117
4.3 In-Situ Load Test Protocols.....	121
4.4 Load Testing Results and Discussion.....	122
4.5 Wheel Load Distribution within Bridge Deck.....	131
4.6 Concluding Remarks	138
4.7 References	140
Chapter 5 – Numerical Simulation of Shrinkage-Induced and Vehicle-Induced Stresses	183
5.1 Introduction	183
5.2 FE Modeling of Bridge Superstructure	183
5.3 Simulation and Evaluation of Shrinkage-Induced Strains.....	186
5.4 Simulation and Evaluation of Vehicle-Induced Strains.....	197
5.5 Concluding Remarks	199
5.6 References	201
Chapter 6 – Summary, Conclusions, and Recommendations.....	221
6.1 Summary	22x
6.2 Conclusions	22x
6.3 Recommendations	22x

ACKNOWLEDGEMENTS

The authors would like to acknowledge the support and help from the following individuals at the Wisconsin Department of Transportation: Travis McDaniel, Bruce Karow. The authors would also like to acknowledge the help of Professor Jian Zhao, University of Wisconsin at Milwaukee and Dr. Nicholas Hornyak of Collins Engineers, Inc. The research team is also grateful for the help of Stu Kastein at Fond du Lac County Highway Department and all the summer work crews at Fond du Lac County for their terrific help in conducting the load testing. The authors would also like to acknowledge the help of the Fond du Lac County Sheriff's Office.

EXECUTIVE SUMMARY

This report outlines activities undertaken during a five-year monitoring study of Wisconsin's first IBRC bridges (B-20-133/134 and B-20-148/149). It provides detailed background on the IBRC program and the bridge superstructures constructed in Waupun, WI and Fond du Lac, WI. The five-year research effort completed several related, yet distinct, studies designed to assess the likely long-term performance of Wisconsin's IBRC structures and also provide direction with regard to further investigation into the performance of these structural systems so that the technologies fostered by them can be introduced in bridge superstructure design going forward.

The report describes the design and calibration of portable strain sensors suitable for use in the proposed research effort and a laboratory-based experimental program designed to evaluate the impact of moisture and freeze-thaw cycling on the shear strength at the interface between the FRP-SIP formwork and concrete. The laboratory studies completed indicate that freeze-thaw cycling and the presence of water could be detrimental to the FRP-SIP-formwork-concrete interfacial shear strength. Simplified finite element modeling and analysis of a similar FRP-SIP deck system suggests that shear demands at the concrete FRP-SIP interface are very low and not of sufficient magnitude to cause concerns regarding long-term performance of the stay-in-place FRP system. The reduction in strength due to moisture presence and freeze-thaw cycling seen in the laboratory studies is significant, but does not bring the shear strength at the interface down to levels where the system would be compromised. The laboratory studies conducted to evaluate the reduction in shear strength resulting from freeze-thaw cycling and moisture presence were very conservative and do not fully represent the situation present in the field. In other words, the laboratory testing setup is an extreme scenario that is an approximation of the field conditions. Field conditions are likely to be much more favorable and the resistance to freeze-thaw degradation is felt to be much higher in the actual structure.

The report outlines a thorough visual benchmark condition evaluation of the bridges at Waupun and Fond du Lac. Common NDE methods were reviewed for their potential application in the present research effort and future evaluation of these bridges. A laboratory-based evaluation of the infrared thermography technique for application in the present research effort was conducted. Tap testing with an impact hammer

was shown to be the most useful method for monitoring the IBRC bridges. Infrared thermography was found to be the least likely to yield useful results.

The presence of moisture accumulation at the interface between the FRP-SIP formwork and concrete in the Waupun bridge system was assessed using a digital hygrometer. No moisture was found when drilling the hygrometer probe holes so there is no concern that moisture is actually accumulating at the interface of the FRP-SIP formwork and the concrete deck as of the date of this report. It should be understood that relative humidity is one measure of the tendency for the FRP-SIP formwork to inhibit moisture egress from within the deck and may be an indicator for the tendency for moisture to accumulate at the interface. However, the ability of humidity readings to reliably indicate levels of moisture to expect at the interface remains to be definitively proven. It is recommended that further analysis with regard to relative humidity be undertaken in future research efforts as it may be a useful tool for long-term evaluation of bridge decks with FRP-SIP formwork.

The report describes two in-situ load tests of bridges B-20-133 and B-20-148 conducted to evaluate critical load transfer mechanisms that could give the research team indication of degradation with time. Bridge deck displacements relative to the girders in both bridges did not change significantly over the two-year period of evaluation. It was found that the wheel load distribution widths present in the FRP-SIP bridge deck system of B-20-133 could be predicted using procedures found in U.S. design specifications. Furthermore, this load transfer mechanism did not change significantly (if at all) over the two year evaluation period. Although not fully evaluated in the present research report, the in-situ testing conducted illustrated that the wheel load distribution widths in B-20-148 are consistent, but narrower, than that in B-20-133. Strain gradients over the height of the girders in the Fond du Lac bridge load tested clearly exhibit composite behavior and this behavior did not significantly (if at all) change with time. Lane load distribution factors for wide-flange bulb-tee composite bridge girder systems (e.g. that used in B-20-148) can be computed accurately with standard design/analysis procedures found in modern U.S. bridge design specifications. These lane load distribution factors did not change from the original July 2005 load tests and the July 2007 load test conducted in this research study. The in-situ load testing conducted indicates that the long-term

performance of the IBRC bridges are expected to be no different than any other traditionally constructed bridge of similar superstructure configuration.

The finite element simulations conducted indicate that drying shrinkage appears to be capable of causing transverse (and possibly longitudinal) bridge deck cracking at very early stages in the life of the decks in the Waupun bridges. The simulations conducted indicate that cracking may occur as early as 4-8 days after bridge deck placement. An FE simulation of the tensile strains and stresses induced by HL-93 vehicle-type loading was conducted and it was found that tensile stresses induced by HL-93 vehicle loading were found to be on the order of 20% of the typical magnitudes assumed for the tensile strength of concrete material. When these are superimposed onto the states of stress likely present 10-days after casting the bridge deck, it is likely that the combined effects of vehicle-induced stresses and shrinkage-induced stresses will result in transverse cracking over the interior pier supports in the bridges in Waupun. The FE simulations conducted as part of this effort clearly support idea that there should be no difference between and IBRC bridge and its counterpart with regard to behavior leading to cracking since shrinkage-induced straining and traffic loading are the likely reasons for the transverse cracking. Furthermore, the deck connection detail at the central diaphragms (over the interior piers) in the FRP-SIP formwork bridge at Waupun is expected to neither improve nor detract from the behavior with regard to cracking.

Chapter 1

Introduction, Literature Review and Synthesis

1.1 Introduction

Across the United States a massive network of transportation infrastructure exists. This network evolved to include a web of iron rail lines spurred by the industrial revolution and eventually concrete and asphalt roads for the automobile. Throughout this progression the highway bridge has evolved to meet these demands. These highway bridges have become increasingly complex, relying on the development of modern materials, changing economic conditions, and advanced engineering to meet project goals.

Acknowledging the importance of fostering new materials and engineering methods, the United States Department of Transportation (USDOT) initiated the Innovative Bridge Research and Construction (IBRC) program under the Transportation Equity Act for the 21st Century (TEA-21) as a venue for the demonstration of new and groundbreaking material used in the construction of transportation structures (FHWA 2005). This program fostered development of numerous novel materials and their applications in bridge engineering and their future use in construction. The first installment of funding was allocated for the period between 1998 and 2004 and accounted for \$7 million in research and development projects and \$122 million of construction projects (Conachen 2005).

Evaluation of fiber-reinforced polymer (FRP) materials has happened frequently in the IBRC program. Although the material has been in use for a number of years, its implementation in infrastructure has been slow. Sources of this delay stem from inconsistency in material properties, non-ductile failure mechanisms, general unfamiliarity among designers, and cost. FRP composites are composed of oriented fibers, typically carbon or glass, embedded in a polymeric resin and cured to form a single composite material. The matrix of resin and fiber is usually drawn through a die during a process called pultrusion, pressed into the desired shape prior to the set-up or curing of the resin, or cured in the final shape intended for the application. Often this process can be costly as the machinery required may

not be readily available to industry and set up of the pultrusion process can be labor intensive. However, large-scale production can be rapid and very little preparation is required after the curing process.

FRP bars or multi-directional grillages have many advantages and can be used in lieu of steel reinforcing bars in reinforced concrete. The tendency for conventional steel reinforcement to corrode within a bridge component (*e.g.* deck) suggests that FRP reinforcement is an ideal substitute for mild-steel reinforcing bars in concrete. In 2002, 27.1% of the bridges in the United States were classified by the DOT as structurally deficient or functionally obsolete (ASCE 2005). A major cause of deficiency for these structures is gradual deterioration of the steel reinforcing contained within concrete decks and the concrete spalling that follows. Penetration of water through the concrete decking in conjunction with high concentrations of chlorides commonly found in salts used for de-icing and snow removal facilitate this corrosion. FRP systems are generally not affected by corrosion and are immune to the effects of chlorides and therefore can be a major source for combating this deterioration (Jacobson 2004a).

FRP materials are also capable of developing significantly larger tensile stresses than mild steel. Currently, common strengths of steel reinforcing bars reach a maximum of 75 ksi, while glass-fiber reinforced polymers (GFRP) and carbon-fiber reinforced polymers (CFRP) have been found to achieve maximum stresses of 230 and 535 ksi, respectively (Dietsche 2002b). These higher stress levels combined with the lower density of FRP relative to that of steel, may allow for less material used in design and, in turn, offer cost savings.

1.2 Motivations for Present Research Effort

The Innovative Bridge Research and Construction (IBRC) program was created to find innovative materials for highway bridges, demonstrate their application in infrastructure projects, monitor their performance, and create a research, development, and technology-transfer program. The primary goal of the IBRC program was to develop and demonstrate new, cost-effective, highway bridge applications of innovative materials (IBRC 2006). There is/was an expectation that this program would result in new,

more durable structures that need less frequent maintenance and rehabilitation with shorter work times for improvements, and, lower costs with an improved load capacity.

The Wisconsin Department of Transportation; along with the University of Wisconsin – Madison, a structural engineering consultant (Alfred Benesch and Co.), and a bridge construction contractor (Lunda Construction, Inc.), took a significant step in the direction of formalizing the use of novel structural engineering systems for bridges when they successfully proposed and received funding through the IBRC Program. The goals of this program pertinent to the present research effort are:

- develop new, cost-effective innovative material applications in highway bridges;
- develop engineering design criteria for innovative products and materials for use in highway bridges and structures.

To meet these goals, WisDOT and the University of Wisconsin at Madison conducted experimental validation of a novel fiber-reinforced polymer (FRP) composite stay-in-place form system; a novel FRP grillage system for bridge deck reinforcement; and a deck replacement scenario involving precast prestressed concrete bridge deck panels. All of these were designed to be innovative, economical, and durable substitutes for traditional concrete deck components and rehabilitation techniques used in highway bridges. The experimental efforts supported tentative guidelines for design that then supported generation of construction drawings.

With experimental validation of the innovative systems completed; design of the innovative bridge superstructures completed, construction of two of the bridges completed in fall 2005, a significant final step required was to “close the loop” in the innovation process. The innovative bridges constructed require a monitoring period (*e.g.* 5 years) to evaluate durability of the new systems when compared to traditional deck systems after imposition of traffic loading. Furthermore, in-situ load testing of the innovative bridges was required to validate the load transfer mechanisms used in the design phase with field-obtained data.

In order to complete WisDOT’s process of innovation in bridge deck design, the proposed research effort set out to complete the following for WisDOT’s IBRC bridges:

- evaluate the extent of annual bridge deck deterioration;
- identify the sources of deterioration in the innovative systems;
- validate the load transfer mechanisms present using field-acquired data;
- identify changes in the innovative deck design procedure that will enhance deck durability;
- identify changes in the innovative deck design procedure that will result in design methodologies that more closely resemble the in-situ behavior;
- quantify the effect of bridge deck-to-diaphragm connection variations;
- provide recommendations for designing and prolonging the life of FRP reinforced bridge decks.

Sources of cracking in the “traditional” deck systems that have been paired with the innovative systems were found to be important as they aided in the proposed research efforts goal of identifying sources of deterioration in the innovative systems. In-situ testing of only the innovative deck systems was carried out. The traditional systems have had a long history of design and construction and therefore, validation of load transfer mechanisms in these structures is not necessary.

The Wisconsin Department of Transportation (WisDOT) IBRC bridges that are the focus of the present research effort are bridges B-20-133/134 in Waupun, Wisconsin and bridges B-20-148/149 in Fond du Lac, Wisconsin. Each bridge group is a traditionally constructed superstructure and a novel FRP-based superstructure. The following sections in the report outline pertinent details of these bridge pairs that set the foundation for the present research effort.

1.3 Bridges B-20-133/134 – Waupun, Wisconsin

The first pair of bridges is located in Waupun, WI. Their WisDOT designations are B-20-133 for the IBRC bridge and B-20-134 for the conventional steel-reinforced bridge deck. An overview photo of the pair of two-span continuous superstructures is shown in Figure 1.1. These bridges are part of the overpass for US 151 above State Highway 26. The location is schematically shown in Figure 1.2. The deck in bridge B-20-133 uses FRP grid reinforcement and FRP stay-in-place (SIP) forms that are coated with an adhesive called Concrecive® (Degussa 2010) and 1/4" (maximum) aggregate. The aggregate

adhered to the SIP form is intended interlock with the concrete poured on top of it so the SIP form can act as positive moment reinforcement for the deck. A mock up is shown in Figure 1.3. The typical bridge deck cross-section is shown in Figure 1.4 and the aggregate-adhered FRP-SIP formwork is shown in Figure 1.5.

The girders in these bridges are two-span continuous precast prestressed concrete girders that act compositely with the bridge deck. Each of the continuous spans is approximately 110 feet long. The girders are standard Wisconsin 54-inch deep I-girders. The two-span superstructure configuration is accomplished by using glass fiber-reinforced polymer reinforcing bars in the bridge deck at the interior pier location. Standard WisDOT continuous barriers are present and the reinforcement at the overhangs and the barriers are conventional mild-steel reinforcing bars.

Evaluation of the structural performance of this deck configuration was done at UW-Madison (Dieter 2002; Dieter et al. 2002). Deck panels were tested to determine critical modes of failure and strength safety factors. Positive moment beams, negative moment beams were also tested for ultimate strengths, and two span fatigue beams were used to test the fatigue strength of the FRP system. Deck panels tested showed the ultimate strength due to punching shear with decks using full coverage, gave a factor of safety exceeding 8. (Dieter 2002; Dieter et al. 2002). The deck system was subjected to 2 million loading cycles in the fatigue beam tests without distress (Dieter 2002; Dieter et al. 2002).

The FRP materials for the SIP form and grid were broken into 3 categories. GV1, GV2, and GV3, GV being an abbreviation for glass/vinylester. The FRP grid used in B-20-133/134 is classified as GV2 and the FRP form is classified as both GV2 and GV3. The areas for this material characterization and analysis are shown in Figure 1.6. Areas 1, 3, 6, and 7 were classified as GV2 material, and areas 2, 4, and 5 are classified as GV3 material (Dietsche 2002a).

Various ASTM tests were conducted to determine the mechanical properties of the FRP grid and SIP forms to establish the criteria needed to develop the IBRC specifications. The FRP grid met all of the IBRC specifications, and the FRP deck GV2 materials performed very well, but the GV3 portions fell short in a number of areas including longitudinal tensile and compressive strength, longitudinal short

beam shear strength, and longitudinal tensile modulus. The GV3 material was thought to have performed at a level less than the target level because of issues that came up during testing (Dietsche 2002a). It was recommended that there be more testing done to improve quality control of FRP manufactured elements and that the material specifications be standardized (Dietsche 2002a).

University of Wisconsin at Madison researchers also evaluated the effects of freeze/thaw on the shear strength of the aggregate coated formwork (Helmuehler et al. 2002). Because the SIP FRP forms are expected to act as the positive moment reinforcement for the bridge deck, it is important to understand how the aggregate/concrete interlock will work after freeze-thaw cycles are endured. To show a difference between control coating and full coating (what is applied in the actual system), specimens were made that experienced no freeze/thaw cycles with no aggregate coating, control aggregate coating, and full aggregate coating. All freeze thaw specimens were tested with the control coating. After experiencing 0 (control), 100, 150, or 200 freeze/thaw cycles while immersed in water. The freeze/thaw control group with control coating showed an ultimate bond stress of 310 psi. Freeze-thaw cycles of 100, 150, and 200, had ultimate bond stresses of 280, 280, and 200 psi, respectively. The results of the experimental testing indicated that a decrease in the available bond strengths from freeze/thaw effects is likely.

Initial in-situ load tests of B-20-133/134 have been conducted by the University of Missouri – Rolla (Hernandez et al. 2005a). Deflections of the girders and deck under loading induced by three-axle dump trucks were measured. Strain gauges were also mounted in the bridge deck on the FRP grid during construction, but the readings from the strain gauges were unreliable. Deflections for both bridges were found to be below the AASHTO limit of $L/800$.

1.4 Bridges B-20-148/149 – Fond du Lac, Wisconsin

The De Neveu Creek IBRC Bridges (B-20-148/149) are located on U.S. Highway 151 south of Fond du Lac, Wisconsin and is part of a new bypass system around the City. A photograph of the structure can be found in Figure 1.7 and its location is illustrated in the map shown in Figure 1.8. Each bridge

superstructure configuration is simple-span with length of approximately 130 feet. Each bridge carries two lanes of highway traffic. The structure is skewed approximately 25 degrees and contains minimal super-elevation. Seven prestressed concrete stringers support the 8" thick FRP-grillage-reinforced concrete deck. The overhangs in the bridge deck are reinforced with traditional epoxy-coated mild-steel reinforcement and the barriers included steel reinforcement as well. The girders are intended to act compositely with the FRP-reinforced deck. Shear transfer is provided by epoxy-coated mild-steel reinforcing bars. Stringers are of WisDOT type 54W precast prestressed concrete and spaced transversely 6'-5" on center. Figure 1.9 provides a cross section of the bridge and illustrates this narrow spacing of the stringers.

The FRP grillage reinforcement is a system of pultruded FRP I-bars developed for implementation in bridges B-20-133 and B-20-148. The FRP reinforcement is a bi-directional grating system consisting of two individual layers of reinforcement, with one layer placed directly over the other layer. Figure 1.10 illustrates the double-mat FRP grillage. Each grating layer contains two separate types of pultruded FRP elements. The primary reinforcing member is an I-bar positioned in the transverse direction of the deck, perpendicular to the traffic lane. Orthogonal to the I-bars, or parallel to the direction of traffic, are cross-rods. Each cross-rod is constructed of three independently pultruded elements, which are assembled in the manufacturing facility. Figure 1.11 illustrates the grillage components. Further details with regard to the grillage system and material properties are available (Jacobson 2004a). The bi-directional grid was found to have met all the IBRC specifications for use as a reinforcing material (Dietsche 2002a).

Tests were done on slabs and beams made using the double layer of grids. Slabs were made to test punching shear capacity, service load performance, fatigue cycling, and load distribution. In addition, beams were created to test negative moment capacity and fatigue. Punching shear and service load performance was tested in several different configurations: simply supported; two-span conditions; and using supports that simulate the 54W precast girder flanges (Jacobson 2004b).

All slabs failed in punching shear though quite a bit of flexural cracking was observed in all the tests. A flexurally restrained system, which was assumed to be the best representation of bridge B-20-148, had factors of safety exceeding 10 when compared to HS-20 wheel loads and fatigue damage after 2 million cycles was found to be negligible (Jacobson 2004b). The beam tests conducted indicated shear was the mode of failure. The FRP I-bar reinforcement also exhibited shear failures. Prior to shear failure, beam tests showed the FRP deck system had a negative moment capacity 2.5 times greater than the ACI nominal moment capacity (Jacobson 2004b).

Initial in-situ load testing was again done by the University of Missouri – Rolla (Hernandez et al. 2005b). Similar magnetically mounted prisms were used to measure deflection of the girders and deck under loading induced by three-axle dump trucks. Readings from internal strain gauges installed during construction were unreliable. Trucks were placed in several configurations to generate maximum deflections. Deflections were found to be under the AASHTO L/800 limit.

1.5 Literature Review

The previous IBRC research efforts described earlier sets the table for the present long-term monitoring effort. It is prudent to review literature that can aid in influencing the development of the methodology used to conduct the present five-year monitoring program. The present section of the report outlines previous research efforts related to construction and monitoring of bridge superstructures and components that involve full-depth FRP panel decks. Research efforts that involve stay-in-place formwork and the impact of freeze-thaw cycling on performance are reviewed. Finally, recent research efforts involving instrumentation and in-situ monitoring of bridge superstructure and superstructure components are described.

Full Depth FRP Panel Decks

The Tech 21 Bridge in Butler County, OH started as a U.S. Department of Defense contract to design a short-span composite bridge that would be able to withstand military tank loading (Foster et al. 2000).

The bridge deck was composed of three sections in a trapezoidal box beam shape. The bridge deck was covered with an asphalt wearing surface weighing more than the bridge itself. The bridge was continuously monitored by an instrumentation system. It used 120 sensors to measure chemical or water incursion in the epoxy adhesive as well as strains. The sensors are hooked up to a data acquisition box just off the bridge that records data 24 hours a day. In August of 1998, load tests were done to measure strain and deflection. The tests subjected the bridge to live loads just under the AASHTO HS-20 truck with deflections were under the AASHTO limit.

Another bridge deck using only GFRP that was heavily monitored and instrumented was constructed in South Carolina (Coogler et al. 2005). The deck was composed of pultruded GFRP tubes that were sandwiched between top and bottom face plates. The tubes and face plates were assembled using adhesive. It was instrumented to measure longitudinal and transverse strain as well as deflection during a long-term monitoring project.

The Salem Avenue Bridge, which was built with four different types of FRP reinforcement, was an experimental venture into bridge deck composites (Reising et al. 2004). The bridge was divided into four regions and a different FRP manufacturer provided an FRP reinforcement system for each region. Out of six manufactures that were invited to participate in the construction, four agreed to participate. Each company provided an FRP system for one fourth of the bridge deck. One company supplied pultruded FRP stay-in-place deck panels that were used as the positive moment reinforcement. The system is very similar to the system used in B-20-133 studied in this thesis. The rest of the systems relied on FRP systems that would have an overlay to protect the surface of the panels. The Salem Avenue Bridge is a five-span continuous haunched steel plate girder. A monitoring program was designed to compare the performance of the four deck panels over two years with static and high-speed truckload test. The three full depth FRP decks showed loss in composite action with the girders shortly after installation. The hybrid system with stay-in-place forms was found to perform very well and exhibit composite action with the girders, similar to the original reinforced concrete deck. However, it was noted, that it did not have the same benefits as the all FRP deck systems including dead load reduction and reduced

construction time (Reising et al. 2004). More on the static testing of the FRP deck panels can be found in (Harik et al. 1999).

Stay-in-Place (SIP) Formwork

Stay-in-place metal formwork (SIPMF) has been used in many states across the country. Inspection techniques for SIPMF and the deterioration of these bridges have been recommended (Grace and Hanson 2004). A survey of the Departments of Transportation in each state was conducted to find out if they used SIPMF and if not, why they did not. The most common reason for not using SIPMF was due to the difficulty of inspecting the underside of the deck. With SIPMF it is impossible to use traditional visual indicators of deterioration. Other Non-Destructive Evaluation (NDE) techniques have to be used to determine the condition of the concrete and the extent of potential damage. Other problems indicated were the potential for increased freeze-thaw damage due to the possibility of moisture retention on the SIPMF and the possible corrosion of the forms over time (Grace and Hanson 2004).

Ten bridges were inspected in the state of Michigan (Grace and Hanson 2004), five had SIPMF and five were conventionally formed with wood. Five full depth cores were obtained from the top of the decks in each bridge depending on accessibility for a total of 50 core specimens. One core from each bridge was visually inspected, two cores were compression tested with vertical strain gauges attached to determine the compressive strength of the concrete, and two were tested with ultrasonic testing using commercial hardware on 1-3in thick slices. Ultrasonic testing was done to find variation in the quality of the concrete through the depth of the deck since this is not possible to find using compression tests. From the cores, the ultrasonic tests showed that both bridge systems had similar pulse velocities in the slices. There were no adverse effects found from the SIPMF through the depth of the deck. The compressive strength tests showed that the concrete used in the decks with SIPMF and without SIPMF were similar as well. The average compressive strength of a deck core without SIPMF was 6.98 ksi and the deck with SIPMF reached 6.65 ksi. The modulus of elasticity was found to be 4,800 ksi without SIPMF and 4,090 ksi with SIPMF (Grace and Hanson 2004).

In addition to the cores, crack density comparisons were made between the decks with and without SIPMF. Crack densities were calculated as length of cracks (in.) per unit area of deck (sq. ft.). The field inspection showed the decks without SIPMF had a slightly higher, but not significantly higher, crack density at $1.7\text{in}/\text{ft}^2$ where the decks with SIPMF had a crack density of $1.5\text{in}/\text{ft}^2$ (Grace and Hanson 2004). A second independent study suggested that SIPMF does not have an adverse effect on the quality of the concrete, but can enhance corrosion effects (Guthrie et al. 2006). Non-corrosive SIP formwork such as the one used in the Waupun Bridge B-20-133 would not have this potentially negative impact.

Impact of Freeze-Thaw Cycles

In order to gauge the impact of freeze/thaw cycles on FRP systems it is necessary to look at previous freeze/thaw testing done on bridge components using FRP materials and systems as well as methods to determine the number of freeze/thaw cycles a bridge in the field will likely see during its service life. The first part of this section will look at previous freeze/thaw testing done on decks made with SIPMF and concrete retrofitted with bonded FRP. Retrofitting in this case means the FRP was bonded to existing concrete components using epoxy adhesive. The second part will look at an algorithm developed to estimate the annual number of freeze/thaw cycles that will occur in a bridge deck based on observed weather data.

In addition to looking at how stay-in-place forms affected the concrete quality as previously described test specimens were made in the lab for freeze-thaw and saltwater tests to look at the contact and bond between the concrete and the SIPMF (Grace and Hanson 2004). Pulse echo tests done before freeze-thaw cycling were used to determine the contact quality between the SIPMF and concrete deck on experimental slabs made in the lab. After the initial loading and cracking, specimens were placed in a holding tank that could fit eight slabs at a time located inside an environmental chamber. The holding tank was filled with water and the temperature was cycled according to ASTM C666 to 300 and 600 cycles. Pulse echo tests done on specimens after 300 freeze-thaw cycles showed a complete loss of

contact. However, they regained contact again after 600 cycles, which was attributed to the accumulation of mineral precipitate between the SIPMF and the concrete (Grace and Hanson 2004).

Retrofitting damaged or cracked concrete structures often involves adhesively bonded FRP plates or sheets. The FRP plates then become tensile reinforcement or confinement for the concrete. One concern about this retrofitting practice is the bond strength between the FRP plate and the concrete especially after freeze/thaw induced strains from thermal expansion and contraction (Bisby and Green 2002). With this retrofitting technique catching on in Canada and the Northern United States, freeze/thaw bond deterioration is a significant concern. The impact of freeze-thaw on this bond was tested through flexural tests done on beams that were reinforced on the bottom with FRP. Four different types of FRP plates from three different manufacturers were used. To ensure that there was no deterioration in the concrete due to freeze-thaw, the concrete mix was designed using accepted admixtures to mitigate freeze/thaw damage (including approximately 7% air entrainment). The specimens were subjected to 0, 50, 150, 200, or 300 freeze/thaw cycles after which they were tested until failure in four point bending.

The experimental results indicated that freeze/thaw did not significantly damage the adhesive bond. In several cases it was seen that the bond strength decreased between the initial test with no freeze/thaw cycles and 50 freeze/thaw cycles. After that, the bond strength increased slightly with more and more freeze thaw cycles in all cases. The failure mode was also documented for each specimen. Some specimens experienced failure with shear peeling where a layer of concrete between the FRP plate and internal steel peeled away. Others experienced debonding at the epoxy-concrete interface where a thin layer of concrete substrate was pulled off with the epoxy. Glass FRP (GFRP) strip system failures varied with some failing by debonding, and some failing in sheet tensile rupture after partial debonding (Bisby and Green 2002).

Instrumentation and In-Situ Monitoring

As state or federal governments own a majority of bridge structures in the United States, a number of government agencies have produced documents recommending procedures for their instrumentation and

monitoring. As of recent times, the Federal Highway Administration (FHWA) produced guidelines for the instrumentation of bridges, specifically those utilizing high performance concretes in their construction (FHWA 1996). Similarly, the National Cooperative Highway Research Program (NCHRP) has developed research initiatives aimed at identifying guidelines for load testing when rating bridges (NCHRP 1998). Conforming to these guidelines, academia frequently carries out the load testing of structures. An excellent summary documenting the need for diagnostic bridge testing and recommendations for the instrumentation of structures is available (Farhey 2005).

The FHWA publication (FHWA 1996) was created in response to the ever-expanding use of high performance concretes in practice and the corresponding lack of pertinent research on the material. The document notes that there are a number of methods available for the instrumentation of structures; however, this discussion is limited to short-term monitoring only. For clarity, short-term monitoring is focused on testing that imposes loads on a structure over a period of a few hours. Specifically, both static and dynamic live load testing can be considered short-term monitoring. Furthermore, long-term loading involves monitoring a structure over a significantly longer period, typically months or years. Long-term monitoring typically focuses on effects due to shrinkage of concrete, creep of a structure, effects due to cyclic changes in temperature, other time-dependent effects, and fatigue.

Both the FHWA and NCHRP recommend that short-term strain acquisition be performed by electrical resistance type gauges. Vibrating-wire type gauges are not capable of rapid acquisition, but are best suited for long-term monitoring of strains that result from temperature-induced effects. Field attachment of strain gauges can be difficult. Weldable strain gauges are very good alternatives for structural steel applications. If monitoring strain in concrete reinforcement is desired, it is recommended that that gauges should be adequately protected from both the placement of concrete and the fresh concrete itself. As each manufacturer produces strain gauges of differing specifications, protection should adhere to the manufacturer's recommendations. Furthermore, the FHWA acknowledges that gauges can be mounted to exterior surfaces of hardened concrete. Although more difficult to perform successfully, gauges can be bonded to smooth surfaces, which typically provide an adequate substrate.

Troweled, broom finish and other rough finished surfaces can be more difficult to install gauges and require surface preparation, but have been performed successfully in the past.

Temperature fluctuations are also of importance when obtaining measurements. Typically electrical resistance strain gauges are available with a temperature-compensated backing to match the intended substrate being monitored. While this backing eliminates much of the potential thermal effect, no two materials have exactly the same coefficient of thermal expansion allowing for the possibility of thermal differences between them. Compensation for these differences is prudent and should be employed for both measuring instruments and also for any changes in the substrate itself (NCHRP 1998). A simple solution recommended to address temperature changes is to conduct testing near sunrise as temperature gradients are at a minimum (FHWA 1996).

Finally, instruments used in any monitoring project require that an appropriate level of resolution be available. In short-term monitoring values of strain smaller than $100 \mu\epsilon$ are common (FHWA 1996). Usage of high impedance strain gauges, typically 350 or 1000 ohms, improves the signal-to-noise ratio of measurements (NCHRP 1998). Resolution of instruments also requires analysis of region of the substrate to be sampled. When monitoring a heterogeneous substrate, e.g. reinforced or prestressed concrete, large gage lengths are required to eliminate local effects (Farhey 2005). Although use of a larger gage length averages measurements over a region, it also limits local effects that may omit valuable readings.

A single, reliable method of measuring displacement was felt to be non-existent for bridge girders (FHWA 1996). However, the use of calibrated surveying equipment or taut-wire measurement has proven to be successful in practice. Taut-wire measurements require the installation of a wire, stretched between two known points of reference with a known tensioning force. Measuring the movement of girder relative to the wire can produce displacement values. However, utilization of precise surveying equipment may offer greater flexibility when site conditions limit physical contact-type measurement of displacements on a bridge. Placement of optical sensors, prisms, or other similar surveying equipment on the structure allow for it to be observed from a distance using a calibrated surveying station.

Displacements can also be measured with electrical transducers, e.g. potentiometers, linear variable

differential transformers (LVDT's) or dial gauges but require a stable mounting location. These methods are typically not practical for displacement monitoring of long-span girders and best suited for local measurements.

Specific product recommendations (FHWA 1996). The following instruments are recommended for use in the instrumentation of structures and monitoring of bridge superstructures and substructures.

Short-term monitoring:

Internal adhered gauges on steel reinforcement -

- Micro Measurements CEA-06-250-UW-350 or CEA-06-250-UW-120
- Micro Measurements CEA-06-250-AE-350

External adhered gauges on hardened concrete -

- Micro Measurements EA-05-20CBW-120 or EA-06-20CBW-120
- Micro Measurements EA-05-40CBY-120 or EA-06-40CBY-120

External weldable gauges on structural steel -

- Texas Measurements TML AWC-8B

Long-Term Monitoring:

Vibrating Wire Gauges –

- Geokon VCE-4200 or VCE-4210
- Roctest EM-5

It should be noted that a substantial body of knowledge regarding bridge monitoring and instrumentation exists in the form of various journal articles, research papers and other engineering publications. In fact, a substantial portion of mechanical measurement curricula may be applied to diagnostic bridge monitoring in the form of displacement and strain measurement. The documents presented in this section are intended to illustrate that significant efforts focusing on structural bridge monitoring have previously been performed by a number of agencies and organizations, and those reviewed are most pertinent to the current effort.

The Ohio Bridge (HAM-126-0881) is a three-span steel girder bridge with a conventionally reinforced concrete deck (Lenett et al. 2001). Construction of the bridge started in 1995 and it was commissioned in 1997. With a goal being to produce a complete scientific view of the loads typical bridge structures endure over the course of their service lives, researchers monitored loads and displacements present in the bridge for nearly all aspects of the project (Lenett et al. 2001). Data was recorded during fabrication of the steel stringers, during transportation to the jobsite, and through erection. Long-term strains and temperature data are still being monitored today through a permanent data acquisition system. The effort put forth by the researchers for this investigation and subsequent evaluation was exhaustive and included a multitude of topics related to conventionally-constructed steel stringer bridge structures. For this reason, only aspects of the project's instrument evaluation and selection and live load testing were reviewed.

The researchers conducted an extensive evaluation of commercially available instrumentation equipment citing a number of conclusions. Extensive discussion of the instrumentation implemented was provided (Lenett et al. 2001). Instrumentation devices intended to monitor slowly-varying phenomena were read using a Campbell Scientific CR-10 system. The unit was capable of scanning one channel at a time and obtains data at 64 Hz. High-speed devices were read using a MEGADAC system produced by Optimum Electronics. The system utilized a high-speed interface (up to 25 kHz) between the analog-to-digital converter and a computer. This allowed sampling of data during higher speed testing. This system was limited to the high-speed devices and installed in a permanent structure located near the bridge. Displacement transducers used for the project were Celesco PT101-SWP string potentiometers and Trans-Tek 244 DC-LVDT linearly variable differential transformers (LVDTs).

Electrical resistance gauges selected for the high-speed data acquisition varied according to their installation locations (Lenett et al. 2001). Gauges to be mounted on the steel stringers were of weldable and manufactured by Texas Electronics. Strain gauges of this type were also located on the transverse diaphragms, or cross-frames, of the bridge in multiple locations. Gauges to be installed in the concrete deck were of embedded type and cast directly into specified location in the concrete. Special care was

taken during casting of the deck to ensure correct location of each sensor. The embedded sensors were Micro Measurements EGP series gauges.

Two live load tests were conducted. Vehicles specified for testing were two three-axle dump trucks, of which the independent loads were documented at the time of testing (Lenett et al. 2001). It was acknowledged that the weight of each truck pair varied from the benchmark to in-service tests and properly recognized in all following results. The first test was a static, post-construction test to benchmark the load and displacement data of the structure prior to traffic loading. Eleven different load cases were conducted at varying locations to profile the strain response of the structure. Each load case consisted of locating the test vehicles at points of interest along the spans. The trucks were always positioned adjacent to each other, or longitudinally in a tailgate-to-tailgate fashion.

A follow-up load test was conducted once the structure had been in service for over one year (Lenett et al. 2001). Similar truck positions were utilized as the benchmark test; however, the in-service condition prohibited locating trucks adjacent to each other. In order to conduct each load case, control measures were installed to limit traffic to only a single lane of the bridge. To obtain data for each load case, the test vehicle was positioned in the closed lane next to the open traffic lane. When ready, temporary traffic stops were imposed to eliminate transient loading from passing vehicles and data collected. As only a single lane of the bridge was loaded with a test vehicle, as opposed to the twin loading of the benchmark test, corresponding results were then superimposed for comparison.

Results from the two sets of load tests yielded the following conclusions. The intermediate cross-frames contributed to the internal redundancy of the structure and spread the distribution of loads laterally throughout the structure. These frames were located at 14' intervals between all stringers. Composite action of the stringers and deck exists throughout the center span, which was intended for in design. Partial composite action was observed in exterior spans during the benchmark load test. This partial composite behavior, although common in structures of this type, was not intended. However, after completion of the second load test, the eastern exterior span had lost all indication of partial composite action while the western exterior span had decreased its degree of this behavior.

The new Route S655 Bridge over the Norfolk/Southern rail line near Landrum, South Carolina, replaced an antiquated steel and timber deck structure. The previous two-lane structure had been in service as early as 1946 and was not in sufficient condition to safely carry two lanes of modern traffic. Completed in 2001, the new structure spans 60 feet with five steel stringers and a unique glass-fiber reinforced polymer (GFRP) deck (Turner 2003). Steel wide-flanged stringers are located with an 8'-0" center-to-center spacing, which, as indicated by the author is intended to challenge the limits of the GFRP deck (Turner 2003).

The commercially available deck panels are composed entirely of built up sections, each consisting of approximately ten pultruded elements (Turner 2003). The *Duraspan*® panels were produced by Martin Marietta Composites (www.martinmarietta.com/Products/composites.asp). Each element is connected to adjacent elements with an adhesive resin. Pre-assembled panels composed of these elements were delivered to the site and installed longitudinally atop each stringer (Turner 2003). Additionally, each deck panel was intended to act compositely with the steel stringers and thus significant investigation of the connection's shear transfer performance is documented (Turner 2003). The experimental testing incorporated composite behavior the stringers but the steel stringers were designed to act in a non-composite manner.

A variety of instruments were installed on the bridge for the data acquisition during load tests (Turner 2003). Duplicate electrical resistance strain gauges were installed at eighth points along the span. Weldable gauges were installed on the steel girders and oriented longitudinally to obtain strain distribution through the depth of the stringers. Complementing the weldable gauges, adhesive-applied gauges were installed on the GFRP deck in both longitudinal and transverse directions. The transverse gauges on the deck were intended to provide strain data relating to the behavior of the deck in resisting wheel loads. Longitudinal gauges were intended to produce strain data that would relay information pertinent to the degree of composite behavior of the deck and stringers. In addition to the strain gauges, draw wire transducers (DWT) were installed to measure vertical deflection of the deck relative to the top

of the stringers. Finally, surveying prisms were installed at locations along the lower flange of the stringers to monitor the deflection.

In-situ load testing utilized three-axle dump trucks classified between an AASHTO HS23-44 and HS25-44 load (Turner 2003). Five load testing scenarios were conducted. The objectives of these load tests were to determine behavior in both instrumented and un-instrumented areas of the structure; to determine behavior of the GFRP panels under two-lane loading; quantifying the negative bending behavior of the GFRP deck over an interior stringer; and to determine positive bending response of the GFRP deck between stringers (Turner 2003).

Strain distribution through the depth of the cross-section was analyzed to evaluate the degree of composite action between girders and GFRP decking (Turner 2003). It was noted that the magnitude of many of the values recorded in these load tests were equal to or smaller than the accuracy of the data acquisition system. The in-situ load testing indicated that partial composite action was present between the girders and deck. Measured lane-load moment distribution factors of the steel stringers were also evaluated and compared to design procedures found in the U.S. design specifications (AASHTO 2002; AASHTO 2006). The in-situ load testing results indicated that load distribution factors were consistent with values predicted by expressions found in these specifications (Turner 2003).

The Fairground Road Bridge is a three-span, two-lane structure spanning the Little Miami River in Greene County, Ohio (BDI 2002). The tested structure is composed of structural steel stringers and the same GFRP deck panels utilized in the S655 Bridge (Turner 2003). Composite action is achieved steel studs in a cellular pocket filled with high strength grout. The focus of investigation for this project was primarily the analysis of composite behavior between the FRP deck panels and steel stringers and load rating of the structure.

To study the composite behavior of the deck system and stringers, strain transducers manufactured by Bridge Diagnostics Incorporated (www.bridgetest.com/index.htm) were installed on the stringers of the structure with a small number of transducers installed directly on the FRP deck panels for verification of results. These strain transducers are shown in Figure 1.16. Four locations along the length

of the bridge were selected as instrumentation points. These locations leverage symmetry of the superstructure to reduce the cost of installation. A top and bottom flange longitudinal transducer was installed on each of the stringers at instrumentation points for a total of 32 units. Verification of strain distribution through the bridge cross-section was conducted via two additional longitudinal transducers installed on the FRP deck near the top flange of an interior stringer at mid-span of the outer span. Also, two transducers were installed transversely on the FRP deck between stringers to monitor the bending behavior of the FRP deck itself. Vertical displacement of the FRP deck was monitored using linearly varying differential transformers (LVDT) were installed atop the pier as well (BDI 2002).

The load test consisted of slowly moving (less than 5 mph) three-axle dump truck across the structure in a series of four prescribed paths. The authors did not disclose detail of load location but did note that duplicate runs were performed to check consistency of data. Stationary, static load testing of the structure was not performed. While truck passes were being made, continuous monitoring of the sensors occurred. Relative distance of the vehicle along the bridge was also monitored. It is of note that data acquisition of the live load test was sampled at a rate of 40 Hz. A final high-speed test was also conducted with the test vehicle moving at approximately 45 miles-per-hour to estimate the impact effect of design vehicles.

The data collected produced a number of interesting results. Using the assumption of elastic response the authors calculated the neutral axis of each stringer based on the strain readings recorded. The location of the neutral axis of each stringer was found to be consistent with others in the structure and also indicated some degree of composite action (BDI 2002).

Structure B of the Bridge Street Bridge in Southfield, Michigan utilizes a double-tee beam stringer system that utilizes CFRP tendons in lieu of conventional steel prestressing tendons (Grace et al. 2002; Grace et al. 2005). Additionally, external post-tensioned carbon fiber cables were draped along the lengths of each beam to provide supplementary longitudinal strength while similar carbon fiber cables were post-tensioned transversely at each stringer diaphragm. The concrete deck is reinforced with CFRP grids, which is topped with a conventional concrete wearing surface. The only conventional

reinforcement present in each beam is mild steel shear stirrups located throughout the web of each double-tee. Six of the beams on Structure B were instrumented for long-term monitoring and subjected to an in-situ load test to study their behavior relative to AASHTO design specification procedures (AASHTO 2002; AASHTO 2006).

Each of the three superstructure spans consists of four adjacent double-tee beams each reinforced longitudinally using LeadlineTM prestressing tendons (www.mkagaku.co.jp/english/corporate/008.html) and four external, post-tensioned carbon-fiber composite cables (CFCCTM, www.tokyoropeco.jp/english/). All four girders in a span were also post-tensioned transversely with CFCC tendons. A lateral diaphragm cast into each girder provides anchorage for each tendon. Horizontal deck reinforcement is composed of multiple bi-directional NEFMACTM (www.autoconcomposites.com/index.html) grids of 0.394" diameter carbon fiber reinforcing bars. Specified 28-day concrete strengths were 7,500 psi for the girders and 5,500 psi for concrete deck topping.

As monitoring of this structure was conducted from fabrication through to construction and beyond, a majority of all instruments were installed at the precast facility. All twelve double-tee beams were instrumented to monitor stress levels during fabrication and prestressing. However, only six beams were instrumented with long-term monitoring equipment for in-situ observation. Beams to be monitored in the field contained both internal and external vibrating-wire strain gauges installed at the mid- and quarter-span points of each beam, as well as displacement sensors. At each strain monitoring section, (quarters and mid-span) gauges were installed up both webs of the double-tees. Gauges were located near the bottom of each web, at mid-height, near the top in the decking, and one in the concrete topping. Each beam contains a total of 30 gauges with only the nine concrete topping sensors installed in the field.

Positioning of the six long-term instrumented beams was such that the width of one entire span was instrumented and a single representative beam was instrumented in the other two spans. Although not relevant to the scope of this discussion, it is interesting to note that a load cell was installed for each

longitudinal external post-tensioned cable for the instrumented beams to monitor their levels of prestressing force throughout the life of the structure.

Two three-axle dump trucks were used in four separate load cases during the in-situ (field) load testing. Each test required multiple readings because the vibrating-wire strain gauges needed to "settle". Vehicles were located in their desired position and remained in place for a period no less than five minutes to obtain adequate strain readings. During the interior beam tests, trucks were positioned for maximum positive bending moment adjacent to the sidewalk on the span. The sidewalk limits the distance in which a vehicle may approach the exterior beams. One test was conducted in the fully instrumented north span another was carried out in the complimentary south span. For the exterior load test the trucks were positioned to produce maximum positive bending moment near the exterior parapet of the span. Similar to the interior beam tests, the exterior load tests were conducted in the fully instrumented north span and also the middle span for comparison.

The authors combined the data from the interior and exterior load tests through superposition of strain readings on each beam to compute distribution factors for the girders. Distribution factors were calculated based on total strain in a specific beam relative to total strain of all beams. The calculated distribution factors agreed very well with distribution factors obtained using U.S. design specifications (AASHTO 2002; AASHTO 2006; Grace et al. 2002; Grace et al. 2005). It was recommended that usage of the AASHTO specifications (AASHTO 2002; AASHTO 2006) was appropriate for design of prestressed concrete beams externally reinforced with carbon-fiber reinforcement (Grace et al. 2002; Grace et al. 2005).

1.6 Literature Synthesis

The use of Fiber-Reinforced Polymer (FRP) components in bridges has significantly advanced from complete FRP bridge decks to integrating FRP into the concrete bridge deck and girders. With regard to Wisconsin's IBRC bridges, experimental testing prior to construction showed that the FRP materials can meet the requirements for use as reinforcement in a concrete bridge deck with material standardization. In

addition, specimens tested showed a capacity above what would be required in the field with factors of safety approaching 5-10 for the different deck configurations. Therefore, the strength of the deck systems are more than adequate, but their long-term performance and the impact of environmental conditions on their performance remain uncertain.

Research done by others indicated that steel stay-in-place formwork was found to have a negligible effect on the quality of concrete in a bridge deck. Even though these steel forms were not expected to act as reinforcement, the concrete appeared to bond to the metal forms after exposure to freeze-thaw cycles. Once the test specimen cracked, the bond between the steel SIP form and concrete was almost non-existent. Therefore, the steel-SIP form deck is not expected to hurt the quality of the concrete, but simple cracking can break the bond between the SIP form and concrete. This indicates that there is the potential for reduction in shear strength at this same interface when FRP-SIP form is utilized. The presence of the bonded aggregate on the FRP-SIP form will help resist this bond-breaking scenario, but former research suggests that this needs further evaluation.

Freeze-thaw testing done on FRP retrofitted to concrete has shown varying results. In the case of externally bonded FRP plates, freeze-thaw cycling appeared to increase the bond capacity. This, however, is a very different scenario from how the new decks are constructed with FRP reinforcement. Testing done using specimens modeled the system in bridge B-20-133 indicated that freeze-thaw cycling had some impact on the shear strength at the FRP formwork - concrete interface, but the results were largely inclusive as a result of the testing arrangement. The effects of freeze-thaw cycling on a deck with FRP-SIP forms and the understanding that water will get down to the level of the FRP-concrete interface remains a critical issue to be understood in order to assess the long-term performance of the FRP-SIP deck system.

A great deal of information exists pertaining to the topic of bridge monitoring. However, information directly related to the static, live load testing of structures is not easily obtained. A vast majority of bridges in the United States are inspected from a visual perspective only as the initial cost of instrumentation often prohibits the scientific evaluation of them. Structures selected for monitoring are

limited among the bridge inventory, but this monitoring has proven to provide valuable insight into their performance. Review of these monitoring efforts also offered insight into procedures used for successful monitoring of the IBRC structures. Methods of interpreting data relating to the distribution of vehicle loads among bridge stringers and evaluation of the composite nature of each different structure are presented in the research carried out, providing a rational basis for implementation on the IBRC structure of this study.

The successes of these projects provide a proving ground for use of commercially available instruments. The monitoring efforts reviewed illustrate the preference of electrical-resistance strain gauges for short-term load testing, as well as the use of high-speed data acquisition systems for data collection. Additionally, testing illustrated the benefits of vibrating-wire gauges, but also the lengthy acquisition process required if they are used. The use of removable strain sensors composed of electrical resistance gauges appears very beneficial for the present monitoring effort.. Extensive amounts of labor were required for the attachment of electrical resistance gauges. Experiences of the WisDOT IBRC team (e.g. inconclusive strain gauge instrumentation of the De Neveu Creek Bridge) indicate that it is exceedingly difficult and unreliable to use field-bonded strain gauges. Thus, removable sensors are preferred for the present monitoring effort to ensure their repeated use over time. Fabrication of strain sensors in a controlled environment increases consistency among the sensors and also limits possible damage from peripheral sources, e.g. the environment, wildlife and possibly vandals.

The previous research efforts suggest that cost of instrumentation is also of concern. The suite of equipment utilized in the four monitoring projects reviewed noted incorporated a substantial financial investment. The budget for the present five-year monitoring effort is very, very low. Use of compact electrical-resistance strain gauges bonded directly to the superstructure produces valuable information at a low cost when the substrate is composed of homogenous materials such as steel stringers. However, experience has proven that larger, more costly instruments are required for satisfactory strain data collection on heterogeneous materials such as concrete. The cost of larger gauges or removable sensors frequently exceeds \$500 per instrument, commanding a significant per-gauge investment. The instrument

array specified for this project, which will be outlined later in this report, includes 32 locations of strain gauges. Considering the per-instrument cost of commercially available sensors and the financial capital available for this project development of an alternative, a cost effective instrument is imperative.

Finally, the previous work conducted on the Waupun and De Neveu Creek IBRC bridges provides a baseline for analysis of new data generated in the present effort. The load deflection data obtained in these previous efforts illustrates global performance of the structure and performance conforming to conventional U.S. design specifications. Collection of further data is required as a number of performance aspects of the novel structures are not fully understood. For example, it would be very beneficial to have information describing the strain profile of the girders and concrete deck will allow for assessment of composite action between the superstructure elements. Documentation of any variation in the strain profile of the structure is important and provides insight into its performance over time. Observation of the transverse behavior of the FRP-reinforced concrete decking with very closely-spaced concrete wide-flange girders is also required. Assumptions made in the design of the concrete deck require verification if the system is to be implemented elsewhere. Finally, an understanding of the strip widths of bridge deck with FRP-SIP formwork as positive moment reinforcement requires further evaluation.

1.7 Layout of Research Report

This research report outlines activities conducted during a five-year monitoring program of two of three Wisconsin IBRC bridges. The development of reliable and portable strain sensors is reviewed in detail. Experimental testing designed to quantify the degradation in bond between concrete and the FRP-SIP formwork that results from freeze-thaw cycling is outlined. Statistical evaluation of this bond strength is discussed and 95% confidence shear strengths are given for scenarios that involve freeze-thaw cycling.

The benchmark condition evaluation of bridges B-20-133/134 and B-20-148/149 is discussed. Thorough evaluation of nondestructive evaluation (NDE) methodologies and equipment is conducted and recommendations related to the appropriate use of NDE methods as part of the present effort are made.

Detailed discussion of the in-situ instrumentation and load testing protocols are provided. Two in-situ load tests conducted in July 2007 and July 2009 are outlined. Comparison of lane load girder distribution factors measured to those recommended using U.S. design specifications is made. Measured wheel load distribution widths within the FRP-SIP bridge deck are compared to those computed using U.S. design specification procedures and strain profiles over the height of girders validating composite behavior is also provided. Comparisons of the load testing results with those of previous IBRC efforts and those obtained over the two-year interval between in-situ load tests that were included in this effort are also given.

Finally, the initial condition of the Waupun IBRC bridge decks suggests that the significant transverse cracking present in both bridge decks may be caused by shrinkage-induced cracking. Therefore, an analytical effort designed to simulate the effects of traffic-induced loading and shrinkage-induced strains on bridge deck behavior is undertaken and described in detail.

1.8 References

- AASHTO. (2002). *Standard Specifications for Highway Bridges, Customary Units, 17th Edition*, American Association of State Highway and Transportation Officials, Washington, DC.
- AASHTO. (2006). *AASHTO LRFD Bridge Design Specifications Including 2006 Interim Revisions, Customary U.S. Units, 3rd Edition*, American Association of State Highway and Transportation Officials, Washington, DC.
- ASCE. (2005). "Report Card for America's Infrastructure." American Society of Civil Engineers, Reston, VA.
- BDI. (2002). "Load Test and Rating Report - Fairground Road Bridge, Greene County, Ohio." Bridge Diagnostics, Inc. (www.bridgetest.com/index.htm)
- Berg, A. C., Bank, L. C., Oliva, M. G., Russell, J. S., and Jeffrey, S. (2004). "Construction of a FRP Reinforced Bridge Deck on U.S. Highway 151 in Wisconsin." 83rd Annual Meeting of the

- Transportation Research Board, National Research Council, Transportation Research Board, Washington, DC, CD-ROM.
- Bisby, L. A., and Green, M. F. (2002). "Resistance to Freezing and Thawing of Fiber-Reinforced Polymer-Concrete Bond." *ACI Structural Journal*, 99(2), 215-223.
- Conachen, M. J. (2005). "Modular 3-D FRP Reinforcing System for a Bridge Deck in Fond du Lac, Wisconsin," University of Wisconsin, Madison, WI.
- Coogler, K., Harries, K. A., Wan, B., Rizos, D. C., and Petrou, M. F. (2005). "Critical Evaluation of Strain Measurements in Glass Fiber-Reinforced Polymer Bridge Decks." *Journal of Bridge Engineering*, 10(6 November/December), 704-712.
- Degussa. (2010). "Concresive® 1090 Technical Data Guide."
<http://www.mullerconstructionsupply.com/EpoxyAndGrout.html>.
- Dieter, D. A. (2002). "Experimental and Analytical Study of Concrete Bridge Decks Constructed with FRP Stay-In-Place Forms and Grid Reinforcing," MS Thesis, University of Wisconsin at Madison, Madison, WI.
- Dieter, D. A., Dietsche, J. S., Bank, L. C., Oliva, M. G., Russell, J. S., and Jeffrey, S. (2002). "Concrete Bridge Decks Constructed with Fiber-Reinforced Polymer Stay-In-Place Forms and Grid Reinforcing." 81st Annual Meeting of the Transportation Research Board, National Research Council, Transportation Research Board, Washington, DC, CD-ROM.
- Dietsche, J. S. (2002a). "Development of Material Specifications for FRP Structural Elements for the Reinforcing of a Concrete Bridge Deck," MS Thesis, University of Wisconsin at Madison, Madison, WI.
- Dietsche, J. S. (2002b). "Development of Material Specifications for FRP Structural Elements for the Reinforcing of a Concrete Bridge Deck," University of Wisconsin-Madison, Madison, WI.
- Farhey, D. N. (2005). "Bridge Instrumentation and Monitoring for Structural Diagnostics." *Structural Health Monitoring*, 4(4), 301-318.

- FHWA. (1996). "Implementation Program on High Performance Concrete - Guidelines for Instrumentation of Bridges." *FHWA-SA-96-075*, Federal Highway Administration, Washington, DC.
- FHWA. (2005). "IBRC Program Information, <http://ibrc.fhwa.dot.gov/know/program.cfm>." FHWA, ed.
- Foster, D. C., Richards, D., and Bogner, B. R. (2000). "Design and Installation of Fiber-Reinforced Polymer Composite Bridge." *Journal of Composites for Construction*, 4(1), 33-37.
- Grace, N., and Hanson, J. (2004). "Inspection and Deterioration of Bridge Decks Constructed using Stay-In-Place Metal Forms and Epoxy-Coated Reinforcement." Department of Civil Engineering, Lawrence Technological University, Southfield, MI.
- Grace, N., Navarre, F. C., Nacey, R. B., Bonus, W., and Collavino, L. (2002). "Design-Construction of Bridge Street Bridge - First CFRP Bridge in the United States." *PCI Journal*, 47(5), 20-35.
- Grace, N. F., Roller, J. J., Nacey, R. B., Navarre, F. C., and Bonus, W. (2005). "Truck Load Distribution Behavior of the Bridge St. Bridge, Southfield, Michigan." *PCI Journal*, 50(2), 77-89.
- Guthrie, W. S., Frost, S. L., Birdsall, A. W., Linford, E. T., Ross, L. A., Crane, R. A., and Eggert, D. L. "Effect of Stay-In-Place Metal Forms On Performanc of Concrete Bridge Decks. ." *Transportation Research Board Annual Meeting*, Washington, DC, (CD-ROM).
- Harik, I., Alagusundaramoorthy, P., Siddiqui, R., Lopez-Anido, R., Morton, S., Dutta, P., and Shahrooz, B. "Static Testing on FRP Bridge Deck Panels." *International Society for the Advancement of Material and Process Engineering Symposium & Exhibition*, 1643-1654.
- Helm Mueller, E. J., Bank, L. C., Dieter, D. A., Dietsche, J. A., Oliva, M. G., and Russell, J. S. (2002). "The Effect of Freeze-Thaw on Bond Between FRP Stay-In-Place Deck Forms and Concrete." CDCC 2002, 2nd International Conference on Durability of Fiber Reinforced Polymer (FRP) Composites for Construction, Montreal, Quebec, CAN, 1643-1654.
- Hernandez, E., Galati, N., and Nanni, A. (2005a). "In-situ load testing of Bridges B-20-133 and B-20-134, Waupun, WI. ." Center for Infrastructure Engineering Studies, University of Missouri – Rolla.

- Hernandez, E., Galati, N., and Nanni, A. (2005b). "In-situ load testing of Bridges B-20-148 and B-20-149, Fond du Lac, WI. ." Center for Infrastructure Engineering Studies, University of Missouri – Rolla.
- Jacobson, D. A. (2004a). "Experimental and Analytical Study of Fiber Reinforced Polymer (FRP) Grid-Reinforced Concrete Bridge Decking," University of Wisconsin-Madison, Madison, WI.
- Jacobson, D. A. (2004b). "Experimental and Analytical Study of Fiber Reinforced Polymer (FRP) Grid-Reinforced Concrete Bridge Decking," MS Thesis, University of Wisconsin, Madison, Wisconsin.
- Lenett, M. S., Hunt, V. J., Helmicki, A. J., and Aktan, A. E. (2001). "Instrumentation, testing, and monitoring of a newly constructed reinforced concrete deck-on-steel girder bridge- Phase III." *Research Report UC-CII-01/1*, University of Cincinnati, Cincinnati, OH.
- NCHRP. (1998). "Manual for Bridge Rating Through Load Testing." *Research Results Digest 234*, National Cooperative Highway Research Program.
- Reising, R., Shahrooz, B., Hunt, V., Neumann, A., and Helmicki, A. (2004). "Performance Comparison of Four Fiber-Reinforced Polymer Deck Panels." *Journal of Composites for Construction*, 8(3 - June), 265-274.
- Turner, M. K. (2003). "In-situ Evaluation of Demonstration GFRP Bridge Deck System Installed on South Carolina Route S655." University of South Carolina.



Figure 1.1 South Side of US 151 Overpass bridge, B-20-133



Figure 1.2 Location of B-20-133/134

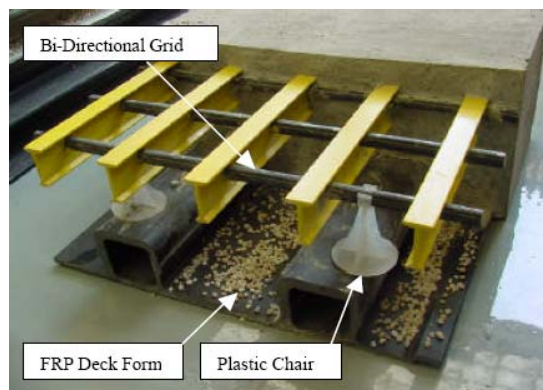


Figure 1.3 Mock-Up of the SIP FRP Form and FRP Reinforcement (Dieter et al. 2002)

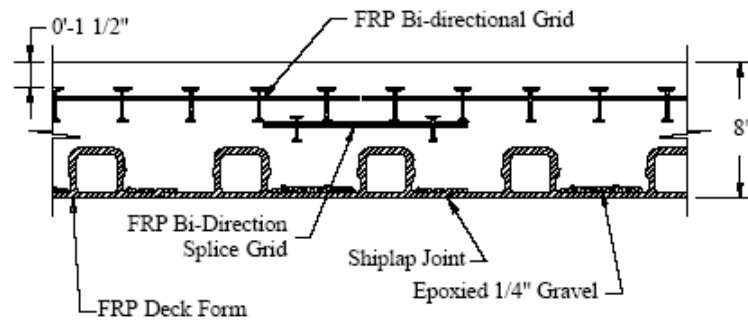


Figure 1.4 Cross-Section of B-20-133 Bridge Deck (Dieter et al. 2002)



Figure 1.5 Stay-in-place Decking with Concrete and Aggregate (Berg et al. 2004).

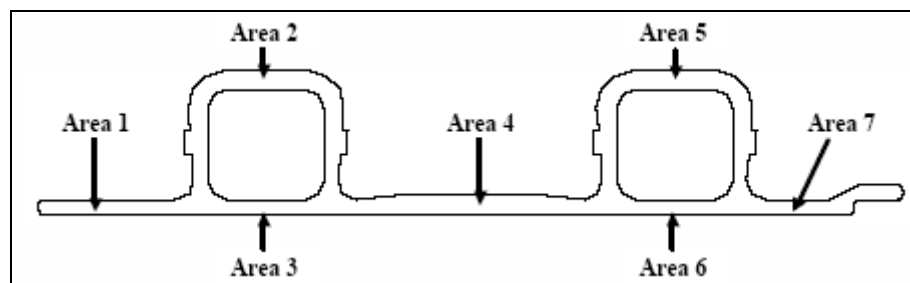


Figure 1.6 Areas of FRP SIP Form (Dieter et al. 2002)



Figure 1.7 The De Neveu Creek Bridge, WI B-20-148.

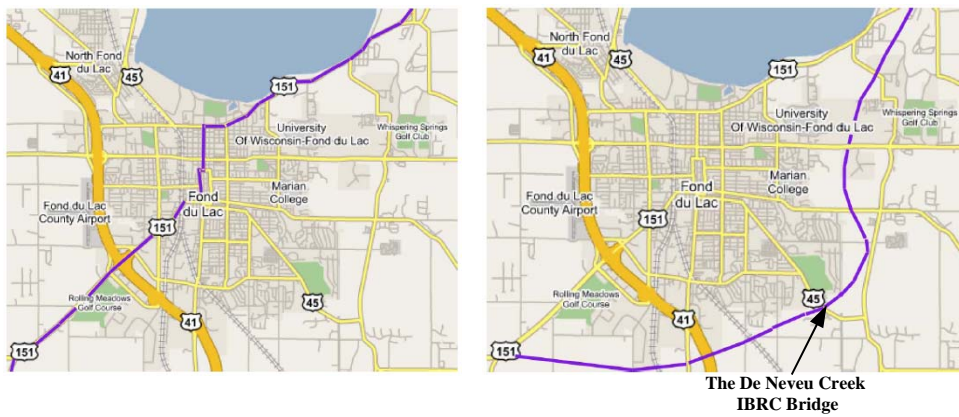


Figure 1.8 Wisconsin Highways 151 before (left) the bypass and after (right). Adapted from (Conachen 2005).

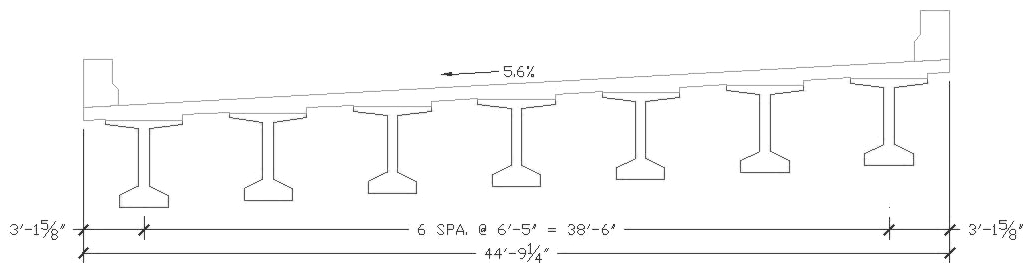


Figure 1.9 Cross section of the De Neveu Creek Bridge.

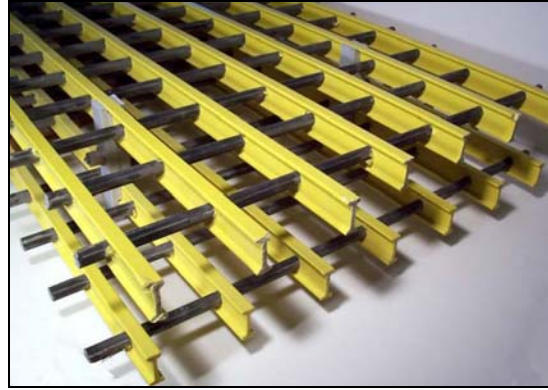


Figure 1.10 Assembled FRP grillage (Conachen 2005).

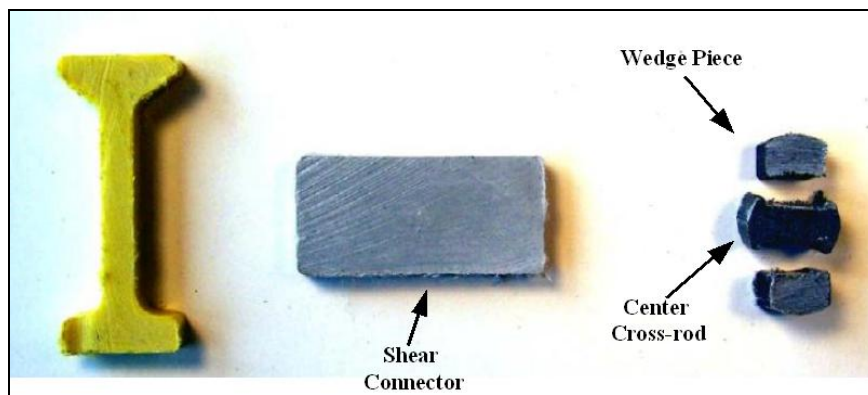


Figure 1.11 Cross sections of FRP materials used (Conachen 2005).



Figure 1.12 Bridge Diagnostics Strain Transducer (BDI 2002).

This page has intentionally been left blank.

Chapter 2

Sensor Development and Laboratory Studies

2.1 Introduction

Although the majority tasks of this research were focused on in-situ monitoring and load testing of bridges associated with the IBRC effort, laboratory work was also performed to develop in-situ load test sensors and seek understanding of potential long-term performance issues and parameters related to the IBRC bridge superstructure configurations and components. A novel portable strain sensor was developed and tested in laboratory. In order to understand the deterioration of the deck using FRP sit-in-place formwork subjected to freeze-thaw attack which is a potential cause for deterioration in Wisconsin, concrete prisms bonded with FRP strips were subjected freeze-thaw cycles and tested under direct shear force. Several Non-Destructive Evaluation (NDE) methods were studied and evaluated through literature review and Infrared Thermography (IRT) was used to test a prototype bridge deck with FRP sit-in-place formwork to evaluate their likelihood in detecting damage and deterioration in the IBRC bridge decks. This chapter of the research report outlines details related to these initiatives.

2.2 Development of Portable Strain Sensors

In order to properly monitor the strain response of the IBRC bridges over the long term, proper instruments to measure the strain should be selected. Normally, electrical resistance strain gages are the best instruments to measure strain if the short-term behavior of the structure is of interest. However, installation of individual electrical resistance gauges directly to the structure has a number of drawbacks. Primarily, the labor involved in properly bonding the gauges to a structure is significant. The reliability of field applied gauges is also questionable. Previous attempts to record strain response of the IBRC bridges by other researchers testify to this. Additionally, gauges installed directly on the structure are not removable and are vulnerable to environmental degradation and damage. After consulting manufacturers

of portable strain instrumentation devices within the industry, it was found that the cost to implement the proposed instrumentation plan would be prohibitive if a pre-manufactured system was utilized. As a result, it was decided that development of a new cost effective, reliable and removable strain sensor would be the best option for the present research effort.

The Portable Sensors

The quarter bridge configuration of the Wheatstone bridge can be constructed rapidly and offers an acceptable degree of precision. It was felt that the additional sensitivity gained by implementation of a half or full bridge circuit did not justify the increased expense and labor associated with these configurations. For example, implementation of a full bridge circuit requires more sensors and the installation of three additional strain gages. While the expense of additional strain gauges is directly offset by the elimination of completion resistors used in a quarter bridge circuit, the installation of the additional gauges incorporates added labor. This stems from the fact that installation of circuit completion resistors is quite simple relative to the installation of four gauges in the field. Bonding of multiple strain gages in a constrained region becomes increasingly difficult and leaves significantly less room for error. Thus, there is additional labor cost and installation time with full and half bridge circuits. If sources of error and signal conditioning are addressed (*e.g.* lead wire resistance, temperature compensation) the quarter bridge configuration can provide satisfactory measurements at low cost. Using this rationale, the quarter bridge configuration was selected for the new strain sensor.

The strain gages selected were Micro-Measurements CEA-06-250UN-350 gauges. These 350-ohm gages offer an increased electrical sensitivity over conventional 120-ohm gages. Also, a thin coating is installed over the foil resistive array by the manufacturer, adding increased protection. It is important to note that all strain gages were bonded according to the procedures outlined by the manufacturer in a low modulus carrier to be described in greater detail. All gauges used for this project were bonded to their substrate carrier with Micro-Measurements M-Bond 200 adhesive.

The portable strain sensor is really nothing more than a low-modulus of elasticity material carrier for the strain gauges and conventional Vishay strain gauges. A number of materials were evaluated

before final selection for the strain gauge carrier. To achieve the objective of developing a removable and portable strain sensor, it was decided that the quarter bridge strain gauge needed to be bonded to a suitable carrier that could be installed and removed each time a load test was executed. This carrier would then be bolted to the structural component, transmitting any strain to the carrier then the strain gauge. A wide array of materials for embedded and externally mounted sensors are available, however, they are most often polymer composites and low modulus metals (*e.g.* Aluminum).

Based on the preliminary research conducted (Schneeman 2006), a prototype sensor constructed of Series 6/6 Nylon was manufactured by ROMUS, Incorporated (ROMUS 2005). Its low modulus (approximately 400,000 psi) and relatively low cost was ideal for both performance and mass-production of sensors. The material is also easily machined allowing for detailed designs to be translated into prototypes. The prototype of the sensor was a rectangular bar 1.00" wide by 4.00" long with a thickness of 0.25." Figure 2.1 illustrates the final geometry of the prototype while Figure 2.2 shows completed strain sensors without their protective external coating or electrical connector tabs.

Two 0.386 in. diameter holes were located 0.50" from each end centered on the width of the sensor carrier, allowing for mechanical anchorage via epoxy-adhered threaded studs. These holes define the effective gage length of the sensor to be 3.00." Additionally, a central depression 0.50" wide by 1.50" long was machined 0.20" into the sensor. A secondary depression 0.20" deep and 0.25" wide was machined into a single end of the main depression to allow for strain relief of the lead wires. Strain relief is achieved by bending the lead wires into the depression and anchoring them with a quickset epoxy. These depressions allow for the strain gage, necessary soldering and lead wire adhesive to be below the surface of the sensor, reducing the risk of accidental damage to the gage. Further detail of the sensors can be found in Schneeman (2006).

To attain a satisfactory level of environmental protection, the central depression of each sensor is filled with a rubber-like compound, M-Coat J, manufactured by Micro-Measurements. This material is a two-part polysulfide liquid polymer that completely seals the gage (Micro-Measurements 2004). The polymer is relatively soft and will not affect the strain response of the sensors. Care was taken to isolate the exposed lead wires and gage from the M-Coat with a Teflon-adhesive tape provided by Micro-

Measurements. Additionally, to ensure rapid deployment of each sensor, individual lead wires exiting the strain sensor contain an individual, insulated quick-disconnect tab. These connections can be made quickly and repetitively without an appreciable amount of electrical resistance. Male tabs were soldered to the lead wires on the sensor to ensure a durable connection, while the female tabs will be installed on the lead wires of the bridge by crimping.

Anchorage of the Sensor

Mechanical anchorage for each sensor is to be provided by two 1/4" diameter, 3" long bolts with standard plain washers on each face of the sensor. Each stud utilized 1-inch embedment into the cover concrete. Each bolt was A307 steel. An appropriate size nut with 120 lb-in of torque, confines the washers and sensor. Deformed washers, also called star washers, are not recommended, as they will significantly scar and deform the nylon when tightened. Each bolt is to be set in a 5/16" diameter hole and adhered with a high strength construction epoxy. Figure 2.3 is a schematic depicting typical field installation. Transfer of load is accomplished by friction between the substrate, washers, and the nylon strain gauge carrier. It does not rely on bearing of bolts. Each attachment hole on the sensor is oversized for two primary reasons. The over-sizing eliminates the possibility of the bolts bearing directly on the nylon. Through laboratory testing and numerical modeling it was found that bolt bearing causes significant local deformations, ovaling of the hole, and disrupting strain distribution through the sensor. Figure 2.4 illustrates this effect. Additionally, use of slightly oversized holes allows for reasonable out-of-plumb tolerances for the field installation of the threaded studs.

Laboratory Validation

To provide a consistent venue for evaluating the performance of sensors, a constant-moment bending test was developed. This configuration produces a constant curvature over a user-controlled length of the beam thus providing a constant strain at any fiber along the entire length of the constant moment section. Figure 2.5 shows the test frame and beam configuration used while Figure 2.6 provides further detail.

The primary bending member was a W6x20 shape, approximately 9' long, bent about its minor axis. Minor-axis bending was utilized to eliminate any lateral-torsional buckling/instability effects when subjecting a segment of the beam to pure bending. Load was applied by a hand-actuated hydraulic ram, which was monitored by a calibrated electronic load cell. Mid-span deflections of the primary beam were monitored throughout testing. A linear displacement sensor (LDS) and a dial gage were located on the beam for verification of displacements. The LDS monitored the displacement of the beam web, 4' from each support and at mid-span of the W6. Spatial constraints forced locating the dial gage 4' from each support but on the bottom exterior flange of the primary beam. The load cell and the LDS were connected to a common data acquisition module facilitating synchronized load and strain readings.

Two sets of holes, 21/64" in diameter, were machined into a single flange of the W6 beam. Each set of holes was offset vertically 1.76" from the centerline of the web and centered at the mid-span of the beam as shown in Figure 2.7. The holes were set at a gage of 3". Each sensor was attached with two Grade 8 bolts with 5/16" diameter. The tightening nuts were then gradually torqued in an alternating fashion to 120 lb-in using a calibrated torque wrench. Special care was given to sensor location when tightening the nuts. If during the tightening process the sensor moved from its intended location, the nuts would be loosened and re-tightened with the sensor in its appropriate location. This was done to ensure that the sensors were oriented parallel to the flanges of the test beam at the target 1.76" locations. Complementing these holes for strain sensor attachment were standard strain gages, bonded directly to the beam on the opposite flange and centered in the same locations (Figure 2.7). This series of sensors produces a tensile/compressive pair of readings, each with a bonded gage complementing a strain sensor for a total of four strain channels.

After the beam testing was setup in the lab, several parameters were evaluated to find the best installation method for the sensors. First, the torque level on the sensor's bolts was evaluated. Two strain sensors were installed on the test W6 beam and tightened to a pretension corresponding to a torque of 120 lb-in. The test beam was then loaded to 5 kips and strain, load, and deflection data were recorded. The frame was unloaded and sensors were removed and re-installed with a pretension corresponding to 180 lb-in torque. The beam was loaded again to 5 kips. This process was carried out for three additional pairs

of sensors. All specimens were attached to the beam with a washer only on the outside face of the sensor while the inside face was in direct contact with the beam. A total of four tests were conducted at the 120 lb-in setting and four at the 180 lb-in setting. The tensile and compressive values for the sensors and complementary strain gages were then averaged and compared. It was observed that for tensile readings no change occurred. On the other hand, compressive readings strain sensor values were 4% closer to the bare gage values at the higher, 180 lb-in setting than the lower torque setting, albeit with greater uncertainty (Schneeman 2006). While the higher pretension value did return results closer to the bare gage values, implementation of this pretension in the field would require an embedment length greater than 1". This deeper embedment is not recommended as it may penetrate the prestressing steel of the girders. Additionally, the higher threaded stud pretension setting tended to significantly deform the soft nylon sensor material, which may lead to long term differences in individual sensor response as the instrument is removed and reinstalled. Therefore, 120 lb-in torque was used in the field installation.

A test was performed to evaluate the effect that various support conditions had on the strain sensors. Two conditions were selected in the evaluation: one with a standard washer on each surface of the nylon strain sensor, and another with a single washer on the outside of the sensor. In the latter case, the sensor is closer to the substrate being monitored, but is also rigidly supported in compression by the substrate. Data for this case was recorded during the torque level load test. Four pairs of sensors were attached to the test beam, all with 120 lb-in torque levels but with washers on both nylon surfaces. The beam was then loaded to 5 kips and data recorded. It was found that the tensile response of the sensors was nearly identical for each washer condition. However, the double washer condition produced results closer in magnitude in compression to the corresponding tensile case. Having sensors that behave similarly in tension and compression is desirable and therefore, all sensors used in this project utilize a washer on both faces of the polymer strain gauge carrier.

Heating due to the excited voltage can affect the reading of the strain gages. As a precautionary measure, a test was conducted to evaluate if the excitation voltage level selected for the sensors was in fact appropriate. Four independent strain sensors were configured in a temperature-compensating half bridge circuit and tested using bolt pretensions outlined previously. The half bridge configuration (Figure

2.8) eliminates temperature effects as both sensors experience equal resistive changes due to any heating. The experiments conducted were subjected to 2.5 volts of exciting voltage for a minimum of 20 minutes to allow long-term heating to take place in the sensors. Each half bridge circuit contained a sensor subjected to deformation by the bending test (R_{SENSOR}) while the other sensor (R_{Dummy}) was undisturbed.

All sensors attached to the test beam were tightened to 120 lb-in and were installed with only a single washer on the outside face of the sensor, even though double washers are recommended for field implementation. Strain values recorded during this test were then compared to data recorded from the other tests that were configured in the standard, quarter bridge circuit that does not compensate for temperature effects. Overall, no difference was observed between the temperature compensated half bridge sensors and the standard quarter bridge sensors. Thus, the excitation level (2.5 volts) used for this project is valid and is not expected to produce error in strain readings.

Finite Element Analysis

To verify the response of the strain sensors from the constant-moment beam test, a series of finite element models were constructed using the finite element analysis software package ANSYS (ANSYS 2005). Both three-dimensional (3D) models of the W6 test beam and the nylon strain sensor were constructed.

The material model used for beam model included a modulus of elasticity of 28,500 ksi and a Poisson's ratio of 0.30. The modulus of elasticity was back-calculated from observed deflection values of the test beam and assumed cross-sectional properties. Additionally, these values are similar to typical values for steel material. The geometry of the beam was modeled using dimensions for a W6x20 found in the AISC manual (AISC 2001). These dimensions were input in a two-dimensional (2D) plane and meshed using PLANE42 elements. Once the 2D model of the beam's cross-section was constructed with an appropriate arrangement of elements, it was extruded longitudinally, creating the third dimension of the model. The 3D elements used were of type SOLID95, of which every element contains 20-nodes has three degrees of freedom (DOF) per node – translation in the nodal X, Y, and Z directions. These 20-node “brick” elements were used throughout the FE model.

Boundary conditions of the beam model were provided at individual nodes for support and loading conditions. Nodes representing the roller supports at beam-ends were restrained in the vertical (Y) direction. Also, one end of the beam was restrained in both the horizontal (X) and longitudinal (Z) directions. Figure 2.9 illustrates the boundary conditions imposed on the beam model.

Loads were also applied directly to the nodes at locations where the W8 spreader beam contacts the main test beam. Idealized as roller supports, an aggregate load of 5,000 lbf was applied to the twelve nodes contacting the spreader beam. A force of 416.67 lbf was applied to each node in four groups of three, simulating the total force applied by the hydraulic ram. After the FE model was constructed and configured, a solution was produced. Maximum vertical deflection was recorded at mid-span with a magnitude of 0.2 inches (downward). This value agrees well with deflections recorded during laboratory testing at mid-span of the beam, which had a range of 0.19 to 0.20 inches.

The FE simulation indicated that the strains at the level corresponding to the location of the bonded gages on the test beam were $\pm 350 \mu\epsilon$. These values are similar to those strains observed in testing (364 $\mu\epsilon$ compression and 380 $\mu\epsilon$ tension). Therefore, both the strain and deflection values validated that the strain gages bonded to the steel test beam were adequately shunt calibrated and working properly.

In order to better understand the behavior of the portable strain sensors, an FE model of the strain sensor was developed. The strain sensor behavior under different support conditions (washer presence in tests) and under varying pretensions (torque level tests) was not made clear during laboratory testing. It was of great importance that a FE model of the sensor be created, providing an alternative venue for comparison and evaluation. As the geometry of the sensor is asymmetrical, a detailed FEM was created in a similar manner as the beam model.

The material model used for modeling the strain sensor included a modulus of elasticity of 400 ksi and a Poisson's ratio of 0.38. These properties were chosen, as they are common values for the sensor's base material, Nylon 6/6. Initially, a 2D model of the strain sensor was created using PLANAR82 elements and mapped meshing. All geometric details to be encountered within the sensor were incorporated into this 2D model. This was done so that extrusion of areas could be performed in stages, replicating the geometry of the sensor. An illustration of the extrusion process is given in Figure

2.10. As with the beam model, all 3D elements were SOLID95 elements, composed of 20-nodes and of brick shape. Further details of the FE model development can be found in Schneeman (2006).

The boundary conditions of the sensor model varied greatly as it is difficult to simulate the actual loading of the sensor through the washers and threaded studs. Recall that all load transfer is to be achieved by the friction between nylon and washer; the magnitude of such a friction force is challenging to reproduce. In lieu of applying loads to the sensor model, it was decided that applying a prescribed longitudinal displacement to the sensor model would accurately simulate the beam test. A single end would be displaced while the other would be restrained from displacement. This displacement of ± 0.00111 in. represents the displacement of the bolts anchored in the test beam and was calculated using a strain of $\pm 370 \mu\epsilon$, which is an approximate midpoint for the strains experienced by the strain gauges bonded to the test beam during laboratory testing.

By displacing the nodes in the FE model of the sensor by ± 0.00111 in., the model could simulate the sensor deformation seen in the laboratory tests. However, how to apply this displacement was not originally clear. It was decided that creating a suite of various boundary conditions could “envelope” the true behavior of the sensor, providing a venue for comparison. Further, these variations in boundary conditions could help explain the results seen during the testing done to evaluate the presence of washers on the sensor and the results of the torque level tests. To envelope the proper boundary conditions of the FE model of the sensor, a number of trials were conducted focusing on evaluating two primary situations. First, the regions affected by bolt hole displacement were addressed. By systematically adjusting the boundary conditions around the bolt holes, an accurate simulation of the contact each washer has on the sensor was developed. Additionally, the interaction between the sensor and the steel beam was addressed. Manipulation of the boundary conditions on the surface between the sensor and the steel beam were varied to study the presence washers have on the behavior of the sensor. The condition where no washers were present between the steel beam and the sensor was evaluated, as well as the condition where they were separated by a washer. Six models were evaluated (Schneeman 2006) and it was found that the boundary conditions illustrated in Figure 2.11 had best correlation with the experimental results.

The strain contour of the model is shown in Figure 2.12. The magnitude of strain produced by the final sensor model compares relatively well to that reported during laboratory testing. In tension, the mean strain value recorded when using washers on all faces of the sensor was 399 $\mu\epsilon$. The compression case observed a mean value of 419 $\mu\epsilon$. While the tension value is quite similar to the FEM results, the slightly larger difference for compression is deemed satisfactory given the complex interaction of the sensor and washers under compression. As the finite element model of the strain sensor produced consistent results it is felt that the constant-moment beam test would be an appropriate method to document the individual behavior of the strain sensors.

Calibration of Individual Strain Sensors for Field Implementation

To ensure accurate performance of the strain sensors in the field, a calibration procedure was performed documenting the unique response of each individual sensor manufactured under tensile and compressive loads. Individual calibration is required for all of the strain sensors as irregularities in manufacturing produce behavior distinctive to each specific instrument.

To ensure similar performance of the test frame and beams during the many load tests, each roller support was welded to a primary member. Each roller received two tack welds per side of the beams using a small wire welder. Welding the roller supports to beams eliminated the possibility for independent movement but did not provide any rotational restraint to the system. Figure 2.13 illustrates locations of welds. Additionally, locations of members in the test frame were continuously monitored, limiting the possibility of any relative movement that could introduce error into the recorded data.

All of the load tests were conducted in the following manner. Two sensors per test were mounted to the W6x20 test beam, with one in compression and the other tension. Each individual nylon strain sensor was installed on the flange with two Grade 8 5/16" diameter bolts. Washers were placed on the inner and outer surface of the nylon so that neither the beam nor the fastening nut contacted the sensor. Each nut was then tightened to a torque of 120 lb-in in alternating fashion. The lead wires of each sensor were then connected to an additional length of wire, which was connected to the data acquisition module. The other strain sensor was then installed in a similar manner. As was done with the load tests conducted

during development and experimentation of the nylon strain sensor, complementary strain gages were bonded directly to the opposite flange of the main test beam. The centerlines of these gages were located at the same elevation, which, in theory, should produce similar magnitudes of strain. Also similar to previous load tests, load and displacement were continuously monitored during testing by a calibrated load cell, linear position sensor (LPS), and dial gage. The load cell was located directly under the loading ram on the W8x31 spreader beam while the LPS and dial gage were located at mid-span of the main test beam.

Prior to load tests, calculated values for shunt calibration of the strain gages and sensors were produced. Individual resistances of the four strain channels (two 120-ohm bonded gages, two 350-ohm strain sensors) were read with a multi-meter and recorded. The simulated tensile strain was then calculated using the measured resistance of each shunt resistor and the manufacturer's gauge factor. The hydraulic ram was hand operated, increasing the load level as uniformly as possible until a maximum load of approximately 3-kips was reached. Data acquisition was then suspended and the beam slowly unloaded. Strain sensors were then removed and reinstalled in reverse locations to record their opposite strain response, or removed entirely for two new sensors to be tested. A total of 35 sensors were tested in both compression and tension. Further details of the calibration procedure can be found in Schneeman (2006).

In order to quantify individual strain sensor response relative to the bonded strain gauges, a calibration factor was developed. Given the predominantly linear response of the strain sensors, it was decided that a simple coefficient multiplier would be satisfactory. The following expression illustrates the calibration factor used,

$$CF_i = \frac{(\varepsilon_{SENSOR})_i}{\varepsilon_{Gage}}$$

where $(\varepsilon_{SENSOR})_i$ is the strain recorded in nylon sensor "i", and ε_{Gage} is the strain recorded in the corresponding bonded strain gauge. The typical measured strain response of both the bonded strain gages and the portable sensor is shown in Figure 2.14.

It can be seen from this figure that the strain sensors and gages (solid lines) very nearly match their linear trend lines (dotted), which pass through the origin. Further, the R-squared values for a linear

fit of the measured data are noted, indicating that the trend lines are very nearly equal. On the other hand, slight discrepancies exist. .

To produce the calibration factors for each gage, a load level of 2,500 lbf was arbitrarily selected at which strain readings would be analyzed. From Figure 2.14 it can be seen that when loaded at an appropriate rate the data forms a nearly linear line ($R^2 = 0.99$), thus any load level would be appropriate to select data from. At this load, three strain values (the sensors mounted to the beam and both bonded strain gauges) were sampled and averaged. The ratios for compression and tensile response of the strain sensor under loading were computed. Table 2.1 illustrates typical calculations performed for each load test, producing calibration factors for two gages simultaneously.

Calibration factors developed for use with field-acquired data are listed in Table 2.2. If a reading is indicated as compressive, multiplication of the recorded strain reading by the compressive calibration factor unique to that gage will produce the corrected strain reading. Likewise, the opposite is true for tensile readings. It can be seen that for a majority of the strain sensors, tensile and compressive response is similar. From the results of the FE sensor model, calibration factors should theoretically be identical between tension and compression. However, the anchorage behaves differently in compression relative to tension, resulting in variation in the response of the strain sensors. Overall, the calibration factors for most sensors are relatively similar. It can be seen that in all but three sensors below, the compression calibration factor was larger than the tensile factor, indicating a consistently different response.

2.3 Freeze-Thaw Testing

Bridge B-20-133 uses FRP grid reinforcement and FRP Stay-in-Place (SIP) forms that are coated with an adhesive called Concresive® (to bond 6.35 mm aggregate to the FRP form (Berg 2004). The aggregate adhered to the SIP form is intended to interlock with the concrete poured on top of it so the SIP form can act as positive moment flexural reinforcement for the bridge deck. Full-depth cracking was observed in this bridge deck (Martin 2006) and as a result, it is reasonable to assume that water has a direct path to the FRP-concrete interface. With the FRP formwork in place, the water does not have a way to be removed from the system. This indicates that there is potential for water to be trapped between the FRP and

concrete, which could have a detrimental effect during a freezing event. Because the SIP FRP forms are expected to act as the positive moment reinforcement for the bridge deck, it is important to understand how the aggregate/concrete interlock is affected by cyclic freezing and thawing. Hygrometer testing discussed in other chapters of this report sheds further light on the potential for moisture to accumulate at the concrete FRP-SIP interface.

Freeze-thaw testing done on FRP retrofitted concrete components has shown varying results (Bisby and Green 2002; Krishnaswamy and Lopez 2006). In a case of externally bonded FRP plates, freeze-thaw cycling appeared to increase the bond capacity (Bisby and Green 2002). Testing done using specimens intended to simulate the system in bridge B-20-133 indicated that freeze-thaw cycling had some impact on the shear strength at the FRP formwork - concrete interface, but the results were largely inconclusive (HelmueLLer et al. 2002). Therefore, the effects of freeze-thaw cycling on a deck with FRP-SIP forms remains a critical issue to be understood in order to assess the long-term performance of the FRP-SIP deck system and rationally plan inspection methods to monitor long-term behavior.

Materials

The concrete used in this part of research was ready-mixed with a mix design targeted to correspond to WisDOT Class D concrete, which is used for bridge decks. The slump of the concrete was 114 mm and air entrainment was $6\pm 0.5\%$. The entrained air ensured that there was minimal deterioration in the concrete due to freeze-thaw cycles. Five cylinders were tested at 28-day curing times and the average compressive strength was 44.6 MPa. FRP strips were cut from the FRP-SIP sheets between the void space boxes (Berg 2004) using an abrasive blade in a table saw. They were then cut to length using an abrasive blade in a miter saw. Strips of FRP used in the specimens were 63.5 mm wide and 254 mm long. Further details of the materials and specimen fabrication can be found in Martin (2006).

Single-Shear Specimens

Epoxy adhesive, trade named Concrecive®, was prepared as required by the manufacture and applied to the FRP strips. The 6.35 mm aggregate supply was obtained through sieving and it was randomly applied

on the FRP surface before the adhesive cured in a manner that met the bridge deck specifications. The aggregate covered 35%-45% of the surface as required in the specifications (Berg 2004). After the adhesive cured, the FRP strips were laid flat at the bottom of formwork and the side with aggregate was faced up. Concrete was then placed on top of the FRP sheets in the forms. The specimens were 63.5 mm wide, 88.9 mm high and 355.6 mm long. The concrete block of the specimens was 254 mm long as shown in Figure 2.15.

The forms were stripped after 2 days and the specimens were then covered with plastic and left to cure. After 26 days (28-day total cure time), the specimens were randomly placed into three groups. The first group was tested in a direct shear apparatus (Figure 2.16) without any exposure to moisture or freeze-thaw cycles (C-group); one was placed in the freeze-thaw chamber submersed in water and subjected to freeze-thaw cycles (F-group), and one was placed in room temperature water in concrete cylinder molds for a time-period equivalent to that required to attain the necessary number freeze-thaw cycles in the F-group specimens (W-group). Further details are available (Martin 2006).

Test Setup

The test setup (Figure 2.16) was designed to simulate direct shear at the concrete-FRP interface. The plates that pinched the FRP strip to pull it off were knurled on the inside to inhibit slipping. A calibrated load cell and a data acquisition system were used to record the load during the test. Throughout the testing, a slow rate of loading (approximately 74 N/s) was used. Before specimens were tested, the ends of the concrete were squared off with an abrasive saw as depicted schematically in Figure 2.17. This ensured that the specimens were tightly clamped in the apparatus with nearly uniform compression thereby minimizing horizontal slip. Each specimen, after this initial cutting, was placed in a Riehle UTM and clamped into place by tightening the bolts after leveling the specimen and making sure it was in line with the load cell and plates that pinched the FRP strip (Figure 2.16). The bolts pinching the plates together were tightened with extreme care to prevent twisting the FRP strip relative to the concrete block. The FRP strip was also as close to vertical as possible so direct peeling forces on the FRP plate were

minimized. Photographs and further details of the experimental testing apparatus and the testing protocol are available in Martin (2006).

Freeze-Thaw Cycles

Weather data and heat transfer theory can be used to predict the number of freeze/thaw cycles concrete bridge decks and concrete pavements may experience in a typical year (Greenfield et al. 2003; Bentz 2000). This study used the algorithm developed by Bentz (2000) to estimate the number of freeze-thaw cycles expected in the bridge deck considered. Two cities that are the closest to Waupun geographically are Alpena, MI and Waterloo, IA. B-20-133 in Waupun lies between these two cities. Alpena, MI concrete pavements are expected to experience 102 freeze-thaw (F/T) cycles per year and concrete bridge decks are expected to see 107 annual F/T cycles. Simulations for Waterloo, IA indicated that 72 F/T cycles could be expected for pavements and 86 cycles could be expected for bridge decks. Using the latitude proximity of Waupun, WI to these two locations as a basis for prediction, it was assumed that the bridge deck in Waupun could see 90-100 annual F/T events. Estimates for the number of F/T cycles give meaning to the number of freeze-thaw cycles used in the lab. The experiments conducted in this research assumed that any damage done to specimens with 100 F/T cycles would give indication of the damage that could be expected after a typical year. Cumulative damage expected after multiple years of exposure should not be extrapolated using the research results reported here.

The freeze-thaw testing was conducted using the ASTM C666 standard procedure A (ASTM 2003). Using this procedure, the specimen is completely immersed in water during the freeze-thaw cycles. The specimens in an ASTM-compatible freeze-thaw chamber were placed so the FRP strips were on top in the bins. Each compartment was filled with water so the FRP was completely submerged. Containers were refilled throughout the freeze-thaw process so the FRP would remain submerged during all 100 cycles. The chamber was set to cycle from 4.4° and -17.8° C then from -17.8° to 4.4° C. Further details regarding the chamber and testing protocol are available (Martin 2006).

Freeze-Thaw Testing Results

The majority of specimens exhibited the failure mechanisms shown in Figure 2.18(a). Very few stones were sheared and even fewer were pulled out of the Concrecive®. Because of an inherent eccentricity in the testing set up, the specimens were not experiencing pure shear stress. Small normal forces were always present in the bottom of the specimen, which will start the FRP sheet peeling away from the concrete near the strength limit state. This was observed during every test. Once this happened, the FRP was quickly pulled off. It is therefore recognized that the shear strength calculated is not a true measurement of the shear capacity at the interface, but it will be defined as the nominal shear strength to facilitate comparisons. An effective area was defined individually for each specimen. If a specimen had areas of honeycombing, those areas were not included in the computed area over which the shear stress was assumed to act. Every specimen was reduced slightly to account for the area around the edges or other casting defects. The nominal shear was calculated using maximum load divided by this effective area. Table 2.3 presents the load at failure of the specimen, the effective bond area observed, the nominal shear stress calculated, and the number of aggregates on a 254 mm line (Figure 2.18b).

After the freeze-thaw specimens were removed from their containers, it was discovered that five of the thirteen specimens had the FRP sheets separated from their concrete blocks. This was expected as the water was allowed to completely and easily penetrate the FRP-concrete interface and F/T could cause direct expansion and separation of the FRP sheet from the concrete block. The remaining specimens were numbered F1-F8 and prepared for testing. It is important to note that 38% of the specimens suffered complete bond failure prior to testing. However, the freeze-thaw chamber immersion scenario is not indicative of the actual condition likely to be seen in the bridge. Therefore, while it is noteworthy that 5 specimens did not survive the freeze-thaw cycling, these results were not used in the statistical analysis of the experimental results.

One other observation made during testing was that the interface surface on the concrete in contact with the FRP strip was very shiny. One of the tested specimens was cut to evaluate the distribution of coarse aggregates through the specimen with special interest being at the FRP-concrete interface. It was observed that the shininess seen in the concrete blocks at the interface between the

concrete and FRP was caused by the Concreasive® surface it was cured against. The coarse aggregates were adequately dispersed in the block and over-vibration in the specimens did not occur.

Statistical Analysis

Using the statistical analysis packages in Excel, each set of data was tested against a normal and lognormal Cumulative Distribution Function (CDF) model using a Kolmogorov-Smirnov (K-S) test. A K-S test of good fit compares the observed cumulative frequency and the theoretical cumulative distribution function using a user-defined probability density function. In this study, lognormal and normal probability density functions were considered. The maximum difference, S_n , between the observed and theoretical distribution is compared to a value based on a set significance level and the sample size, D_n^α . All tests were done assuming a significance level of $\alpha = 0.05$. If the maximum difference, S_n , is less than D_n^α , the assumed distribution is acceptable (Haldar and Mahadevan 2000).

It was found that all three groups of data could be modeled using a normal distribution or a lognormal distribution. However, the maximum difference in the lognormal model was less than the maximum difference in the normal model. Normal and lognormal distributions are very similar to one another, and when the same mean and standard deviation is used there is almost no difference between them (Haldar and Mahadevan 2000). For this reason, it was decided to model the experimental data using a normal distribution (Martin 2006).

In design, magnitudes of strength or demand are often quantified at 95% confidence levels and therefore this confidence level was selected in this research for comparison. Table 2.4 presents mean values and 95% confidence values (assuming a normal probability density function) for the nominal shear strength at the FRP-concrete interface. The mean nominal shear stress was reduced 13% by water exposure only and 16% by 100 freeze-thaw cycles. However, the 95% confidence level was dropped 20% by water exposure and 40% by freeze-thaw as a result of the increased variability in the experimental results.

Finite element analysis conducted by Martin (2006) using a simplified model of the bridge FRP-SIP bridge deck system indicated that the service-level shear-strength (non-cyclic) demand for fully

composite action at the FRP-concrete interface in the Waupun bridge deck may only be as high as 0.24 MPa (less than one-half the 95% confidence level shear strength after 100 F/T cycles). Thus, the interface between the concrete and FRP-SIP form will likely not see demands that warrant concern, but it may be prudent to monitor long-term performance of the FRP-concrete composite deck system with in-situ load testing, coring, and future detailed finite element analysis.

2.4 Conclusions

This chapter of the research report outlined three distinct phases in the 5-year effort. The first was devoted to the development and calibration of portable strain sensors that were used during the two in-situ loads. The chapter also outlined a series of freeze-thaw tests designed to evaluate the impact of freeze thaw cycles on the shear transfer mechanism at the interface of the FRP-SIP formwork and the bridge deck concrete. The chapter concluded with the fabrication of a bridge deck prototype and application of InfraRed Thermography (IRT) to detect de-bonding in the in-situ FRP-SIP bridge deck.

Thirty-five portable strain gauges were developed and calibrated through the research effort. These sensors and the data acquisition software system developed (Schneeman 2006) were used during both in-situ load tests carried out in July 2007 and July 2009. Tension and compression calibration factors were developed through controlled physical testing for each portable sensor. The sensors and the data acquisition hardware and software (Schneeman 2006) are available for other testing efforts.

The research completed indicates that freeze-thaw cycling and the presence of water could be detrimental to the FRP-concrete interfacial shear strength. The mean nominal shear stress was reduced 13% by water exposure alone and by 16% after 100 freeze-thaw cycles. A design-level shear strength corresponding to 95% confidence after 100 F/T cycles reduced 40% when compared to control specimens. Even specimens exposed to water for 14 days without F/T cycling experienced a 95% confidence-level shear strength reduction of 20%. FE analysis of the deck system using simplified models (Martin 2006) suggests that shear demands at the concrete FRP-SIP interface are not of sufficient magnitude to cause concerns regarding long-term performance.

The laboratory studies conducted to evaluate the reduction in shear strength resulting from freeze-thaw cycling and moisture presence were very conservative and do not fully represent the situation present in the field. In other words, the laboratory testing setup is an extreme scenario that is a relatively crude approximation of the field conditions. Field conditions are likely to be much more favorable and the resistance to freeze-thaw degradation is felt to be much higher in the actual structure.

2.5 References

- AISC (2001). "LRFD Manual of Steel Construction - 3rd Edition," American Institute of Steel Construction, Chicago, IL.
- ANSYS. (2005). "ANSYS University Intermediate, Release 10.0.," ANSYS, Inc, Canonsburg, PA.
- ASTM (2003). "Standard Test Method for Resistance of Concrete to Rapid Freezing and Thawing," ASTM C 666/C 666M – 03, West Conshohocken, PA, 2003.
- Bentz, D.P. (2000). "A Computer Model to Predict the Surface Temperature and Time-of-Wetness of Concrete Pavements and Bridge Decks," NISTIR 6551, U.S. Department of Commerce, 2000.
- Berg, A.C. (2004). "Analysis of a Bridge Deck Built on U.S. Highway 151 with FRP Stay-In-Place Forms, FRP Grids, and FRP Rebars," Master's Thesis, University of Wisconsin – Madison, 2004.
- Bisby, L.A. and Green, M.F. (2002). "Resistance to Freezing and Thawing of Fiber-Reinforced Polymer-Concrete Bond," *ACI Structural Journal*, **99**(2), 2002, 215-223.
- Greenfield, T., Takle, E., Tentinger, B., Alamo, J., Burkheimer, D. and McCauley, D.(2003). "Bridge Frost: Observations and Forecast by Numerical Methods," *Proceedings of the 2003 Mid-Continent Transportation Research Symposium*, Ames, IA., 2003, CD-ROM.
- Haldar, A. and Mahadevan, S. (2000). "Probability, Reliability, and Statistical Methods in Engineering Design," John Wiley and Sons, Inc., 2000.
- Helmuller, E.J., Bank, L.C., Dieter, D.A., Dietsche, J.S., Oliva, M.G. and Russell, J.S. (2002). "The Effect of Freeze-Thaw on Bond Between FRP Stay-In-Place Deck Forms and Concrete," *Proceedings of CDCC 2002, 2nd International Conference on Durability of Fiber Reinforced Polymer (FRP) Composites for Construction*, Montreal, CANADA, May 29-31, pp. 141-152.

- Krishnaswamy, R. and Lopez M.M.(2006). "Time Performance of Concrete-CFRP Bond under the Effects of Freeze-Thaw Cycles and Sustained Loading," TRB 2006 Annual Meeting CD-ROM.
- Martin, K.M. (2006). "Impact of Environmental Effects on, and Condition Assessment of, IBRC Bridge Decks in Wisconsin," Master's Thesis, Marquette University, 2006.
- Micro-Measurements (2004). "Instruction Bulletin B-147-4." Application of M-Coat J Protective Coating, Vishay Micro-Measurements, Revised March, 1996.
- ROMUS (2005). "Strain Sensor Shop Drawings." ROMUS Incorporated, Milwaukee, WI.
- Schneeman, C.L. (2006). "Development and Evaluation of a Removable and Portable Strain Sensor for Short-term Live Loading of Bridge Structures," Master's Thesis, Marquette University, 2006.

Table 2.1 Calculation of Portable Sensor Calibration Factors

	Sensor #005		Sensor #006	
	Top Nylon [uStrain]	Top gage [uStrain]	Bot. Nylon [uStrain]	Bot. gage [uStrain]
	-172.4567	-174.029	183.514	180.1114
	-172.4568	-174.0334	183.5069	180.1181
	-172.4558	-174.0382	183.4995	180.125
Average =	-172.46	-174.03	183.51	180.12
St Dev =	0.00	0.00	0.01	0.01
Calibration Factor =	0.991		1.019	

Table 2.2 Calibration Factors for Portable Sensors.

Sensor	Compression	Tension
001	1.064	0.964
002	1.093	0.965
003	1.093	1.159
004	1.145	1.045
005	0.991	0.925
006	1.026	1.019
007	1.006	0.975
008	0.877	0.786
009	1.053	1.070
010	1.123	1.091
011	1.080	1.043
012	1.020	0.999
013	1.139	1.028
014	1.151	1.073
015	1.069	1.013
016	1.036	0.999
017	1.069	0.967
018	0.983	0.935
019	1.064	0.972
020	1.129	1.044
021	0.978	0.934
022	0.911	0.851
023	1.079	1.044
024	0.999	0.945
025	1.073	1.026
026	1.103	1.026
027	1.020	0.959
028	1.131	1.033
029	1.049	0.985
030	0.952	0.922
031	0.957	0.940
032	0.979	0.923
033	0.962	0.910
034	1.111	1.026
035	0.989	0.997
Average	1.043	0.988

Table 2.3: Single-Shear Specimen Failure Results.

	Specimen Designation	Load at Failure (kN)	Effective Area (mm ²)	Nominal Shear Stress (MPa)	Number of aggregates on a 254 mm Line
Control - No Freeze/Thaw or Water Exposure	C1	-	-	-	15
	C2	14.38	12323	1.17	27
	C3	16.47	15355	1.07	21
	C4	18.34	14710	1.25	21
	C5	-	-	-	24
	C6	22.11	15355	1.44	16
	C7	-	-	-	20
	C8	14.69	14516	1.01	18
	C9	12.84	15355	0.83	16
	C10	15.67	14516	1.08	15
	C11	15.87	15355	1.03	20
Moisture Control - 17 Days of Water Exposure (100 F/T cycle equivalent)	W1	18.30	15355	1.19	15
	W2	13.42	15355	0.88	22
	W3	9.37	13742	0.68	20
	W4	10.19	12129	0.84	21
	W5	21.56	15355	1.41	21
	W6	14.35	15355	0.94	25
	W7	-	-	-	17
	W8	12.38	15355	0.81	19
	W9	21.08	15355	1.37	20
	W10	8.54	15355	0.56	18
	W11	14.72	15355	0.96	15
	W12	-	-	-	17
	W13	-	-	-	18
Freeze/Thaw - 100 Cycles	F1	20.39	15355	1.33	33
	F2	8.30	15355	0.54	16
	F3	14.44	15355	0.94	19
	F4	8.62	15355	0.56	22
	F5	20.21	15355	1.25	26
	F6	-	-	-	25
	F7	14.21	15355	0.92	11
	F8	-	-	-	15

Table 2.4: Single-shear means and 95% confidence levels.

Specimen Group	Nominal Shear Stress (MPa)	
	Mean	95% Confidence
Control	1.11	0.96
Moisture Control	0.96	0.76
Freeze/Thaw	0.94	0.57

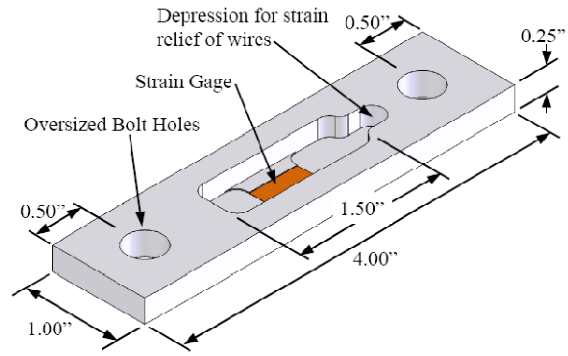


Figure 2.1: Configuration of the strain sensor.



Figure 2.2: Constructed strain sensors without connection tabs or protective coating.

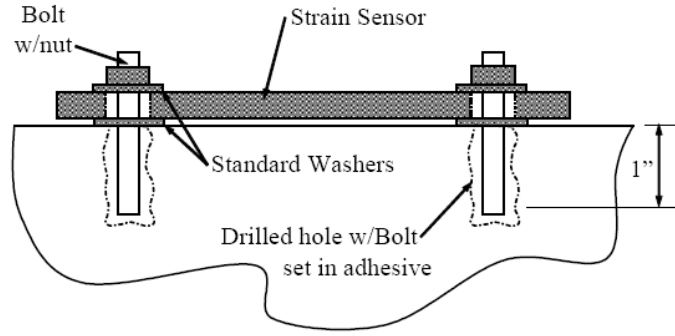


Figure 2.3: Field installation of the strain sensor to concrete.

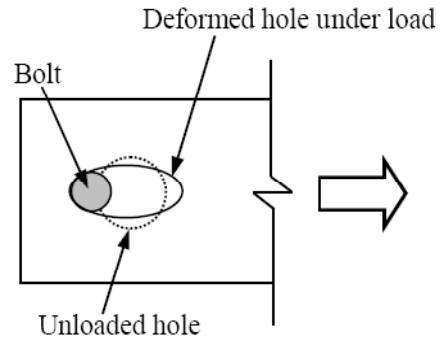


Figure 2.4: Ovalization of a bolt hole under loading.



Figure 2.5: Four-point bending test used for strain sensor evaluation.

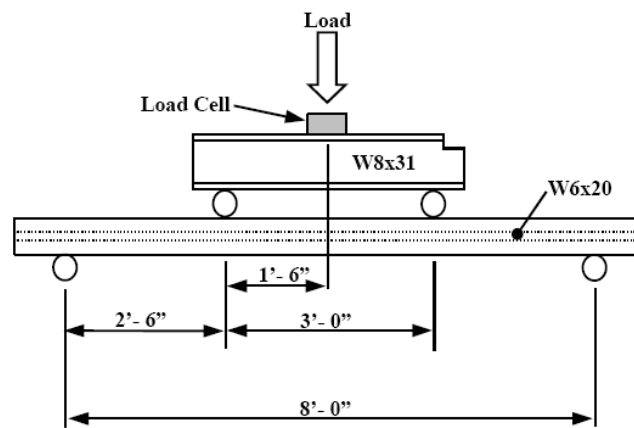


Figure 2.6: Dimensioned constant-moment beam testing schematic.

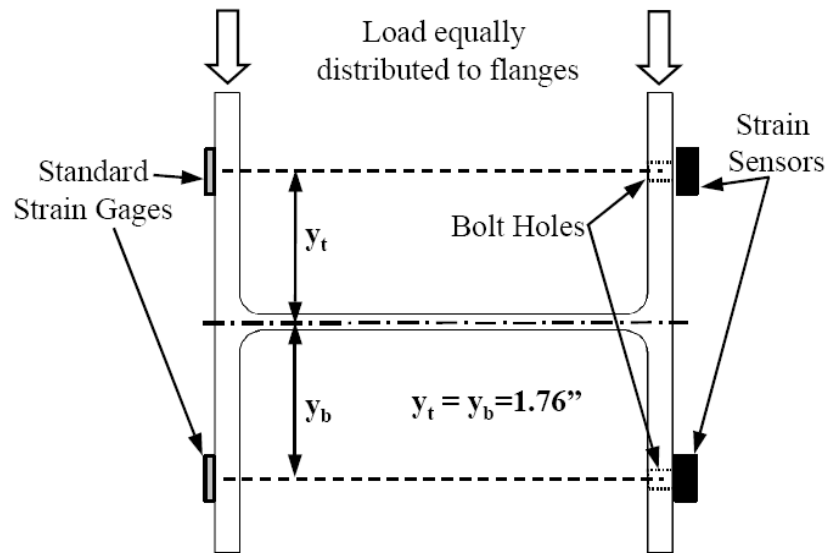


Figure 2.7: Mid-span layout of Strain sensors and complementary strain gages.

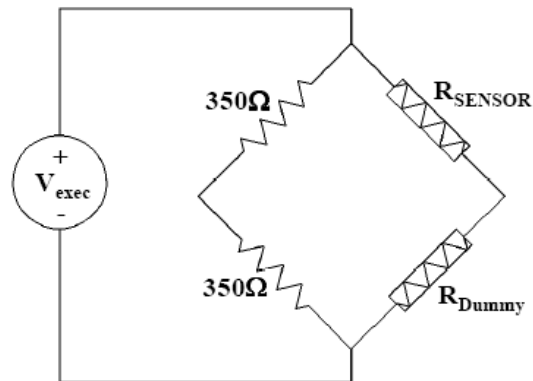


Figure 2.8: Half bridge temperature compensating circuit.

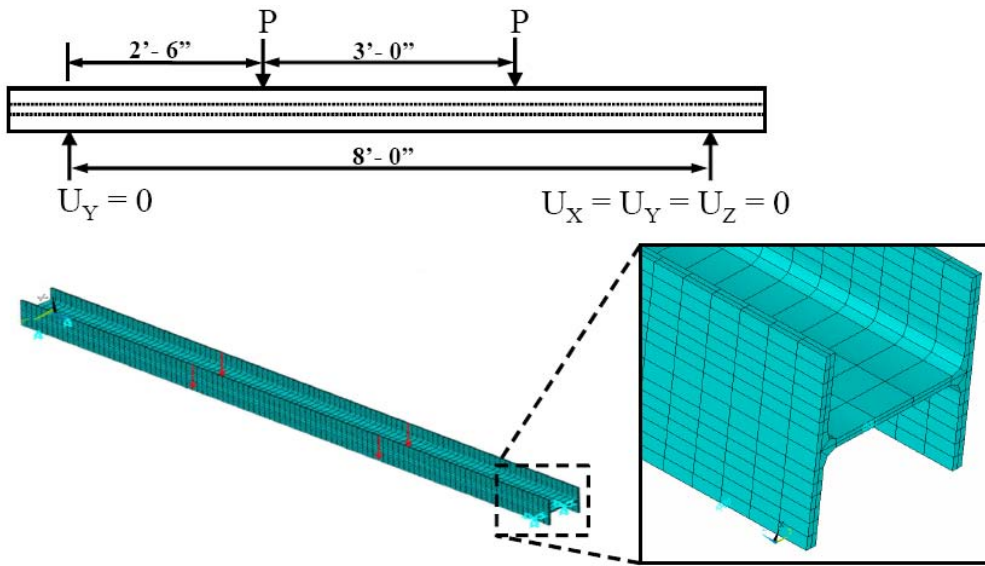


Figure 2.9: Boundary conditions of the 3D beam model.

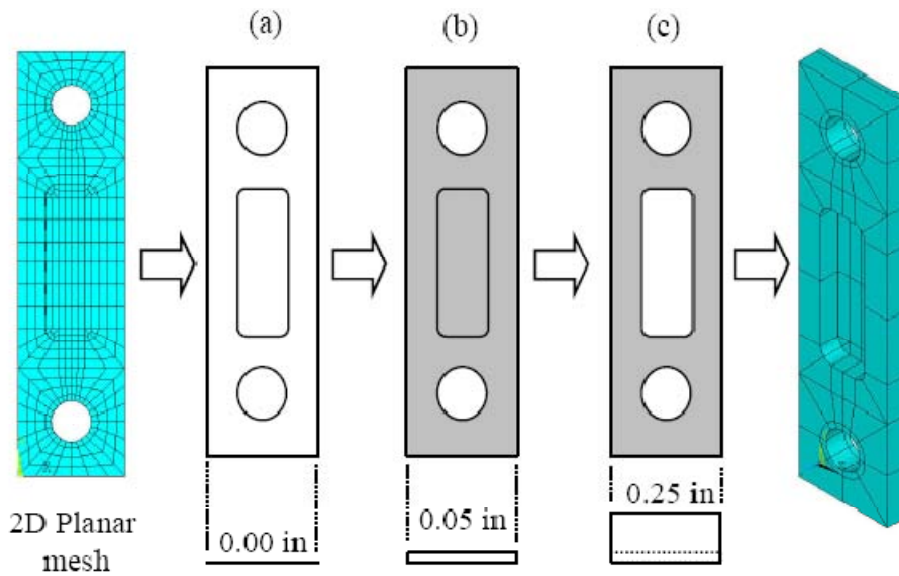


Figure 2.10: The extrusion process uses to build a 3D model of the sensor. It can be seen that from figure (a) the entire 2D planar mesh is extruded 0.05" in figure (b). The center depression is then created in figure (c) by extruding all areas around the depression.

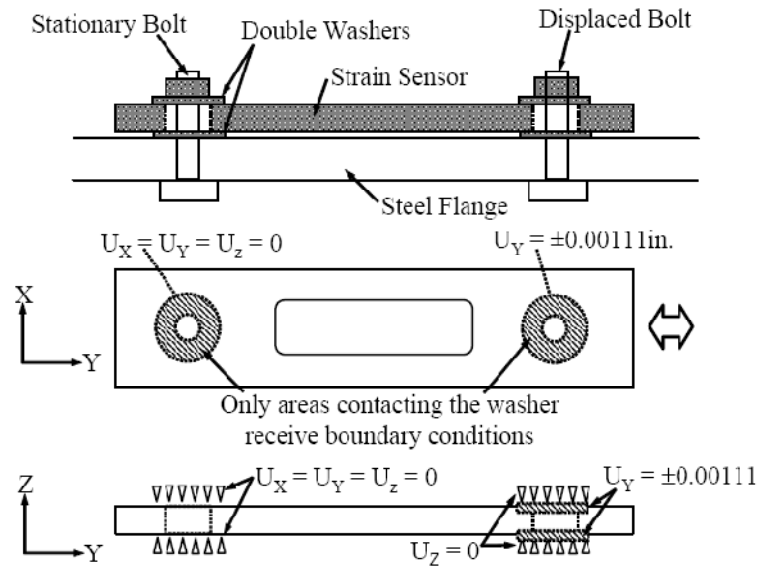


Figure 2.11 Boundary conditions for both compression and tensile cases of sensor model.

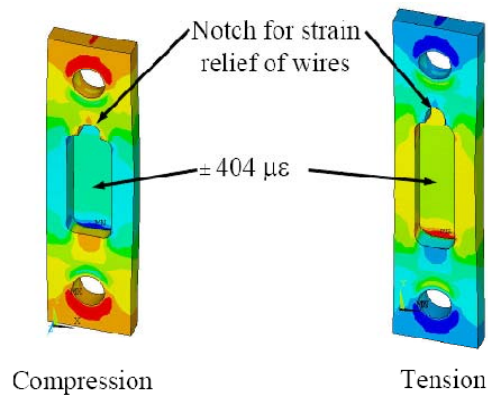


Figure 2.12: Longitudinal strain distribution for tension and compression cases for the sensor model.

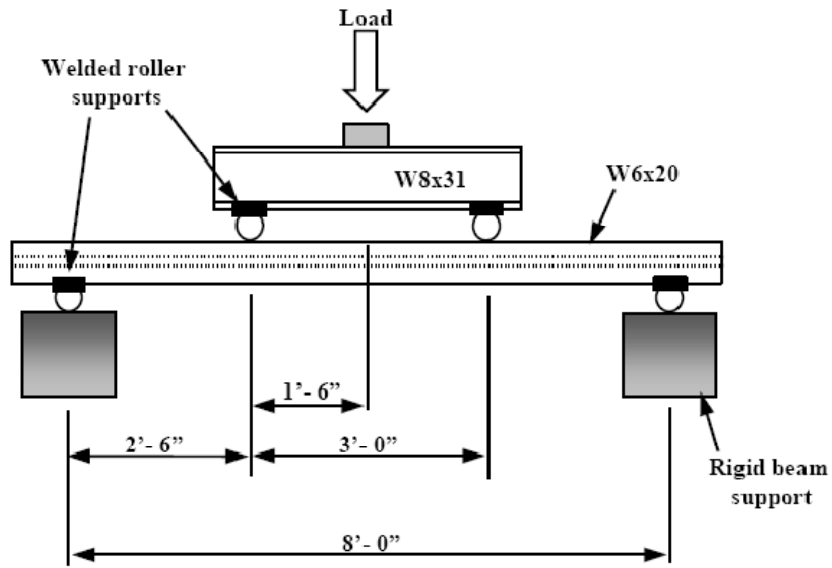


Figure 2.13: Weld locations on beam members for the constant-moment load test.

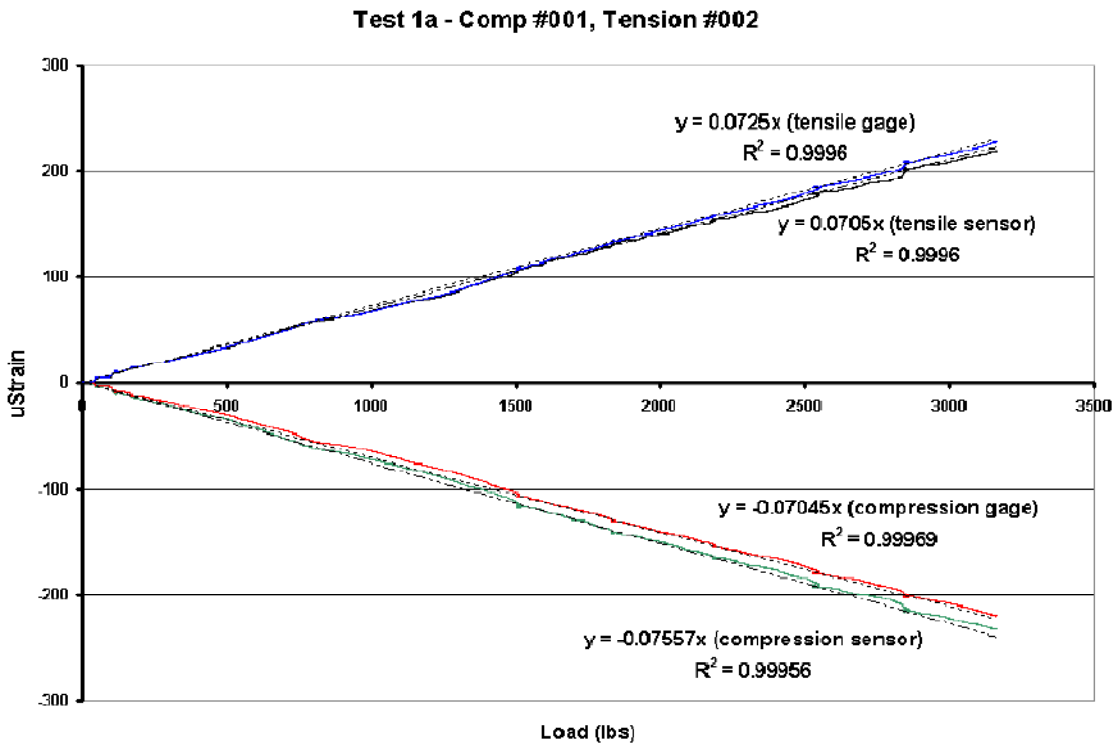


Figure 2.14: Typical response of strain gages and sensors under applied loading.

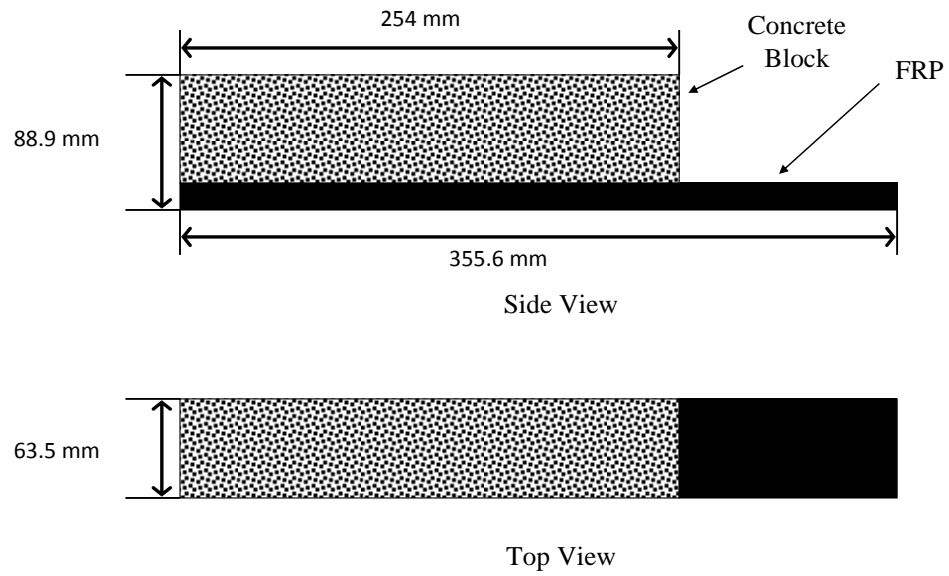


Figure 2.15: Specimen top and side views.

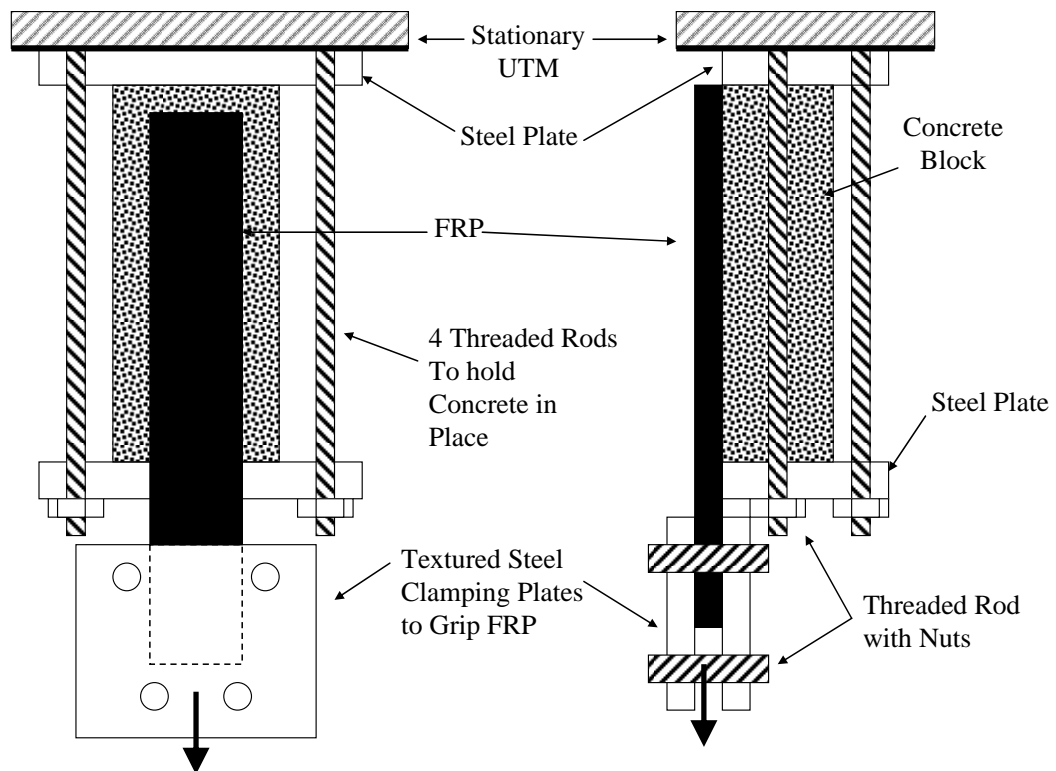


Figure 2.16: Single-shear testing setup.

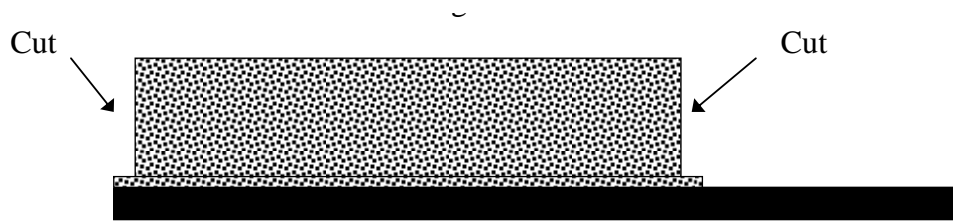


Figure 2.17: Cuts on each end of the concrete block to square it with the FRP.



(a)



(b)

Figure 2.18 : Typical single-shear specimen failure: (a) failure surfaces; (b) typical 254 mm line drawn to check aggregate coverage (Berg 2004).

Chapter 3

In-Situ Monitoring and Non-Destructive Evaluation

3.1 Introduction

The IBRC monitoring project for bridges B-20-133/134 and B-20-148/149 was a five year program that involved in-situ load testing, laboratory work, and numerical simulation of superstructure response. An in-situ monitoring program was conducted to establish benchmark condition of the bridge superstructure systems, evaluate nondestructive evaluation (NDE) techniques that may facilitate gathering information suitable for quantifying long-term performance, and gather information related to egress of moisture into the FRP-SIP bridge deck system utilized in bridge B-20-133. This chapter in the report is, in large part, based upon the graduate research work of Martin (2006). Further details regarding the information in the chapter are available (Martin 2006).

This chapter of the report outlines initiatives in these three areas carried out during the IBRC monitoring project and provides a detailed benchmark condition evaluation of each bridge superstructure system, makes recommendations regarding the suitability of various NDE methods in attaining information pertinent to long-term performance assessment, and discusses data gathered to evaluate the severity of moisture egress into the FRP-SIP formwork deck system.

3.2 Benchmark Condition Evaluation of B-20-133/134

A day was spent at bridges B-20-133/134 to document an initial crack map and the overall condition of each bridge. MU-IBRC team members visited B-20-133/134 on October 25, 2005. Visual inspection of the bridge superstructures was completed and pictures were taken to document the condition of key superstructure elements. The bridges examined are shown in Figure 3.1. Bridge B-20-133 is the IBRC

Bridge with the FRP-SIP formwork system and B-20-134 is the conventionally-constructed steel-reinforced concrete bridge deck system.

Visual Condition Survey

A visual inspection of B-20-133/134 following the WisDOT standard procedure was completed. The research team filled out a typical WisDOT inspection report for each bridge superstructure. The visual inspection examined all superstructure elements including the abutments, piers, deck surface, deck soffit (underside), and parapets. Figures 3.2 and Figure 3.3 show the inspection report filled out after the visual inspection on October 25, 2005. It should be noted that the initial and subsequent inspection reports are available in the on-line WisDOT Highway Structure Information System (HSIS).

The visual inspections revealed that both bridges were in very good condition at the time of inspection and this condition did not appreciably change since their original inspection done by WisDOT. It was noted on the second page of the inspection report in Figure 3.2 that the research team's visual inspection of the bridge deck's underside was impossible to conduct on B-20-133 since the FRP-SIP formwork is present.

Crack Map and Photographic Documentation

A crack map was created by locating visually-apparent cracks on the bridge deck and transferring them to a scaled drawing of the bridge deck plan. Construction crayon marks every ten feet on the edge of the deck that matched up with lines every ten feet scaled on a plan drawing helped with this process. Only hairline cracks were seen in both bridges. Typical cracks are shown in the left image of Figure 3.4 and these cracks are enhanced on the right.

The crack map presented in Figure 3.5 shows the cracked state of the two bridge decks on October 25, 2005. In general, the cracking is extensive in both bridge decks. It can be seen that most of the cracks are concentrated in the negative moment regions above the central piers. It does appear that the cracking is distributed more uniformly in B-20-134 (conventionally reinforced deck) when compared to the deck in B-20-133 (FRP-SIP formwork system). The extensive cracking in the early life of these

bridge decks is of concern and subsequent simulation efforts conducted by the research team to help quantify reasons for this will be discussed in later chapters of this report. Both bridge decks exhibit typical cracking at acute corners in skewed superstructures that result from free shrinkage restraint in the bridge deck.

The plan views shown in Figure 3.6 constitute a picture index for bridges B-20-133/134. It shows the intended target location and direction of the pictures taken to document the bridge condition. The number in the circle on the index corresponds to the photo number in parenthesis in each figure caption. The arrow accompanying each number shows the direction the photo was taken.

Bridge B-20-134, the sister bridge to B-20-133, serves as a comparison for the innovative use of FRP. Bridge B-20-133 is the innovative bridge using FRP SIP formwork and a single layer of FRP grillage reinforcement. In the pictures for B-20-133, the most southern girder is labeled #1 and the northern most girder, #3. All pictures from the inspection are included in Figures 3.7 through 3.17. It should be noted that not all photos indexed in Figure 3.6 are included in this report. All photos can be found in Martin (2006).

Hairline cracks in the bridge decks have propagated to and through the parapet with efflorescence showing on the underside of the overhang of each bridge deck shown in Figure 3.7 and 3.8. As seen in Figure 3.6, cracking on both bridges is primarily located near the abutments and the central pier. Bridge B-20-133 appears to have less frequent cracking at the mid-span location between the abutment and central pier. This may be a result of the SIP FRP formwork restraining shrinkage of the deck as well as the tight spacing of the FRP grillage. Both the innovative and traditionally constructed twin has significant efflorescent cracks in the bridge deck overhang.

Figures 3.10 and Figure 3.11 show the interior diaphragm looking east and west at the southern sides of the central piers. There is similar cracking seen around the interface between the girders and the central diaphragm. The northern parapets also show cracks around the central pier and efflorescence on the underside of the bridge deck soffit as seen in Figure 3.11 and 3.12. The northern parapets within the

spans pictured in Figures 3.13 and 3.14 do not show cracking and efflorescence to the same extent as the parapets around the central pier.

The only thing quite different about the two bridges is the underside of the decks. Bridge B-20-133 has FRP-SIP formwork so inspecting the concrete deck condition from the underside is impossible. Accumulation of moisture at the interface of the concrete deck and FRP-SIP formwork was of concern and this is evaluated more thoroughly in a subsequent section of this chapter. Figure 3.15 shows typical and sporadically located blistering in the FRP formwork sheets found in the benchmarks inspection. This blistering is naturally occurring resin defects arising from the manufacturing process. Excess glue or sealant used between FRP SIP sheets during construction can also be seen in Figure 3.15. This is not detrimental.

The underside of B-20-134 is unobstructed and cracks with efflorescence are prevalent on the underside of the bridge deck. Figure 3.16 shows full depth diagonal and transverse cracks near the abutment. Full depth cracks are seen through the entirety of the bridge deck. Figure 3.17 shows transverse full depth cracks along the west span of B-20-134 going all the way to the central pier. It is suspected that full-depth cracks in the FRP-SIP formed deck are also present, but this was never confirmed.

3.3 Benchmark Condition Evaluation of B-20-148/149

An initial crack map for bridges B-20-148/149 was also generated to document the condition of these bridge superstructures. On October 27, 2005, MU-IBRC team members performed a visual inspection of bridges B-20-148/149. Figure 3.19 is an overview photograph showing the bridges in October 2005. It should be noted that traffic in 2005 was relatively light (much less than it is currently). The visual inspection included a walk-around under and on the bridges. Photographs were taken to document the condition of key elements in the bridge superstructures.

Visual Condition Survey

The visual inspection was performed in a manner similar to that of B-20-133/134. In addition, WisDOT standard bridge inspection report forms were filled out by the research team. These completed forms

serve as supplemental information to that obtained in the regularly scheduled WisDOT inspections, which are available on the HSIS website. Figure 3.19 includes the completed WisDOT inspection reports for the two bridges done on October 27, 2005. The MU research team found that the bridge superstructures were in excellent condition and very little (if any) changes occurred since the initial inspection recorded in the HSIS database. Bridge B-20-148 is the IBRC Bridge with FRP grillage reinforcement and B-20-149 is the conventionally reinforced bridge.

Crack Map and Photographic Documentation

A crack map similar to that generated for B-20-133/134 was also generated for B-20-148/149. These two bridge decks were remarkably free of cracking at the time of this inspection. A typical crack is shown in Figure 3.21. The overall crack maps for both bridge decks shown in Figure 3.22 indicate that the bridges have very little cracking at this point in their service life. Only small cracks were found in B-20-149, the mild-steel reinforced bridge, near the abutment joints and on the parapet.

It is interesting to note that the cracking in these simply-supported superstructures is limited to locations near the abutments where shrinkage restraint is more likely to be present. The overall span of these bridge superstructures is similar to the spans found in the continuous superstructures of bridges B-20-133/134. However, the extent of cracking in the simply supported configuration is much less than the continuous configuration. This suggests that shrinkage-induced cracking is much more likely in continuous-span superstructures and that live loading-induced tensile strains in the deck resulting from the continuous-span configuration. This likelihood is evaluated more thoroughly using finite element simulation in another chapter of this report.

Bridge deck schematics for B-20-148/149 with picture indices that document photograph numbers and direction it was taken are given in Figure 3.23. The photographs illustrate the condition of key bridge elements at the time of the visual inspection (late October 2005). A complete set of photos and index is available (Martin 2006). Figures 3.24 and 3.25 show overall road surface condition and typical traffic flow/content on the day of the visual inspection.

Figure 3.26 and 3.27 show the north side of the eastern abutments of each bridge. Figure 3.27 also illustrates the location of the data acquisition junction box that was used for wiring data acquisition instruments the load testing conducted during the research effort. Figures 3.28 and 3.29 document the northern parapets of each bridge. Bridge B-20-149 (Figure 3.28), the steel-reinforced bridge deck, features a pedestrian walk way on the North side of the bridge deck. No cracking was found through the visual inspection at the overhanging portion of the decks for either bridge.

The concrete diaphragms at the abutments for both bridges were in excellent condition. Figures 3.30 and 3.31 illustrate the condition of these superstructure components on the day of the benchmark condition survey. Figures 3.32 and 3.33 illustrate the condition of the underside of the bridge deck in the vicinity of the steel diaphragms. No cracking is seen in the underside of the deck, and the galvanized steel diaphragms have no signs of deterioration.

The only cracks found through the visual inspection were in the steel-reinforced bridge (B-20-149). Figure 3.34 documents one of the few cracks found in the parapets of these bridges. In general, the cracks were of hairline width and they did not project down into the bridge deck overhang. Therefore, it can be surmised that these cracks were simply shrinkage cracks arising from the slip forming of the parapet and were not shrinkage cracking in the deck projecting into the parapet wall.

3.4 Evaluation of NDE Techniques

The initial condition of bridges B-20-133/134 and B-20-148/149 fostered examination of non-destructive evaluation (NDE) methodologies to help understand the likely causes of the initial cracking, evaluating the extent to which further deterioration is progressing and perhaps most importantly, generating and understanding the impact of moisture penetration in the bridge deck with FRP-SIP formwork (B-20-133).

This section of the report outlines a review of NDE techniques that may be suitable for understanding long-term degradation within the bridge superstructures considered in this research effort. It also outlines a short study to evaluate the extent to which moisture has penetrated the FRP-SIP formwork bridge deck when compared to the conventionally constructed bridge deck.

Chain Dragging

Chain dragging is a popular acoustic-emission-based technique for locating subsurface delamination in the concrete above bridge deck reinforcement and stratification-type delamination in concrete (Guthrie, *et al.* 2006). To date, chain dragging is the only NDE tool capable of detecting locations of potential delamination. A typical implementation of chain dragging employs a steel chain being dragged along the deck or test area in a carefully determined path. A technician listens for changes in the acoustic response of the deck. Since this is only a location test, another test must be used to determine the size of the delaminated area. Usually a hammer or tap test follows the chain dragging and this follow-on test is described in the next section.

It is difficult to say if chain dragging would be useful for locating delamination present on the bottom of an 8" deck with FRP-SIP formwork. In most cases, delamination of the concrete above reinforcing steel is in the upper section of the deck. Further testing would be needed to show this as a valid approach to finding potentially un-bonded areas in the FRP-SIP formwork bridge decks. However, the technique is likely to remain useful in determining delaminations in the concrete matrix near the surface of the deck that may or may not result from the very closely spaced FRP grillage reinforcement. The close proximity of the grillage reinforcement near the surface of the deck may have resulted in difficulty in properly consolidating the concrete during placement. However, it should be noted that this tendency is no different than that for the conventionally reinforced bridge deck. Attempting to detect delaminations at the interface between the FRP-SIP formwork and concrete deck is not within the realm of practicality with the chain dragging NDE technique and therefore, it was not implemented in this study.

Once a bridge deck is in service, carrying out chain dragging on the bridge deck would require that lane closures be executed. This traffic control was not accounted for in the project budget and therefore, it was a second difficulty associated with implementing chain dragging in the present study. These two difficulties associated with chain dragging coupled with its lack of perceived benefit in assessing the tendency for delamination at critical interfaces in the FRP-SIP bridge deck system suggested that it would not be a useful NDE methodology for the present study.

Tap Testing

Traditional tap testing or coin tap testing is one of the simplest NDE tests to execute, but is also the hardest to quantitatively interpret. The test simply requires the inspector to tap a small coin-like disk on the structure in question. The tap test has traditionally been qualitative, relying on an inspectors hearing to detect defective regions (Starnes and Carino 2003). The other problem with using it on large structures is that it is a point test. It would be very time consuming to tap the entirety of the underside of a bridge deck.

The research team did identify a research group attempting to create a quantitative and automated coin tap method. At the time of the research conducted by Martin (2006), a team at the Center for Non-Destructive Evaluation at Iowa State University was working on improving the coin tap test and to develop a Computer-Aided Tap Tester (CATT). The system uses an accelerometer to measure the amount of contact time the tip has with the material in question. For composites, debonding would be indicated by a longer contact time because the material is more flexible than a bonded composite material.

The instrumented tapping system is intended to have imaging capabilities that would be able to quantitatively relate to the local stiffness of the structure to potential delamination. The methodology and procedure was developed to inspect the integrity of airplane and helicopter components. The system was intended to be simple to apply; would have low cost to implement; and inspectors would not need extensive training (CNDE 1999). A visit to the CNDE in Ames, IA by Martin (2006) showed that the CATT would not be a very good choice for the present research effort because the tip of the CATT is extremely small and intended for very thick composite materials and not reinforced concrete bridge decks. Figure 3.35 illustrates the typical CATT equipment and images obtained through implementation.

The company that makes the accelerometer tip that is used in the CATT system also manufactures impact hammers. These hammers in the vibration division of the company can be used for modal analysis, structural testing, resonance determination, and civil infrastructure health determination (PCB 2006). The hammers use the same principle as the coin tapping test and the CATT, but a larger mass to deliver the initial impact. Typical hammers are shown in Figure 3.36. The tip of each hammer has a response accelerometer attached to it which measures the motion of the test specimen as a result of

the impulse force provided by the hammer. They have the ability to include computer-based data acquisition while inspecting a structure.

If the FRP-SIP formwork on the bottom of the bridge deck is separating from the concrete deck (*i.e.* delaminating), it should be more flexible and show a longer contact time when hit with an impact hammer. This would be a good test to use to quantify the degree to which debonding has taken place between the FRP-SIP formwork and the concrete bridge deck. An expected contact time for a good bond scenario would have to be established to compare the values found on the bridge deck. The present research effort did not have funds sufficient to calibrate this methodology for use in bridge infrastructure systems and therefore, it was not applied in the present effort. It should be noted that implementing tap testing on the underside of the bridge deck is feasible and it is recommended that a research effort be undertaken to quantify the capabilities of this method for determining the extent to which debonding is present in the FRP-SIP bridge deck system.

Ultrasonic Testing

Ultrasonic testing measures the speed of waves traveling through materials. Ultrasonic systems, digital or analog, typically have four components: transducer, pulse generator (clock), receiver/amplifier, and a display (screen). Figure 3.37 schematically illustrates these components. The clock or pulse generator sends voltage to the transducer which creates an impulse that excites the material being tested. The material reflects the wave created by the impulse back to the transducer. The transducer then sends a voltage signal to the receiver or amplifier. These are all recorded on a screen that displays the time between the transducer sending the impulse and receiving the reflected wave. This time can then be related to the pulse velocity when the thickness of the testing material is known. It has been reported that pulse velocities can then be correlated to material quality or bond quality (Hellier 2001).

Because transducers are used to generate and intercept the pulses on either side of a specimen, it is more difficult to do this test in-situ on a bridge deck. For example, to determine the quality of concrete, cores would have to be taken from the bridge to be evaluated. As the quality of concrete decreases so

does the pulse velocity. Testing has shown that pulse velocities over 4,600 m/s (15,100 ft/s) indicate very good quality concrete where velocities lower than 2,100 m/s (6,900 ft/s) indicate very poor quality concrete (Grace and Hanson, 2004). These velocities can also be used to estimate the unconfined compressive strength of concrete.

Ultrasonic testing could be useful on a predetermined problem area from chain dragging or tap testing. This would be another way to quantify delaminations after the delamination has been located. Typically the transducers used are small and it would be unrealistic to use them to examine the entire underside of the deck. Testing would have to be done to correlate the pulse velocities to the FRP-SIP being bonded or un-bonded. Overall, it is unlikely that ultrasonic testing would be a useful tool in assessing the long-term performance of the IBRC bridge superstructures.

Infrared Thermography

Infrared thermography (IRT) is based on the principle that subsurface defects affect the heat flow in a material (Rens, Nogueira and Transue 2005). The technique became a recognized standard method for NDE by the American Society for Nondestructive Testing in 1992. As conduction occurs in a bridge deck, any discontinuities in the material will interrupt the heat transfer and show a localized temperature change. Infrared systems such as cameras and scanners are used to detect these differences. Most of these applications require a trained professional interpretation because of the many variables that go into IRT such as emissivity, thermal coefficients of constituent materials, and temperature are difficult to definitively establish. Even though training is required to interpret results, IRT is fast and it can create images almost immediately. In theory, a trained thermographer can determine the condition of the structure very quickly (Hellier 2001).

The key to infrared thermography in bridge decks is that there must be void space in the material that will transfer heat differently thereby facilitating detection. Concrete is an ideal material for this because, although it has a low thermal conductivity, it is able to retain heat for a long period of time. For bridge decks, the conditions just after sunrise or sunset create an environment where the concrete deck has a different temperature than the surrounding ambient air (Chowdhury *et al.* 2004).

Debonding between the FRP-SIP formwork and the concrete deck is possible to detect with infrared thermography, but is harder to detect since the two materials may have lost bond but could still be in contact with each other. This situation will not provide the necessary void to disrupt the heating flow. IRT has been used in the aerospace industry to detect de-bonded lamina in composite structures because of its sensitivity to voids (Nokes and Hawkins 2001). Theoretically, this technique could be used to show debonding in a bridge deck with the FR-SIP reinforcement.

Bridge decks and test specimens can be heated in a variety of ways. Typically, a bridge deck tested in-situ is allowed to heat in the morning on a sunny day and they are then scanned in the early afternoon. An experiment involving a specimen made of FRP tubes bonded together with adhesive was heated using a hairdryer that piped hot air into the tubular void space. Debonded with void space around it can be found as a cool spot with an infrared scanner or camera. Other ways of heating specimens include heated water and heat lamps (Miceli 2000).

Debonding can be confirmed by a tap test once found by an IRT camera or scanner. Tests using this technique in Ohio showed that IRT was successful in finding debonding in composite retrofit systems (Nokes and Hawkins 2001). The tap test was found to be essential in minimizing false positive debonded areas found by the IRT scanner. IRT could identify and monitor debonding; however it was found that a debonded area must change by 50% to confidently indicate growth in the debonded area (Nokes and Hawkins 2001).

Marquette University tested out IRT on a scale-model section of the FRP-SIP bridge deck with FRP grillage reinforcement (Martin 2006). The full-scale prototype was used for this evaluation prior to load testing. The bridge deck is shown in Figure 3.38. Planned locations of debonded formwork were fabricated into the bridge-deck prototype. The FRP-SIP formwork was covered in Concreasive® and aggregate as formulated in the original design specifications with the exception of several locations intentionally masked to create areas un-bonded areas. These un-bonded areas were then intended to be test locations for the IRT method. Additional details related to the means of establishing un-bonded zones within the bridge deck prototype are available (Martin 2006).

IRT relies on temperature gradients being present through the thickness of the bridge deck. Therefore, the laboratory environment required heating the top surface of the deck using a 900-Watt heating lamp suspended above the slab. The laboratory setup used to generate thermal gradient through the deck prototype is shown in Figure 3.39.

After allowing the slab to heat up for 4 hours in the morning, a trained thermographer from a local consulting firm well-versed in the use of IRT equipment examined the bridge deck. The equipment consisted of a receiver and monitor, VHS recorder, and IRT camera. With this equipment, still photos and video can be taken. Figure 3.40 illustrates the typical IRT equipment used in this experiment. With the slab sufficiently heated to generate adequate thermal gradient through the thickness, the IRT camera was used to scan the underside of the deck with the goal being to locate the intentionally delaminated locations within the bridge deck. Pictures were also taken looking down the hole in the SIP formwork. Typical IRT photos of the bridge deck are shown in Figure 3.41.

Although very useful in being able to detect honeycombing in the concrete at the edge of the deck (Figure 3.41), it appeared that the intentionally delaminated locations in the deck could not be found because there was no void (air spaces) between the concrete and FRP-SIP formwork. If the two are in contact with each other, IRT cannot find a delamination. The air (or other) space must be there to interrupt the heat transfer. While this might not be a problem for retrofitted FRP that is peeling away from concrete, the SIP formwork would most likely not have the void space needed for reliable detection of debonded regions at the FRP-concrete interface using IRT.

3.5 In-Situ Moisture Evaluation in Waupun Bridges

The presence of moisture at the interface between the FRP-SIP formwork and the concrete deck was shown to affect the shear transfer capacity at this interface (Martin 2006). As a result, the research team sought to investigate and quantify the extent to which moisture may be accumulating at this interface. It is well known that permeability of moisture through concrete is a long-term process and given the fact that the concrete decks in bridges located in Waupun, Wisconsin (B-20-133 and 134) are 8 inches thick; it is not expected that significant moisture migration into the bridge decks has taken place. However, the

research team did seek to evaluate the difference in relative humidity between the two bridge decks to see if there is a tendency for the FRP-SIP formwork to facilitate a humid environment (relative to the conventional bridge deck). This evaluation was done using a digitally read hygrometer probe shown in Figure 3.42.

Two humidity tests were conducted for bridge B-20-133 (7/30/08 and 9/11/08) and one humidity test for B-20-134 (9/11/08) using the digital hygrometer. The hygrometer probe is inserted into holes drilled to varying depths within the bridge deck from the underside. Holes were drilled into the underside of the bridge deck at three different depths: 1-in, 2-in., and 3 inches. This leaves 5 inches (minimum) of concrete cover over the holes. A series of 6 holes were drilled across the underside of the bridge decks in both B-20-133 and B-20-134. The holes then had plastic probe jackets/sleeves inserted into them. Orange protective cups were then attached to the probe sleeves. The scenario described is shown in Figures 3.43(a) and 3.43(b). A close up of the probe inserted into the sleeve with protective cup is shown in Figure 3.43(c).

Data for all hygrometer tests is given in Tables 3.1 through 3.3. The motivation for the hygrometer studies was to evaluate the tendency for the FRP-SIP formwork to facilitate moisture retention within the bridge deck and most importantly at the interface between the FRP-SIP formwork and the concrete deck. As can be seen in the tables, the hygrometer probe depths that are 1 and 2 inches from the deck soffit exhibit higher humidity levels than those in the traditional deck at the same depths. Therefore, it can be concluded that the FRP-SIP is inhibiting evaporation of moisture from the deck soffit surface and the stay-in-place form is acting as an impermeable moisture egress barrier from the deck. Hygrometer readings at 3 inches show relatively consistent results between the two bridge decks.

No moisture was found when drilling the hygrometer probe holes so there is no concern that moisture is actually accumulating at the interface of the FRP-SIP formwork and the concrete deck. It should be understood that relative humidity is one measure of the tendency for the FRP-SIP formwork to inhibit moisture egress from within the deck and may be an indicator for the tendency for moisture to accumulate at the interface. However, the ability of humidity readings to reliably indicate levels of

moisture to expect at the interface remains to be definitively proven. It is recommended that further analysis with regard to relative humidity be undertaken in future research efforts as it may be a useful tool for long-term evaluation.

3.6 Conclusions

Three major items were discussed in the present chapter. Initial benchmark condition assessments of the IBRC bridge superstructures were described in detail. Evaluation of available NDE techniques, including a laboratory evaluation test for IRT, was conducted. Finally, in-situ moisture testing through use of digital hygrometer was described.

After approximately one year of traffic loading, bridges B-20-133/134 showed significant transverse cracking around the central piers and along the abutment joints. Therefore, it is likely that moisture has a direct path to the zone where aggregate interlock between the FRP-SIP formwork and concrete is needed to accomplish the shear transfer needed to ensure that positive tension reinforcement for the bridge deck exists. Without a way to escape, moisture may freeze and thaw as the climate changes during the seasons.

Bridges B-20-148/149 are in excellent condition. These bridges show virtually no signs of deck cracking other than a few hairline cracks located at the abutments and in the parapet(s). The bridge deck with FRP reinforcement showed no cracks. No cracks were observed to extend through the bridge deck thickness. The lack of cracking present in the simply-supported superstructure when compared to the two-span continuous superstructures found in bridges B-20-133/134 suggests that further study of the continuous superstructure configuration is warranted. Further evaluation of the simply supported bridge superstructures (B-20-148/149) is not warranted.

The NDE techniques of infrared thermography, chain dragging, tap testing, and ultrasonic testing, were reviewed. Tap testing with an impact hammer appears to be the most useful methods for monitoring the bridges studied in the present effort. Infrared thermography is the least likely to yield useful results for monitoring the IBRC bridges. Without an air void at the interface between FRP-SIP form and the concrete deck, there will not be a disruption of the heat transfer and IRT will not show debonding.

Whichever NDE method is chosen to inspect the bridge decks with FRP-SIP, it must be realized that any NDE technique will only be able to look at about half of the FRP area in contact with concrete. The tops of the void spaces that result from the FRP-tubes in the SIP formwork will be impossible to inspect because of the layer of FRP below the openings. This makes it very difficult to get a good idea of how much area is adequately interlocked once a test has been established to determine the quality of the interlock between the aggregate and FRP. It may be that coring the bridge deck and examining the resulting concrete quality and the interface between the concrete and FRP-SIP formwork is the most useful NDE/NDT methodology for the IBRC bridge at Waupun. It is conceivable that cores can be taken at regular intervals and monitored using procedures employed in Grace and Hanson (2004).

No moisture was found when drilling the hygrometer probe holes so there is no concern that moisture is actually accumulating at the interface of the FRP-SIP formwork and the concrete deck as of the date of this report. It should be understood that relative humidity is one measure of the tendency for the FRP-SIP formwork to inhibit moisture egress from within the deck and may be an indicator for the tendency for moisture to accumulate at the interface. However, the ability of humidity readings to reliably indicate levels of moisture to expect at the interface remains to be definitively proven. It is recommended that further analysis with regard to relative humidity be undertaken in future research efforts as it may be a useful tool for long-term evaluation.

3.7 References

- Chowdhury, R., Attanayaka, A.M.U.B., Aktan, H.M. (2005). "Non-Destructive Evaluation of Concrete Components Using Infrared (IR) Thermography for Void Detection and Moisture Evaluation", *Transportation Research Board Annual Meeting*, National Academies, (CD-ROM).
- CNDE (1999). "Tap Test Improved by Instrumentation Development" *Center for NDE News*, Volume 10, Issue 2, Iowa State University, Ames, Iowa.
- Grace, N. and Hanson, J. (2004). *Inspection and Deterioration of Bridge Decks Constructed Using Stay-In-Place Metal Forms and Epoxy-Coated Reinforcement*, Department of Civil Engineering,

Lawrence Technological University, Southfield, MI.

Guthrie, W.S., Frost, S.L., Birdsall, A.W., Linford, E.T., Ross, L.A., Crane, R.A., Eggert, D.L. (2006).

"Effect of Stay-In-Place Metal Forms on Performance of Concrete Bridge Decks", *Transportation Research Board Annual Meeting*, National Academies, (CD-ROM).

Hellier, C. (2001). *Handbook of Nondestructive Evaluation*, McGraw Hill.

Martin, K.E. (2006). *Impact of Environmental Effects On, and Condition Assessment Of, IBRC Bridge Decks in Wisconsin*, MS Thesis, Marquette University, Milwaukee, Wisconsin, May.

Miceli, M. (2000). *Assessment of Infrared Thermography as NDE method for Investigation of FRP Bridge Decks*, MS Thesis, Virginia Polytechnic Institute and State University, Blacksburg, Virginia.

Nokes, J.P. and Hawkins, G.F. (2001). *Infrared Inspection of Composite Reinforced Concrete Structures*, Ohio Department of Transportation, Columbus, OH.

PCB (2006). *PCB Piezotronics*, <http://www.pcb.com>, accessed January through April 2006.

Rens, K.L., Nogueira, C.L., Transue, D.J. (2005). "Bridge Management and Nondestructive Evaluation", *Journal of Performance of Constructed Facilities*, Volume 19, No. 1, February, pp. 3-16.

Starnes, M.A. and Carino, N.J. (2003). *Infrared Thermography for Nondestructive Evaluation of Fiber Reinforced Polymer Composites Bonded to Concrete*, NISTIR 6949, U.S. Department of Commerce, Washington, D.C.

Table 3.1 Relative Humidity Test Data for Bridge B-20-133 (FRP-SIP) July 30, 2008

Probe Depth from Deck Soffit	Time of Test	Within Bridge Deck		Ambient	
		Temperature (deg. C)	Relative Humidity (%)	Temperature (deg. C)	Relative Humidity (%)
1-in with cap	9:50 am	23.8	72	25	57.1
1-in without cap	10:28 am	26.1	73.1	26.5	49.7
2-in with cap	11:27 am	23.3	76.6	25	53.9
2-in without cap	12:01 pm	26.5	79.6	27	48.5
3-in with cap	10:54 pm	23.9	77.5	23.9	53.2
3-in without cap	12:30 pm	27.6	88.9	27.8	46.8

Table 3.2 Relative Humidity Test Data for Bridge B-20-133 (FRP-SIP) September 11, 2008

Probe Depth from Deck Soffit	Time of Test	Within Bridge Deck		Ambient	
		Temperature (deg. C)	Relative Humidity (%)	Temperature (deg. C)	Relative Humidity (%)
1-in with cap	1:57 pm	19.2	73.0	21.6	61.7
1-in without cap	1:31 pm	18.9	72.2	20.5	63.9
2-in with cap	1:10 pm	17.6	76.6	19.7	66.6
2-in without cap	12:45 pm	16.9	73.8	18.6	73.4
3-in with cap	12:22 pm	16.6	76.1	18.1	67.6
3-in without cap	12:00 pm	16.3	73.4	17.9	69.0

Table 3.3 Relative Humidity Test Data for Bridge B-20-134 (traditional) September 11, 2008

Probe Depth from Deck Soffit	Time of Test	Within Bridge Deck		Ambient	
		Temperature (deg. C)	Relative Humidity (%)	Temperature (deg. C)	Relative Humidity (%)
1-in with cap	11:22 am	17.1	63.4	18.1	66.7
1-in without cap	10:58 am	16.6	63.4	18.2	66.5
2-in with cap	10:31 am	13.9	66.8	17.0	72.4
2-in without cap	10:01 am	13.7	89.3	16.4	76.9
3-in with cap	9:12 am	13.7	73.1	16.1	73.8
3-in without cap	8:43 am	13.6	69.8	16.7	71.5



Figure 3.1 Looking North at the Southern Side of B-20-133/134

BRIDGE INSPECTION REPORT

Wisconsin Dept. of Transportation
DT2007 7/2003 (Replaces DT1544) s.84.17 Wis. Stats.

Inventory Data

Feature On: USH 151 NB		Maintainer: STATE HIGHWAY DEPT.	Structure Number: B-20-0133	
Feature Under: STH 28		Sect/Twn/Rng: S28 T14N R15E		
Location: 3.3M N JCT STH 49				
County: FOND DU LAC		Municipality: TOWN-WAUPUN (20042)		
Inv Rating: HS24.2	Rdwy Width: 39.4	Deck Width: 42.0	Existing Posting:	
Oper Rating: HS48.9	Total Length: 219.2	Deck Area: 9206	ADT On: 7300	Yr: 1998 ADT Under: Yr:

Inspection Type (* = Additional Applicable Form(s) Required)

	Routine Visual	Fracture Critical*	In-Depth*	UW-Dive*	UW-Surv.*	UW-Probe/ Visual*	Movable*
Last Insp.	2003-12-08						
Frequency	6						
Recom. Freq.							
	Initial*	Damage	Interim	Load Posted	SI & A Field Review*		
Last Insp.							
Frequency	N/A						
Recom. Freq.	N/A				Item No. Needing Change		

Load Rating Information

Overburden	File Meas. (in): 0.0	File Insp. Date:	Insp. Meas. (in):	Type: CONCRETE
Section Loss	File Meas. (%):	File Insp. Date:	Insp. Meas. (%):	Describe:
Should structure be re-rated for load carrying capacity? (Y/N)		Reason:		Date last rated:

Expansion Joints

Location	Type	Temp. File Insp. Date	File Insp. (in.)	New Insp. (in.)	Signing Condition			Comments
					Type of Marker	File	Y N N/A	
					Bridge Markers	Y		
					Narrow Bridge	N		
					One Lane Road	N		
					Vertical Clearance	N		
					Weight Limit	N		
					Other(Addl. Sign)	N		

Clearances (Cardinal = N or E)

	File Meas. (ft.)	File Date	New Meas. (ft.)
Min. Vertical Clearance Under (Cardinal)	18.12		
Min. Vertical Clearance Under (Non-Cardinal)	19.02		
Min. Vertical Clearance On			

Structure Type

Construction/Rehabilitation History

Material	Configuration	# of Spans	Overall Length	Year	Work Performed	Plan	Shop
PREST CONCRET	DECK GIRDER	1	107.3	2003	NEW STRUCTURE	PLAN	
PREST CONCRET	DECK GIRDER	1	107.3				

Inspection Information

Special Requirements	Y/N	Comments
Traffic Control	N	
Access Equipment	N	
Other	N	

Inspector Information

Team Leader Name and No. Printed MU-IBRC TEAM		Team Member(s) Name(s) Printed	
Team Leader Signature		Insp. Date 2005-10-25	Inspection Agency MARQUETTE UNIVERSITY
District/Local Manager and No. Printed		District/Local Manager Signature	
		Review Date	

Figure 3.2 B-20-133 Inspection Report (continued)

Element Inspection (X) Check Elements Inspected						Structure Number				
Ck	Elem.	Env.	Description	Unit	Total QTY	Quantity in Condition States				
						1	2	3	4	5
X	26	4	Conc Deck/Coald Bars	SF	9205	9205				
	Comments: (Reint with fiber-reinforced polymer & and stay-in-place forms) Angled/longitudinal cracking near expansion oints and transverse cracking around central pier.									
X	109	3	P/S Conc Open Girder	LF	1076	1076				
	Comments:									
X	172	3	Painted Steel Diaphr	EA	16	16				
	Comments:									
X	205	3	R/Conc Column	EA	3	3				
	Comments:									
X	215	4	R/Conc Abutment	LF	99	99				
	Comments:									
X	234	4	R/Conc Cap	LF	45	45				
	Comments:									
X	250	3	Concrete Diaphragm	EA	12	12				
	Comments: Cracking around PRST Girders									
X	321	4	R/Conc Approach Slab	EA	2	2				
	Comments:									
X	331	4	Conc Bridge Railing	LF	494	494				
	Comments: HL vert cracks and efflorescence showing on underside of parapet overhang									
X	343	2	Crushed Aggregate Sp	EA	2	2				
	Comments:									
X	358	4	Deck Cracking SmFlag	EA	1	1				
	Comments: HL transverse cracks near pier									
X	359	4	Und Dk Surf SmFlag	EA	1	1				
	Comments: Unable to view concrete surface – Stay-in-Place Deck forms									
X	400	4	Concrete Wingwall	EA	4	4				
	Comments:									

General Inspection/Maintenance Notes

Figure 3.2 B-20-133 Inspection Report (continued)

NBI Ratings						Maintenance Recommendations		
NBI	File	New	NBI	File	New	Item	Cost	Comments
Dec	9	9	Culvert	N				
Superstructure	9	9	Channel	N				
Substructure	9	9	Waterway	N				

Page 3 of 3

Figure 3.2 B-20-133 Inspection Report

BRIDGE INSPECTION REPORT

Wisconsin Dept. of Transportation
DT2007 7/2003 (Replaces DT1544) s.84.17 W.s. Stats.

Inventory Data

Feature On: USH 151 SB		Maintainer: STATE HIGHWAY DEPT.	Structure Number: B-20-0134	
Feature Under: STH 26		Sect/Twn/Rng: S26 T14N R15E		
Local on: 2.2N S JCT STH Y				
County: FOND DU LAC		Municipality: TOWN-WAUPUN (20042)		
Inv Rating: HS24.4	Rdwy Width: 39.4	Deck Width: 42.0	Existing Posting:	
Oper Rating: HS48.9	Total Length: 219.2	Deck Area: 9206	ADT On: 7300 Yr: 1998	ADT Under: Yr:

Inspection Type (* = Additional Applicable Form(s) Required)

	Route Visual	Fracture Critical*	In-Depth*	UW-Dive*	UW-Surv.*	UW-Probe/Visual*	Movable*
Last Insp.	2003-12-08						
Frequency	6						
Recom. Freq.							
	Initial*	Damage	Interim	Load Posted	SI & A Field Review*		
Last Insp.							
Frequency	N/A						
Recom. Freq.	N/A				Item No. Needing Change		

Load Rating Information

Overburden	File Meas. (n): 0.0	File Insp. Date:	Insp. Meas. (n):	Type: CONCRETE
Section Loss	File Meas. (%):	File Insp. Date:	Insp. Meas. (%):	Describe:
Should structure be re-rated for load carrying capacity? (Y/N)			Reason:	Date last rated: 2002-03-12

Expansions Joints

Local on	Type	Temp.			Signng Condition			Comments
		File Insp. Date	File Insp. (n.)	New Insp. (n.)	Type of Marker	File	Y/N/N/A	
					Bridge Markers		Y	
					Narrow Bridge		N	
					One Lane Road		N	
					Vertical Clearance		N	
					Weight Limit		N	
					Other(Addl. Sign)		N	

Clearances (Cardinal = N or E)

	File Meas. (ft.)	File Date	New Meas. (ft.)
M n. Vertical Clearance Under (Cardinal)	18.12		
M n. Vertical Clearance Under (Non-Cardinal)	18.29		
M n. Vertical Clearance On			

Structure Type

Construction/Rehabilitation History

Material	Configuration	# of Spans	Overall Length	Year	Work Performed	Plan	Shop
PREST CONCRET	DECK GIRDER	1	107.3	2003	NEW STRUCTURE	PLAN	
PREST CONCRET	DECK GIRDER	1	107.3				

Inspection Information

Special Requirements	Y/N	Comments
Traffic Control	N	
Access Equipment	N	
Other	N	

Inspector Information

Team Leader Name and No. Printed MU-IBRC TEAM		Team Member(s) Name(s) Printed	
Team Leader Signature		Insp. Date 2005-10-25	Inspection Agency MARQUETTE UNIVERSITY
District/Local Manager and No. Printed		District/Local Manager Signature	
		Review Date	

Figure 3.3 B-20-134 Inspection Report (continued)

Element Inspection (X) Check Elements Inspected						Structure Number				
Ck	Elem.	Env.	Description	Unit	Total QTY	Quantity in Condition States				
						1	2	3	4	5
X	26	4	Conc Deck/Coatd Bars	SF	9205	9205				
	Comments: Angled/longitudinal cracking near expansion joints and transverse cracking around central pier.									
X	109	3	P/S Conc Open Girder	LF	1076	1076				
	Comments:									
X	172	3	Painted Steel Daphn	EA	16	16				
	Comments:									
X	205	3	R/Conc Column	EA	3	3				
	Comments:									
X	215	4	R/Conc Abutment	LF	99	99				
	Comments:									
X	234	4	R/Conc Cap	LF	45	45				
	Comments:									
X	250	3	Concrete Daphragm	EA	12	12				
	Comments: Cracking around PRST Girders									
X	321	4	R/Conc Approach Slab	EA	2	2				
	Comments:									
X	331	4	Conc Bridge Ra iling	LF	494	494				
	Comments: HL vert cracks and efflorescence showing on underside of parapet overhang									
X	343	2	Crushed Aggregate Sp	EA	2	2				
	Comments:									
X	358	4	Deck Cracking SmFlag	EA	1	1				
	Comments: HL transverse cracks near pier									
X	359	4	Und Dk Surf SmFlag	EA	1	1				
	Comments: HL transv cracks with efflorescence									
X	400	4	Concrete Wingwall	EA	4	4				
	Comments:									
<u>General Inspection/Maintenance Notes</u>										

Figure 3.3 B-20-134 Inspection Report (continued)

NBI Ratings						Maintenance Recommendations		
NBI	File	New	NBI	File	New	Item	Cost	Comments
Deck	9	9	Culvert	N				
Superstructure	9	9	Channel	N				
Substructure	9	9	Waterway	N				

Figure 3.3 B-20-134 Inspection Report

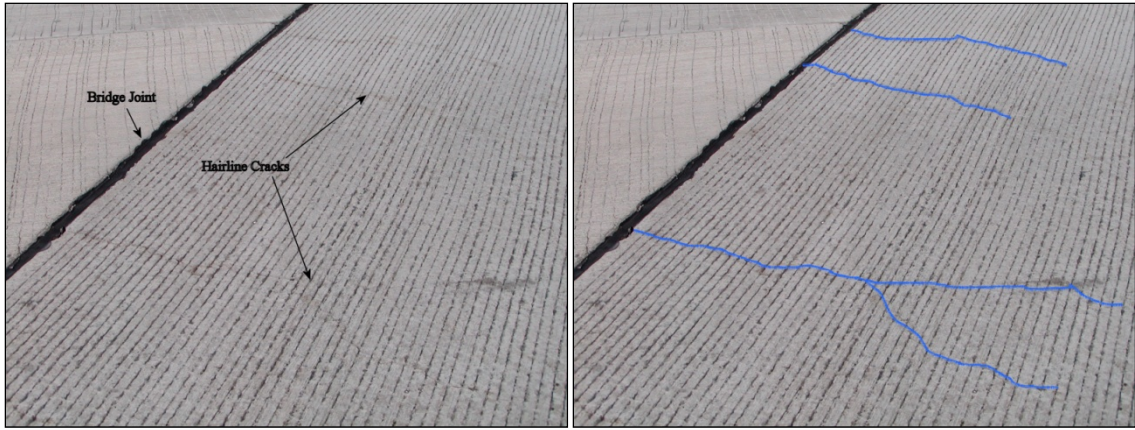


Figure 3.4 Hairline Cracks Near the Bridge/Abutment Joint

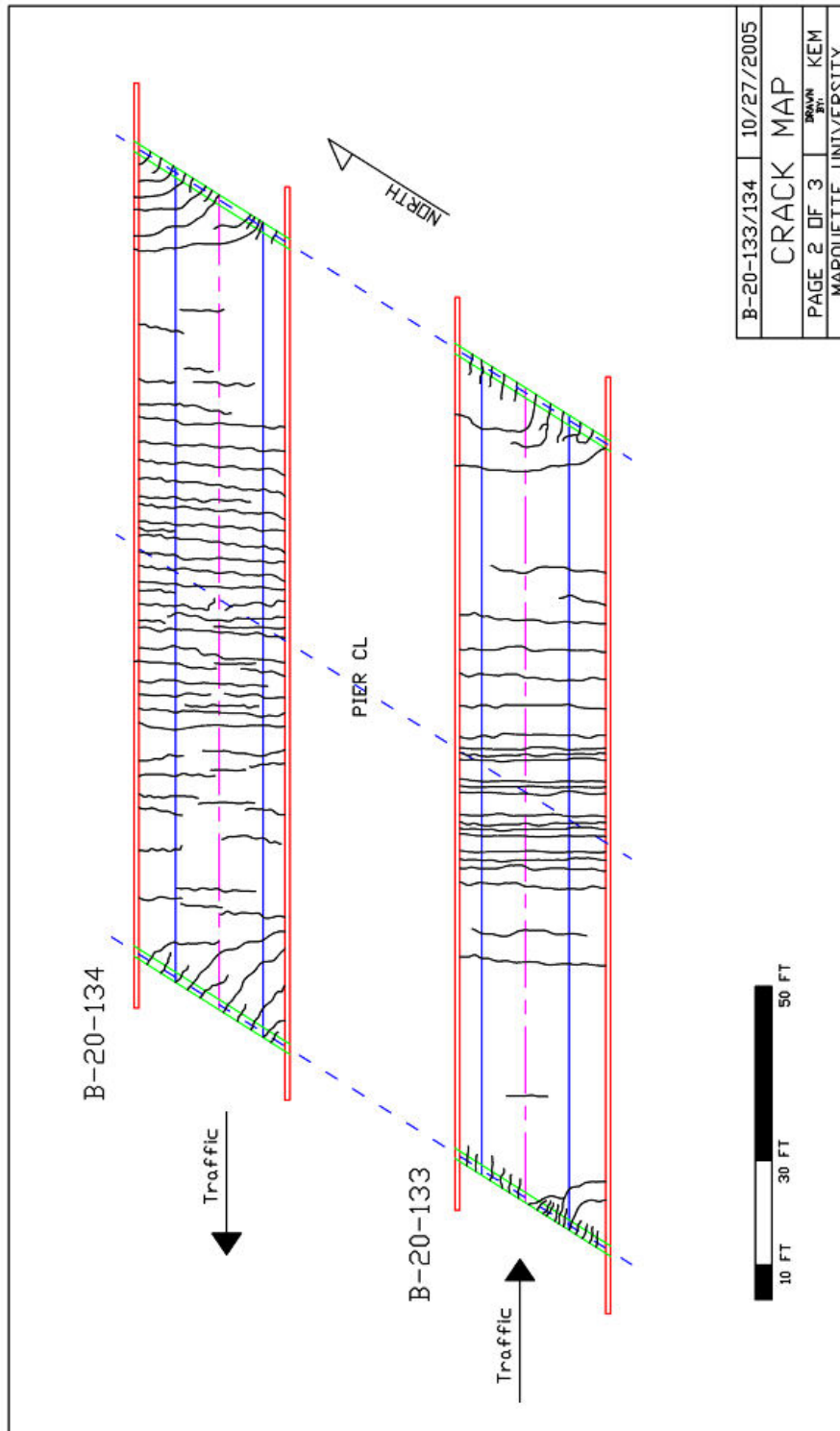


Figure 3.5 Crack Map of B-20-133/134

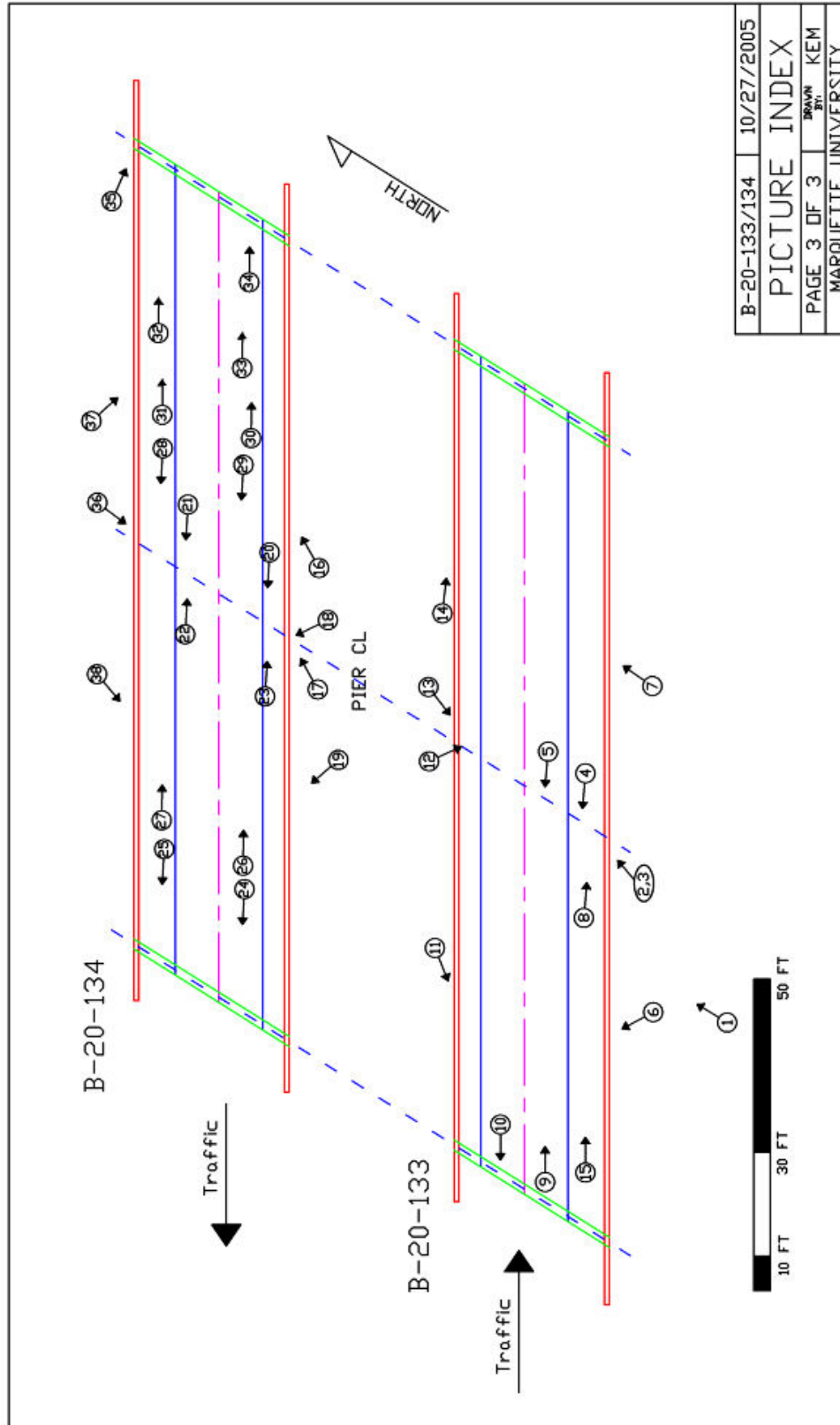


Figure 3.6 Picture Index of B-20-133/134



Figure 3.7 (3) Cracking with Efflorescence South Side of B-20-133 Above Central Pier



Figure 3.8 (17) East Side of Central Pier on the Southern Side of B-20-134



Figure 3.9 (4) Interior Diaphragm of B-20-133 Above Pier, at Girder 2 Looking West



Figure 3.10 (20) Pier Diaphragm Looking West Between Girder 1 and 2, B-20-134



Figure 3.11 (12) North Side Pier B-20-133



Figure 3.12 (36) Center Pier Exterior on North Side, B-20-134



Figure 3.13 (11) West Span B-20-133, North Side



Figure 3.14 (38) West Span B-20-134, North Side



Figure 3.15 (9) West Span Blisters and Sealant Seep-Through in FRP-SIP Deck Between Girder 3 and 4 Near West Abutment, B-20-133



Figure 3.16 (24) Underside of Bridge Deck at North Abutment, Girders (From Left to Right) 1, 2, and 3, B-20-134



Figure 3.17 (26) West Span Looking East at 1st diaphragm, Girders (From Left to Right), 3, 2, and 1, B-20-134



Figure 3.18 (1) B-20-148 South side looking NE

BRIDGE INSPECTION REPORT

Wisconsin Dept. of Transportation
 DT2007 7/2003 (Replaces DT1544) s.84.17 W s. Stats.

Inventory Data

Feature On: USH 151		Maintainer: STATE HIGHWAY DEPT	Structure Number: B-20-0148	
Feature Under: DENEVEU CR		Sect/Twn/Rng: S25 T15N R17E		
Location:		County: FOND DU	Municipality: TOWN-FOND DU LAC (20018)	
Inv Rating: HS23	Rdwy Width: 41.4	Deck Width: 44.7	Existing Posting:	
Oper Rating: HS73	Total Length: 134.4	Deck Area: 6007	ADT On: 6000 Yr: 2000	ADT Under: Yr:

Inspector Type (* = Additional Applicable Form(s) Required)

	Routine Visual	Fracture Critical*	In-Depth*	UW-Dive*	UW-Surv.*	UW-Probe/ Visual*	Movable*
Last Insp.							
Frequency							
Recom. Freq.							
	Initial*	Damage	Interim	Load Posted	SI & A Field Review*		
Last Insp.	2004-12-17						
Frequency	N/A						
Recom. Freq.	N/A				Item No. Needing Change		

Load Rating Information

Overburden	File Meas. (n): 0.0	File Insp. Date:	Insp. Meas. (n):	Type: CONCRETE
Section Loss	File Meas. (%):	File Insp. Date:	Insp. Meas. (%):	Describe:
Should structure be re-rated for load carrying capacity? (Y/N)			Reason:	Date last rated:

Expansions on Joints

Location	Type	Temp.			Sighting Condition			Comments
		File Insp. Date	File Insp. (n.)	New Insp. (n.)	Type of Marker	File	Y/N/N/A	
					Bridge Markers	N	N	
					Narrow Bridge	N	N	
					One Lane Road	N	N	
					Vertical Clearance	N	N	
					Weight Limit	N	N	
					Other(Addl. Sgn)	N	N	

Clearances (Cardinal = N or E)

	File Meas. (ft)	File Date	New Meas. (ft.)
Min. Vertical Clearance Under (Cardinal)			
Min. Vertical Clearance Under (Non-Cardinal)			
Min. Vertical Clearance On			

Structure Type

Material	Configuration	# of Spans	Overall Length	Construction/Rehabilitation History			
				Year	Work Performed	Plan	Shop
PREST CONCRET	DECK GIRDER	1	130	2004	NEW CONSTRUCTION	PLAN	

Inspector Information

Special Requirements	Y/N	Comments				
Traffic Control						
Access Equipment						
Other						

Inspector Information

Team Leader Name and No. Printed MU-IBRC TEAM		Team Member(s) Name(s) Printed	
Team Leader Signature		Insp. Date 2005-10-27	Inspection Agency MARQUETTE UNIVERSITY
District/Local Manager and No. Printed		District/Local Manager Signature	
		Review Date	

Figure 3.19 B-20-148 Inspection Report

Element Inspection (X) Check Elements Inspected						Structure Number				
Ck	Elem.	Env.	Description	Unit	Total QTY	Quantity in Condition States				
						1	2	3	4	5
X	28	3	CONC DECK/COATD BARS	SF	6007	6007				
	Comments:									
X	109	2	P/S CONC OPEN GIRDER	LF	917	917				
	Comments:									
X	172	2	PAINTED STEEL DIAPHR	EA	12	12				
	Comments:									
X	215	2	R/CONC ABUTMENT	LF	199	99				
	Comments:									
X	250	2	CONCRETE DIAPHRAGM	EA	12	12				
	Comments:									
X	321	3	R/CONC APPROACH SLAB	EA	2	2				
	Comments:									
X	331	3	CONC BRIDGE RAILING	LF	330	330				
	Comments: VERY FEW SML VERT CRACKS									
X	342	2	RIP RAP SLOPE PROTECT	EA	2	2				
	Comments:									
X	358	4	DECK CRACKING SM FLAG	EA	1	1				
	Comments:									
X	359	4	UND DECK SURF SM FLAG	EA	1	1				
	Comments:									
X	400	2	CONCRETE WINGWALL	EA	4	4				
	Comments:									

General Inspection/Maintenance Notes

BOTN ABUTMENTS PROTECTED WITH HEAVY RIP RAP – NO SCOUR PRESENT

NBI Ratings						Maintenance Recommendations		
NBI	File	New	NBI	File	New	Item	Cost	Comments
Deck	9	9	Culvert	N	9			
Superstructure	9	9	Channel	9	9			
Substructure	9	9	Waterway	9	9			

Figure 3.19 B-20-148 Inspection Report (continued)

BRIDGE INSPECTION REPORT

Wisconsin Dept. of Transportation
DT2007 7/2003 (Replaces DT1544) s.84.17 W s. Stats.

Inventory Data		Mainline: STATE HIGHWAY DEPT		Structure Number: B-20-0149	
Feature On: USH 151		Sect/Twn/Rng: S25 T15N R17E			
Feature Under: DENEVEU CR		County: FOND DU		Municipality: TOWN-FOND DU LAC (20018)	
Inv Rating: HS23	Rdwy Width: 41.4	Deck Width: 44.7	Existing Posting:		
Oper Rating: HS73	Total Length: 134.4	Deck Area: 6007	ADT On: 6000 Yr: 2000	ADT Under: Yr:	

Inspection Type (* = Additional Applicable Form(s) Required)							
	Route Visual	Fracture Critical*	In-Depth*	UW-Dive*	UW-Surv.*	UW-Probe/ Visual*	Movable*
Last Insp.							
Frequency							
Recom. Freq.							
	Initial*	Damage	Interim	Load Posted	SI & A Field Review*		
Last Insp.	2004-12-20						
Frequency	N/A						
Recom. Freq.	N/A				Item No. Needing Change		

Load Rating Information				
Overburden	File Meas. (n): 0.0	File Insp. Date:	Insp. Meas. (n):	Type: CONCRETE
Sect on Loss	File Meas. (%):	File Insp. Date:	Insp. Meas. (%):	Describe:
Should structure be re-rated for load carrying capacity? (Y/N)			Reason:	Date last rated:

Expansions Joints				Signng Condition			
Location	Type	Temp.		Type of Marker	File	Y N N/A	Comments
		File Insp. Date	New Insp. (n.)				
				Bridge Markers	N	N	
				Narrow Bridge	N	N	
				One Lane Road	N	N	
				Vertical Clearance	N	N	
				Weight Limit	N	N	
				Other(Addl. Sign)	N	N	

Clearances (Cardinal = N or E)	File Meas. (ft.)	File Date	New Meas. (ft.)
Min. Vertical Clearance Under (Cardinal)			
Min. Vertical Clearance Under (Non-Cardinal)			
Min. Vertical Clearance On			

Structure Type		Construction/Rehabilitation History					
Material	Configuration	# of Spans	Overall Length	Year	Work Performed	Plan	Shop
PREST CONCRET	DECK GIRDER	1	130	2004	NEW CONSTRUCTION	PLAN	

Inspection Information		
Special Requirements	Y/N	Comments
Traffic Control		
Access Equipment		
Other		

Inspector Information			
Team Leader Name and No. Printed MU-IBRC TEAM		Team Member(s) Name(s) Printed	
Team Leader Signature		Insp. Date 2005-10-27	Inspection Agency MARQUETTE UNIVERSITY
District/Local Manager and No. Printed		District/Local Manager Signature	Review Date

Figure 3.20 B-20-149 Inspection Report

Element Inspection (X) Check Elements Inspected						Structure Number				
Ck	Elem.	Env.	Description	Unit	Total QTY	Quantity in Condition States				
						1	2	3	4	5
X	26	3	CONC DECK/COATD BARS	SF	7361	7361				
	Comments:									
X	109	2	P/S CONC OPEN GIRDER	LF	1179	1179				
	Comments:									
X	172	2	PAINTED STEEL DIAPHR	EA	16	16				
	Comments:									
X	215	2	R/CONC ABUTMENT	LF	124	124				
	Comments:									
X	250	2	CONCRETE DIAPHRAGM	EA	16	16				
	Comments:									
X	321	3	R/CONC APPROACH SLAB	EA	2	2				
	Comments:									
X	331	3	CONC BRIDGE RAILING	LF	340	340				
	Comments:									
X	334	3	METAL RAIL COATED	LF	164	164				
	Comments:									
X	342	2	RIP RAP SLOPE PROTECT	EA	2	2				
	Comments:									
X	358	4	DECK CRACKING SM FLAG	EA	1	1				
	Comments:									
X	359	4	UND DECK SURF SM FLAG	EA	1	1				
	Comments:									
X	400	2	CONCRETE WINGWALL	EA	4	4				
	Comments:									

General Inspection/Maintenance Notes

BOTN ABUTMENTS PROTECTED WITH HEAVY RIP RAP – NO SCOUR PRESENT

NBI	NBI Ratings				
	File	New	NBI	File	New
Deck	9	9	Culvert	N	9
Superstructure	9	9	Channel	9	9
Substructure	9	9	Waterway	9	9

Maintenance Recommendations		
Item	Cost	Comments

Figure 3.20 B-20-149 Inspection Report (continued)



Figure 3.21 (6) Hairline Crack on Deck of B-20-149 with Scale

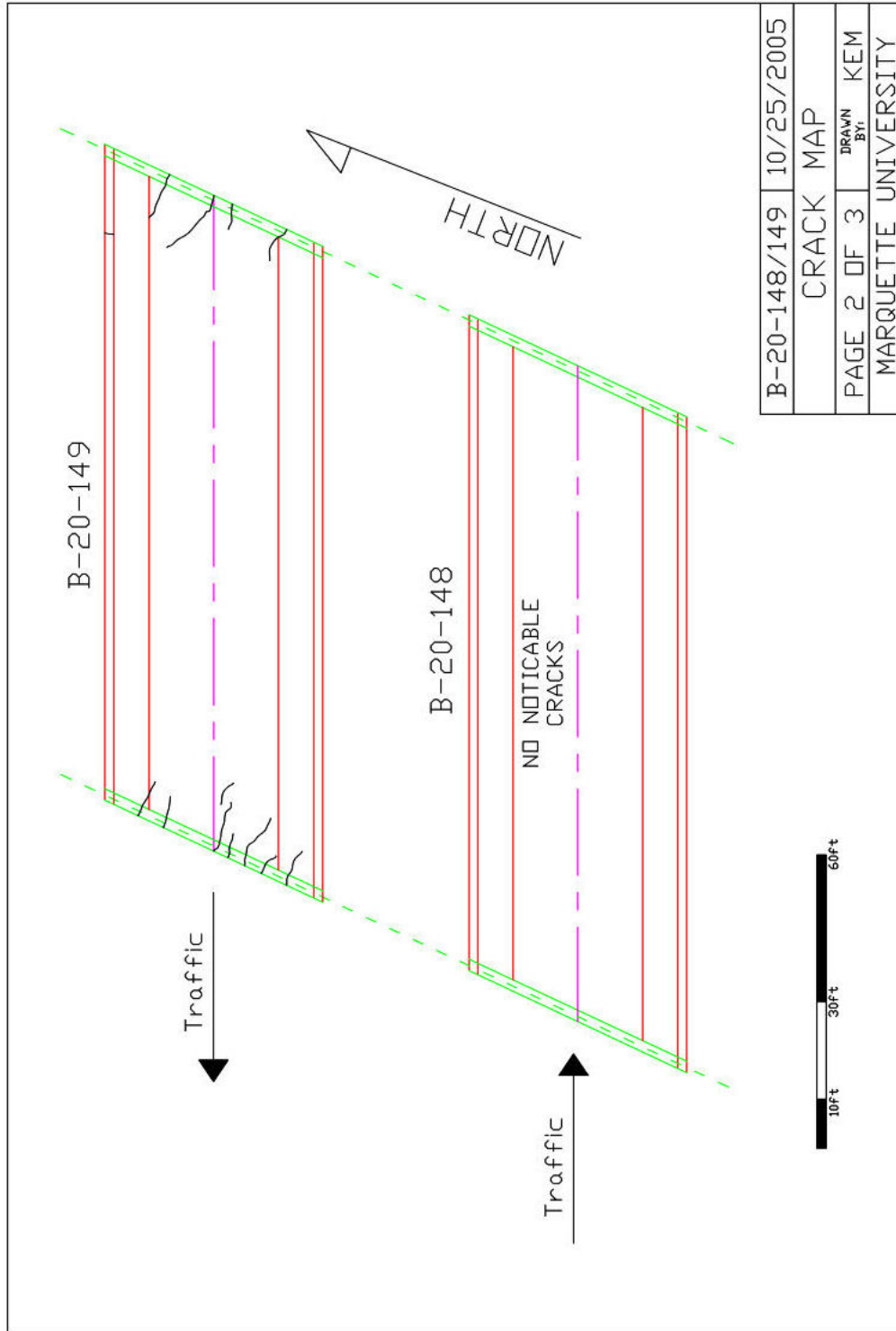


Figure 3.22 B-20-148/149 Initial Crack Map

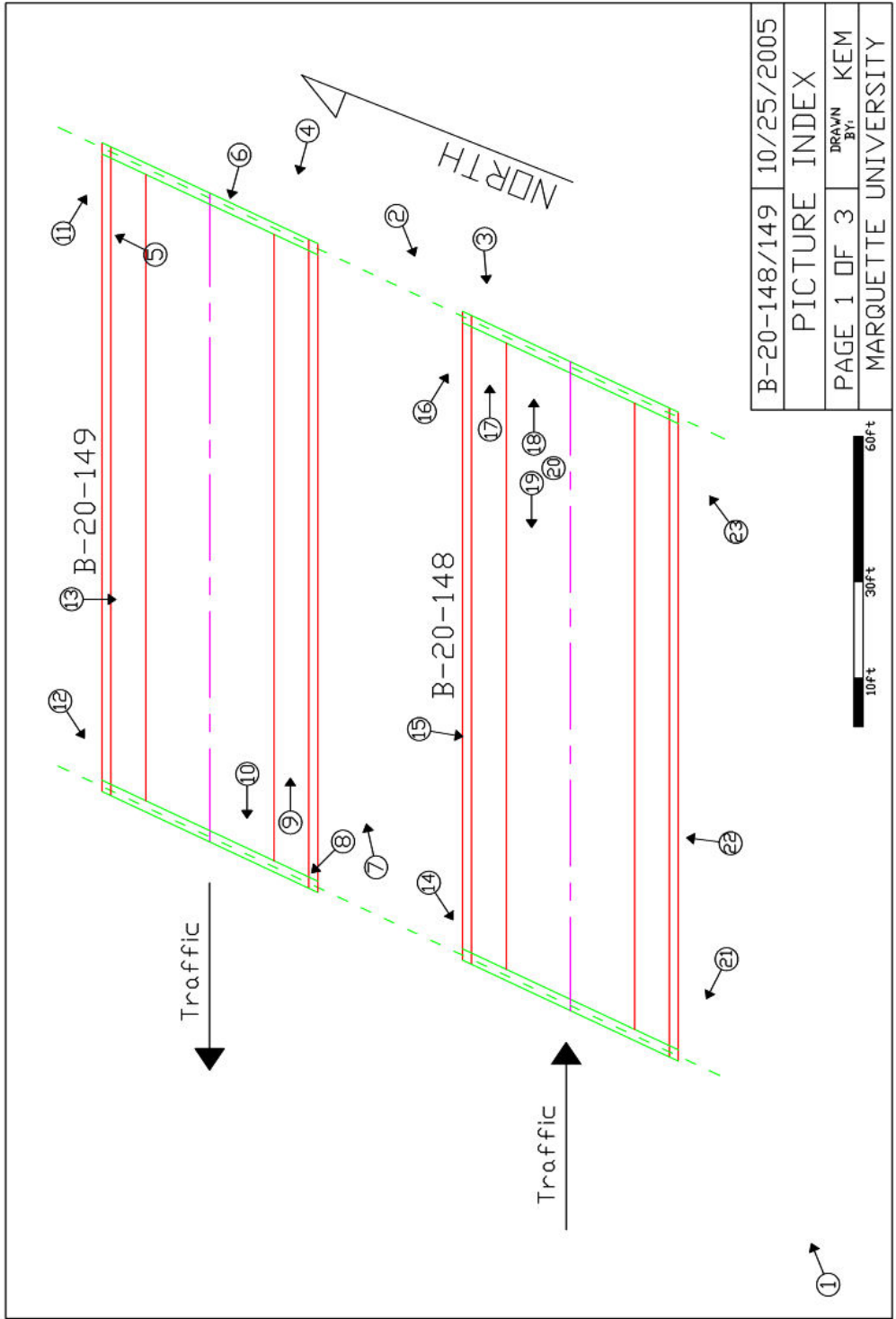


Figure 3.23 Picture Map For B-20-148/149



Figure 3.24 (3) Deck of B-20-148 with Traffic Looking West



Figure 3.25 (4) Deck of B-20-149 with Traffic Looking West



Figure 3.26 (16) East Abutment on North Side of B-20-148 with Data Acquisition Box Looking SW



Figure 3.27 (11) North side of East Abutment of B-20-149 Looking SE



Figure 3.28 (15) Exterior Girder (#7) on North Side of B-20-148 Looking South



Figure 3.29 (13) Underside of Pedestrian Walkway on North Side of B-20-149



Figure 3.30 (18) East Abutment Between Girders 5 and 6 of B-20-148 Looking East



Figure 3.31 (10) West Abutment Between Girders 2 and 3 of B-20-149



Figure 3.32 (9) 1st Diaphragm between Girders 1 and 2 on B-20-149



Figure 3.33 (19) First Diaphragm under B-20-148 Between Girders 5 and 6 with Wiring for Load Testing



Figure 3.34 (5) Northern Parapet Crack on B-20-149

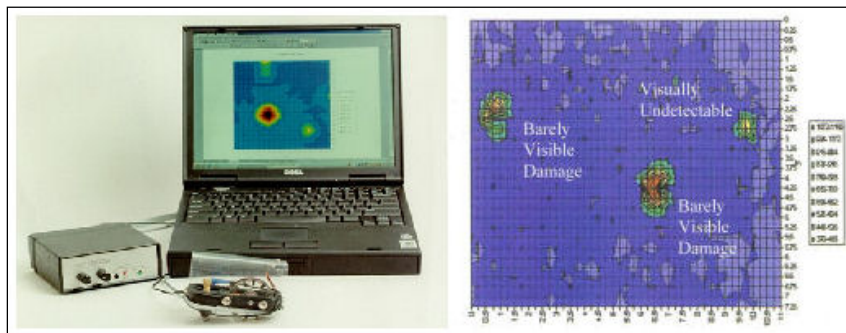


Figure 3.35 Computer Aided Tap Tester (CATT) and Testing a Heater Blanket of an American Airline MD80 (UCOMPO 2006)



Figure 3.36 Modally Tuned® ICP® Impact Hammers (PCB 2006)

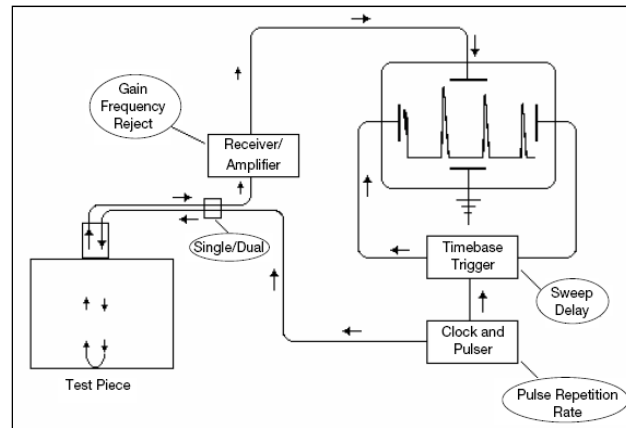


Figure 3.37 Ultrasonic Analog Diagram (Hellier 2001).



Figure 3.38 Deck Slab with SIP FRP Forms and FRP Reinforcement



Figure 3.39 Heating up the Slab



Figure 3.40 IRT Monitor and VHS Recorder and Camera

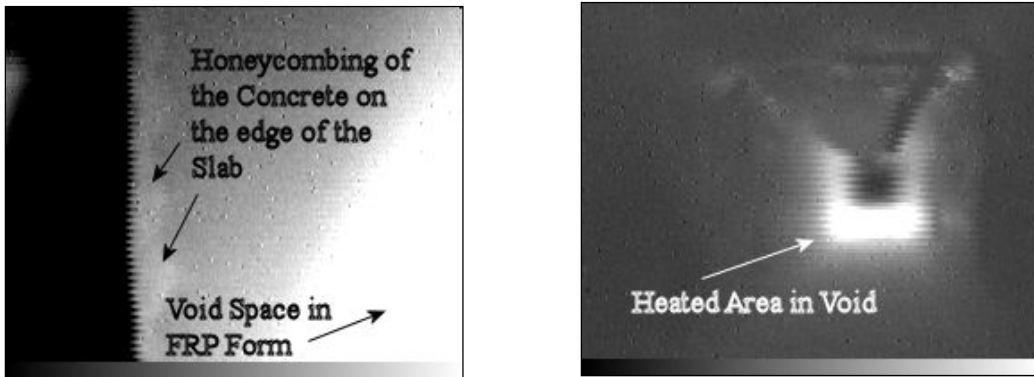


Figure 3.41 IRT Scans of the FRP SIP Form Slab



(a)



(b)

Figure 3.42 Digital Hygrometer with Probe: (a) Complete Hygrometer Instrument; (b) Probe with Cord Lead.



(a)



(b)



(c)

Figure 3.43 In-Situ Hygrometer Testing Arrangement: (a), (b) Probe Inserts with Plastic Protective Cups; (c) Close up of Probe Lead and Protective Cup.

This Page Has Been Intentionally Left Blank

Chapter 4

In-Situ Load Testing

4.1 Introduction

The research project included a component relate to in-situ load testing of the bridges. Two in-situ load tests were performed on each of the two IBRC bridges. The in-situ load testing was limited to tests done on the innovative bridges: B-20-133 and B-20-148. The traditionally constructed bridges were not subjected to in-situ load testing.

The load testing included acquisition of strain and deflection data related to the bridge decks and girders. The in-situ load testing was conducted with a two-year separation with the goal being to evaluate changes in response over this period, which may indicate degradation in the superstructure. Performance parameters evaluated through the load testing to track degradation include: wheel load distribution within the bridge deck, composite action in the girders, and bridge deck deflections relative to the girders. This chapter of the report outlines the in-situ instrumentation arrangement, the load testing protocols used, data acquired from the two in-situ load tests, and discussion of the test data.

4.2 In-Situ Instrumentation

The strain sensors developed as part of the research effort were used in the load testing conducted. Draw Wire Transducers (DWT's) were also incorporated into the load testing program. The objectives of in-situ load testing included determination of:

1. the strain profile through the precast girders and the bridge deck;
2. the transverse distribution of wheel loads in bridge deck;
3. the longitudinal distribution of lane loading among the girders within the superstructure;
4. the deflection of the bridge deck relative to the precast girders.

The portable strain sensors developed by Schneeman (2006) were utilized to measure normal strain in various bridge superstructure components (e.g. bridge deck, girders). Mounting the portable strain sensors in the field required that two wedge-type expansion anchors be drilled into the cover concrete (1-inch of embedment). These mounting "studs" were then left in place at each location where a strain transducer was to be mounted. The portable strain transducers could then be bolted on to the bridge component using these studs and then removed after the load testing was completed. Typical mounting of the strain sensors is shown in Figure 4.1. Calibration of the sensors for this mounting is discussed in Schneeman (2006) and earlier in this report.

Wiring of the strain sensors was accomplished using 6-pin mini-DIN connectors. This facilitated plugging and unplugging the sensors as the load tests were initiated and completed, respectively. The wiring and connectors were left in the field. Connections were protected using desiccant bags sealed with the DIN plugs in plastic bags as shown in Figure 4.2.

Commercially available draw wire transducers (DWT's) were used to measure the deflection of the bridge deck relative to the bridge girders. These are often called string potentiometers and the research effort used UniMeasure, Inc. model PA-30 DWT's. These devices have a measuring string 30" long, which gives flexibility in attaching the potentiometers as shown in Figure 4.3. Further discussion of their mounting during specific load tests will be addressed in later sections of this chapter.

This study is aimed at evaluating the long term behavior of the IBRC bridges and as a result, permanent equipment (e.g. wiring, junction boxes, NEMA 6P enclosures with screw terminals) were installed and left in place thereby reducing effort for the load tests performed in this research and possible future tests. The mounting bolts for strain gauges, lead wires for the instruments, protective PVC piping and an electrical enclosure box were installed on each bridge. Examples of the PVC wiring runs, the enclosure box, and the data acquisition system are shown in Figures 4.2 and 4.4.

Instrumentation of B-20-133 was limited relative to B-20-148. A schematic illustrating the instrumentation in plan is shown in Figure 4.5. The instrumentation in this bridge structure was focused on measuring the distribution of wheel loads within the bridge deck and the deflection of the bridge deck relative to the girders. Additional schematics outlining the conduit runs and a reference point used in

locating the instrumentation in plan is shown in Figure 4.6. Figure 4.6(a) also includes a schematic illustrating how the DWT's were mounted to measure deck deflections.

Figure 4.7 illustrates the data acquisition system (DAQ) with enclosure. The enclosure contains terminal bars with 6-pin DIN connector pig-tails that were plugged into the back of the portable DAQ system. The enclosure is water tight and is permanently mounted to the abutment diaphragm.

The DWT mounting arrangement is shown in Figure 4.7(b). The DWT string was attached to an eye bolt that was permanently mounted to the underside of the bridge deck using a wedge-type expansion anchor. Aluminum UniStrut cross members were mounted to the girders using wedge-type expansion anchors and steel angles. These horizontal members are shown in Figure 4.7(b) and the DWT is attached to this cross-member with the string extended vertically to the underside of the bridge deck. The DWT string is located within a relatively sheltered region under the bridge deck. As a result, the strings are not exposed to wind, which can disturb the deflection readings as a result of the string vibrating in the wind stream. While the area between the girders and under the deck soffit is not completely sheltered, it did limit vibrations induced in the DWT strings due to wind. Threaded studs for mounting the portable strain transducers are also shown in Figure 4.7(b).

The instrumentation for bridge B-20-148 is a bit more extensive than bridge B-20-133. A schematic of the instrumentation in plan is given in Figures 4.8, 4.9, and 4.10. The focus of the load testing on this bridge is to experimentally determine the following: (a) bridge deck deflection relative to the girders (DWT instruments); (b) girder lane load distribution factors (LM and LT instruments); (c) transverse wheel loading distribution widths (TW instruments); (d) strain distribution over the height of the girder-deck composite section (LM and SP instruments).

Longitudinal distribution of load between the girders was conducted by attaching individual strain sensors to the underside of bridge girders at mid-span (LM strain gauges) and a third-point of the span (LT strain gauges). As there are seven girders, fourteen individual sensors were installed with each sensor being centered transversely on the girder. The location and distribution of these sensors in the superstructure is shown in Figure 4.8

The strain profile of the bridge deck and girders is important to verify that composite action exists between the deck and girders. The B-20-148 super-structure was designed assuming composite action and verification of such behavior is required. Additionally, any degradation of this composite behavior over time wanted to be measured. By locating the strain sensors at the girder bottom flange, girder top flange, and on the FRP-reinforced deck as indicated in Figure 4.11, the strain variation over the height can be recorded. Girders G1 and G2 were installed strain sensors as in Figure 4.10(a) for this purpose.

The FRP grillage used for primary reinforcement of the concrete bridge deck is a new material and structural system. Significant laboratory testing has been conducted to date (Bank et al. 1992a; Bank et al. 1992b; Jacobson 2004), but in-situ validation is lacking. Work by Conachen (2005) attempted to address the issue, but due to the failure of instruments, little insight into the transverse behavior of the bridge's deck resulted. Thus, an array of strain sensors was installed on the underside of the bridge deck between Girders G2 and G3 (see Figures 4.8 and 4.9a) to evaluate wheel load distribution in the deck. The sensor array located between mid- and third-span of the bridge and was significantly far from the abutments. Therefore, the bridge's skew is not expected to have any effect on the test data of the deck at the location of the sensor array. The study of University of Wisconsin at Madison (Dieter 2002) indicated that the effective distribution region of a single HS-20 wheel load (approximately 20.8 kips) on this FRP reinforced concrete deck was no more than 36" in either direction from the contact area. Therefore, the five strain sensors were spaced at intervals of 18 inches in 72 inches of deck in longitudinal direction.

An enclosure similar to that used in B-20-133 was used in this bridge and Figure 4.12(a) illustrates the mounting of this enclosure to the east abutment on the bridge. Figure 4.8 illustrates the location of the enclosure in plan. Six-pin DIN plug pigtailed were also used to attach to the data acquisition (DAQ) system. These pigtail connectors are also housed within the NEMA 6P water tight enclosure and serve as a permanent repository of sensor wiring.

Figure 4.12(b) illustrates the DWT mounting system. This system is identical to that used in Bridge B-20-133. The DWT string is also protected from wind as a result of the DWT being mounted between the girders and below the bridge deck soffit. Typical mounting of portable strain sensors to the

lower flange of the girders is shown in Figure 4.12(c). Conduit runs used to facilitate long-term wiring runs for the load testing are shown in Figure 4.12(d).

4.3 In-Situ Load Test Protocols

The load testing involved protocols designed to gather the desired load transfer characteristic information for both bridges. The first involved marking the bridge decks with wheel targets for the drivers. This pavement marking was done each time load testing was conducted and it involved simple paint marking on the bridge deck. The deck surface marking and method used to position the truck wheels on the bridge deck are shown in Figure 4.13.

Calibrated (i.e. weighed) tri-axle dump trucks were utilized during all load tests. Six dump trucks were used. Figure 4.14 illustrates important information for vehicles used during the July 2007 load test. Trucks used in July 2007 had gross vehicle weights ranging from 54,480 lbs to 58,700 lbs. Front axles were weighed and the entire vehicle was weighed. These two weights were used to compute rear axle loads (assumed equally distributed between tandem axles). Figure 4.14 also illustrates vehicle tire contact patches measured prior to load testing. Figure 4.15 illustrates information for vehicles used in the July 2009 load testing. The dump trucks used for the July 2009 load test had gross vehicle weights ranging from 64,800 lbs to 66,900 lbs. The weights of these vehicles (on average) are 16% more than the July 2007 load test (56,767 versus 65,933 lbs). The fourth axles were maintained in the up position during all load testing and therefore, the loads on these axles was not accounted for or included.

Figure 4.16 illustrates the loading protocol used to examine the wheel load distributions within the bridge deck of bridge B-20-133. This loading protocol is known as "travel path 1" and the data acquisition file used to plot/reference the data is File1. It should be noted that the exterior deck span strain and deflections are being evaluated with this loading protocol and as a result, the left front wheel of the truck is positioned along a longitudinal line at mid-span of this exterior bridge deck span.

Loading protocol two for bridge B-20-133 is shown in Figure 4.17. This loading protocol is termed "truck travel path 2" and it is intended to measure deck deflection and wheel load distribution

within the first interior deck span in the superstructure. The data acquisition file used to reference data for this load testing protocol is File2. The right front wheel of the truck is used as the target wheel for the load testing. The truck driver was required to hit painted marks (Figure 4.13) on the bridge deck surface.

It should be noted that all load testing was done under live traffic with the passing lane subjected to closure. This limited truck positioning on the bridge deck surface to locations where the calibrated vehicle would remain exclusively in the passing lane.

The loading protocols used for bridge B-20-148 are shown in Figures 4.18, 4.19, 4.20, and 4.21. Loading protocol 1 shown in Figure 4.18 was used to establish maximum deflections relative to the girder due to front wheel loads in the exterior bridge deck span. Loading protocol 2 shown in Figure 4.19 was used to establish maximum deck deflections in the first interior span of the bridge deck. Loading protocol 3 shown in Figure 4.20 was established to examine the distribution of wheel loading within the bridge deck in the first interior bridge deck span. The final loading protocol (number 4) used for this bridge is shown in Figure 4.21 and it was used to establish lane loading distribution factors for the bridge superstructure.

Position of trucks during load testing protocol 4 in Figure 4.21 is shown in Figure 4.22(a). The lead truck in this grouping was given pavement markings on which to land the front wheel of the vehicle. The remaining two trucks in the train were simply instructed to align themselves with the lead truck and position themselves bumper to bumper. Typical wheel loading positions for the wheel load distribution protocols were accomplished using paint markings on the deck as shown in Figure 4.22(b).

4.4 Load Testing Results and Discussion

Two load tests were conducted as part of the monitoring effort: July 2007 and July 2009. This section of the report outlines the results of the two load tests conducted. It should be noted that the two load tests conducted two years apart were intended to capture significant structural load transfer mechanism changes over this two year period and therefore, identify any significant changes that would warrant degradation within the superstructure systems. Similarly, any lack of change in these load transfer mechanisms would suggest that no degradation has occurred over this two-year period.

4.4.1 Bridge B-20-133

Figure 4.23 illustrates the bridge deck deflections relative to the girders seen in the two load tests. The vehicle travel paths used to generate this data was travel path 1 shown in Figure 4.16. Figure 4.23(a) and 4.23(b) illustrate the deck deflections measured in the July 2007 and July 2009 load tests, respectively. DWT-1 is the draw wire transducer intended to measure exterior deck span deflections and DWT-2 is intended to measure the deflections in the first interior span of the deck. Front wheels for the vehicles were intended to be positioned at mid-span of the exterior deck span. As a result, it was expected that DWT-1 data would have larger magnitude displacements.

Peak deck deflections measured by DWT-1 during the two load tests are comparable to one another with the peak magnitudes on the order of 0.015 inches. Measurements obtained via DWT-2 exhibit significant difference owing to the difficulty in positioning vehicles upon the bridge deck with respect to the locations of the sensors. However, the peak deformations within the first interior bridge deck span are on the order of 0.005 inches during the July 2009 load test and 0.010 inches during the July 2007 load test. The peak deformations do not illustrate any significant difference over the two year period and therefore, one can conclude that there has been no significant change in the flexure load transfer mechanism in the bridge deck.

Vehicle travel path two is shown in Figure 4.17 and the DWT results for the two loading tests are shown in Figure 4.24. Peak vertical deck displacements relative to the girders during the July 2007 and 2009 load tests were on the order of 0.01 to 0.015 inches. DWT-1 (exterior deck span) magnitudes are larger than those of DWT-2. Furthermore, DWT-2 results (interior deck span) should have been larger in the research team's opinion since the vehicle wheels were thought to be at mid-span of the first interior deck span. However, the magnitudes of DWT-2 readings were less than those of DWT-1. This can be attributed to the difficulty of positioning the vehicles directly over the deck sensors. However, the magnitudes have not significantly changed from one another during the two load tests and therefore, it can be concluded that significant changes in the load transfer mechanism have not occurred and therefore, there is a very low likelihood of degradation within time. It should be noted that the negative deck

deflection readings in Figures 4.23 and 4.24 are a result of bridge deck rebound as the vehicles rapidly exited the bridge deck in reverse.

The wheel load distribution within the bridge deck was also measured. The loading protocol included vehicles entering the bridge, stopping at pre-defined locations labeled on the bridge deck as shown in Figure 4.13(c), being held in place for a set period of time, and then migrating on to the next stop location. Personnel on the bridge deck guided vehicle operators in these sequences.

Figure 4.25 illustrates the bridge deck flexural strains measured in the load tests. Load travel paths used in these load tests are shown in Figure 4.17. TW1 sensors are located along a line centered at mid-span of the exterior deck span. TW2 sensors are located along a line centered at mid-span of the first interior deck span. Travel path 1 is intended to generate larger strains in the TW1 sensors (relative to the TW2 sensors) and travel path 2 is intended to generate larger strains in the TW2 sensors (relative to the TW1 sensors). This difference in sensor strains can be seen when comparing Figure 4.25(a) to Figure 4.26(a) for the July 2007 load test. It is also seen when comparing strain results shown in Figures 4.27(a) and 4.28(a).

Figure 4.25(a) illustrates the wheel load strain distribution at mid-span of the exterior deck span (TW1 sensors) obtained during the July 2007 load test when truck travel path 1 was implemented. Figure 4.26(a) illustrates the strains seen in the TW2 sensors (mid-span of first interior deck span) during that same load test. As expected, there is a variation in peak strains measured at these two sensor lines. The skew present in the bridge superstructure results in TW1 and TW2 sensors not aligning themselves across from one another. Therefore, only carefully drawn conclusions can be made regarding the data seen in the TW2 sensors when travel path 1 is utilized and the TW1 sensors when travel path 2 is utilized. Therefore, discussion will be limited to data obtained in the TW1 sensors and travel path 1 and the data obtained in TW2 sensors and travel path 2.

Figure 4.25 illustrates the wheel load strain distributions seen in the TW1-series sensors measured during the July 2007 and 2009 load tests. Figure 4.25(a) illustrates the expected stepped variation in strain readings from sensor TW1-E2 through TW1-W2. When the vehicle wheel is intended to be placed over TW-W2, this sensor experiences the largest tensile strain. When the wheel is intended to be over

TW1-E2 (far right of figure), sensor TW1-W2 reads the smallest tensile strain. This is consistent with the sensor layouts within the exterior deck span shown in Figure 4.5. The fact that TW1-E1 and TW-E2 read nearly the same strain magnitude at the vehicle stopping points corresponding to data points 3,000 through 3,500 is indicative of the difficulty in positioning wheel loads directly over the top of sensors (see Figure 4.13c).

Comparison on Figures 4.25(a) and 4.25(b) illustrates that there is significant difference in the load testing results in the July 2007 and July 2009 load tests. The differences in the data obtained in these two load tests arise from vehicle positioning and ambient vehicle traffic and not load transfer mechanisms within the superstructure. The vehicles during the July 2009 load test were not positioned in the same locations as in the July 2007 load test. Pauses in vehicle movement seen in Figure 4.25(a) are also not present in Figure 4.25(b) indicating the impact of ambient traffic on the strain sensors.

The load tests were conducted under live traffic with the passing lane temporarily closed for test vehicle positioning. Ambient traffic loading in the driving lane was significantly heavier in July 2009 versus July 2007. As a result, there was significantly more truck and car traffic in the driving lane present nearly continually during the July 2009 load test. The relatively recent opening of USH 151 at the time of the July 2007 load test significantly reduced the volume of ambient traffic present on the bridge when the testing was conducted. As a result, ambient traffic appears to have affected the load testing in July 2009.

Figure 4.26 illustrates the strain distributions measured in TW2 sensors during travel path 1 in the July 2007 and July 2009 load tests. As outlined earlier, the TW1 and TW2 sensors are offset from one another as a result of the skew in the bridge superstructure and as a result, their descriptive use is limited. The results in Figure 4.25(b) and Figure 4.26(b) illustrate strong suspicion that vehicles were not located properly during travel path 1 in the July 2009 load test. Furthermore, the presence of ambient traffic significantly affected the strain readings in the bridge deck during the testing.

Figure 4.27 illustrates the strains measured in the TW1 sensors during travel path 2 in the July 2007 and 2009 load tests. Figures 4.27(a) and (b) clearly indicate the vehicle pause points (i.e. the "flat" segments) and both are devoid of significant evidence of ambient traffic on the bridge at the time of the

test travel path execution. The peak strains seen in each of the two load tests are on the order of $50 \mu\epsilon$ indicating that there is no fundamental changes in the load transfer mechanisms in the deck over the elapsed two year period. Rebound loading is significantly greater during the July 2009 load test, but this is simply attributed to driver change during the latter load test. Figure 4.27 illustrates that there is no significant change in strain readings and therefore, there is no degradation in the load transfer mechanism in the bridge deck.

Figure 4.28 illustrates the strains measured in TW2 series sensors for vehicle travel path 2. Unfortunately, Figure 4.28(b) illustrates that the vehicles were likely not positioned correctly during the July 2009 load test and that there was a significant level of ambient traffic loading present at the time the vehicle load path was executed during the testing.

Figure 4.17 illustrates that dump truck 100 was used in the July 2007 load testing and dump truck 111 was used in the July 2009 load testing. The separation between front and middle axles for these dump trucks (Figures 4.14 and 4.15) is 179 inches and 188 inches, respectively. Therefore, it can be expected that when the front axle is near strain sensor TW-E2, the rear tandem axle group is nearing sensor TW-W2. Therefore, it can be expected that the rear tandem axle group will influence the strain readings throughout all sensors in a line. The extent to which this influence affects the strain readings was impossible to determine with the loading testing protocols used.

Figures 4.29 and 4.30 illustrate the deck deflections measured at DWT-1 and DWT-2 during the 2007 and 2009 load tests. The DWT-1 sensor was located in the exterior deck span and the DWT-2 sensor was located in the first interior deck span. Truck position 1 was intended to generate peak deck displacements in the exterior span and truck position 2 was intended to generate peak deck displacements in the first interior deck span. It should be noted that the separation (longitudinally) between DWT-1 and DWT-2 in the bridge deck is on the order of 100 inches. The spacing between the front axle and middle axle on the load test dump trucks 91 (used in July 2007) and 111 (used in July 2009) is 179 inches and 188 inches, respectively. Therefore, it can be expected that the front and middle axle wheel loads will affect displacement readings in the same way as strain readings likely were affected.

Figure 4.29 indicates that peak deflections at DWT-1 were on the order of 0.003 inches in the July 2007 load test and an upward deflection of approximately 0.005 inches in the July 2009 load test. The upward deflection most likely indicates that the vehicle may not have been in the intended position within the bridge deck. The peak displacement seen during truck load travel path 1 was 0.012 inches in July 2007 and the peak downward displacement measured in July 2009 was on the order of 0.003 inches. Figure 4.30 indicates that truck travel path 2 contains a bit more consistency with regard to DWT-2 with a peak downward deflection measured in July 2007 of 0.014 inches and a peak downward deflection measured in July 2009 of 0.002 inches. Slight upward deflection (e.g. 0.004 inches) at DWT-1 measured in July 2009 makes some intuitive sense as this sensor is a significant distance longitudinally away from (ahead of) sensor DWT-2 and an upward deflection in the bridge deck is conceivable. No significant changes in the peak (magnitude of) deflections occurred in the two load tests, two years apart, and therefore, it is expected that no significant (at least) measurable degradation in the bridge deck load transfer mechanism is present.

4.4.2 Bridge B-20-148

Bridge B-20-148 in Fond du Lac, Wisconsin was also load tested at two times: July 2007 and July 2009. As outlined earlier, the instrumentation and sensor layout was significantly different for this bridge when compared to bridge B-20-133. The present section outlines the load testing results obtained for this bridge and provides observations with regard to what these load tests results mean in relation to bridge superstructure performance.

Figure 4.31 illustrates the bridge deck strain sensor measurements that were intended to quantify the variation in strains longitudinally along the bridge deck indicating how much bridge deck resists vehicle wheel loads. It should be emphasized that sensor TW-E2 was faulty as a result of the data acquisition system port failing and therefore, this sensor as shown in Figure 4.8 was not included in the testing. The load testing conducted in July 2007 (Figure 4.31a) indicates that the vehicle positions were not as intended. The peak tensile strains measured in the bridge deck were approximately $40 \mu\epsilon$ in July

2007 and the same magnitude in July 2009. A peak tensile strain at the underside of the bridge deck of this magnitude is really quite low given that tensile cracking strengths for typical deck concrete will be on the order of $130 \mu\epsilon$. Therefore, one expects that typical vehicle wheel loadings will not cause cracking in the bridge deck.

Bridge B-20-148 also included strain sensors mounted to measure the distribution of lane loading amongst the girders within the superstructure. The sensors designated as LM-1 through LM-7 and LT-1 through LT-7 provide strain measurements that aid in quantifying the lane load distribution factors at mid-span and third points, respectively. Unfortunately, load testing data obtained in July 2009 (Figures 4.32b and 4.33b) were tainted by unexplained spikes in strain data that may have been caused by faulty strain sensor mounting. The reason that faulty sensor mounting is suspected is that the magnitude of tensile and compression strains measured are simply beyond rational magnitudes.

Figure 4.32(a) illustrates that the tensile strains for girders LM-1 through LM-7 range from $60 \mu\epsilon$ tension to essentially zero microstrain. The position of the vehicles illustrated in Figure 4.21 suggests that peak tension strains should exist at the bottom of girders G2. This means that one can expect maximum tensile strains in sensor LM-2 to be obtained. This is indeed the case in the results measured. It is disappointing that the strain data obtained during the July 2009 was corrupted. There are several reasons for this that will be outlined later on in this chapter of the report. However, several very important conclusions regarding degradation in the superstructure can be made with data that was obtained in the July 2009 load test.

The measured strains plotted in Figures 4.32(a) and 4.33(a) can be used to gain estimates of lane-loading distribution factors to compare with design specifications (AASHTO 2006). One can use tension strains measured across all girders in the superstructure to evaluate a lane load distribution factors as follows (SC FRP Research):

$$mg_i = \frac{\mu\epsilon_i}{\sum_{n=1}^{N_G} \mu\epsilon_n} \quad (4.1)$$

where:

$\mu\varepsilon_i$ is the strain measured in girder i

$\sum_{n=1}^{N_G} \mu\varepsilon_n$ is the sum of all strains read across all girders in the superstructure.

Using the strain data given in Figure 4.32(a), the a lane load distribution factor for the mid-span location can be computed as,

$$mg_{LM} = \frac{62}{62 + 55 + 37 + 37 + 16 + 10} = 0.29$$

Using the strain data given in Figure 4.33(a), the a lane load distribution factor for the mid-span location can be computed as,

$$mg_{LT} = \frac{58}{58 + 52 + 42 + 25 + 25 + 10} = 0.27$$

The moment distribution factor at mid-span is slightly larger than that at the 1/3 points and this is consistent with the known behavior for skews nearing 30-degrees (AASHTO 2006).

A distribution factor was also computed as part of the baseline load testing conducted after B-20-148 was completed (Hernandez, *et al* 2005). This distribution factor was computed using beam deflections across the superstructure and its magnitude was reported to be,

$$mg_{LM}^{meas} = 0.23$$

This is very close and agreeable to the data obtained through the present research effort. As a result, one can say that the lane load distribution factor did not change from xxxx 2005 to July 2007 and therefore, there has been no degradation or change in the load transfer mechanism in the superstructure in this regard.

The AASHTO (2006) specifications also contain procedures for estimating how much of the design lane will be carried by a single girder within the bridge superstructure. These calculations performed for girder G2 in the present system are as follows,

$$mg_{ml}^S = \frac{1}{1.20} \left[0.06 + \left(\frac{S}{14} \right)^{0.4} \left(\frac{S}{L} \right)^{0.3} \left(\frac{K_g}{12.0Lt_s^3} \right)^{0.1} \right] = 0.31$$

for a single lane loaded situation. The distribution factors computed using strain readings in the present

research are in excellent agreement with the distribution factor estimated using bridge specification expressions (AASHTO 2006).

It was felt to be very important to make an attempt at quantifying the change in strain readings over the height of the composite girders within the superstructure with time. This would give yet another indication that the load transfer mechanisms within the bridge superstructure were changing with time. Figures 4.34 and 4.35 provide data illustrating the variation in strain at three sensor locations over the height of the girder and the underside of the bridge deck (see Figure 4.11). Figure 4.34(b) and 4.35(b) illustrates some rather puzzling spikes in strain history outside relatively nice strain trajectories that compare well with those in Figure 4.34(a) and 4.35(a). The source of these spikes could not be confidently quantified and therefore, they were ignored in the strain trace.

The peak strain data (plateau portions of the strain trace) in Figures 4.34 and 4.35 were transcribed onto a strain diagram over the height of the cross-section as shown in Figure 4.36. A theoretical composite section should have a linear strain diagram over the height of the cross-section. Furthermore, if the girders and deck were **NOT** acting compositely with one another, the underside of the deck (sensors SP1 and SP2) would not be in compression. Figure 4.36 clearly indicates that composite behavior is occurring in these girders. The data for girder G1 indicates virtually no change in composite behavior from July 2007 to July 2009. Furthermore, the strain readings above the neutral axis for girder G2 had virtually no change from July 2007 to July 2009. The strain readings at the bottom flange of girder G2 were unexpected. While the July 2007 load test yielded expected strain readings, the July 2009 load test results were surprising. A reading of $155 \mu\epsilon$ would indicate significant behavioral change within the system. However, the response seen in girder G1 during this same load test suggests that this extreme strain reading was caused by improper installation of the strain gauge. This will be discussed later in this chapter of the report.

Overall, the data in Figure 4.36 supports the conclusion that there has been no change in the composite stringer-deck load transfer mechanism from July 2007 to July 2009 and therefore, there has been no degradation in the system in this regard.

4.5 Wheel Load Distribution within Bridge Deck

The load testing conducted afforded the opportunity to evaluate wheel load distribution widths within the novel FRP-SIP bridge deck system used in B-20-133. The research team outlined a procedure to compare AASHTO-LRFD (AASHTO 2006) wheel load distribution widths with those suggested using data obtained during the load tests in an earlier research paper (Foley *et al* 2008). The present section provides an overview of this work and further details are available (Foley *et al* 2008).

The distribution of wheel loading within a bridge deck is dependent on three major factors: (a) the deck span length; (b) the restraint characteristics at the ends of the deck span; and (c) the girder stiffness. Experimental evidence (Allen 1991; Batchelor *et al.* 1978; Beal 1982; Csagoly *et al.* 1978) indicates that there is a significant level of membrane arching action present in many bridge decks and flexural models may not be the most appropriate method to compute maximum positive and negative moment stresses within bridge decks. Furthermore, studies have indicated that the stiffness of the girders plays a vital role in limiting the transverse negative bending moments over the girders (Batchelor *et al.* 1978; Beal 1982; Cao *et al.* 1996; Cao and Shing 1999; Csagoly *et al.* 1978; Fang *et al.* 1990; Newmark 1949).

Experiments carried out on scale models (Beal 1982; Fang *et al.* 1990) and full-scale models (Fang *et al.* 1990) have been very valuable in understanding wheel load distribution and have led to validation of analytical procedures to predict stresses within the bridge deck. However, these previous efforts focused on isotropic reinforcement layouts and traditional cast-in-place construction. There has been no data generated to date that supports the validity of applying analysis methods developed for CIP construction to deck systems that utilize stay-in-place FRP formwork as positive moment reinforcement. The present research effort allowed experimental data to be generated in this regard.

The methods for computing live load moments within bridge decks have changed very little from the first proposal formulated by Westergaard (1930). Further work by Newmark (1949) resulted in the basis for the Standard Specification design procedure for bridge deck analysis (AASHTO 2002). The procedure used is quite straightforward. A bridge deck live load moment (per unit width of slab) for a simple span condition is estimated using (AASHTO 2002),

$$M_{LLM} = P_w \left[\frac{S + 2}{32} \right] \quad (\text{units are lbs and feet with result being lb-ft/ft}) \quad (4.2)$$

where: P_w is the wheel loading (HS20 or HS15 using standard specification live load models); and S is the span of the bridge deck (conservatively can be taken as the spacing of the girders if flange widths are relatively small compared to the span). It should be noted that 1 lb-ft/ft is 4.448 N-m/m and equation (4.2) is taken from the U.S. customary units version of the specifications. Bridge decks are often continuous over multiple interior girders and therefore, the simple-span moment per unit width is modified by a continuity factor (AASHTO 2002),

$$M_{LLM} = 0.80 \cdot P_w \left[\frac{S + 2}{32} \right] \quad (4.3)$$

The positive and negative live load bending moments are taken to be the same within the bridge deck and this requires that the structural engineer provide equal mats of steel reinforcement in the top and bottom layers. It should also be noted that equations (4.2) and (4.3) make no distinction of interior and exterior deck span and therefore, are intended to be conservative for interior span bending moment estimations when compared to those estimates generated for exterior deck span conditions.

The procedure implied by equations (4.2) and (4.3) was felt to be over-simplistic by many researchers and experimental and analytical evidence showed that the flexibility of the girders within the superstructure system affects the state of stress within the deck (Batchelor et al. 1978; Beal 1982; Cao et al. 1996; Cao and Shing 1999; Csagoly et al. 1978; Fang et al. 1990) and that simplistic computations may over-estimate negative moment tensile stresses over the girders in the bridge deck. Nonetheless, equations (4.2) and (4.3) were used successfully for decades and the Load and Resistance Factor Design (LRFD) specifications included a significant departure from the former procedure.

The LRFD procedure for bridge decks is very similar to the long-standing distribution-factor procedure used for bridge girder analysis. The LRFD procedure includes definition of a strip width used to facilitate use of bending moments computed using one-dimensional analysis. In other words, the structural engineer conducts an analysis of the bridge deck assuming it is a one-dimensional continuous beam with movable wheel loads within traffic lanes and then converts the bending moments to unit-width

quantities using the strip width. Two strip widths are defined in cast-in-place bridge deck slabs (AASHTO 2006),

Positive Moment Strip Width

$$SW^+ = 26.0 + 6.6 \cdot S \quad (4.4)$$

Negative Moment Strip Width

$$SW^- = 48.0 + 3.0 \cdot S \quad (4.5)$$

The LRFD procedure affords the structural engineer the opportunity to utilize statically indeterminate analysis models and therefore, there is the ability to generate more accurate analysis results through these models. The assumption that bending moment magnitudes be determined through structural analysis was a significant departure from earlier specification procedures. To the authors' knowledge, there is no experimental evidence that demonstrates in-situ bridge behavior of deck systems utilizing the FRP-SIP formwork systems is appropriately modeled using equations (4.4) and (4.5).

The strain measurements from the July 2007 load test were used as the basis for computing estimates for the amount of bridge deck width that resists wheel loading. Truck 100 in the July 2007 load test shown in Figure 4.14 was the vehicle used during loading protocol 1 in Figure 4.16. The strain measurements used as the basis for computations are given in Figures 4.25(a) and 4.28(a).

An influence surface along the TW1 and TW2 sensor arrays (see Figure 4.5) were generated using the data acquired during the load testing. Five strain sensors were used during the testing along each line. The truck wheel was targeted to stop directly above each of these sensors as shown in Figure 4.39. The targeted stops were (in succession): W2, W1, M, E1, and E2. When the calibrated truck wheel was above W2, there were strain readings at the remaining four sensors. It was assumed that this data could be used to generate a symmetric (extrapolated) layout of four additional strain readings to locations with 17.5-inch intervals behind (or in front of) the truck wheel. As a result, five strain readings and four extrapolated symmetric strain readings were generated where applicable.

Figure 4.14(c) indicates that the front and first-rear-tandem axle are separated by 195 inches. Thus, when the front wheel is over sensor E2, the first rear-tandem axle is nearly 10 feet from sensor W2.

An average strain value for each stop (the plateaus in Figures 4.25a and 4.28a) were used as the basis for sensor readings. Table 4.1 illustrates these average values obtained at each sensor location and symmetric extrapolated sensor location values. The bold font values are the strain readings taken in the field and the italicized-font values are the magnitudes at symmetric locations extrapolated from the measured data.

The truck motion can be mentally pictured using the data values in Table 4.1. The exterior span can be considered as an illustrative example. When the front wheel is over sensor TW1-E2, the fifth row in the exterior span segment of the table is referenced. The strain reading for the front wheel at this location is then $75 \mu\epsilon$. There are four strain sensor readings behind the front wheel that provide measured strain data. The four strain readings ahead of the front wheel are therefore, projected (extrapolated) assuming symmetry. When the front wheel is over sensor TW1-M, there are two strain sensors behind and in front of the wheel. As a result, no extrapolation can be done and projected readings at +/- 70 in. and +/- 52.5 in. are not available. In other words, full symmetry with 140-inches of length adjacent to the wheel loading could only be obtained for cases where the front axle was over sensor W2 or E2 (first or last stop on sensors).

The strain readings were used to generate equivalent bending moment magnitudes assuming fully-composite behavior between the FRP-SIP formwork and the concrete deck. Preliminary FEA indicated that this is a reasonable assumption for service-level loads (Martin 2006). The strain readings at the bottom surface of the FRP-SIP formwork were converted to strains using Bernoulli beam theory assumptions,

$$M = \frac{E_{comp} \epsilon I_{comp}}{y_{bot}} \quad (4.6)$$

E_{comp} is the modulus used for the transformed section assuming that the concrete material has been transformed to equivalent FRP material ($5.73 e 6 \text{ psi}$). The modular ratio used for the computations was 1.56. I_{comp} is the second moment of area for the composite cross-section (474.2 in^4). Its magnitude was computed using a 17.5-inch width and data related to the FRP grid and the FRP-SIP formwork panels

(Berg 2004; Dieter 2002; Dietsche 2002). The total height of the in-situ bridge deck is 8 inches. ε is the measured (or extrapolated) strain from Table 4.1 and y_{bot} is the distance from the centroid of the transformed composite deck cross-section to the bottom surface of the FRP-SIP formwork (4.09 in).

The strain readings from Table 4.1 are used to generate bending moment magnitudes acting in the vicinity of the strain sensor and these magnitudes are assumed to be an average across the 17.5-inch width adjacent to the strain sensor (see Table 4.2). The total positive moment resisted within the linear influence surface adjacent to the wheel loads is simply the summation of all moment magnitudes computed using the measured strains. These total moments, designated as M_T^+ are given in Table 4.3. The total moments are then divided by the linear distance defining the area of influence to generate an *average* positive bending moment per unit width. This average positive bending moment is given in Table 4.3 as well. It should be noted that length of influence for W2, W1, M, E1, E2 is 157.5-in., 122.5-in., 87.5-in., 122.5-in., and 157.5-in., respectively.

The bending moments per unit width of length found in Table 4.3 can be compared to the positive bending moment that would be computed for a 10.93-kip wheel load using equation (4.3). This wheel load magnitude is approximately 37% greater than an HL-93 or HS20 truck loading. Table 4.3 illustrates the positive design live load moments that would result if the deck span was taken as 8-foot, 8-inches (see Figure 4.5). As shown in the Table, the Standard specification (AASHTO 2002) methodology conservatively estimates the bending moment per foot of width that would be seen in the deck. As expected, the exterior span would control the positive bending moment magnitude used for design and the Standard specification procedure is more conservative for the interior span. One could use the Standard specification procedure (AASHTO 2002) to conservatively analyze the FRP-SIP bridge deck at load levels slightly above service-level loading using the standard specification procedure.

Developing a comparison of field acquired strip widths with that recommended in the LRFD methodology (AASHTO 2006) is a little bit more cumbersome. First of all, a structural analysis is required to determine the bending moments that would be present in a one-dimensional continuous beam model of the deck. The present work takes a relatively simplistic approach. The peak positive bending

moment within the exterior span of the deck is determined with the assumption that the outside support is a roller, and the first interior support is fixed. This model is justified because there are two equal magnitude wheel loads placed in a nearly symmetric fashion on either side of the first interior girder (see Figure 4.16a). Therefore, there will be very little tendency for the deck to rotate over this interior support. If this assumption is made, the maximum positive bending moment, M_{\max}^+ , in the exterior span with a single concentrated load, P , at mid-span is;

$$M_{\max}^+ = \frac{5}{32} \cdot P \cdot S \quad (4.6)$$

The maximum positive bending moment strip width, SW^+ , for the exterior span can then be computed as follows;

$$M_{\max}^+ = \frac{5PS}{32} = \frac{5(P_w/SW^+)S}{32} \Rightarrow SW^+ = \frac{5P_w S}{32M_{\max}^+} \quad (4.7)$$

In the case of the interior span, the process is the same, but the structural analysis bending moment is computed using,

$$M_{\max}^+ = \frac{PS}{8} = \frac{(P_w/SW^+)S}{8} \quad (4.8)$$

as a result of the fixed-fixed end conditions (see Figure 4.16a). The positive moment strip width for the interior span condition is therefore,

$$SW^+ = \frac{P_w S}{8M_{\max}^+}$$

Strip widths computed using the measured strain data and comparison to the positive moment strip widths computed using equation (4.4) are given in Table 4.3. The average positive moment strip width, SW^+ , for the exterior span computed using the measured strains is approximately 126 inches (3.22 m). The positive moment strip width computed using the LRFD specifications (AASHTO 2006) is 83.4 inches. The average positive bending moment strip width for the interior span condition computed using the field-measured strain magnitudes is larger indicating a greater width of bridge deck resisting wheel loads.

The Standard Specifications (AASHTO 2002) and LRFD Specifications (AASHTO 2006) assume that the predominant load-transfer mechanism in the bridge deck is flexure. Recent research efforts are indicating arching action as a major load-transfer mechanism in many bridge deck configurations. Assuming the concentrated wheel load is at mid-span results in a shear-span-to-depth ratio for the deck of approximately 6.5. This would justify flexural behavior as the dominant load transfer mechanism in the bridge deck and acceptance of Bernoulli beam theory as a model for deck behavior. However, the edge conditions on the slab strip perpendicular to traffic assumed in the development of equations (4.3), (4.4), and (4.5) are likely not seen in the real bridge. As a result, differences in the strip widths computed using measured strains are expected. However, the important item to note is that the AASHTO analysis procedures result in conservative estimates for bending moment on a per-foot basis. The width of slab assumed to resist wheel loading in the LRFD specifications is smaller than that computed using experimentally determined strains from the in-situ testing. Therefore, designers will be evaluating service-level and near service-level behavior in a conservative manner using the specifications as the bending moments on a per-foot basis for design will exceed those likely seen in the bridge.

The AASHTO LRFD design specifications (AASHTO 2006) also include an empirical (tabulated) procedure for conducting live load analysis for bridge decks of "usual" configuration. The conditions defining the typical configuration pertinent to comparisons with the values measured during the in-situ load test are (AASHTO 2006):

- The bridge deck is supported on parallel girders.
- Multiple presence factors and dynamic load allowances are included in the tabular values.
- The bridge deck supported on at least 3 girders.
- The width of the bridge deck is not less than 14 feet between centerlines of the exterior girders.
- The moments in the table are “upper-bounds” for the moments in the interior regions of the slab.

The empirical design method (AASHTO 2006) is applicable for the present bridge deck. However, several assumptions are required in order to make a comparison with the measured values discussed in this manuscript. First of all, an impact modifier equal to 1.33 will be assumed. Secondly, the spacing of

the girders (8 ft 8 inches) and the width of the bridge deck (39 feet) indicate that one design lane will control the magnitudes of the bending moments present in the bridge deck. Therefore, a multiple-presence factor of 1.20 should be considered. Finally, the empirical procedure assumes that a 8-kip wheel load generates the bending moments. The wheel loading in the present in-situ test is 10.93 kips.

The magnitude of the positive bending moment taken from the AASHTO empirical procedure table is 6.09 k-ft for an 8.67 foot span. Accounting for the multiple presence factor, the impact modifier and the wheel load difference built into the tabular value results in an empirical estimate for bending moment equal to,

$$M_{emp}^+ = 6.09 \left(\frac{10.93}{8.00} \right) \left(\frac{1}{1.20} \right) \left(\frac{1}{1.33} \right) = 5.21 \text{ k-ft} = 7.1 \text{ kN-m}$$

As expected, the empirical design procedure provides a conservative estimate for the interior bending moments within the bridge deck. The process also provides a conservative estimate for the bending moments in the exterior span. It is also interesting to note that the present wheel loading is 37% greater than the HL-93 truck wheel loading. As a result, the bending moments used at near service-level evaluations of bridge deck response are conservative when compared to the in-situ magnitudes estimated using the methodology developed in the present study.

4.6 Concluding Remarks

There are two major motivations for the present section within the research report. The first is to summarize what was outlined in the chapter and draw conclusions regarding the information gleaned from the load testing. The second is to provide general comments regarding lessons learned from the load testing and provide insights into improving future load tests to add to the database of information being constructed for these bridges.

The load testing of bridges B-20-133 and B-20-148 was conducted to evaluate several critical load transfer mechanisms that could give the research team indication of degradation with time. As outlined earlier, two load tests were conducted: one in July 2007 and another in July 2009. The load transfer mechanisms evaluated were: (a) wheel load distribution within the bridge deck; (b) composite

beam behavior in the superstructure; (c) lane load distribution within the superstructure; and (d) bridge deck deflection relative to the girders.

Bridge deck displacements relative to the girders in both bridges did not change significantly with time as exhibited in Figures 4.23, 4.24, 4.29, and 4.30. As a result, one can conclude that there has not been a significant change in the bridge deck load transfer mechanism over the two-year period of evaluation and therefore, no degradation in this load transfer mechanism has occurred.

The wheel load distribution widths present in the FRP-SIP bridge deck system of B-20-133 can be predicted using standard design/analysis procedures (AASHTO 2006). Figure 4.27 illustrates that this load transfer mechanism did not change significantly (if at all) over the two year evaluation period and thus, the wheel load distribution within this superstructure did not degrade. Although not fully evaluated in the present research report, Figure 4.31(b) illustrates that the wheel load distribution widths in B-20-148 are consistent, but narrower, than that in B-20-133. This is to be expected since common models for strip width (AASHTO 2006) given by equations (5.4) and (5.5) are functions of beam spacing. The spacing of the girders in B-20-133 (Figures 4.5 and 4.6) is wider than the spacing of the girders in B-20-148 (Figures 4.9 and 4.10) and therefore, this narrower strip width is expected.

Strain gradients over the height of the girders (Figures 4.36) clearly exhibit composite behavior. Furthermore, the strain gradients did not significantly (if at all) change with time and therefore, one can conclude that there was no change in the composite beam load transfer mechanism within bridge B-20-148 over the two-year monitoring period and therefore, no degradation in this regard.

Lane load distribution factors for wide-flange bulb-tee composite bridge girder systems (e.g. that used in B-20-148) can be computed accurately with standard design/analysis procedures found in modern bridge specifications (AASHTO 2006). Furthermore, these lane load distribution factors did not change from July 2005 (Hernandez, *et al* 2005) and the July 2007 load test in this research study. As a result, there was no degradation measured in this regard.

The in-situ load testing conducted as part of the present research effort and a recently completed effort (Hernandez, *et al* 2005) indicate that there has been no observable degradation in the load transfer

mechanisms within the bridge superstructure. The innovative bridges constructed as part of this program, therefore, are performing as expected.

The in-situ load testing conducted was not without difficulty. The portable strain sensors did a terrific job in providing strain readings in a relatively reliable manner. However, there were two glaring difficulties that arose with the instrumentation and the load testing protocols. This section of the report intends to outline some of these difficulties encountered with a eye to future load testing of these and other bridges.

The low modulus polymer strain sensors developed performed very, very well during the research effort. However, there were some installation issues that may have lead to elevated strain readings encountered during the July 2009 load test (especially at B-20-148). The low modulus polymer carrier for the strain gauges was bolted in place. This bolting procedure may have resulted in non-straight orientations for the sensors (see Figure 4.37). As straining in the base material occurred, the studs and may have introduced significant bending strains into the sensors. As a remedy to this, it is recommended that the washers beneath the sensors be better able to bridge the slight spalling that normally accompanies the installation of the threaded studs.

Positioning the wheel loading was perhaps the most difficult task to accurately complete during the load testing. Figure 4.38 illustrates how sensitive the location of the centerline of the truck wheel can be relative to the 17.5-inch spacing of the sensors below the deck. It may have been better off to space out the sensors further than the 17.5 inches used. It also may have been prudent to explore more exact (GPS-based) deck marking procedures. This would have helped to ensure that wheels on the bridge deck were positioned as close as possible to locations directly above the bridge deck sensors below.

4.7 References

AASHTO. (2002). Standard Specifications for Highway Bridges, Customary Units, 17th Edition, American Association of State Highway and Transportation Officials, Washington, DC.

- AASHTO. (2006). AASHTO LRFD Bridge Design Specifications Including 2006 Interim Revisions, Customary U.S. Units, 3rd Edition, American Association of State Highway and Transportation Officials, Washington, DC.
- Allen, J. H. (1991). "Cracking, Serviceability, and Strength of Concrete Bridge Decks." *Transportation Research Record*, No. 1290, 152-171.
- Bank, L. C., Oliva, M. G., and Russell, J. S. (2005). "In-Situ Load Testing of IBRC Bridge." Wisconsin Department of Transportation, Federal Highway Administration, Madison, WI.
- Batchelor, B., Hewitt, B. E., Csagoly, P., and Holowka, M. (1978). "Investigation of the Ultimate Strength of Deck Slabs of Composite Steel/Concrete Bridges." *Transportation Research Record*, No. 664, 162-170.
- Beal, D. B. (1982). "Load Capacity of Concrete Bridge Decks." *Journal of the Structural Division*, 108(ST4), 814-832.
- Berg, A. C. (2004). "Analysis of a Bridge Deck Built on U.S. Highway 151 with FRP Stay-In-Place Forms, FRP Grids, and FRP Rebars," MS Thesis, University of Wisconsin at Madison, Madison, WI.
- Berg, A. C., Bank, L. C., Oliva, M. G., Russell, J. S., and Jeffrey, S. (2004). "Construction of a FRP Reinforced Bridge Deck on U.S. Highway 151 in Wisconsin." 83rd Annual Meeting of the Transportation Research Board, National Research Council, Transportation Research Board, Washington, DC, CD-ROM.
- Cao, L. C., Allen, J. H., Shing, P. B., and Woodham, D. (1996). "Behavior of RC Bridge Decks with Flexible Girders." *Journal of Structural Engineering*, 122(1), 11-19.
- Cao, L. C., and Shing, P. B. (1999). "Simplified Analysis Method for Slab-On-Girder Highway Bridges." *Journal of Structural Engineering*, 125(1), 49-59.
- Csagoly, P., Holowka, M., and Dorton, R. (1978). "The True Behavior of Thin Concrete Bridge Slabs." *Transportation Research Record*, No. 664, 171-179.

- Dieter, D. A. (2002). "Experimental and Analytical Study of Concrete Bridge Decks Constructed with FRP Stay-In-Place Forms and Grid Reinforcing," MS Thesis, University of Wisconsin at Madison, Madison, WI.
- Dieter, D. A., Dietsche, J. A., Bank, L. C., Oliva, M. G., and Russell, J. S. (2002a). "Concrete Bridge Decks Constructed with Fiber-Reinforced Polymer Stay-In-Place Forms and Grid Reinforcing." Annual Meeting of the Transportation Research Board, National Research Council, Transportation Research Board, Washington, D.C., CD-ROM.
- Dieter, D. A., Dietsche, J. S., Bank, L. C., Oliva, M. G., Russell, J. S., and Jeffrey, S. (2002b). "Concrete Bridge Decks Constructed with Fiber-Reinforced Polymer Stay-In-Place Forms and Grid Reinforcing." 81st Annual Meeting of the Transportation Research Board, National Research Council, Transportation Research Board, Washington, DC, CD-ROM.
- Dietsche, J. S. (2002). "Development of Material Specifications for FRP Structural Elements for the Reinforcing of a Concrete Bridge Deck," MS Thesis, University of Wisconsin at Madison, Madison, WI.
- Fang, I. K., Worley, J., Burns, N. H., and Klingner, R. E. (1990). "Behavior of Isotropic R/C Bridge Decks on Steel Girders." *Journal of the Structural Division*, 116(3), 659-678.
- Helmuelter, E. J., Bank, L. C., Dieter, D. A., Dietsche, J. A., Oliva, M. G., and Russell, J. S. (2002). "The Effect of Freeze-Thaw on Bond Between FRP Stay-In-Place Deck Forms and Concrete." CDCC 2002, 2nd International Conference on Durability of Fiber Reinforced Polymer (FRP) Composites for Construction, Montreal, Quebec, CAN, 1643-1654.
- Martin, K. E. (2006). "Impact of Environmental Effects on, and Condition Assessment of IBRC Bridge Decks in Wisconsin," M.S. Thesis, Marquette University, Milwaukee, WI.
- Newmark, N. M. (1949). "Design of I-Beam Bridges." *Transactions of the ASCE*, 114, 997-1022.
- Ringelstetter, T. E., Bank, L. C., Oliva, M. G., Russell, J. S., Matta, F., and Nanni, A. (2006). "Development of a Cost-Effective Structural FRP Stay-In-Place Formwork System for Accelerated and Durable Bridge Deck Construction." Annual Meeting of the Transportation Research Board, National Research Council, Transportation Research Board, Washington, DC.

- Schneeman. (2006). "Development and Evaluation of a Removable and Portable Strain Sensor for Short-Term Live Loading of Bridge Structures," M.S. Thesis, Marquette University, Milwaukee, WI.
- Wan, B., Foley, C. M., and Martin, K. E. "Freeze-Thaw Cycling Effects on Shear Transfer Between FRP Stay-in-Place Formwork and Concrete." The Third International Conference on Durability and Field Applications of Fiber Reinforced Polymer (FRP) Composites for Construction, CDCC 2007, Quebec City, CAN, 227-234.
- Westergaard, H. M. (1930). "Computation of Stresses in Bridge Slabs Due to Wheel Loads." Public Roads, March, 1-23.

Table 4.1 Strain Readings Recorded During Field Loading Tests. (Quantities shown in bold-face font are field-measured quantities.)

Span and Stop Location	Location Relative to Truck Front Wheel								
	Strain ($\mu\epsilon$)								
	-70 in.	-52.5 in.	-35 in.	-17.5 in.	Front Wheel	17.5 in.	35 in.	52.5 in.	70 in.
Exterior Span									
TW1-W2	9	26	23	32	92	32	23	26	9
TW1-W1	n.a.	14	41	59	45	41	41	14	n.a.
TW1-M	n.a.	n.a.	34	26	76	69	21	n.a.	n.a.
TW1-E1	n.a.	22	12	50	126	40	12	22	n.a.
TW1-E2	16	5	30	75	75	75	30	5	16
Interior Span									
TW2-W2	2	6	15	48	51	48	15	6	2
TW2-W1	n.a.	4	11	32	76	24	11	4	n.a.
TW2-M	n.a.	n.a.	18	47	43	20	10	n.a.	n.a.
TW2-E1	n.a.	13	28	25	35	21	25	28	n.a.
TW2-E2	9	19	16	22	36	22	16	19	9

Table 4.2 Averaged Bending Moment Computed at Each Strain Gauge Location.

Span and Stop Location	Location Relative to Truck Front Wheel								
	Average Bending Moment [k-ft]								
	-70 in.	-52.5 in.	-35 in.	-17.5 in.	Front Wheel	17.5 in.	35 in.	52.5 in.	70 in.
Exterior Span									
TW1-W2	0.50	1.44	1.27	1.77	5.09	1.77	1.27	1.44	0.50
TW1-W1	n.a.	0.77	2.27	3.26	2.49	2.27	2.27	0.77	n.a.
TW1-M	n.a.	n.a.	1.88	1.44	4.21	3.82	1.16	n.a.	n.a.
TW1-E1	n.a.	1.22	0.66	2.77	6.97	2.21	0.66	1.22	n.a.
TW1-E2	0.89	0.28	1.66	4.15	4.15	4.15	1.66	0.28	0.89
Interior Span									
TW2-W2	0.11	0.33	0.83	2.66	2.82	2.66	0.83	0.33	0.11
TW2-W1	n.a.	0.22	0.61	1.77	4.21	1.33	0.61	0.22	n.a.
TW2-M	n.a.	n.a.	1.00	2.60	2.38	1.11	0.55	n.a.	n.a.
TW2-E1	n.a.	0.72	1.55	1.38	1.94	1.16	1.38	1.55	n.a.
TW2-E2	0.50	1.05	0.89	1.22	1.99	1.22	0.89	1.05	0.50

Table 4.3 Bending Moment (per foot) and Strip Width Comparison.

Span and Stop Location	M_T^+ [k-ft]	M_{avg}^+ [k-ft/ft]	M_{STD} [k-ft/ft]	SW^+ [in.]	SW_{LRFD}^- [in.]	SW_{LRFD}^+ [in.]
Exterior Span						
TW1-W2	15.05	1.15	2.92	155.4	74.08	83.38
TW1-W1	14.11	1.38		128.9		
TW1-M	12.51	1.72		103.9		
TW1-E1	15.72	1.54		115.7		
TW1-E2	18.09	1.38		129.2		
Interior Span						
TW2-W2	10.68	0.81	2.92	175.2	74.08	83.38
TW2-W1	8.96	0.88		162.3		
TW2-M	7.64	1.05		136.1		
TW2-E1	9.68	0.95		150.3		
TW2-E2	9.30	0.71		201.2		



Figure 4.1 Low-modulus portable strain transducer mounted to lower flange of precast 54W girder.



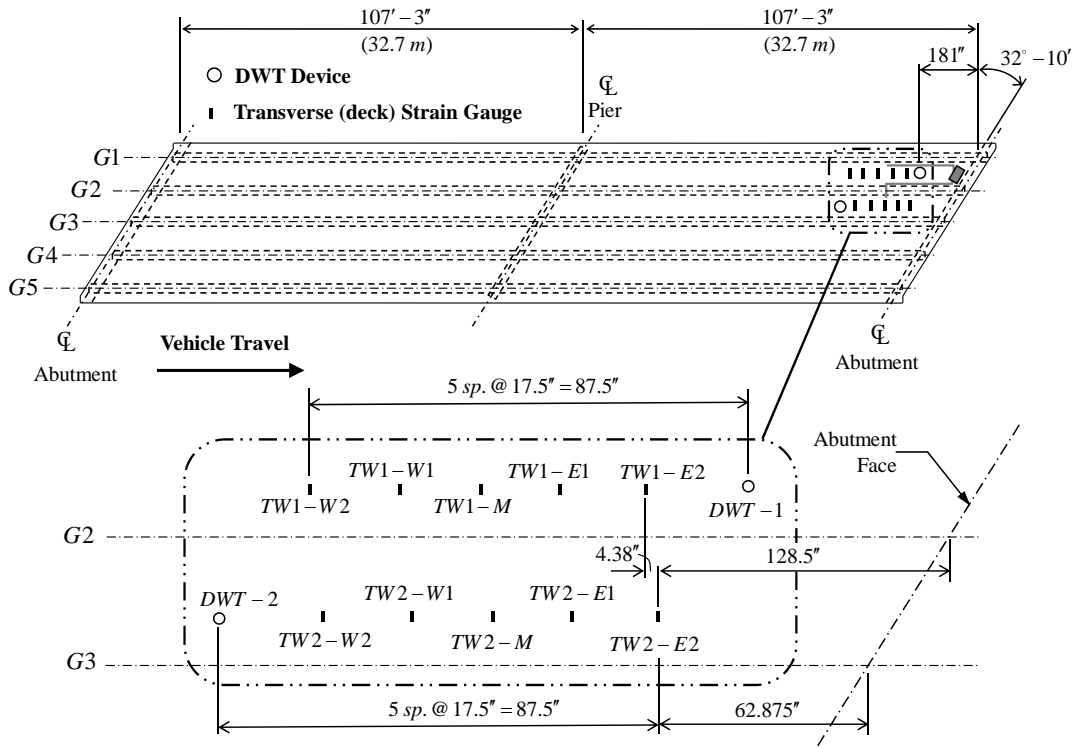
Figure 4.2 Mini-DIN plug environmental protection used in the field instrumentation.



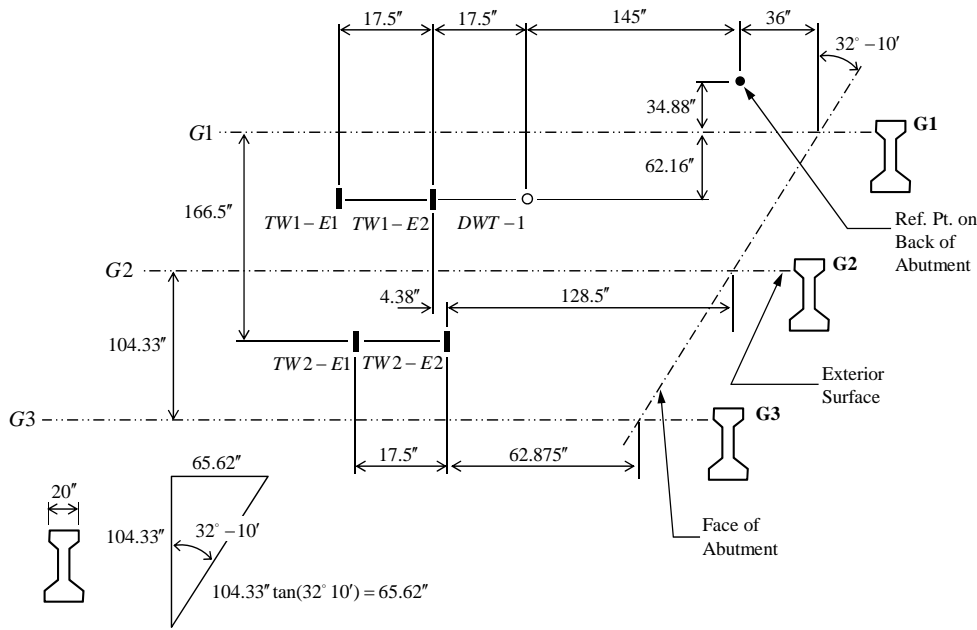
Figure 4.3 String potentiometer (draw wire transducer – DWT) used in this project.



Figure 4.4 Image of Laptop-Based DAQ system and IO Tech DAQ software.

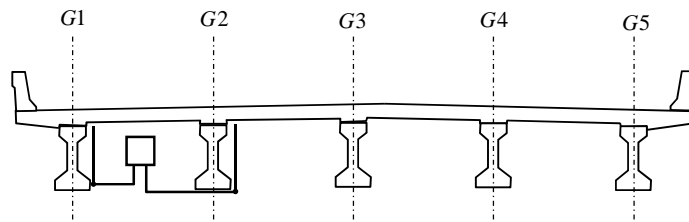


PLAN - Instrumentation Layout: B-20-133

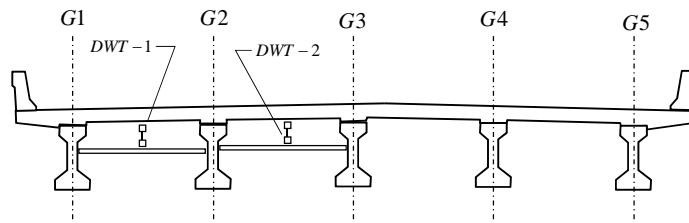


PLAN - Instrumentation Layout: B-20-133

Figure 4.5 Instrumentation Layout and Instrumentation Plan Detail for B-20-133.

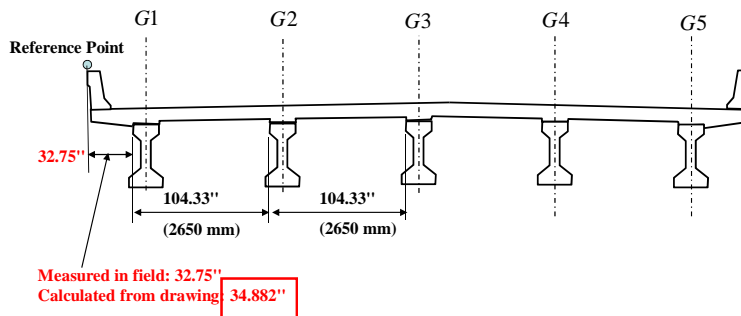


Section Showing Conduit Runs



Section Indicating DWT Device Mounting

(a)



Section Showing Gages Relative Locations in Transverse Direction

(b)

Figure 4.6 B-20-133 Cross-Sections Illustrating Instrument Layout: (a) Conduit Runs and Draw Wire Transducer Mounting; (b) Reference Point Location for Instrumentation.



(a)



(b)

Figure 4.7 Data Acquisition System and Instrumentation Mountings at B-20-133: (a) Enclosure Box and Data Acquisition System; (b) Studs for Draw Wire Transducers and Strain Gauge Mounting

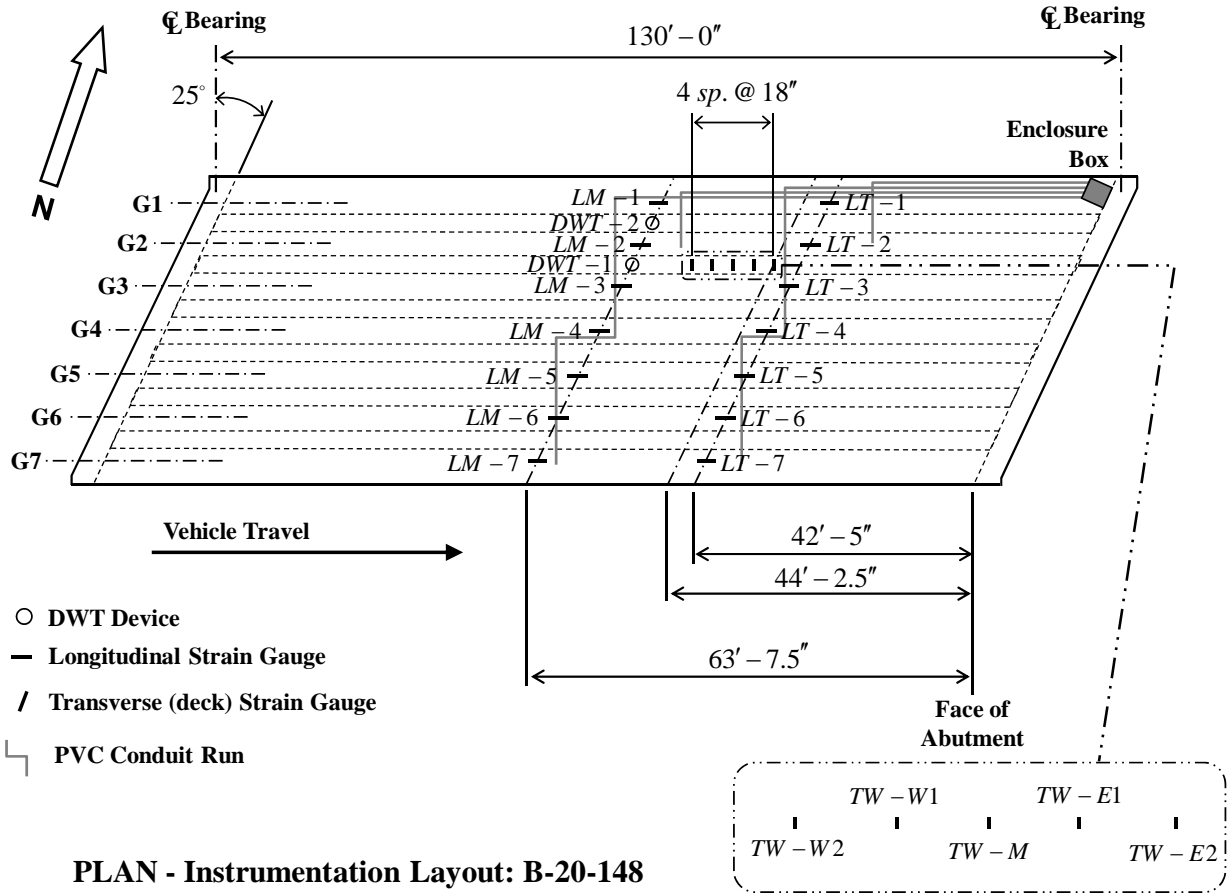
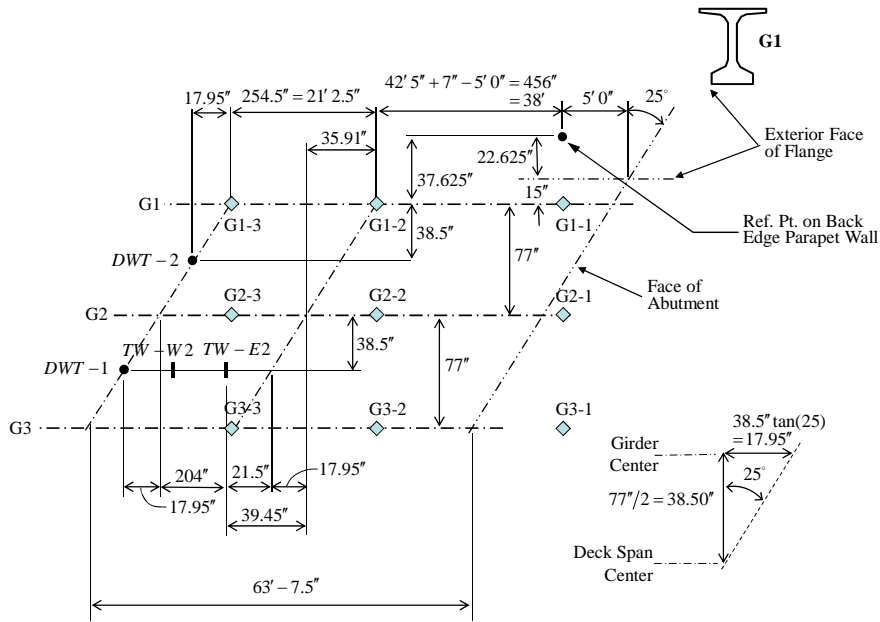
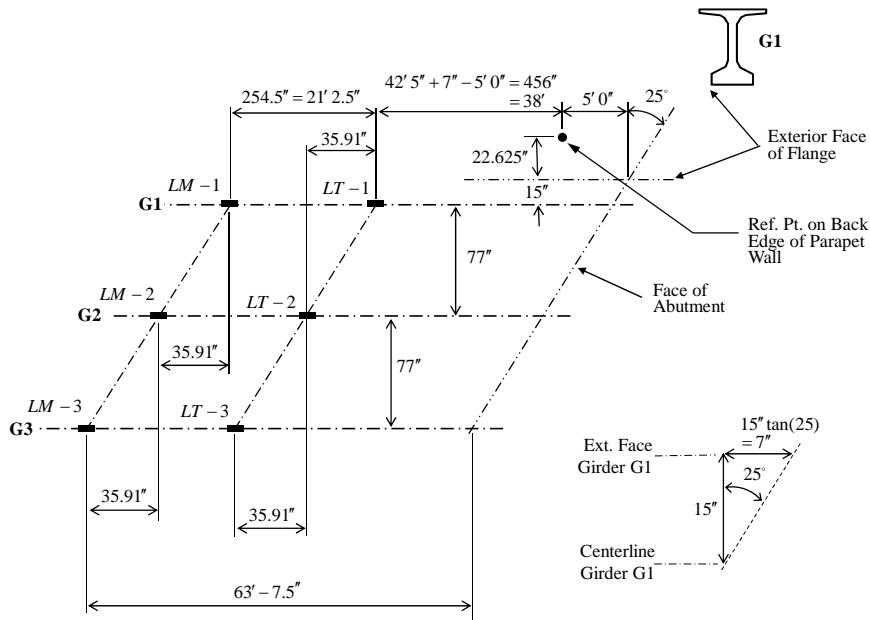


Figure 4.8 B-20-148 Instrumentation Plan with Sensor Locations, PVC Conduit Runs and Enclosure Box Location.



PLAN - Instrumentation Layout: B-20-148

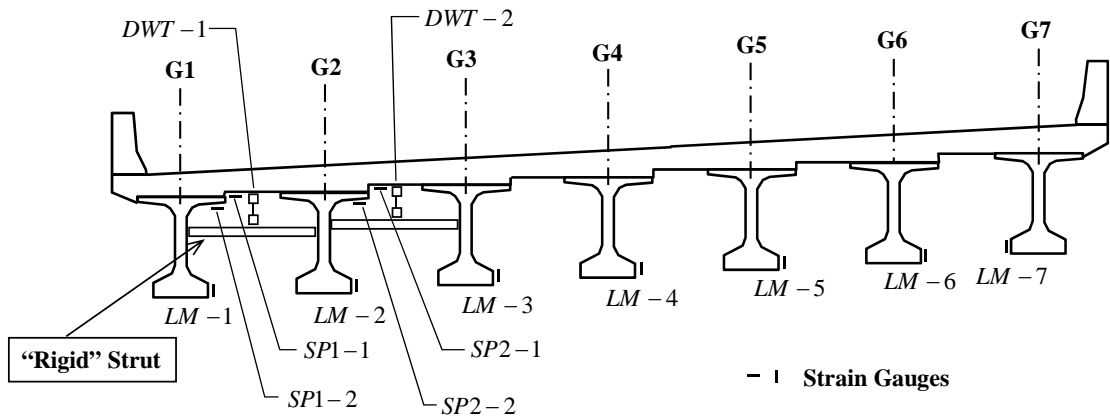
(a)



PLAN - Instrumentation Layout: B-20-148

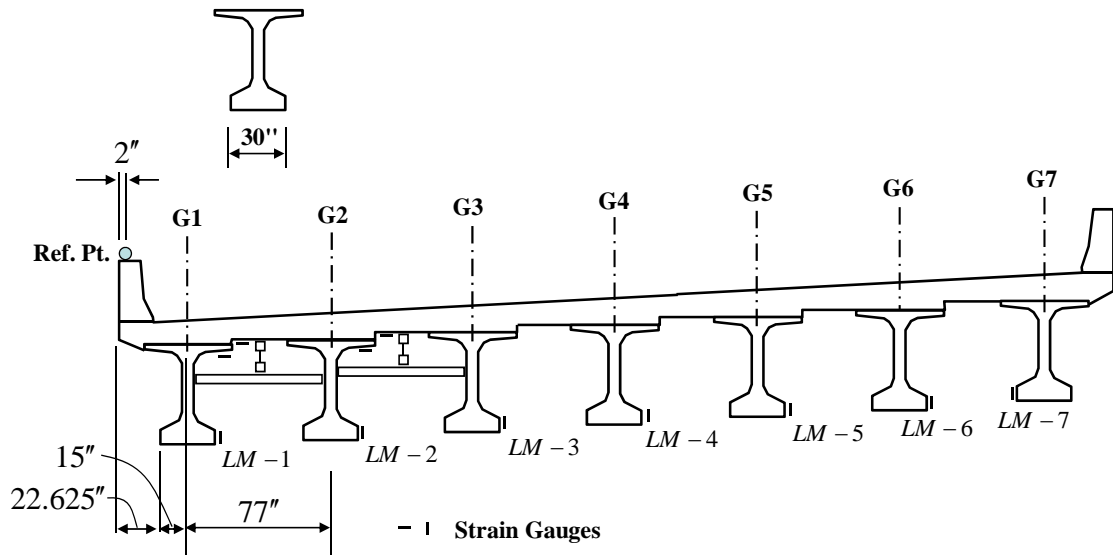
(b)

Figure 4.9 B-20-148 Instrumentation Layout in Plan: (a) Bridge Deck Sensor Layout; (b) Lane Load Distribution Factor Gauge Locations.



BRIDGE SECTION - Mid-Span

(a)



B-20-148 BRIDGE SECTION - Mid-Span

(b)

Figure 4.10 B-20-148 Cross-Sections with Instrumentation Locations and Layout: (a) Sensor Locations within Bridge Cross-Section; (b) Reference Point Location Used to Locate Sensors.

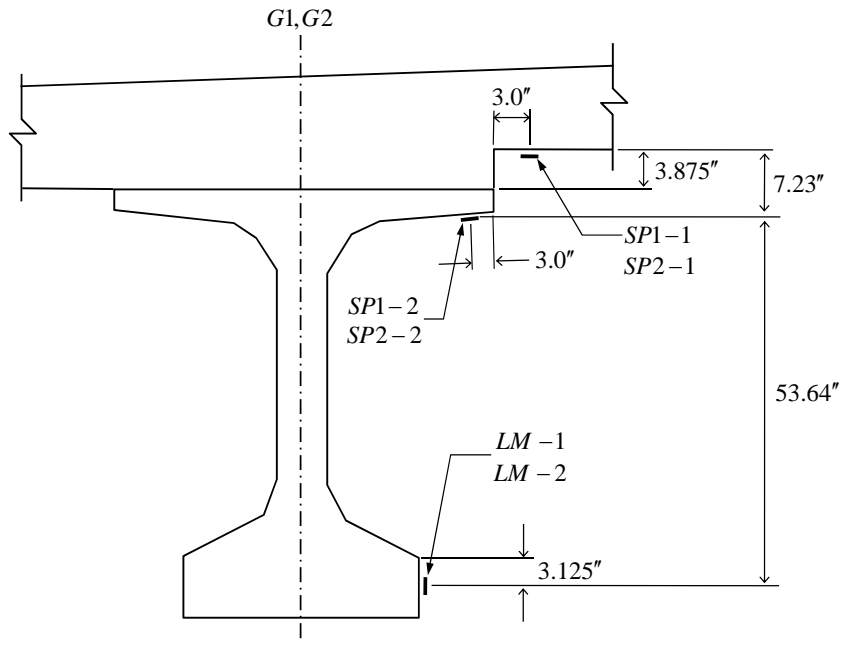


Figure 4.11 B-20-148 Strain Sensor Locations used to Measure Strain Distribution Over Height of Girders.



Figure 4.12 B-20-148 Data Acquisition System and Instrumentation: (a) Data Acquisition System and Enclosure; (b) Draw Wire Transducer Installation; (c) Strain Gauge Installation; (d) Sensor Wiring Runs and Sensor Installation.



(a)



(b)

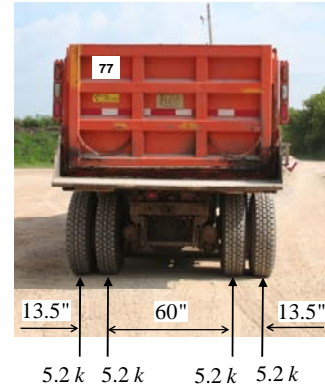
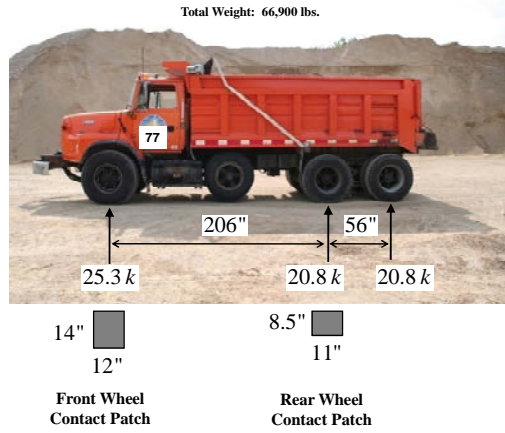


(c)

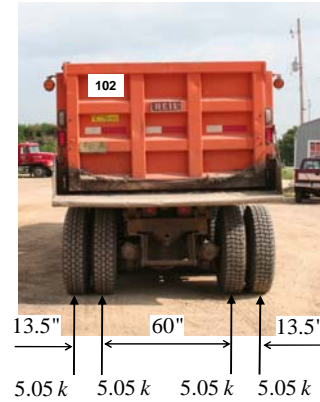
Figure 4.13 Typical Pavement Marking for Load Testing: (a) Bridge B-20-133; (b) Bridge B-20-148; (c) Truck Positioning Guided by Pavement Marking at B-20-133.



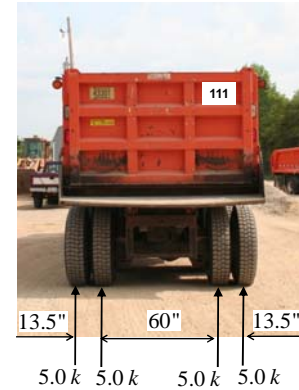
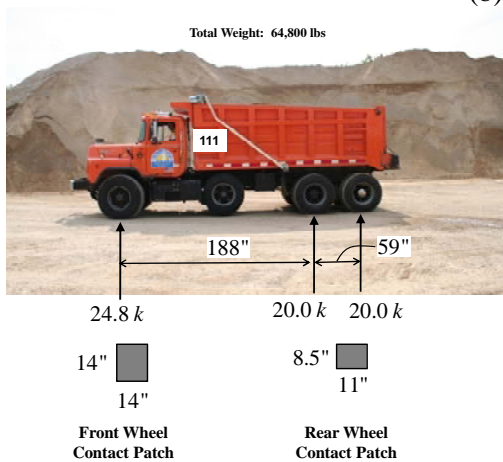
Figure 4.14 Tri-Axle Dump Trucks Loaded with Shoulder Gravel used in July 2007 Load Test: (a) Truck 91; (b) Truck 95; (c) Truck 100.



(a)

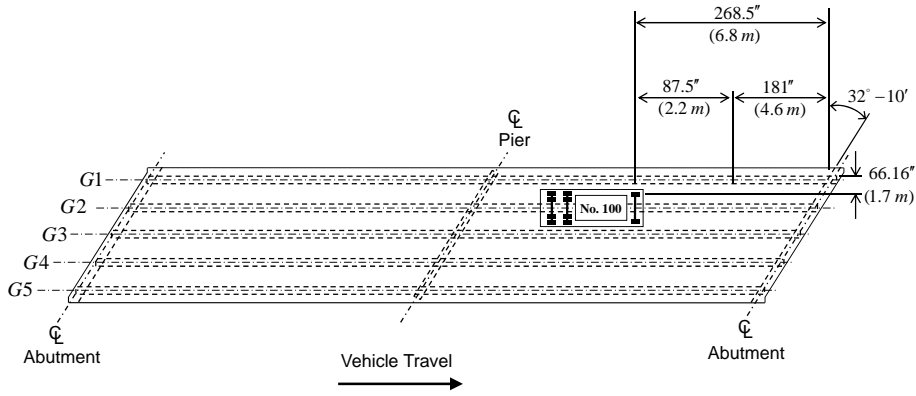


(b)



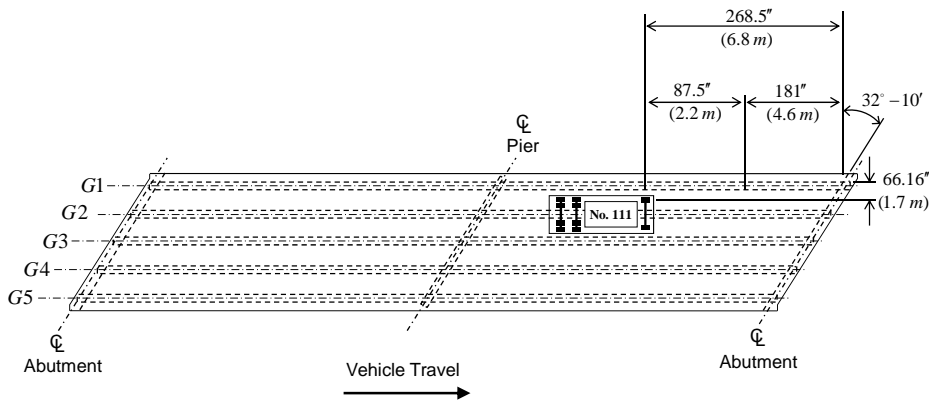
(c)

Figure 4.15 Tri-Axle Dump Trucks Loaded with Shoulder Gravel used in July 2009 Load Test: (a) Truck 77; (b) Truck 102; (c) Truck 111.



July 2007 Load Test
Truck Travel Path 1: Wheel Load Distrib. and Deck Deflection
Data File: File1

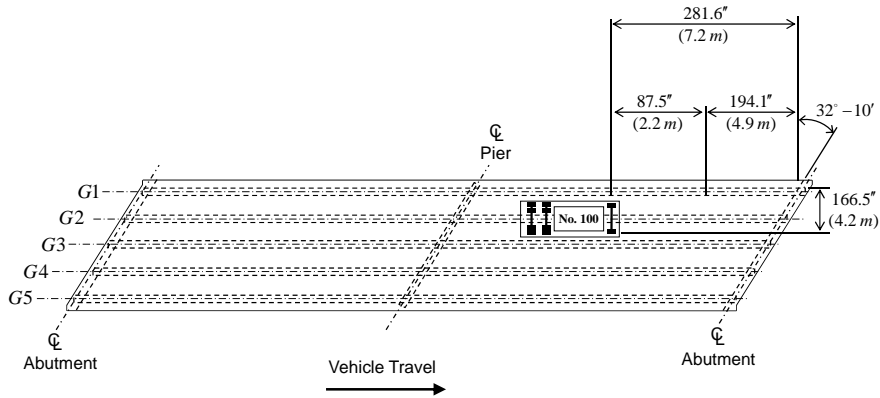
(a)



July 2009 Load Test
Truck Travel Path 1: Wheel Load Distribution and Deck Deflection
Data File: File1

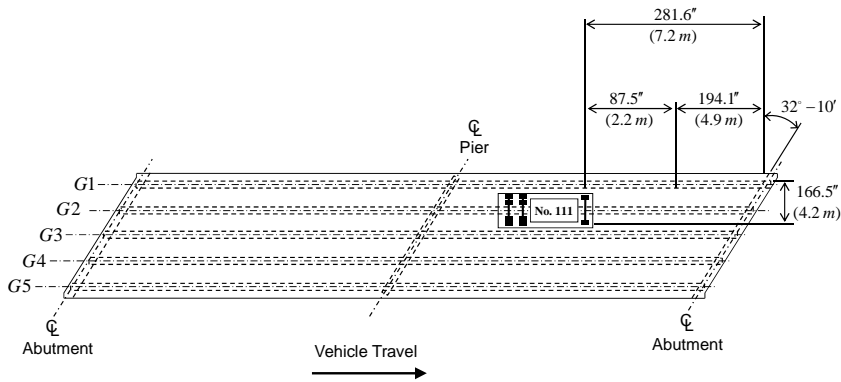
(b)

Figure 4.16 Loading Protocols used to Examine Wheel Load Distribution in the Exterior Deck Spans within the Deck of Bridge B-20-133 During July 2007 and July 2009 Load Tests: (a) July 2007 Load Test; (b) July 2009 Load Test.



July 2007 Load Test
Truck Travel Path 2: Wheel Load Distrib. and Deck Deflection
Data File: File2

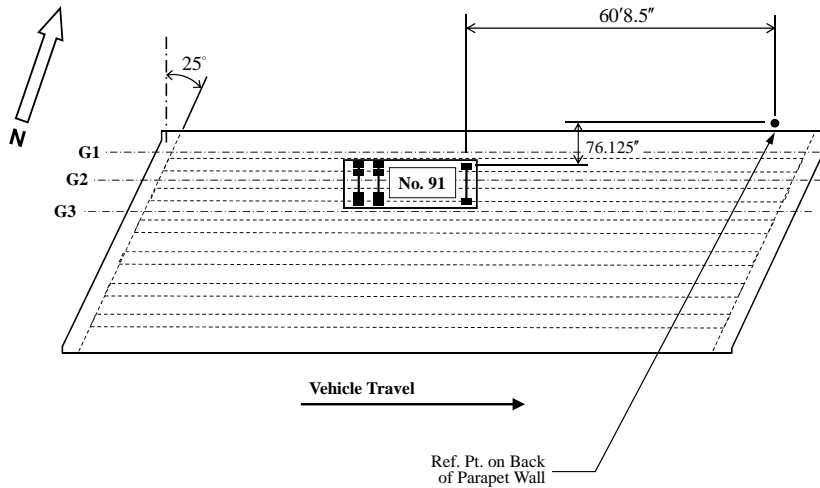
(a)



July 2009 Load Test
Truck Travel Path 2: Wheel Load Distribution and Deck Deflection
Data File: File2

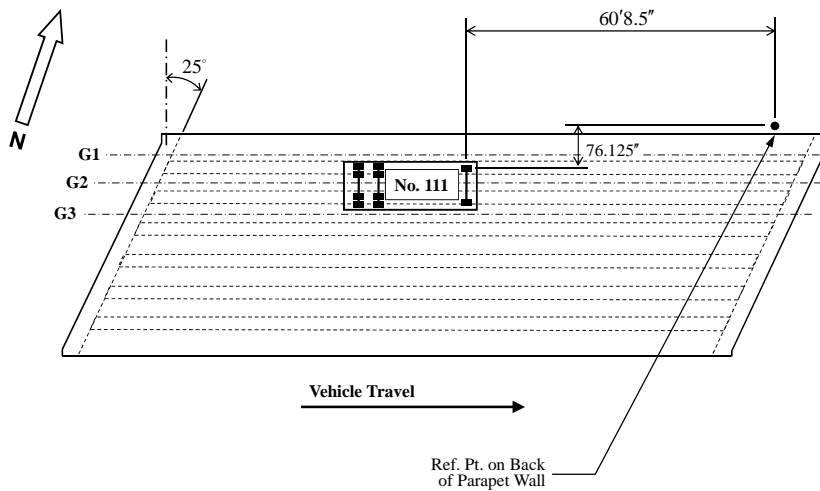
(b)

Figure 4.17 Loading Protocols used to Examine Wheel Load Distribution in the Interior Deck Spans within the Deck of Bridge B-20-133 During July 2007 and July 2009 Load Tests: (a) July 2007 Load Test; (b) July 2009 Load Test.



July 2007 Load Test
Truck Position Number 1 - Deck Deflection
DWT-2 is target: Data File: File1

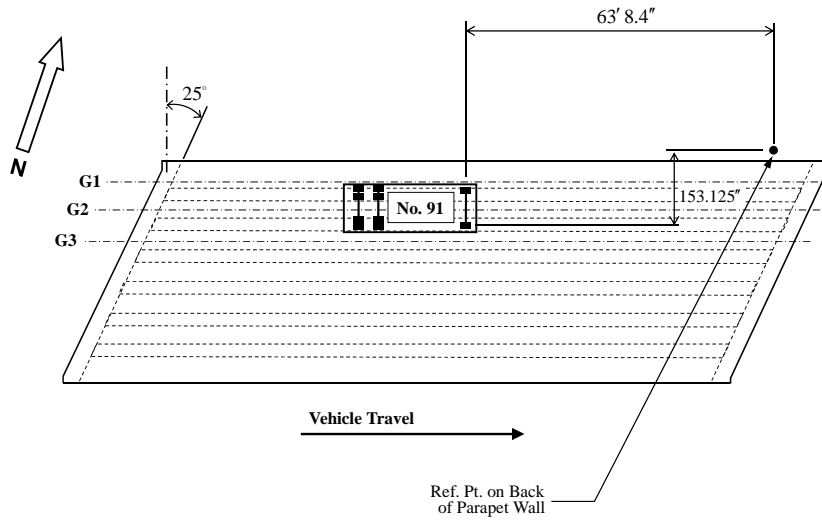
(a)



July 2009 Load Test
Truck Position Number 1 - Deck Deflection
DWT-2 is target: Data File: File1

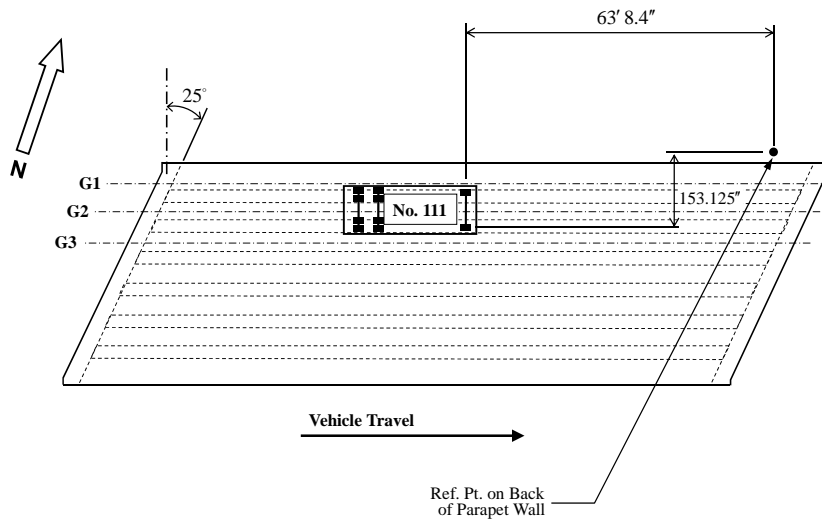
(b)

Figure 4.18 Loading Protocols used to Examine Deck Deflection in the Exterior Deck Spans within the Deck of Bridge B-20-148 During July 2007 and July 2009 Load Tests: (a) July 2007 Load Test; (b) July 2009 Load Test.



July 2007 Load Test
Truck Position 2 - Deck Deflection
DWT-1 Target: Data File: File2

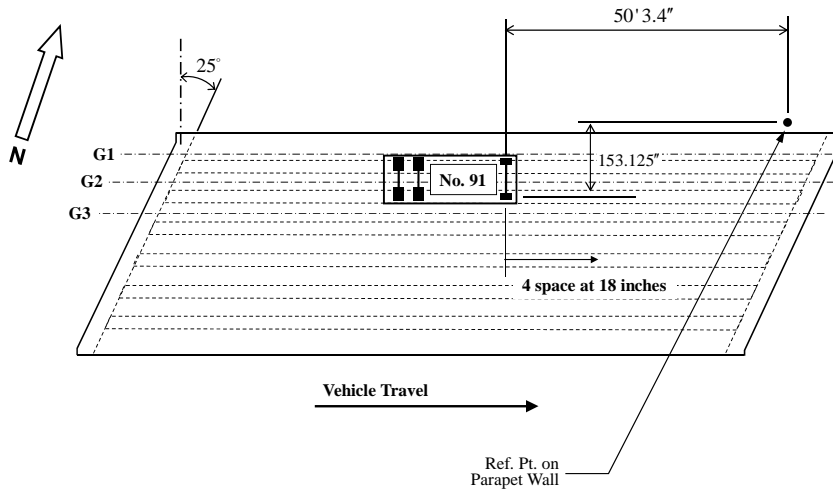
(a)



July 2009 Load Test
Truck Position 2 - Deck Deflection
DWT-1 Target: Data File: File2

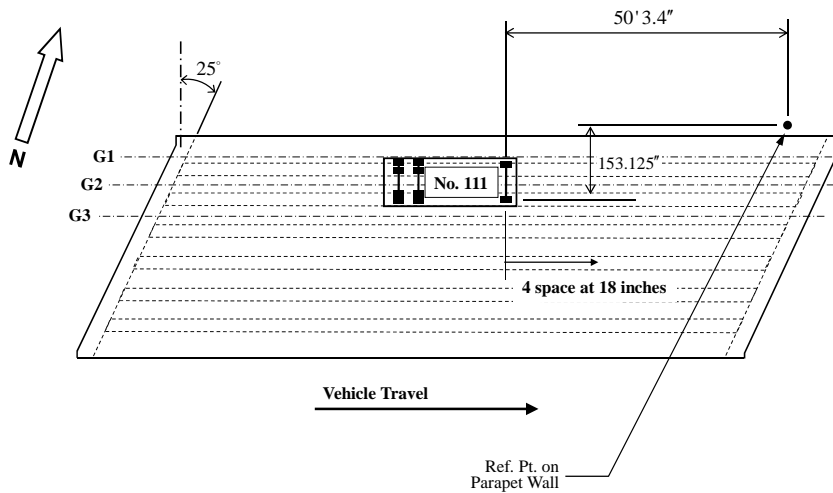
(b)

Figure 4.19 Loading Protocols used to Examine Deck Deflection in the Interior Deck Spans within the Deck of Bridge B-20-148 During July 2007 and July 2009 Load Tests: (a) July 2007 Load Test; (b) July 2009 Load Test.



**July 2007 Load Test
Truck Position Number 3 - Wheel Load Distribution
Data File: File3**

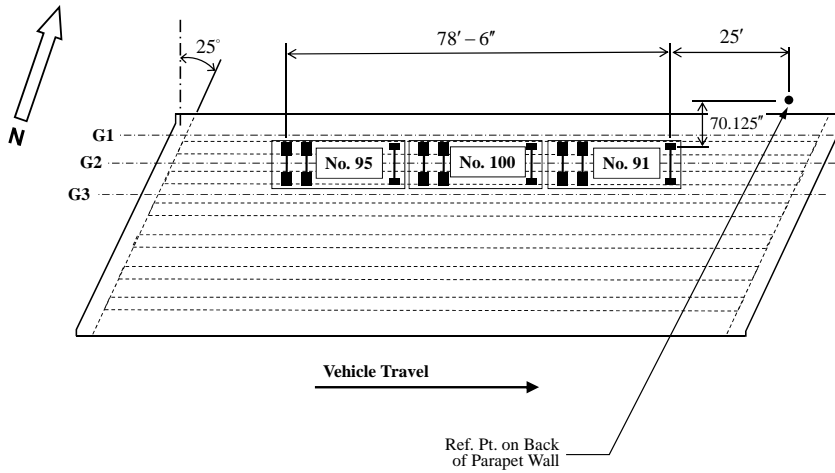
(a)



**July 2009 Load Test
Truck Position Number 3 - Wheel Load Distribution
Data File: File3**

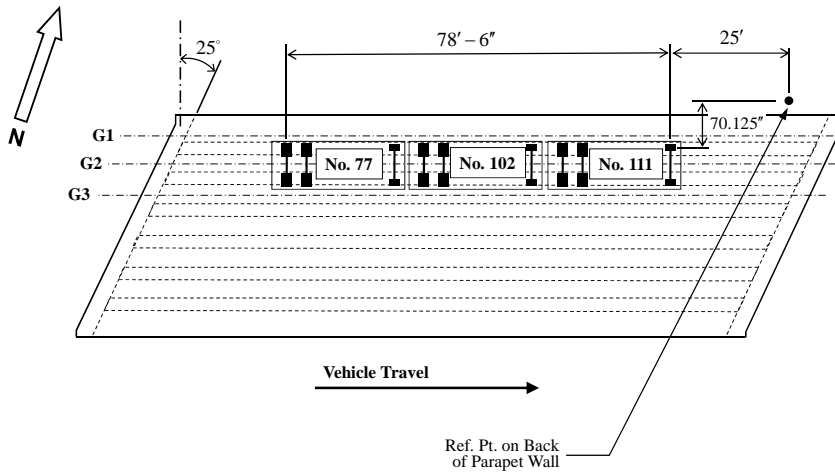
(b)

Figure 4.20 Loading Protocols used to Examine Deck Wheel Load Distribution in the Interior Deck Spans within the Deck of Bridge B-20-148 During July 2007 and July 2009 Load Tests: (a) July 2007 Load Test; (b) July 2009 Load Test.



**July 2007 Load Test
Truck Position Number 4 - Lane Load Distribution
Data File: File4**

(a)



**July 2009 Load Test
Truck Position Number 4 - Lane Load Distribution
Data File: File4**

(b)

Figure 4.21 Loading Protocols used to Examine Lane Load Distribution among the Girders in Bridge B-20-148 During July 2007 and July 2009 Load Tests: (a) July 2007 Load Test; (b) July 2009 Load Test.

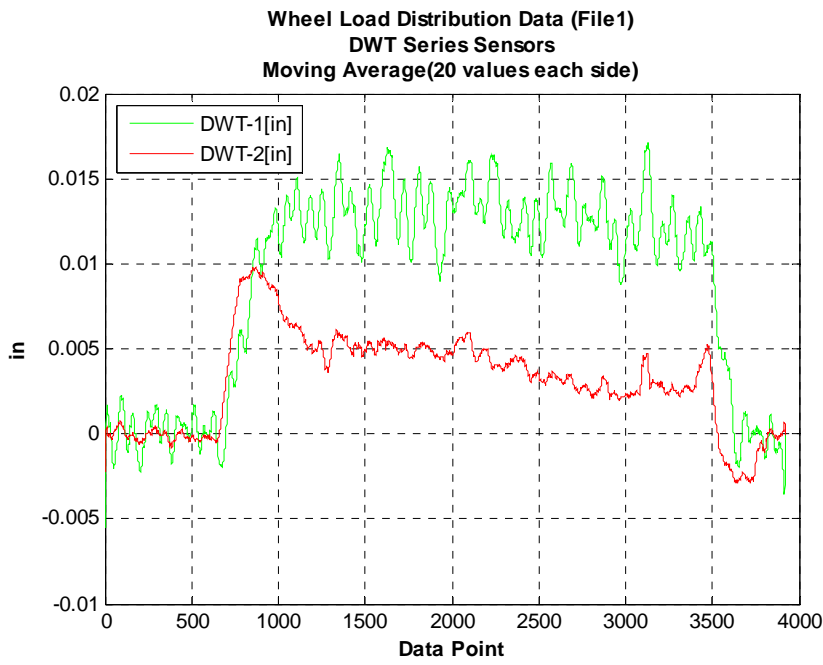


(a)

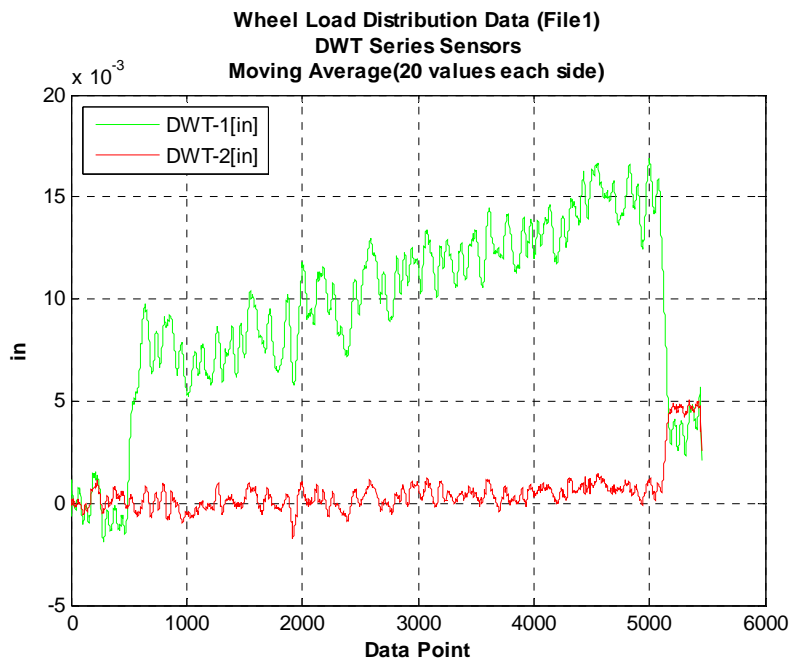


(b)

Figure 4.22 Typical Truck Positioning during Load Testing: (a) Bridge B-20-148 Lane Load Distribution Loading Protocol; (b) Bridge B-20-133 Wheel Load Distribution Loading Protocol.

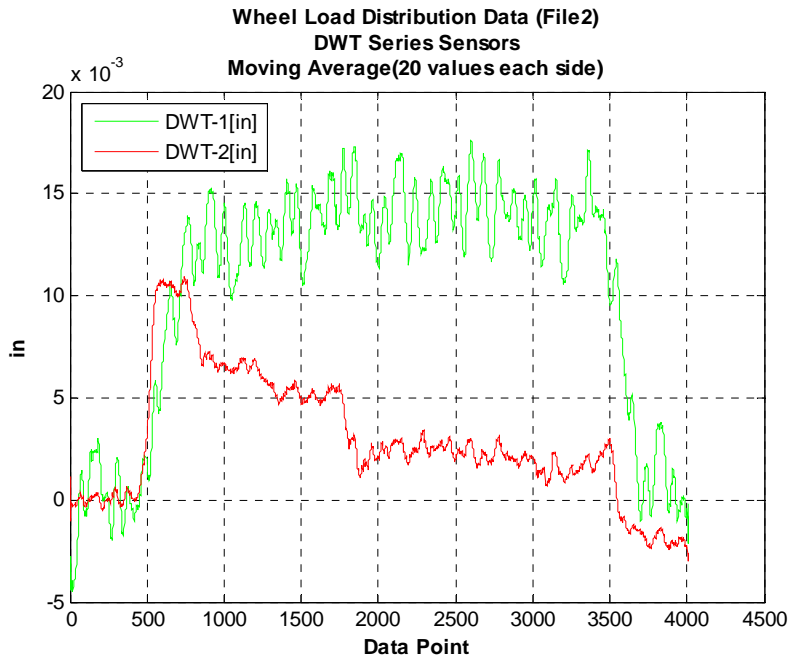


(a)

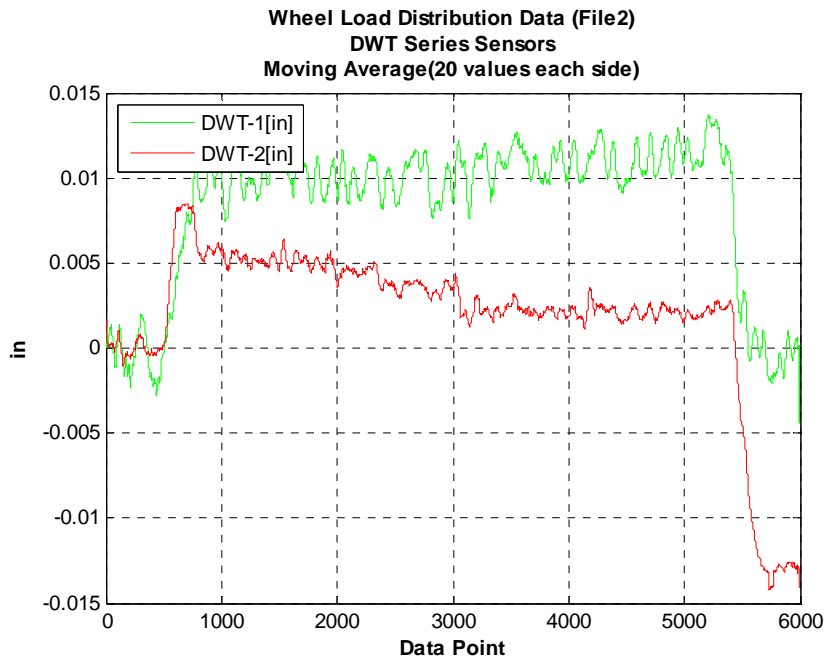


(b)

Figure 4.23 B-20-133 Bridge Deck Displacements Measured for Truck Travel Path 1 (Figure 4.16) during Load Testing: (a) July 2007; (b) July 2009.

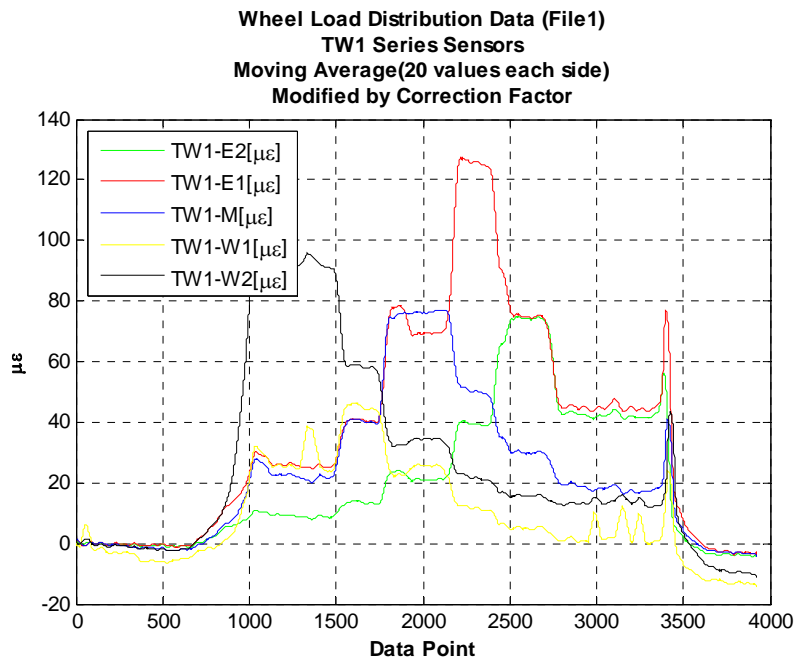


(a)

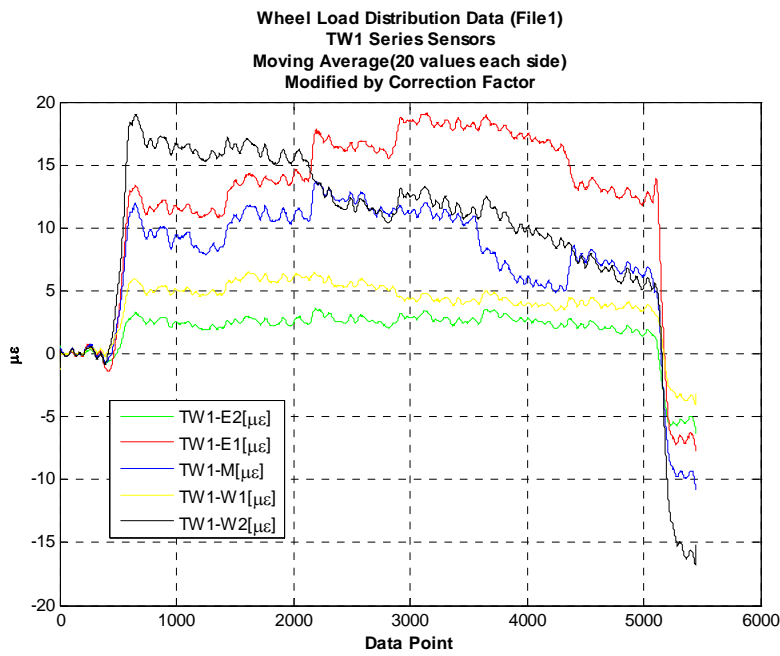


(b)

Figure 4.24 B-20-133 Bridge Deck Displacements Measured for Truck Travel Path 2 (Figure 4.17) during Load Testing: (a) July 2007; (b) July 2009.



(a)



(b)

Figure 4.25 B-20-133 Wheel Load Strain Distribution Measurements in the Exterior Bridge Deck Span during Truck Travel Path 1 (Figure 4.16): (a) July 2007; (b) July 2009.

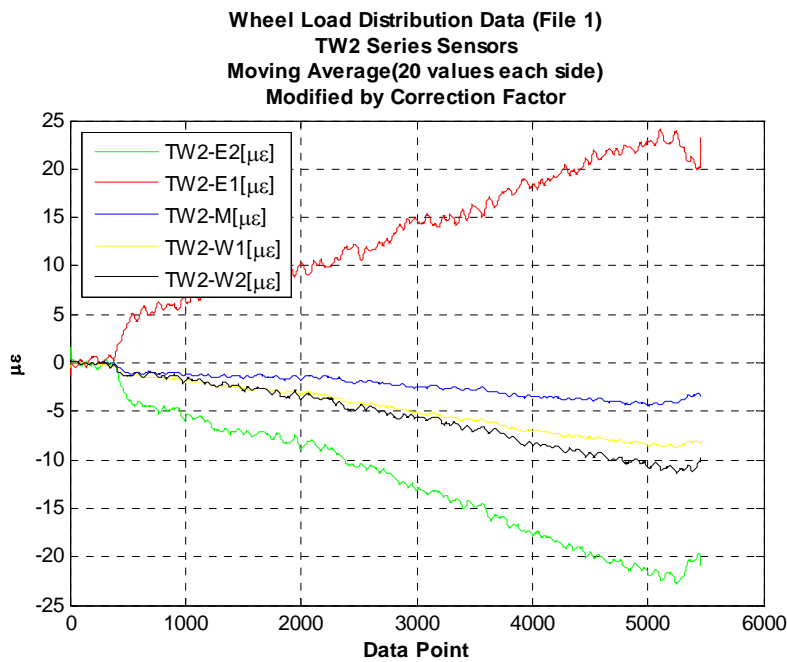
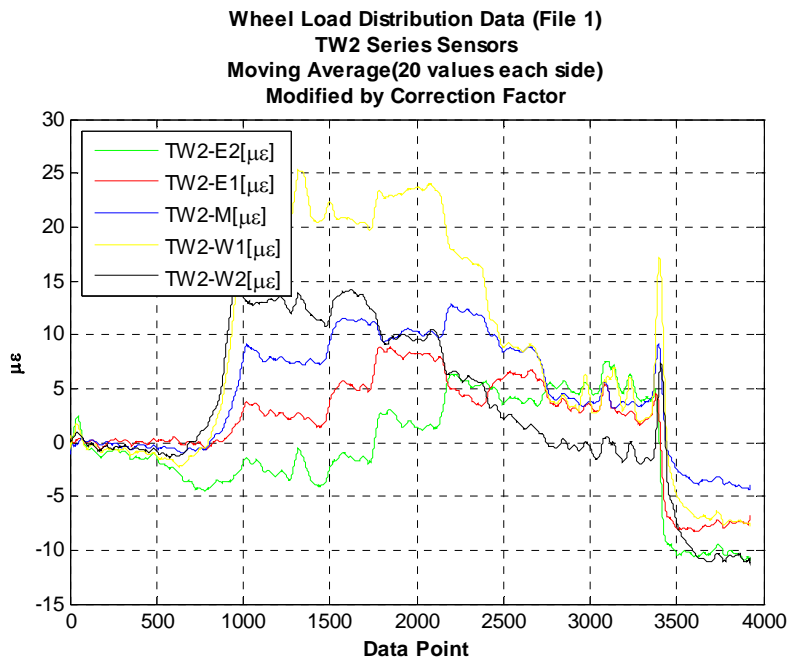
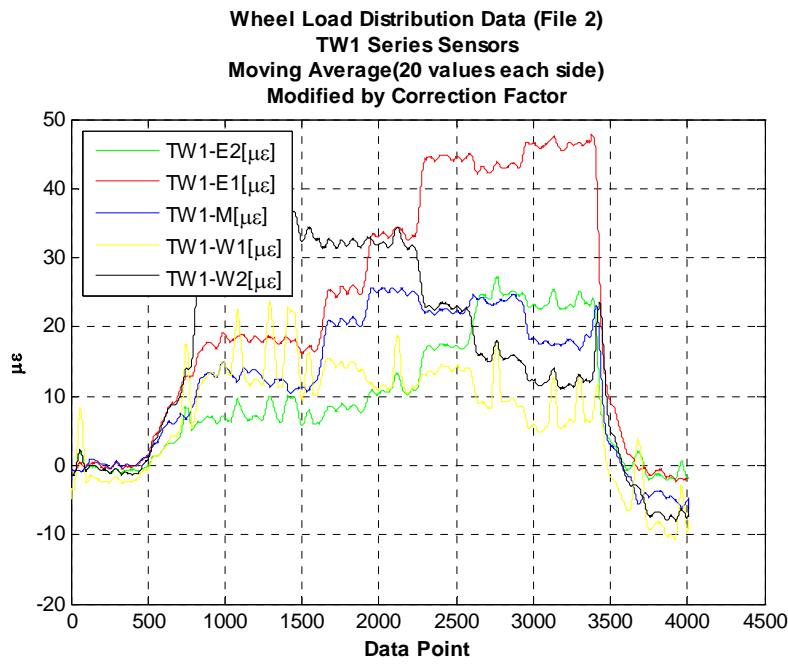
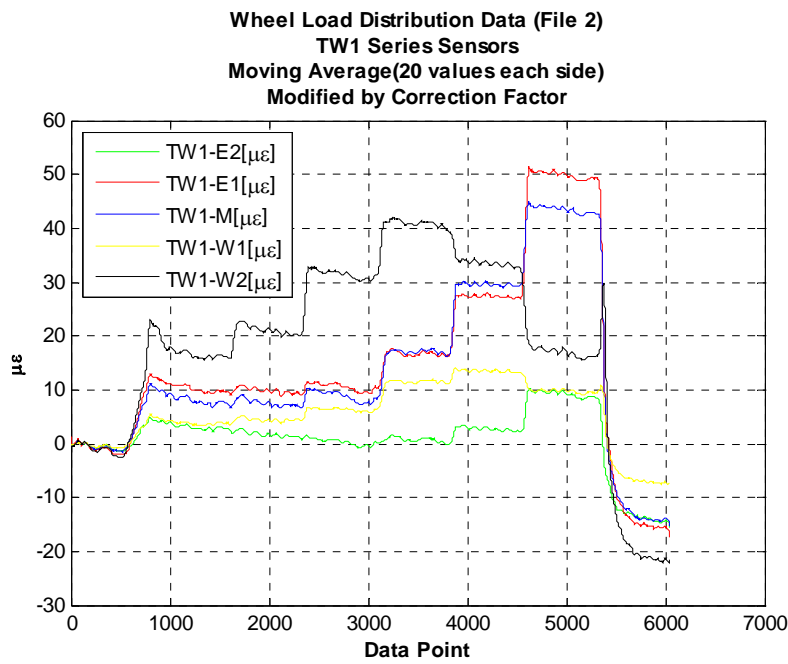


Figure 4.26 B-20-133 Wheel Load Strain Distribution Measurements in the Interior Bridge Deck Span during Truck Travel Path 1 (Figure 4.16): (a) July 2007; (b) July 2009.



(a)



(b)

Figure 4.27 B-20-133 Wheel Load Strain Distribution Measurements in the Exterior Bridge Deck Span during Truck Travel Path 2 (Figure 4.17): (a) July 2007; (b) July 2009.

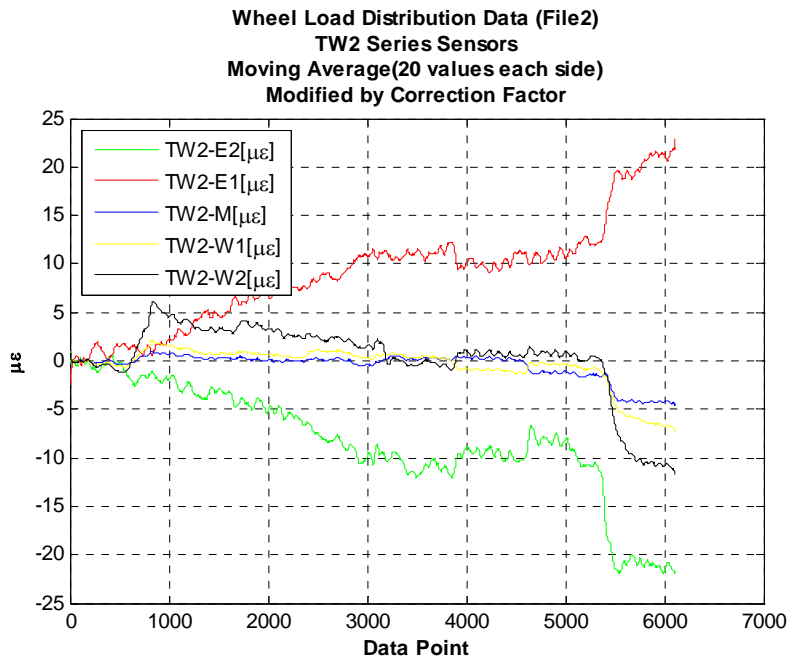
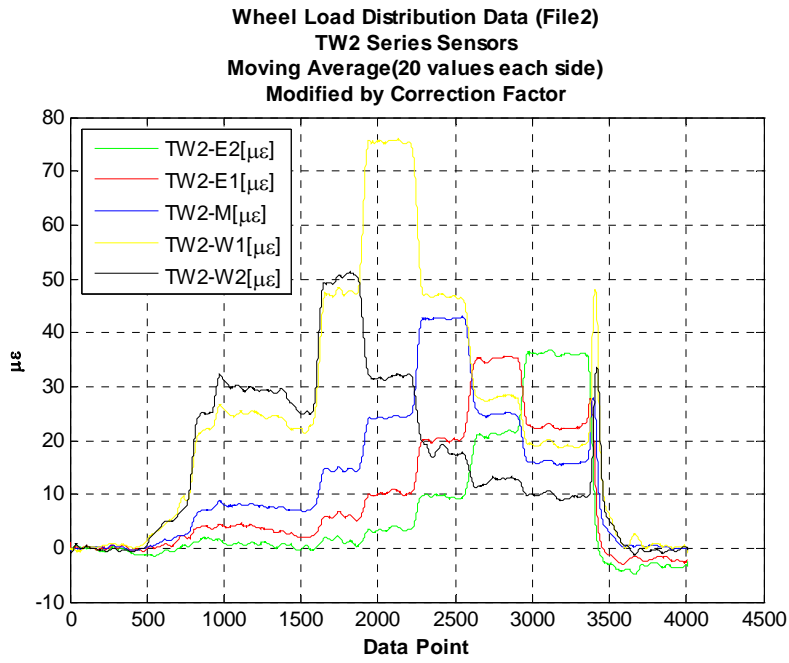
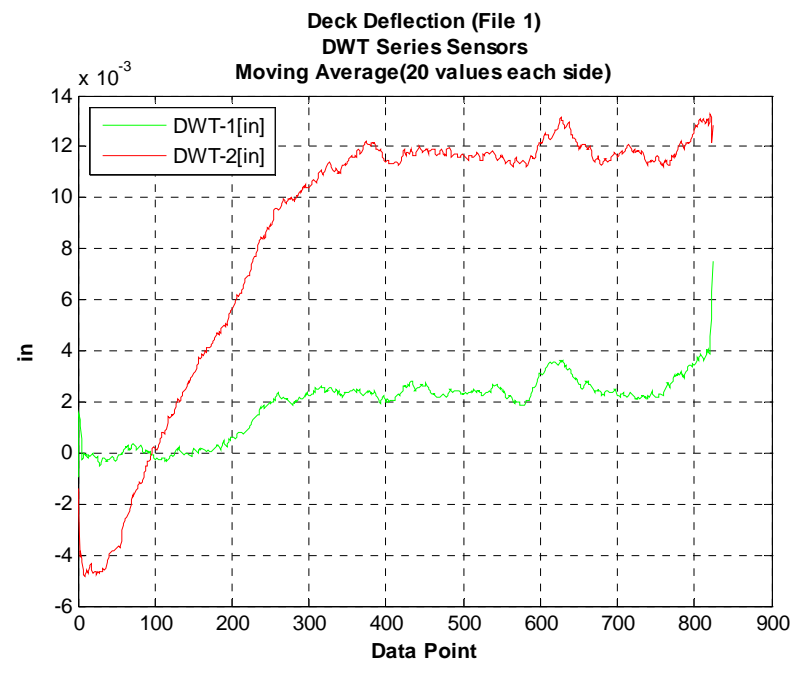
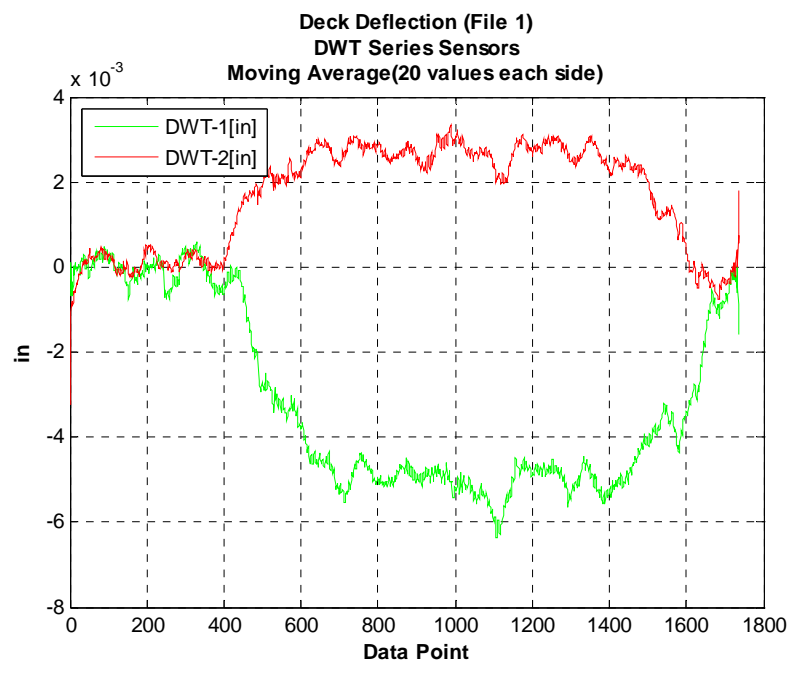


Figure 4.28 B-20-133 Wheel Load Strain Distribution Measurements in the Interior Bridge Deck Span during Truck Travel Path 2 (Figure 4.17): (a) July 2007; (b) July 2009.

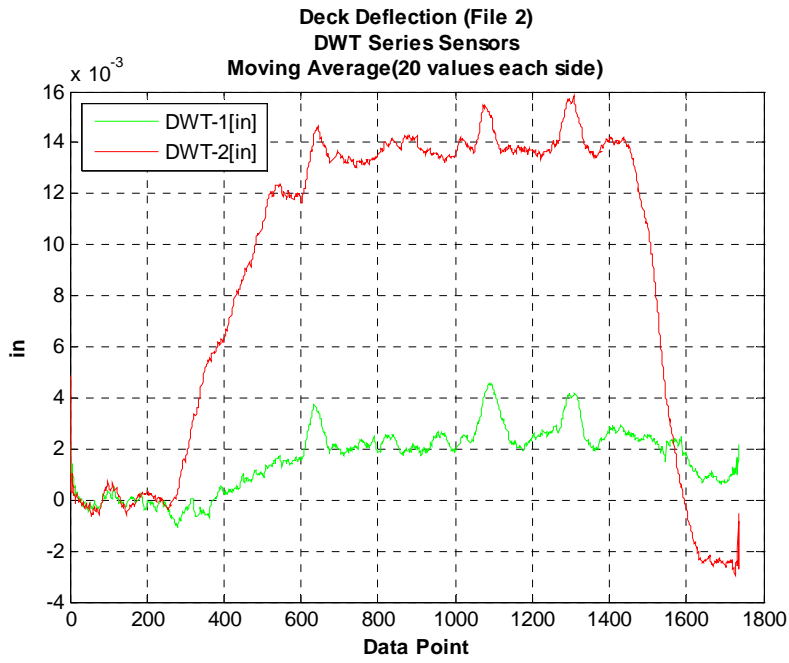


(a)

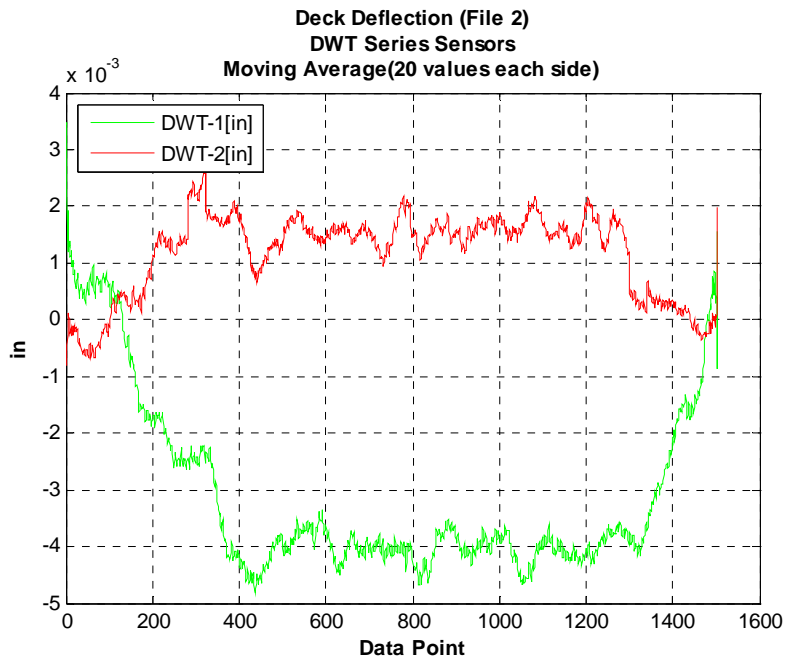


(b)

Figure 4.29 B-20-148 Deck Displacements for Truck Position 1 (Figure 4.18): (a) July 2007; (b) July 2009.

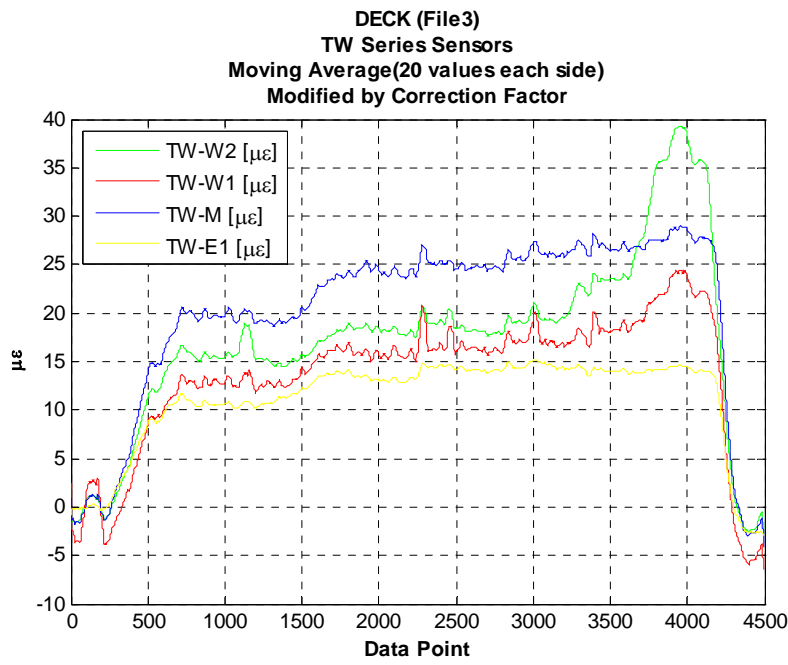


(a)

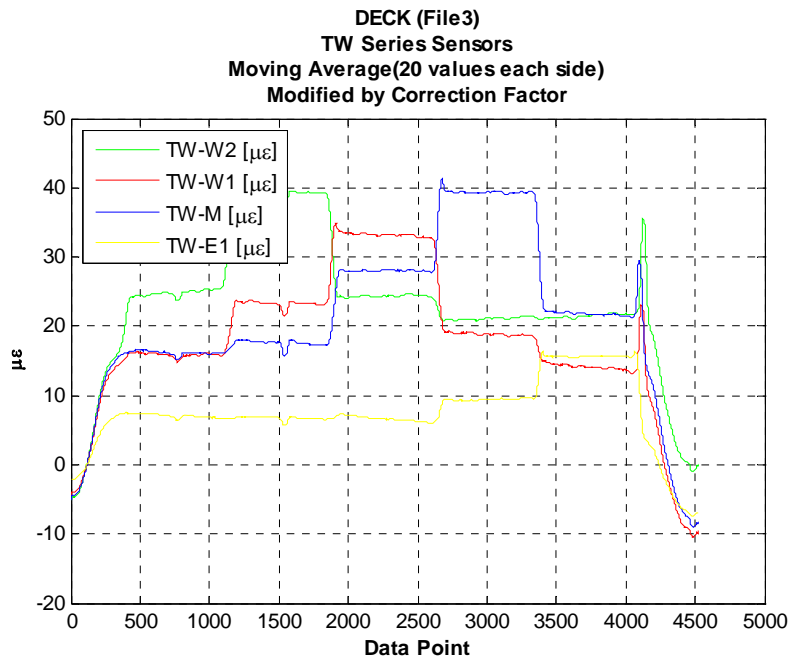


(b)

Figure 4.30 B-20-148 Deck Displacements for Truck Position 2 (Figure 4.19): (a) July 2007; (b) July 2009.

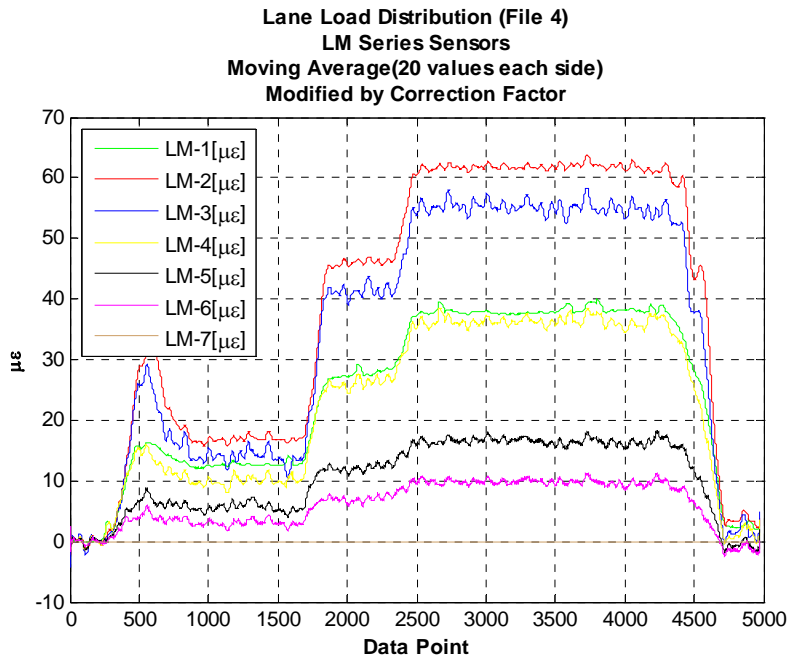


(a)

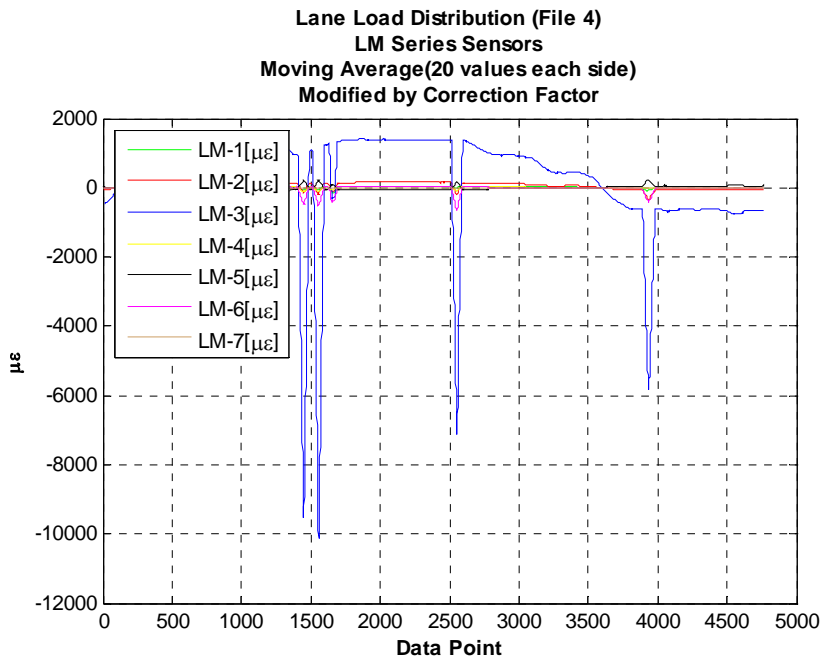


(b)

Figure 4.31 B-20-148 Wheel Load Distribution Strains Measured for Truck Position 3 (Figure 4.20):
 (a) July 2007; (b) July 2009.



(a)



(b)

Figure 4.32 B-20-148 Lane Load Distribution Strains at Mid-Span of Girders for Truck Position 4 (Figure 4.21) Measured During Load Tests: (a) July 2007; (b) July 2009.

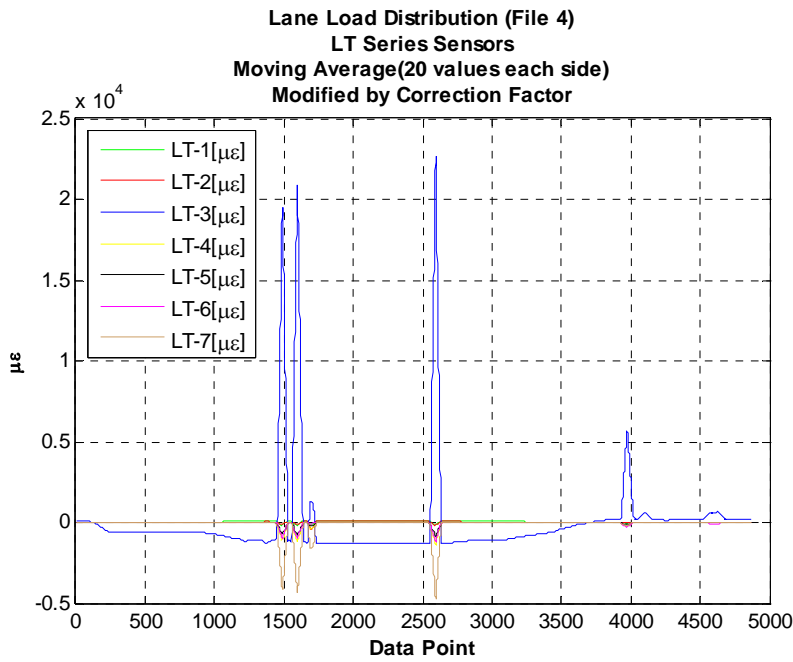
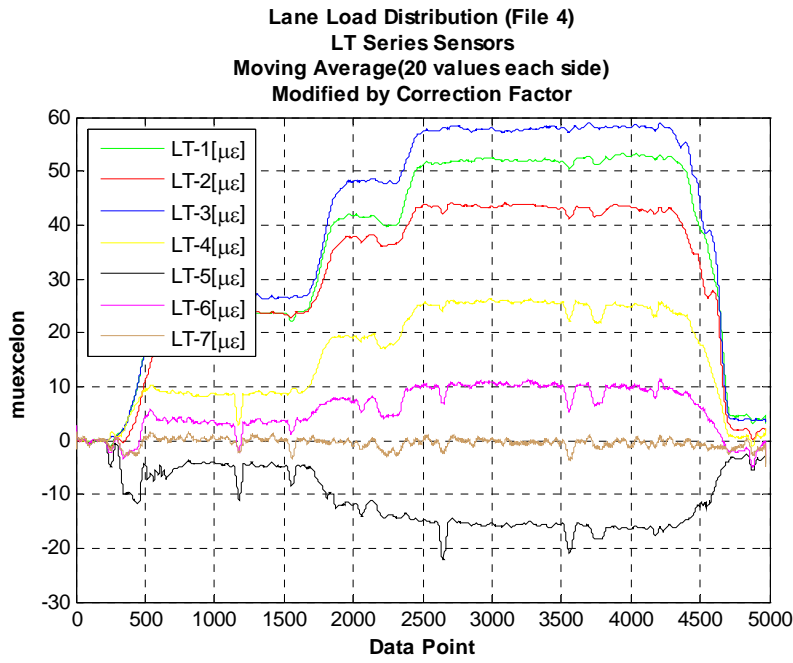


Figure 4.33 B-20-148 Lane Load Distribution Strains at One-Third-Span of Girders for Truck Position 4 (Figure 4.21) Measured During Load Tests: (a) July 2007; (b) July 2009.

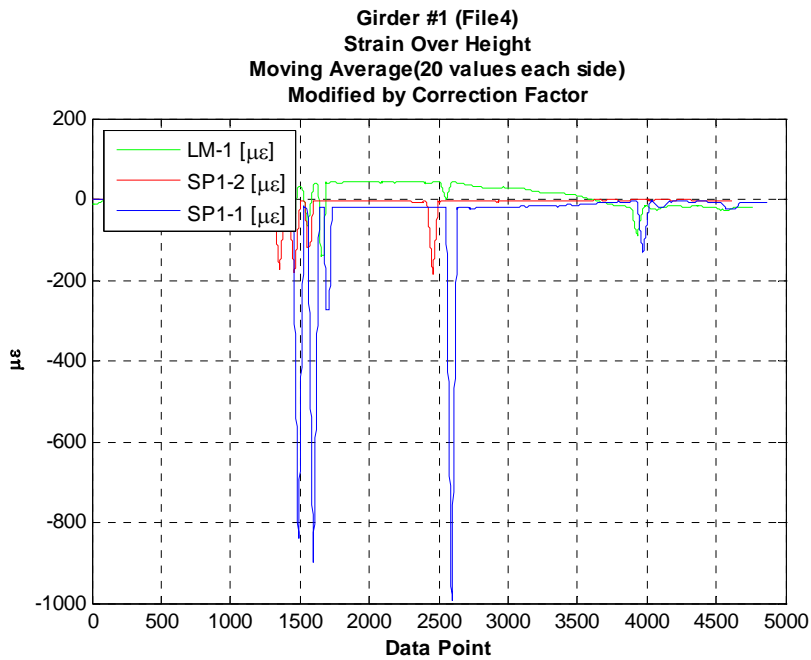
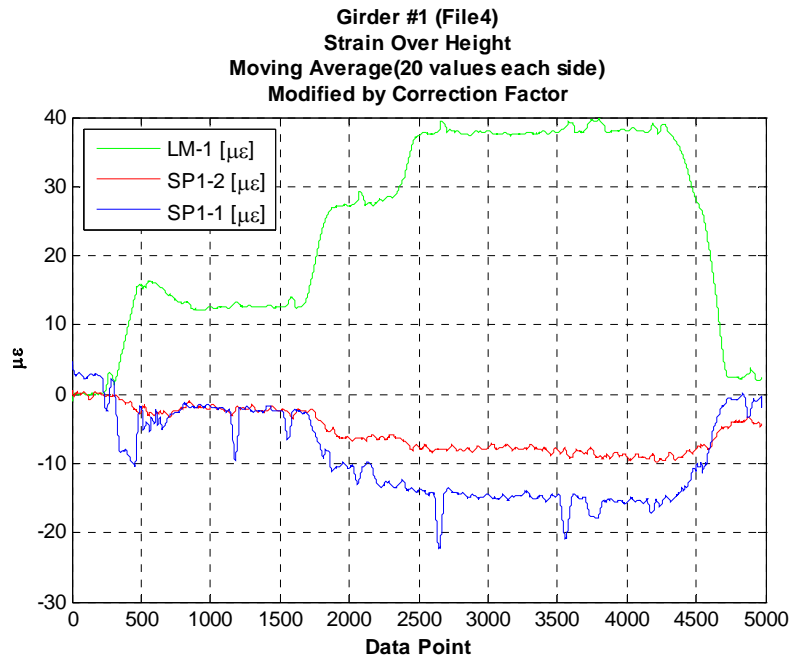
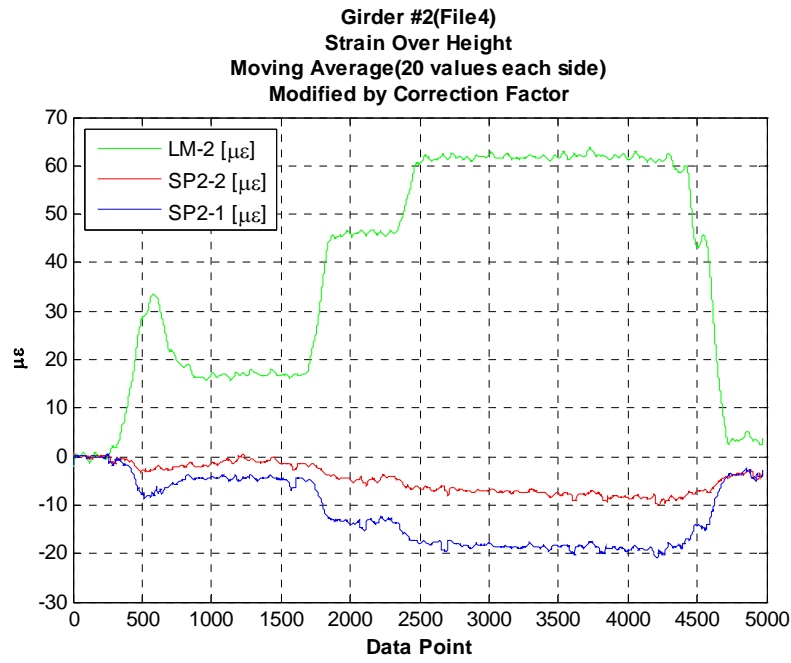
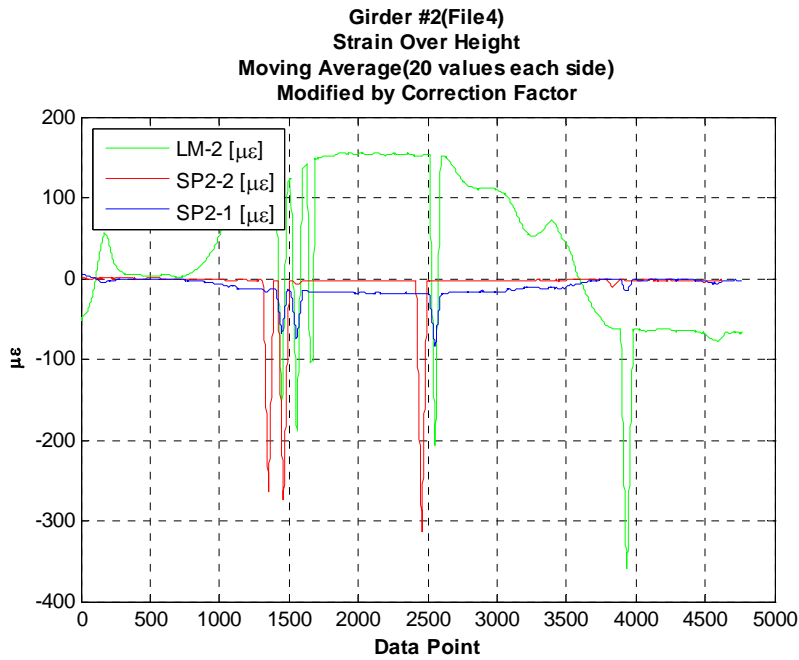


Figure 4.34 B-20-148 Strains over Girder Height for Girder G1 and Truck Position 4 (Figure 4.21)
Measured During Load Tests: (a) July 2007; (b) July 2009.



(a)



(b)

Figure 4.35 B-20-148 Strains over Girder Height for Girder G2 and Truck Position 4 (Figure 4.21) Measured During Load Tests: (a) July 2007; (b) July 2009.

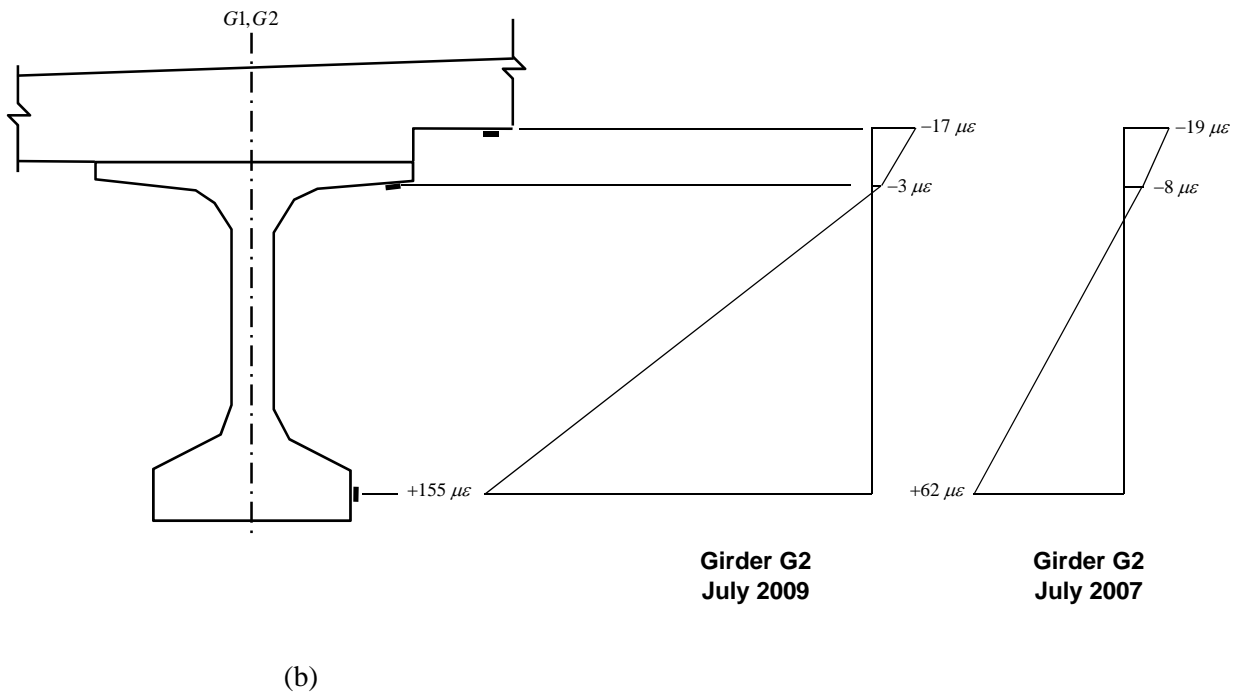
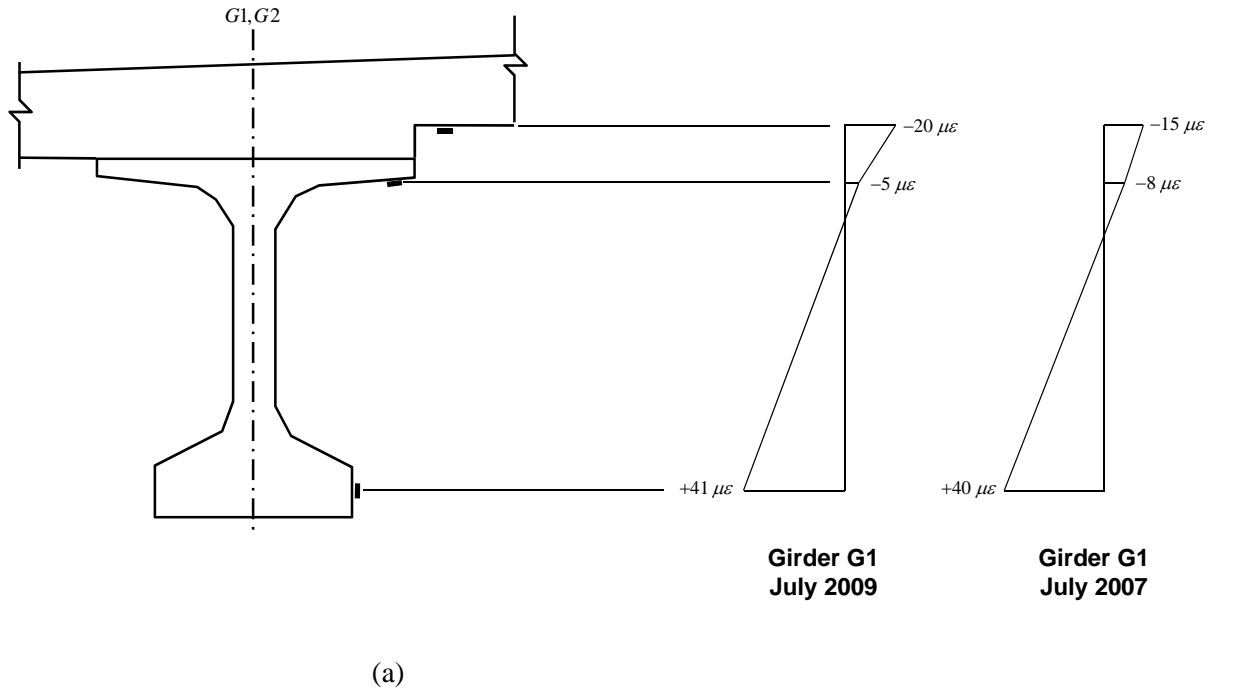


Figure 4.36 B-20-148 Strains over Girder Height for Girders G1 and G2 for Truck Position 4 (Figure 4.21) Measured During Load Tests: (a) Girder G1; (b) Girder G2.



Figure 4.37 Strain Sensor Installation Error with Potential to Cause Error in Strain Readings.



Figure 4.38 Method for Truck Wheel Positioning on Bridge Deck.

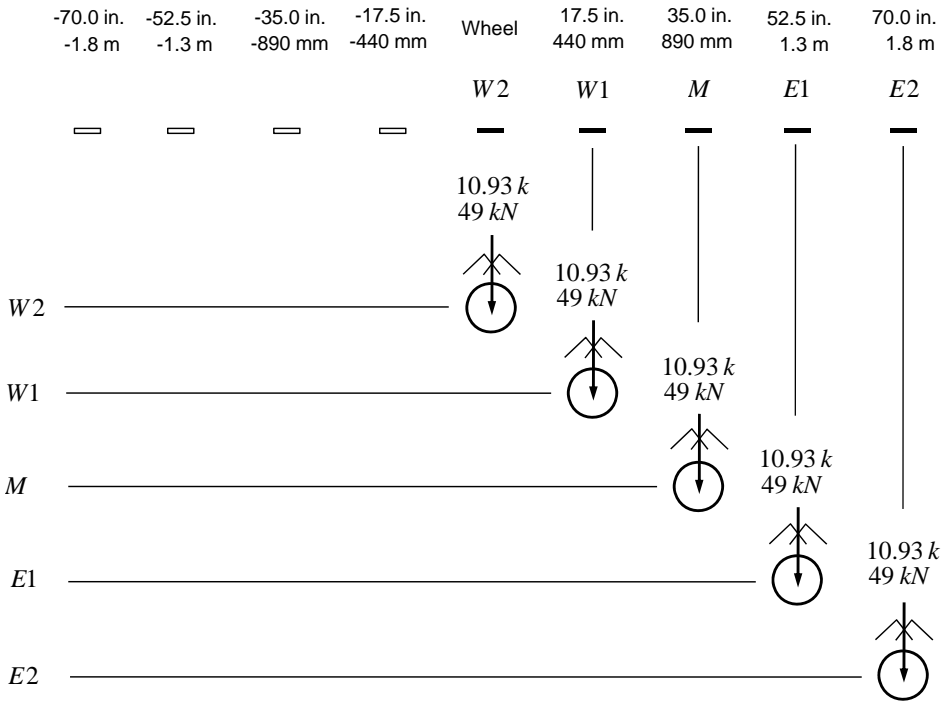


Figure 4.39 Front Wheel Position Relative to Mounted and Symmetrically Extrapolated Strain Sensors.

Chapter 5

Numerical Simulation of Shrinkage-Induced and Vehicle-Induced Stresses

5.1 Introduction

The present chapter outlines finite element (FE) simulation that is used as the foundation for assessing the cause and impact of the cracking that exists throughout the bridge deck in the bridges at Waupun, Wisconsin (bridges B-20-133/134). The simulation results presented here are (in large part) based upon an MS thesis written to assess bridge deck cracking (Komp 2009). The results present here are intended to outline the FE simulation used to document the cause of cracking in these bridge decks. Two sources are examined: (a) shrinkage-induced tensile strains; and (b) typical HL-93 design truck loading. Further detailed discussion of the modeling is available elsewhere (Komp 2009).

5.2 FE Modeling of Bridge Superstructure

The FE simulation conducted in this research was done using the ANSYS Finite Element Analysis System (ANSYS 2007). All structural simulations were conducted using linear-elastic analysis and elements that are standard within the software program. The present section will discuss general modeling approaches used including the elements utilized.

The bridge prototype was modeling after structure B-20-134, located in Waupun, Wisconsin. Figure 5.1 provides an overview photograph of the bridge superstructure. The finite element model was developed using planar elements and subsequent extrusion to solid elements. The three-dimensional solid modeling of the concrete components of the bridge cross-section was done using SOLID 45 elements (ANSYS 2007). The bridge plan is shown in Figure 5.2. To create the skew, each girder and associated deck/barrier was staggered by 1,500 mm (4.9 feet), as shown in Figure 5.2. A close up view of the staggered model (with modeling volumes shown – not elements) is shown in Figure 5.3. The bridge cross-section and area modeling prior to extrusion are shown in Figure 5.4.

The bearing plates for the precast concrete girders were modeled using steel material in lieu of the complex elastomeric bearing materials. The original elastomeric pads had dimensions of 0.50x6.0x30.0 inches and the steel bearing pads in the FE model closely followed these dimensions (within allowable meshing constraints). The bearing pads were given a modulus of elasticity of 29,000 ksi and Poisson's ratio of 0.25. Once modeled, the pads were then centered under the ends of each girder.

The exact restraints at the ends of the bridge are difficult to quantify, and therefore pin-roller supports were assumed for each span. The plates at the exterior support locations in the bridge were modeled with "pin supports" (translational restraints applied at each of the 12 nodes on the center-base of the plates), while the interior support locations included "roller supports" (translational restraints), which were applied at similar locations (Figure 5.5).

Each of the 5 prestressed concrete girders within a given span was modeled using 3D solid elements. These girders span 107'-4" centerline to centerline. The girder spacing was 8'-8" and a 12 inch long space at the ends of the girders was included to accommodate the diaphragms at the interior pier. Solid FE modeling of the girders and their overall dimensions are shown in Figure 5.6. The bridge deck is the primary concern in this thesis, and the girders were modeled without steel reinforcement, and were given a modulus of elasticity consistent with a defined 28-day unconfined compressive strength of 9,000 psi. A Poisson's ratio of 0.2 was selected. (Kachlakev 2001).

Concrete barriers were also modeled using solid elements. Barrier modeling and dimensions are shown in Figure 5.7. The barriers included no reinforcement, were given a Poisson's ratio of 0.2, and a modulus of elasticity consistent with a 28-day unconfined compressive strength equal to 4,000 psi.

For portions of the study targeted toward studying drying shrinkage, the deck was analyzed before the placement of the barriers, and therefore the barriers were either removed completely, or given zero density and very small modulus of elasticity set by trial and error. Details can be found in Komp (2009).

Concrete diaphragms or pilasters were modeled in the 12-inch space between the 5 sets of girders which connect the two spans. The diaphragms were initially modeled using the same shape and physical

characteristics as the concrete girders. The actual dimensions of the diaphragms and the modeling characteristic are given in Figure 5.5 and 5.8.

At the ends of the bridge girders and between girder spans, the lateral stability characteristics of the concrete diaphragms were modeled using nodal restraints. A 6-inch length of the girders was given transverse displacement restraints. The restraints were applied on the exterior nodes on either side of the girder, excluding the nodes that were connected to either the deck or the steel plates (Figure 5.9). In reality, the concrete diaphragms would be cast at an angle similar to that of the skew.

The steel diaphragms present at approximate third points along the girder spans were modeled using a pin-connected model composed of 3D spar (link) elements. These elements are only capable of supporting axial forces. The original diaphragms were channel members (MC-shape) as shown in Figure 5.4. The resulting truss model for the diaphragms is schematically shown in Figure 5.10. The horizontal truss elements were given an area consistent with that of the area of the original MC flanges. The diagonal elements in the truss were assigned using consistent shear deformation characteristics between the channel and truss. The link elements representing steel diaphragms were then added between the girders at approximate third points along the span. The spacing of the X-braced diaphragms in the finite element model is given in Figure 5.10.

The bridge deck was modeled using 3D solid elements. Figure 5.11 illustrates the deck modeling approach utilized. The haunches between the deck soffit and girder top surface s have been omitted in the FE model. In addition, the super elevation of the deck and the rebar (in some cases) were also eliminated to simplify the model. The deck elements were given a Poisson's ratio of 0.2 and a modulus of elasticity consistent with a given unconfined compressive strength (dependent on time). In the linear analysis, the analysis was only carried out until first cracking (modulus of rupture is reached). In general, it is accurate to assume linear behavior until this point, as concrete shows relatively linear behavior up until a stress level near $0.3f_c'$, which is less than the modulus of rupture (Kachlakev 2001).

Steel rebar was modeled using 3D spar (link) elements. The spacing of rebar was set at 6 inches in the longitudinal direction of the bridge model to represent the longitudinal steel based on the nodal

spacing previously created. The area of these elements could be determined by calculating the total amount of longitudinal steel (length*area) originally used in the deck, and altering it based on the previously determined element spacing in the finite element model. The same process was used for the transverse steel. In general, the addition of steel reinforcement to the model required quite a significant amount of computer memory, and therefore it was neglected in some of the linear analyses (Komp 2009).

5.3 Simulation and Evaluation of Shrinkage-Induced Strains

The current section examines the effects of drying shrinkage-induced strains on the concrete bridge deck in bridge B-20-134. The magnitude of shrinkage-induced strains was defined using previous research efforts reviewed in this section. Shrinkage strain magnitudes were then converted into equivalent temperature loads to facilitate FE simulation. The shrinkage strains accumulated over a given day were run as independent linear elastic models. This section of the report outlines the modeling process that was used to simulate the effects of shrinkage-induced strains in the bridge deck.

5.3.1 Shrinkage Strain Model

A representative value of shrinkage strain was developed using the work of Tadros and Al-Omaishi (2003). Shrinkage of the concrete is defined as a decrease in volume under constant temperature due to loss of moisture after concrete has hardened (drying shrinkage). Parametric studies typically focus on water content, type of cement, type of aggregate, ambient conditions (temperature, humidity, and wind velocity) at the time of placement, the curing procedure, the amount of reinforcement, and the volume/surface area ratio of the concrete. The following empirical model has been recommended to model shrinkage-induced strain magnitude (Tadros and Al-Omaishi 2003; Saadeghvaziri *et al.* 2002);

$$\varepsilon_{sh} = -1.2 \cdot k_{vs} \cdot k_{hs} \cdot k_f \cdot k_{td} (0.00078) \quad (6.1)$$

The parameter ε_{sh} is the strain due to shrinkage of the concrete an exposed surface. The constant, 0.00078, represents an estimate for the ultimate shrinkage strain in the concrete. Each component in the shrinkage strain model depends upon many parameters related to concrete compressive strength and time.

This section of the report describes the parameters used to formulate the shrinkage strain model for the finite element simulations.

The first parameter addressed, k_{vs} , intends to account for the effect of the volume-to-surface ratio of the concrete:

$$k_{vs} = 1.45 - 0.13(V/S) \geq 1.0$$

where: V = volume of concrete; and S = surface area of concrete. The volume to surface ratio for the deck in bridge B-20-133 used to establish this coefficient was 3.876 (Komp 2009). With this value of volume to surface ratio, the volume to surface coefficient is 0.95 (not less than 1.0). Thus, the value of this coefficient is taken to be 1.0.

The second parameter, k_{hs} , accounts for the fact that shrinkage is greater in dryer climates than wet climates;

$$k_{hs} = 2.00 - 0.014 \cdot H$$

where: H = relative humidity (%). If the humidity at the site is unknown, the following, Figure 5.12 can be used to estimate the relative humidity at the site. It is felt that the relative humidity within the bridge deck should be higher than that at the external surfaces of the bridge deck (especially early on in the bridge deck's service life). The relative humidity readings in the deck of B-20-133 confirm this.

Relative humidity data for the bridge deck's early life was not available and the research team was forced to make rational assumptions in this regard. The exterior surface of the bridge deck (top) was assumed to be at 70 percent relative humidity consistent with Figure 5.12. The center of the bridge deck was assumed to be at 80% relative humidity. Using these values, the humidity parameters are:

$(k_{hs})_{top} = 1.02$ and $(k_{hs})_{center} = 0.88$. The points at 1/3 from the bottom, 2/3 from the bottom and the bottom of the bridge deck are interpolated and extrapolated using these values. The magnitudes of the humidity coefficient are given in Table 5.1.

The parameter k_f is a factor to take into consideration the effect of concrete strength and can be expressed as;

$$k_f = \frac{5}{1 + f'_{ci}}$$

where: f'_{ci} is the specified unconfined compressive strength of concrete at the time of prestressing for pretensioned members and at the time of initial loading for non-prestressed members (ksi). Assuming that the 28-day strength of the concrete is 4.06 ksi and it achieves 80% of its 28-day strength at 7 days curing time, this coefficient at 7 days is: $k_f = 1.19$.

The final parameter in the shrinkage strain model is the time-dependent factor, k_{td} . It is expressed as;

$$k_{td} = \frac{t}{61 - 4f'_{ci} + t}$$

where: t is the maturity of the concrete (in days). Maturity is defined as the age of concrete between the end of curing and the time being considered. However, for bridge decks where the curing time may be unknown (or varying), the time immediately following placement is used as an initial time. In general, higher strength concretes will produce accelerated early shrinkage.

The concrete strength at the time of loading will again be taken as 7 days and the 28-day unconfined compression strength for the deck concrete is 4.06 ksi. Assuming f'_{ci} of 80% of the 28-day unconfined compression strength leads to the data in Table 5.2 for k_{td} for a 14-day interval.

The shrinkage strain can now be represented as a function of time using equation (6.1). The concrete shrinkage can be extended to an entire year interval to gain appreciation for the rapidity of shrinkage strains forming in the concrete deck. The shrinkage model for a 365-day interval is shown in Figure 5.13. This figure indicates that the model for concrete shrinkage increases greatly during the first 50 days, and then asymptotically reaches a peak value near -0.936×10^{-3} . As expected, this value represents the ultimate shrinkage strain (-0.78×10^{-3}) multiplied by a factor of 1.2 (for immediate drying).

5.3.2 Time-Varying Model for Concrete Strength and Stiffness

In order to analyze the effects of shrinkage strains in a bridge deck with time, it is necessary to understand the change in compressive strength and stiffness of the constituent concrete with time. However, due to variations in mix design (material properties), sites conditions, construction procedures, and design specifications, a generalized scenario was created. Figure 5.14 represents schematic variation in unconfined compressive strength of concrete with time assuming the following: water-to-cement ratio of 0.41; air content of 4.5%; Type 1 cement; 73-deg F temperature during curing for the 28 days. It should be noted that Figure 5.14 suggests that at “time 0”, the concrete will have nearly 20% of its 28-day compressive strength. In general, it is accepted that this value of strength is not reached until day one (Nilson and Darwin 2004), and therefore it was assumed that “time 0” represented day one.

The data in Figure 5.14 and logarithmic interpolation can be used to generate a model for the variation in unconfined compression strength over a 365-day time period. Figure 5.15 illustrates the compression strength model superimposed on a single graph with the shrinkage strain model. As expected, the compression strength of the concrete rises much more rapidly than the shrinkage strain over an initial 14-day period. If the compression strength increases in the manner shown in Figure 5.15, the tension strength of the concrete will increase in much the same rate. In fact, it is often assumed that the tension strength of the concrete is roughly 10% of the compression strength.

The modulus of elasticity is generally known to be related to the unconfined compression strength of the concrete. For moderate unconfined compression strengths, the modulus of elasticity can be computed using the following;

$$E = 57,000\sqrt{f'_c}$$

The increase in the compression strength and the modulus of elasticity over the initial 14-day is shown in the data found in Table 5.3. The compressive strength model illustrates that approximately 80% of the 28-day unconfined compression strength is achieved at 7-8 days. This is consistent with the strengths used in the shrinkage strain model discussed earlier.

5.3.3 Modeling Shrinkage Strain via Temperature Change

Komp (2009) confirmed that shrinkage strains can be accurately represented by applied temperature loadings (change) within finite element analysis. The strain resulting from temperature change is written using the classic relationship below;

$$\varepsilon = \alpha \cdot \Delta T \quad (6.2)$$

where: α is coefficient of thermal expansion for the concrete material ($6.6 \times 10^{-6} / \text{deg } F$); and ΔT is the temperature change. It should be noted that the coefficient of thermal expansion for concrete materials is thought to range between $5 \times 10^{-6} / \text{deg } F$ to $9 \times 10^{-6} / \text{deg } F$. The magnitude of α is important, but not critical. The reason for this is that target shrinkage strains are sought and a combination of coefficient of thermal expansion and temperature change is chosen to meet the shrinkage strain target.

5.3.4 Transient Shrinkage Strain Modeling through Bridge Deck

While empirical equation (6.1) provides an estimate with regard to the shrinkage strain magnitude, this shrinkage is only representative of exposed concrete surfaces. Therefore, while the strain in the concrete at the top and bottom surface can be estimated, nothing is known about values of shrinkage strain across the thickness of the deck, or its variation. Unfortunately, very little research has been done to describe the variation of shrinkage strains throughout the thickness of concrete.

Some research suggests that the gradient of shrinkage strain through the bridge deck thickness can be assumed to be linear with the top surface having the largest value of strain (Krauss and Rogalla 1996). However, other research shows that drying strains (neglecting the effects of ambient thermal heating) within the deck will be equal at the exposed surfaces (top and bottom), thereby creating compression stresses at the center of the deck (Tadros and Al-Omaishi 2003). Assuming the concrete deck formwork will remain in place for some finite time duration during the concrete curing, the linear strain distribution appears logical.

The present study included estimates of relative humidity through the deck thickness. The slope of the shrinkage strain distribution through the thickness of the bridge deck is assumed to be linear. Two

shrinkage-strain magnitudes within the bridge deck (top surface and center) are used to develop a shrinkage strain gradient through the height. The FE model of the bridge deck includes three elements through the deck thickness. Thus, these two points are used to formulate a linear variation for extrapolation and interpolation to these points. Schematic illustration of the interpolation and extrapolation procedure is shown in Figure 5.16.

Modeling the transient shrinkage strain through the thickness of the bridge deck using temperature change gradients begins with assigning target shrinkage strains at points within the bridge deck. This is done using equation (6.1) and the linear interpolation procedure discussed earlier. Table 5.4 contains shrinkage strain variation over the first 14 days after casting. Once these target shrinkage strains are known, temperature changes corresponding to these shrinkage strains can be computed using equation (6.2). Table 5.5 contains the temperature change variation with time that will result in the target shrinkage strains at the four locations within the bridge deck.

5.3.5 FE Modeling Assumptions

In creating a finite model to analyze the affects of concrete shrinkage, three significant assumptions were made. These assumptions are described in the following. Further details regarding the assumptions made are available (Komp 2009). The first significant assumption made is that mild steel reinforcement in the bridge deck was neglected. Cracks generally form above and parallel to transverse and longitudinal reinforcement (Schmitt and Darwin 1995, 1999). It was deemed impractical to model the bonding relationship between rebar and concrete and the actual dimensionality of the rebar within the bridge deck and as such, settlement cracking cannot be captured in the FEA. From a first-principles standpoint, the rebar would have little impact on the stress throughout the deck until cracking occurs. The reinforcement in the deck would lead to a slightly higher composite moment of inertia for the bridge deck, but this amount is small and it was felt that using pure concrete cross-section was sufficient to study bending induced strains.

The self-weight of the bridge superstructure (girders and deck) was neglected. In general, when a bridge deck is placed, the concrete is in a viscous-fluid state, and therefore, formwork is required. The formwork usually consists of a shored plywood formwork system supported on the girders. Therefore, the girders will deflect under the self-weight of the deck. Because the concrete is still fluid, the deck concrete conforms to the shape of the deflected girders without generating large tensile stresses (small or no compression strength and therefore, small tensile strength and very low modulus). Thus, it has been assumed that the concrete deck deforms in a plastic state without inducing significant tensile stresses. It should be noted however, that consideration of concrete placement-sequence or placement-rate is omitted.

The continuous slip-formed barriers were removed in the shrinkage analysis. The variability in barrier placement makes the effects of the barriers on the early life of the bridge deck difficult to determine. In general, barriers are placed at least 3 days after deck casting. However, the exact time is quite variable and unknown. Therefore, there is a finite amount of time (at least 3 days), in which the barriers are not present. Figure 5.13 illustrates that majority of shrinkage-induced straining occurs over a 150-day period for the model employed. Thus, the barriers would likely be cast during a window where large shrinkage strains are occurring. The crack maps discussed earlier in this report indicate transverse cracking occurs across the entire bridge deck width. It is unlikely that barriers at the extreme edges are capable of providing more shrinkage restraint to the deck than the girders below and therefore, the barriers were omitted from the shrinkage-induced strain analysis.

The shrinkage-induced strains were introduced into the FE model via temperature loads (negative temperature changes were used to generate shortening of the material fibers. Nodes in the FE model were selected as the temperature loading sites. There is a set of common nodes at the interface of the bridge deck and the top surface of the precast girders. In order to ensure that the temperature loading did not affect the girders, the girder material was given a coefficient of thermal expansion equal to zero. As a result, the precast girders did not shrink as a result of the temperature loading.

Figure 5.17 illustrates the application of temperature loading into the FE model. As discussed earlier, temperature changes were applied at the top surface, 1/3 the bridge deck height, 2/3 the bridge

deck height, and at the bridge deck bottom surface. As a result, there was a simulation of shrinkage-induced strains throughout the bridge deck height.

A linear elastic analysis was run for the temperature gradient loading case. Upon completion of this analysis, the self-weight of the precast girders and deck were applied. This second analysis was also linear elastic and as a result, superposition of strains is appropriate. Komp (2009) validated this superposition process. The self-weight was based upon a material density equal to 150 pounds per cubic foot.

Nine discrete points in the FE model were utilized to evaluate the results of the shrinkage-induced strain loading scenario. Figure 5.18 illustrates the location of these points with respect to the interior diaphragm and near centerline location of the precast girders. The FEA results are based upon a selection of the bridge deck that is 9,600 mm long 31.4 feet long.

5.3.6 Finite Element Analysis Results and Discussion

Once a cast-in-place bridge deck is placed, the concrete material is consistently gaining strength. The strains resulting from shrinkage in the concrete material is also increasing. Thus, concrete strength and concrete shrinkage are simultaneously increasing (at different rates) during the early life of the bridge deck. The incremental increases in strength and shrinkage were modeled in the present FEA. The strains were applied at discrete time instances in such a manner that the shrinkage strain model (equation 5.1) would be simulated. For simplicity, the strains were lumped into a step function that assumed strains would occur in discrete daily intervals. Figure 5.16 illustrates the step modeling of shrinkage strain assumed in the FE analysis.

Tables 5.3, 5.4, and 5.5 contain the transient variation in concrete material modulus, shrinkage strains, and the corresponding temperature changes used in the 14-day FE simulation. The temperature changes simulating shrinkage strains were applied at the surface, 1/3 down, 2/3 down and the bottom of the bridge deck.

A separate FE simulation was run for each day and with corresponding temperature changes and corresponding changes to the elastic material modulus. After each daily simulation is completed, the stresses developed from each is superimposed (added together) to give the total accumulated stress over the 14-day time period. Therefore, in this way, the FEA simulates the first 14 days in the life of the bridge deck and bridge superstructure.

Figure 5.20 illustrates the longitudinal stress contours in the bridge deck top surface at day 10 in the simulation. The segment of bridge deck used for the contour boundaries is illustrated schematically in Figure 5.18. In general, the girders provide restraint from free bridge deck volume change, and therefore it comes as no surprise that the stresses above the girders are slightly larger. The exception to this appears to occur in two spots directly between the girder spans on the edges between the top and side surface of the deck.

Table 5.6 provides the numerical results for the bridge deck section defined in Figure 5.18. The data in the table is from the finite element simulation for the first 10 days after casting taking into consideration normal stresses in the longitudinal direction and their potential to cause transverse cracking across the width of the bridge deck. Several observations can be made using the data in the table. First of all, there is an increase in stress on the bridge deck directly over girders. The data in the table for these locations corresponds to FE model nodes 1, 3, 5, 7, and 9 in Figure 5.18. It is clear that of the nine reference points selected, the five points directly over the girders have nearly 15% more stress than their four counterparts located in-between the girder spacing.

The finite element simulation of the first 10 days after casting illustrates the concrete will be susceptible to the largest tensile stresses during day 4 after casting (Table 5.6). From the instant the deck is cast, the deck is continuously gaining strength, while at the same time becoming subject to an increasing level of strain resulting from shrinkage as the concrete cures. Depending on the rate at which these two factors vary with time and synergistically interact with one another in the simulation, it would seem logical that there would be a time in which the combination of increased rigidity and shrinkage strains would cause the largest amount of stress. From day 5 onward, there is a slight decrease in average daily stress moving toward day 10.

Concrete gains a majority of its strength (90%) in the first 14 days, while a majority of shrinkage strains (80%) develop in the first 100 days. Therefore, it makes sense that the maximum stresses would occur early in the life of the bridge deck. This is not to say that additional stresses after day four may play a larger role in deck cracking. However, the large early stresses seen in the finite element simulations suggest a need for special attention during the days immediately following casting.

The data in Table 5.6 is founded upon a summation of the stresses from ten individual finite element simulations. The average daily stress is the average tensile stress that occurs at the 9 points across the bridge deck. The cumulative stress is the summation of average stresses up to and including the day in question. There are two common models used for assessing the cracking (tensile) strength of concrete. These are the modulus of rupture and 10% of the unconfined compression strength expressed simply as,

$$f_t = f_r = 7.5\sqrt{f'_c}$$

$$f_t = 0.10f'_c$$

The models for compression strength gain illustrated in Figure 5.15 and Table 5.3 indicate that the unconfined compression strength for the concrete deck material increases daily. As a result, the tensile strength of the concrete defined using both expressions above will change accordingly. Both of these tensile strength models were used to evaluate the tendency for the bridge deck concrete to crack at varying stages during the simulation.

The information in Table 5.6 suggests that if 10% of the concrete's compressive strength were used to define the concrete's tensile strength, the concrete would crack (tensile stress exceeds tensile strength), after four days. If the modulus of rupture was used to characterize the tensile rupture strength of the concrete, it appears as though deck cracks would appear after eight days. Therefore, the finite element simulations indicate that transverse cracking in the bridge deck over the interior pier could be expecting 4-8 days after casting. The type, location, and time frame all agree with actual results, as shown in Figure 5.21.

While the purpose of the simulation discussed here was to evaluate the effects of shrinkage strains on creating stresses that cause early-age transverse cracking in bridge decks, it is also possible to analyze the stresses that would cause longitudinal cracking as well. Figure 5.22 provides a representative finite element stress contour of the transverse direction stresses at the center of the deck.

There are several areas of peak stress represented in the figure. In each case, these areas are centered just to the right (or left) of a girder, and are elongated in the longitudinal (z) direction. This is most likely caused by the modeling of the concrete diaphragms at the center pier in the bridge superstructure. The diaphragm would most likely be cast at an angle consistent with the skew of the bridge superstructure.

However, in the finite element model, the diaphragms at the central pier and abutments were modeled with displacement restraint conditions in the transverse direction. The restraint directions were perpendicular to the girder longitudinal axes instead of to parallel to the skew. As a result, it appears as though the increased stress contours tend to be distorted in a longitudinal direction, as they follow the skewed shape of the bridge. Therefore, the modeling of the diaphragms may cause a slight increase in stress at those locations.

The transverse stresses were found to be generally less than twice the magnitude of the longitudinal stresses. However, this does not imply that the transverse stresses are not important. In fact, it is likely that while not in the same direction, the longitudinal and transverse stresses in combination will cause the deck to crack earlier than either would predict on their own. In analyzing the principle tensile stress over the center girder on the fourth day, a stress of 66 psi was found (compared to 64 psi found in Table 5.6 for node 5 on day 4). Therefore, the principle tensile stress is approximately 3% larger than the longitudinal stress at that same location. However, it is clear that the longitudinal stresses (causing transverse cracking) are still the predominant stresses in the deck.

Figure 5.23 illustrates normal typical transverse stress contour at the underside of the bridge deck. The transverse stresses at the bottom of the deck can be quite large, specifically at locations where the concrete diaphragm, girder, and deck meet. For the strains that develop over day four alone, there is a peak tensile stress of near 406 psi. It should be stressed that a relatively coarse mesh was used in the

finite element analysis, and the peak stress location is directly on an edge between the girder, diaphragm, and deck. This is a location that likely contains a very complicated strain and stress field. The yellow areas on the contour map in Figure 5.22, (slightly removed from the edge) are more representative of the stresses seen in the actual deck. However, these areas still represent a tensile stress of 73 psi, which is still quite significant. These transverse tensile stresses on the underside of the deck are larger than the longitudinal tensile stresses on the top of the deck, and therefore it is possible that cracking may occur on the underside of the deck before the transverse cracks are seen on the top of the deck. Due to memory and computing constraints, no further (more detailed) analysis with refined meshes could be carried out for the bridge. It is recommended that sub-modeling be investigated to further study stresses in these areas.

5.4 Simulation and Evaluation of Vehicle-Induced Strains

Previous research indicates that transverse cracking, specifically over interior piers, appears to be the most prevalent form of early-age cracking seen on bridge decks. The FE simulations discussed in the previous section indicates that concrete shrinkage alone may cause transverse cracking over interior supports early in the life of the bridge superstructure. The impact of vehicle loading in relation to generating early age cracking in the bridge decks at Waupun are now evaluated using FE simulation.

The finite element analysis once again focused on the two lane (one direction of traffic) bridge structure, B-20-134 in Waupun, Wisconsin. Two HL-93 design trucks (AASHTO 2006), whose configuration is shown in Figure 5.24, were used as the vehicle loading scenario. The positioning of the trucks was determined through the use of an influence line for a two span continuous-girder superstructure configuration and locations that would produce maximum negative bending moment in the girders over the interior pier support. Figure 5.25 shows the vehicle load positioning used as the basis of the loading in the FE simulation.

The HL-93 concentrated wheel loads were then converted into pressures that would act over uniformly over tire contact areas. The dimensions of the contact patches for HL-93 design truck model

tires are not defined. As a result, tire contact areas similar to those of the tri-axle dump trucks used in the in-situ load testing were implemented. However, the FE model mesh dictated the size and placement wheel contact areas. Figures 5.26 and 5.27 illustrate the loading magnitudes and the tire contact areas, respectively. It should be noted that 25.4 mm equals 1 inch, 4.445 N equals 1 pound, and 145.143 pounds-per-square-inch is 1 MPa.

A slightly smaller length of bridge deck was used to evaluate tensile strains induced by vehicle loading. The 8,300 mm (27.2 feet) long segment of bridge deck for contour plot reference is given in Figure 5.28. The nodes selected for strain evaluations are the same as those used in the shrinkage simulations.

A linear-elastic analysis was then run with the given tire pressure loadings using an FE model that included girders, deck, and continuous barriers. Mild steel reinforcement in the bridge deck was omitted in the finite element model. Once the linear elastic analysis was completed, the longitudinal tensile stresses in the top surface of the deck were examined. Figure 5.29 illustrates the longitudinal stress contour for the entire bridge deck.

As expected, there are areas of tensile stress are concentrated over the interior pier supports, while the remainder of the top surface is in compression. The girders, deck and barriers act compositely with one another. There are some tension strains at the abutment locations within the bridge deck and this is a result of artificial restraints introduced through diaphragm modeling. The tensile strains are concentrated within a 12,000 mm (39.4 feet) to the left and right of the interior pier support. Figure 5.30 illustrates the stress contour. The tensile stresses also follow the skewed support configuration.

The longitudinal tensile stress contour in the bridge deck is shown in Figure 5.31. The nodal locations are superimposed on this stress contour. Each nodal location corresponds to a centerline location for the longitudinal girders. There are two concentrated areas of peak tensile stress near points 3 and 5. The girder centerlines corresponding to these points are nearest to the wheel lines for the vehicle loading (Figure 5.25). Thus, the design lane loading resides in the region bounded by nodal locations 3, 4, 5, 6, and 7.

Table 5.6 includes the cumulative stress magnitudes resulting from shrinkage-induced strains over the 10-day period immediately following casting the bridge deck. There are now stress results available for HL-93 vehicle effects that can be superimposed onto these previous results. Since the cumulative shrinkage-induced tensile strains are maximum at 10-days after casting, it is interesting to examine the superposition of vehicle-induced tensile strains. One must assess when vehicles are likely to be placed on the superstructure after casting. The likely scenario is that the bridge deck will remain unloaded by barriers and vehicles for at least 10 days. Thus, the present comparison of stresses assumes that barriers and vehicle loading will be present 10 days after casting. This is not likely, but it is a convenient point to freeze tensile stress magnitudes resulting from shrinkage. Table 5.6 illustrates that there is a reduction in daily tensile stresses occurring and this reduction will continue.

Table 5.6 illustrates that the maximum tensile strain resulting from shrinkage 10-days after casting is 591 psi. The peak tensile strain resulting from vehicle loading in the present FE simulation is 115 psi. The superposition of these two stress magnitudes gives 706 psi. If we assume that the tensile strength of concrete is based upon the 28-day unconfined compression strength, the tensile strength of the concrete at the time the vehicle loading is applied is one of two values depending upon the model used,

$$f_t = f_r = 7.5\sqrt{f'_c} = 7.5\sqrt{4,000} = 474 \text{ psi}$$

$$f_t = 0.10f'_c = 0.10(4,000) = 400 \text{ psi}$$

Thus, the superposition of vehicle tensile strains and shrinkage-induced tensile strains results in tensile stress magnitudes are two times the tension strength magnitude using typical models for the concrete.

From the finite element analysis, it would appear as though the combination of traffic loading (HL-93 trucks) and concrete shrinkage is likely to cause transverse cracking in the bridge deck over the interior supports in this bridge.

5.5 Concluding Remarks

A model for the maximum shrinkage strain at the top of the concrete deck bridge deck (Tadros and Al-Omaishi 2003) was used as the foundation for an FE simulation of the early-life behavior of a concrete

bridge deck. This shrinkage strain model was founded upon common parameters: volume-to-surface ratio of the concrete; the average humidity at the bridge location; the unconfined compressive strength of the concrete; and the time over which the concrete cured. The relative humidity of the concrete was obtained through field hygrometer measurements at mid-thickness of the concrete. Based on the relative humidity at mid-depth, the magnitude of shrinkage strain was linearly interpolated throughout the remaining thickness at points that were convenient and consistent with the FE model developed.

The shrinkage strain magnitudes were converted to equivalent temperature loadings suitable for implementation in the finite element software used (ANSYS 2007). The amount of shrinkage strain that would occur over a given day was estimated, and 10 independent linear elastic simulations were run. Only the temperature loads were considered (no self-weight) and the barriers were not included in the finite element model. Further details of the simulations are available (Komp 2009).

The finite element simulations conducted indicate that drying shrinkage appears to be capable of causing transverse (and possibly longitudinal) bridge deck cracking at very early stages in the life of the bridge deck. The simulations conducted indicate that cracking may occur as early as 4-8 days after bridge deck placement. However, this does not take into consideration the principle stress state, or traffic loading. Superposition of shrinkage-related stresses and traffic induced stress may cause the deck to crack at an earlier age. This will be evaluated in the next section of the report.

An FE simulation of the tensile strains and stresses induced by HL-93 vehicle-type loading was conducted. The FE model included precast girders, the bridge deck and barriers. Tensile stresses induced by HL-93 vehicle loading were found to be on the order of 20% of the typical magnitudes assumed for the tensile strength of concrete material. When these are superimposed onto the states of stress likely present 10-days after casting the bridge deck, it is likely that the combined effects of vehicle-induced stresses and shrinkage-induced stresses will result in transverse cracking over the interior pier supports in the bridges in Waupun. The crack maps discussed earlier in this report confirm this behavior.

5.6 References

- AASHTO (2006). "AASHTO LRFD Bridge Design Specifications", 2006 Interim Revisions, 3rd Edition, Washington D.C.
- ANSYS (2007) ANSYS Finite Element Analysis System, Release 11.0.
- Darwin, D., Nilson, A.H., Dolan, C.W. (2004). *Design of Concrete Structures, 13th Edition*, McGraw-Hill Companies, New York.
- Kachlakev, D., Miller, T., Yim, S., (2001). *Finite Element Modeling of Reinforced Concrete Structures Strengthened with FRP Laminates*, Final Report, Oregon Department of Transportation Research Group.
- Komp, J.T. (2009). *Evaluation Of Premature Cracking In Concrete Bridge Decks Using Finite Element Analysis*, MS Thesis, Marquette University, Milwaukee, WI, May.
- Krauss, P.D. and Rogalla, E.A. (1996). *Transverse Cracking in Newly Constructed Bridge Decks*, NCHRP Report 380, Transportation Research Board, National Academies, Washington, DC.
- Martin, K.E. (2006). *Impact of Environmental Effects on, and Condition Assessment of IBRC Bridge Decks in Wisconsin*, MS Thesis, Marquette University, Milwaukee, WI, May.
- Saadeghvaziri, M.A. (2002). *Cause and Control of Transverse Cracking in Bridge Decks*, Department of Transportation Division of Research and Technology, Final Report.
- Tadros, M.K., and Al-Omaishi, N. (2003). *Prestress Losses in Pretensioned High-Strength Concrete Bridge Girders*, NCHRP Report 496, National Cooperative Highway Research Program, Transportation Research Board, National Academies, Washington, DC.
- Schmitt, T.R. and D. Darwin, D.W. (1995). *Cracking in Concrete Bridge Decks*, Report No. K-TRAN: KU-94-1, Final Report, Kansas Department of Transportation.
- Schmitt, T.R. and D. Darwin, D.W. (1999). "Effect of Material Properties on Cracking in Bridge Decks", *Journal of Bridge Engineering*, Vol. 4, No. 1, American Society of Civil Engineers, pp. 8-13.

Table 5.1 Variation in Humidity Coefficient throughout the Deck Thickness (Komp 2009).

Location	k_{hs}
Top of Deck	1.02
1/3 Down	0.927
2/3 Down	0.833
Bottom of Deck	0.74

Table 5.2 Variation in Time Dependent Shrinkage Coefficient (Komp 2009).

Time (days)	k_{td}
1	0.020
2	0.040
3	0.059
4	0.077
5	0.094
6	0.111
7	0.127
8	0.143
9	0.158
10	0.172
11	0.186
12	0.200
13	0.213
14	0.226

Table 5.3 Increase in Modulus of Elasticity with Time for $f'_c = 4,000 \text{ psi}$ (Komp 2009).

Time (days)	Compression Strength (fraction of f'_c)	E_t (psi)
1	0.210	1,652,017
2	0.400	2,280,000
3	0.540	2,649,121
4	0.630	2,861,377
5	0.687	2,988,018
6	0.740	3,101,135
7	0.770	3,163,372
8	0.800	3,224,407
9	0.827	3,277,773
10	0.853	3,339,503
11	0.873	3,368,309
12	0.893	3,406,674
13	0.904	3,427,592
14	0.913	3,444,611

Table 5.4 Shrinkage Strains Gradient through Bridge Deck (Komp 2009).

Time (days)	ε_{sh} (in./in.) $\times 10^{-4}$			
	Top Surface	1/3 Down	2/3 Down	Bottom Surface
1	0.2293	0.2083	0.1873	0.1663
2	0.4494	0.4082	0.3672	0.3260
3	0.6608	0.6003	0.5399	0.4794
4	0.8642	0.7851	0.7061	0.6269
5	1.0600	0.9628	0.8659	0.7689
6	1.2480	1.1340	1.0200	0.9056
7	1.4300	1.2990	1.1680	1.0370
8	1.6050	1.4580	1.3110	1.1640
9	1.7740	1.6110	1.4490	1.2870
10	1.9370	1.7600	1.5830	1.4050
11	2.0950	1.9030	1.7110	1.5200
12	2.2470	2.0410	1.8360	1.6300
13	2.3940	2.1750	1.9560	1.7370
14	2.5370	2.3050	2.0730	1.8400

Table 5.5 Temperature Change Gradient through Bridge Deck (Komp 2009).

Time (days)	ΔT (F)			
	Top Surface	1/3 Down	2/3 Down	Bottom Surface
1	3.474	3.156	2.838	2.520
2	6.809	6.185	5.563	4.940
3	10.01	9.096	8.181	7.264
4	13.09	11.89	10.70	9.499
5	16.06	14.59	13.12	11.65
6	18.91	17.18	15.45	13.72
7	21.66	19.68	17.70	15.72
8	24.32	22.09	19.87	17.64
9	26.88	24.42	21.96	19.50
10	29.35	26.66	23.98	21.29
11	31.74	28.83	25.93	23.02
12	34.04	30.93	27.81	24.70
13	36.28	32.96	29.64	26.32
14	38.44	34.92	31.40	27.89

Table 5.6 Longitudinal Bridge Deck Stress (psi) Variation with Location (Komp 2009).

Node Location	Day									
	1	2	3	4	5	6	7	8	9	10
1	49	64	71	73	73	73	71	70	69	67
2	40	52	57	59	59	58	57	56	55	54
3	45	57	62	64	64	63	62	61	60	58
4	40	52	56	58	58	57	56	55	54	53
5	44	57	62	64	63	63	62	60	59	58
6	40	52	56	58	58	57	56	55	54	53
7	44	57	63	64	64	64	63	61	60	59
8	40	52	57	59	59	58	57	56	55	54
9	49	64	71	74	74	73	72	71	69	68
Average Stress	44	56	62	64	63	63	62	61	59	58
Cum. Avg. Stress	44	100	162	225	289	352	414	474	533	591
$7.5\sqrt{f'_c}$ (psi)	264	364	423	457	477	496	505	515	524	532
$0.10f'_c$ (psi)	85	163	219	256	279	301	313	325	336	347

Figure 5.2 Bridge B-20-134 Plan and Plan View of Deck Finite Element Modeling (Komp 2009).

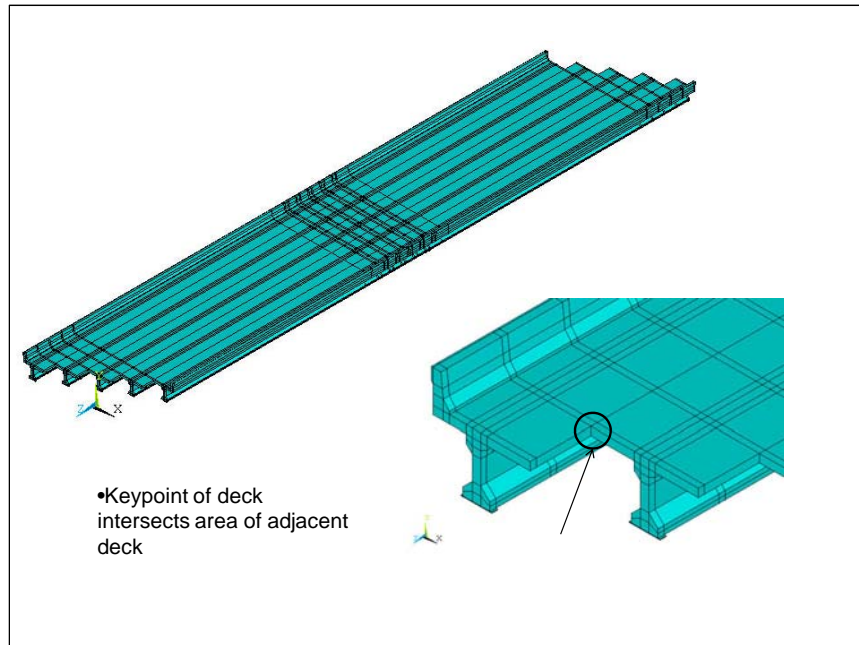


Figure 5.3 Stepped Deck and Girder Terminations to Accommodate Skew (Komp 2009).

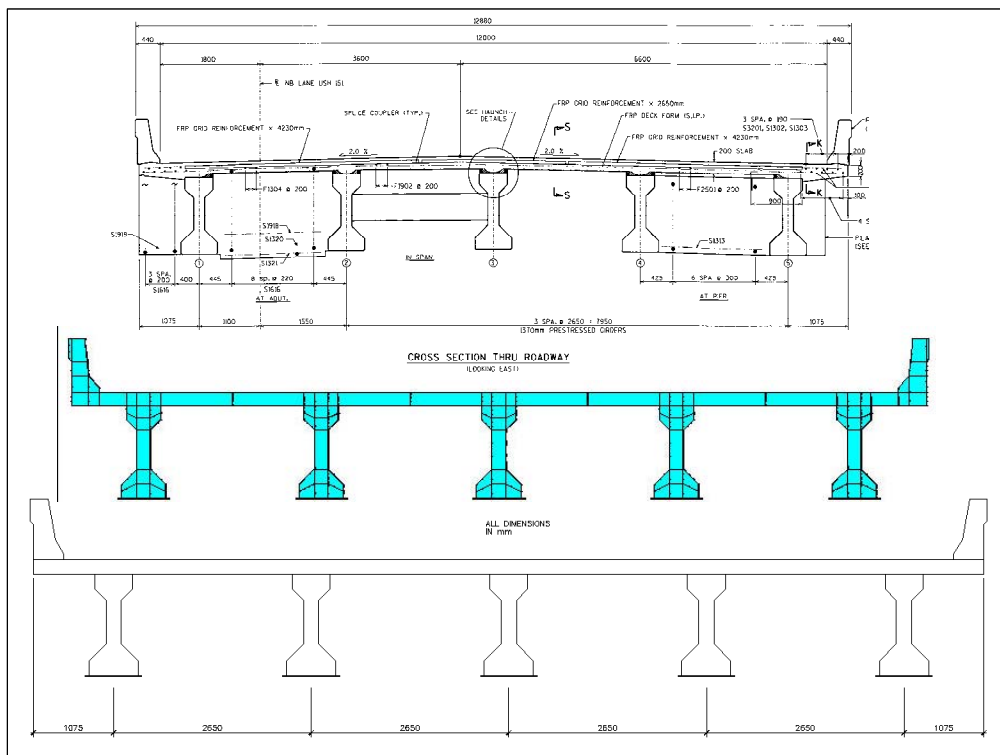


Figure 5.4 Bridge B-20-134 Cross Section (Komp 2009).

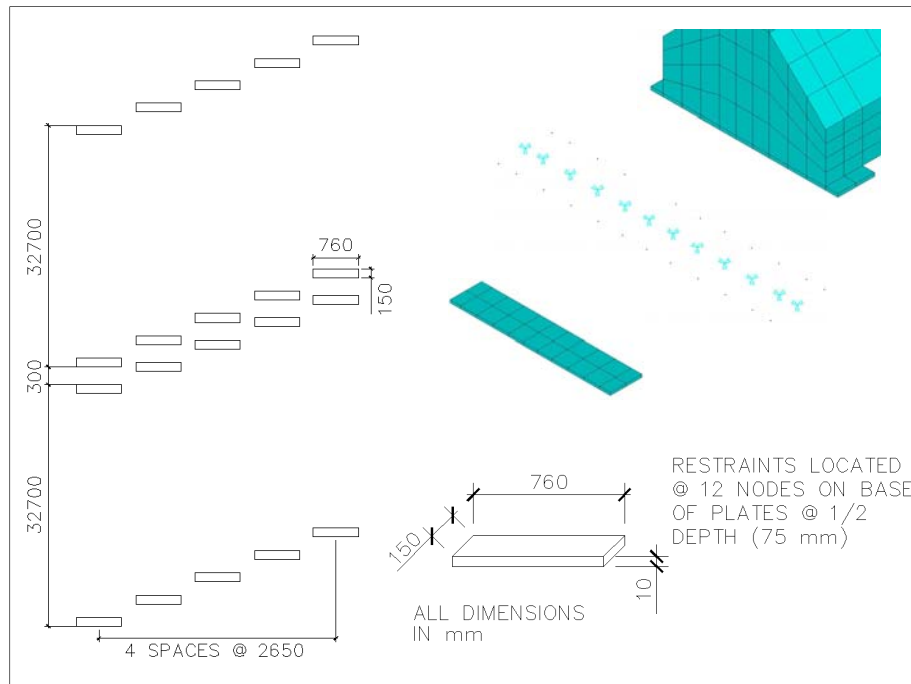


Figure 5.5 Steel Base Plate Modeling (Komp 2009).

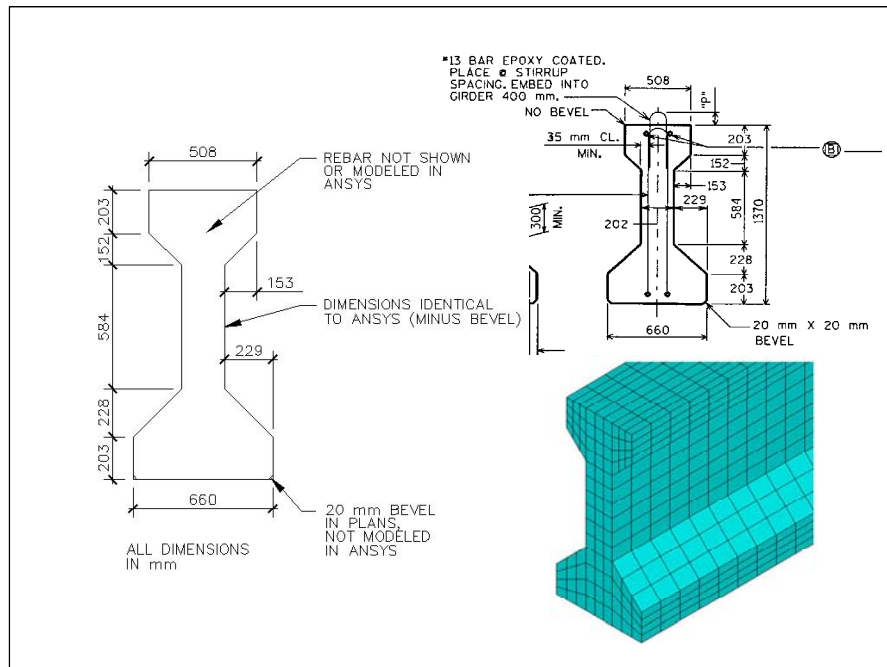


Figure 5.6 Modeling of Standard WisDOT 54'' Deep Precast Girder (Komp 2009).

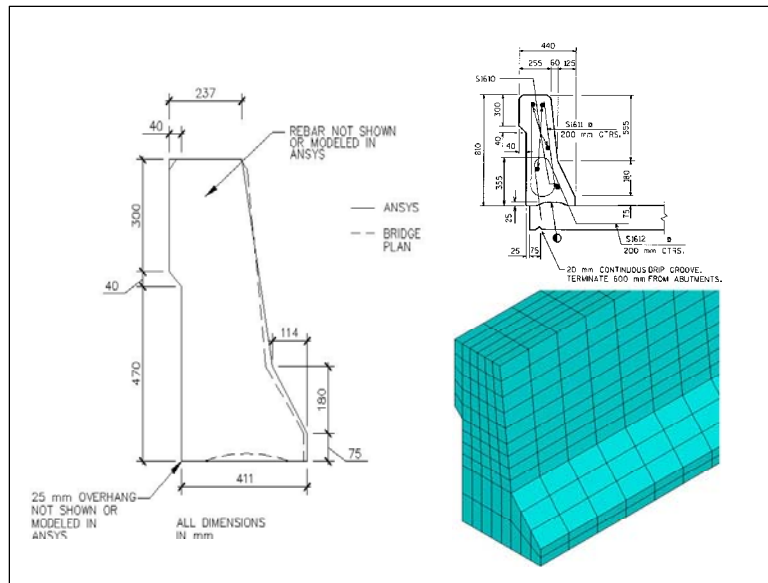


Figure 5.7 Concrete Barrier Modeling (Komp 2009).

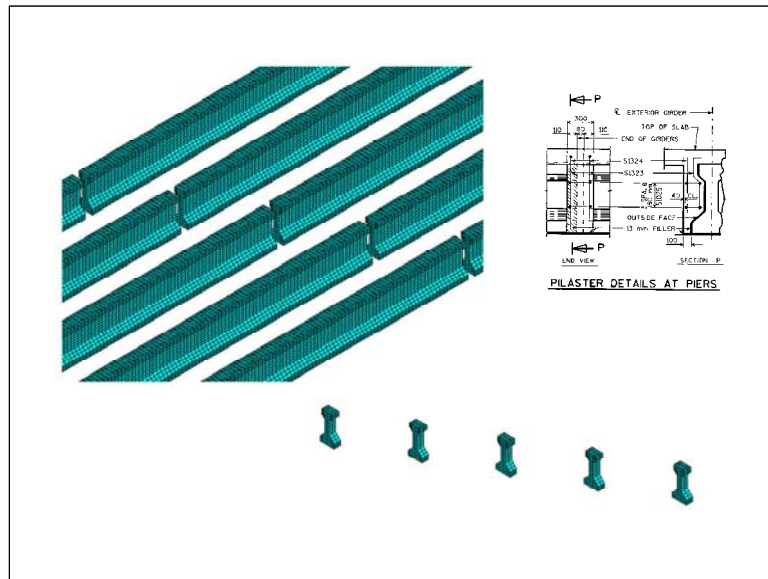


Figure 5.8 Modeling Approach for Concrete Diaphragms at Interior Piers (Komp 2009).

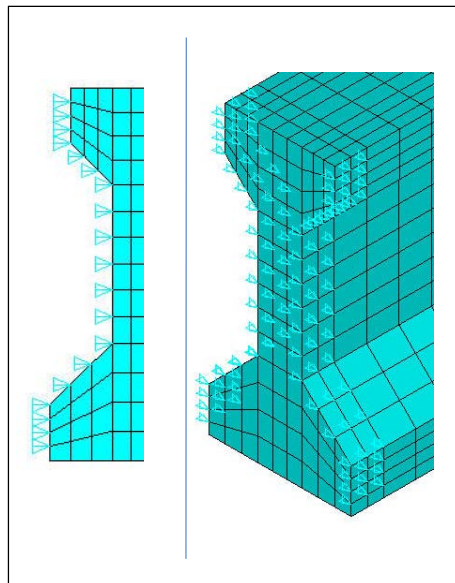


Figure 5.9 End Diaphragm Restraints (Komp 2009).

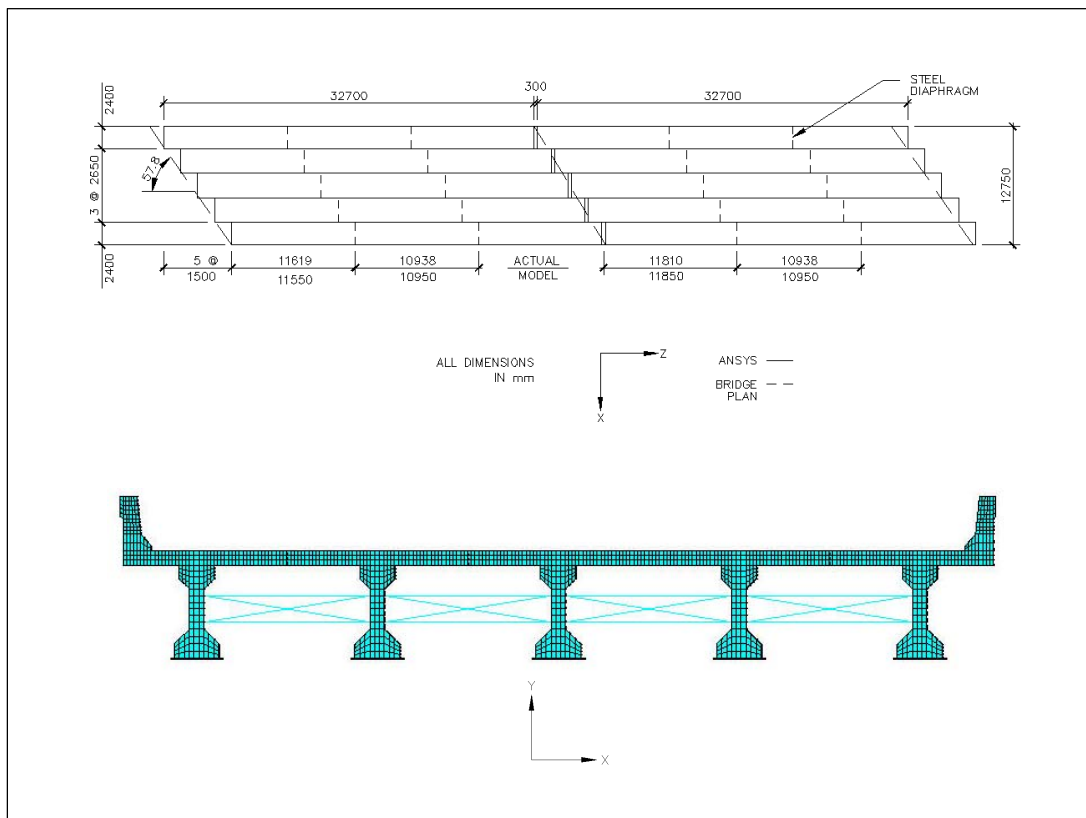


Figure 5.10 Steel Diaphragm Simulation and Locations (Komp 2009).

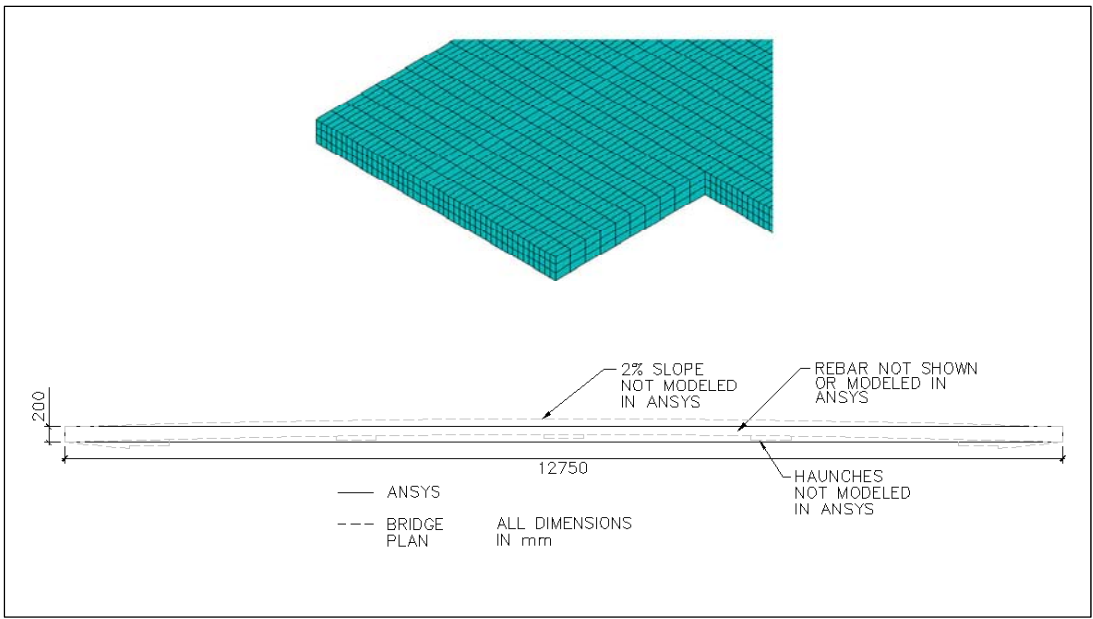


Figure 5.11 Concrete Deck Modeling (Komp 2009).



Figure 5.12 Topographic Map of United States Humidity (Tadros 2003).

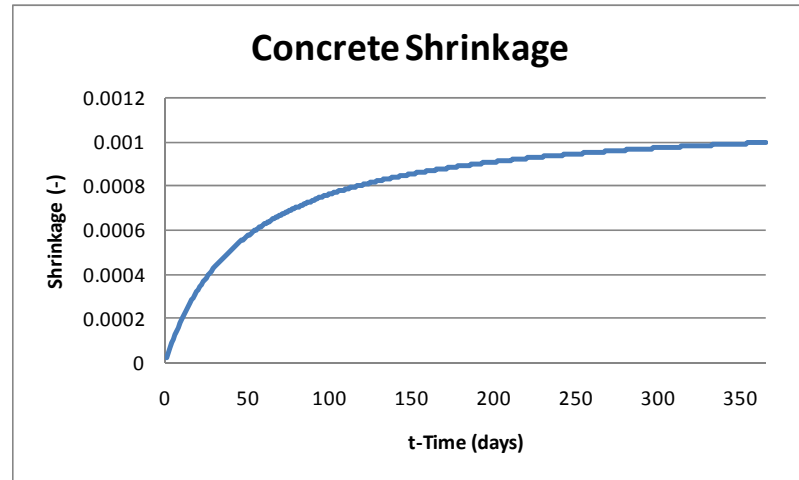


Figure 5.13 Concrete Shrinkage with Respect to Time (Komp 2009).

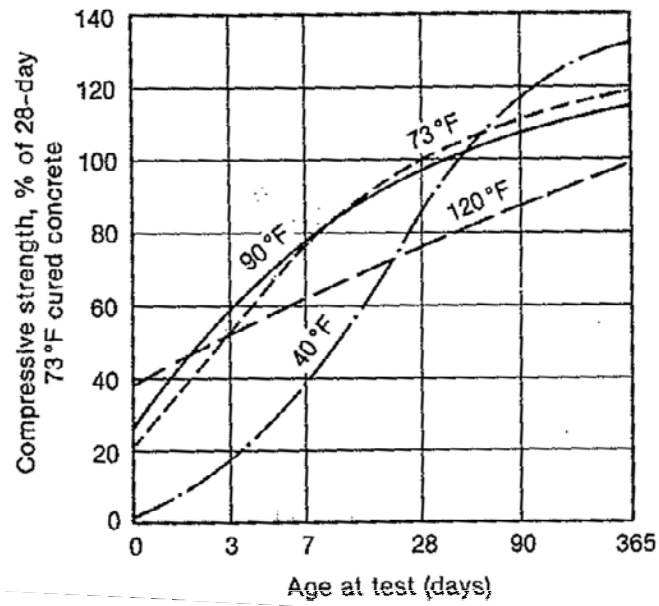


Figure 5.14 Concrete Compressive Strength with Time (MacGregor and Wight 2005).

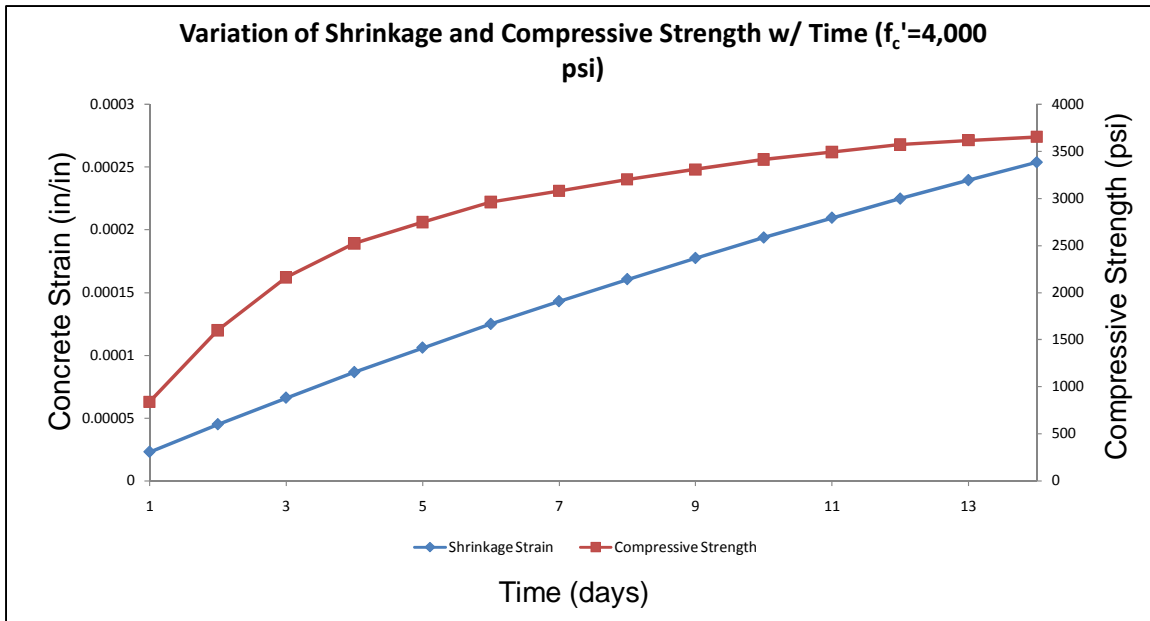


Figure 5.15 Variation of Shrinkage Strain and Compressive Strength (Komp 2009).

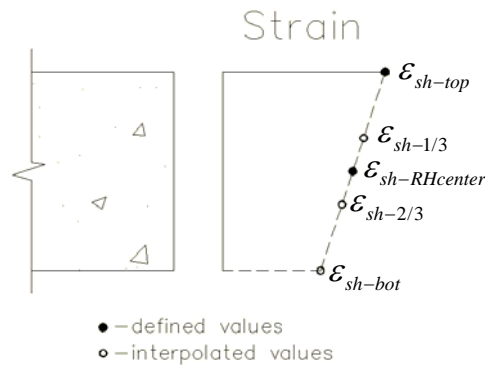


Figure 5.16 Shrinkage Strain Distribution throughout the Deck (Komp 2009).

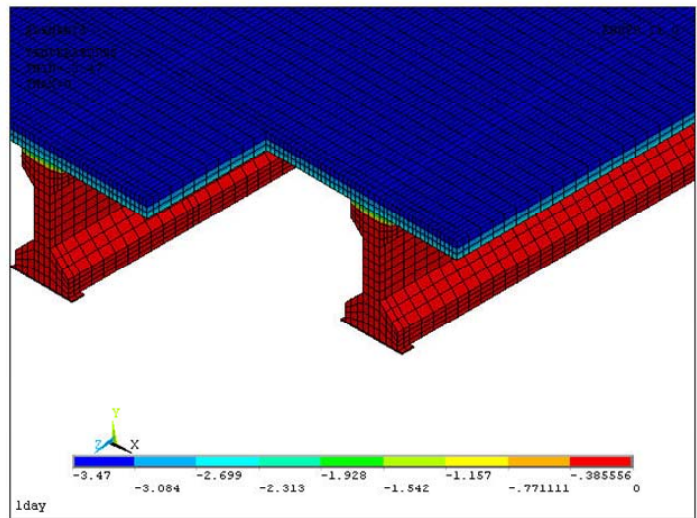


Figure 5.17 Temperature Distribution throughout the Finite Element Model (Komp 2009).

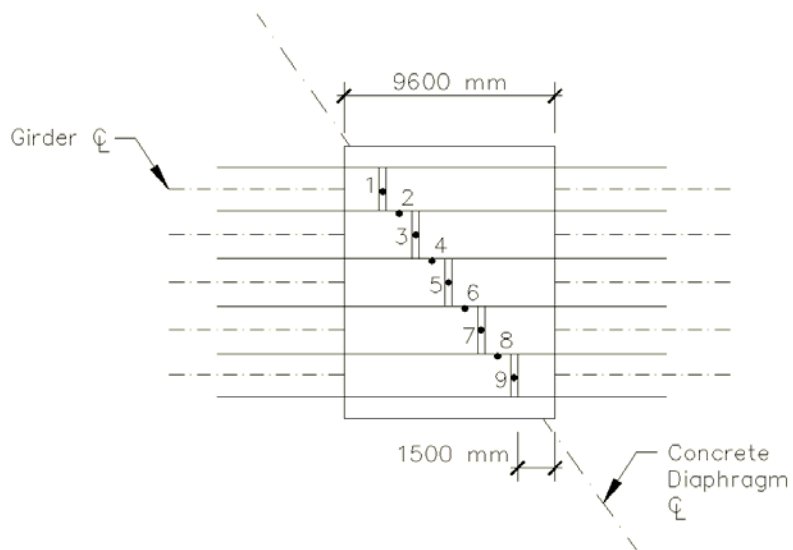


Figure 5.18 Finite Element Model Deck Coordinate Locations (Komp 2009).

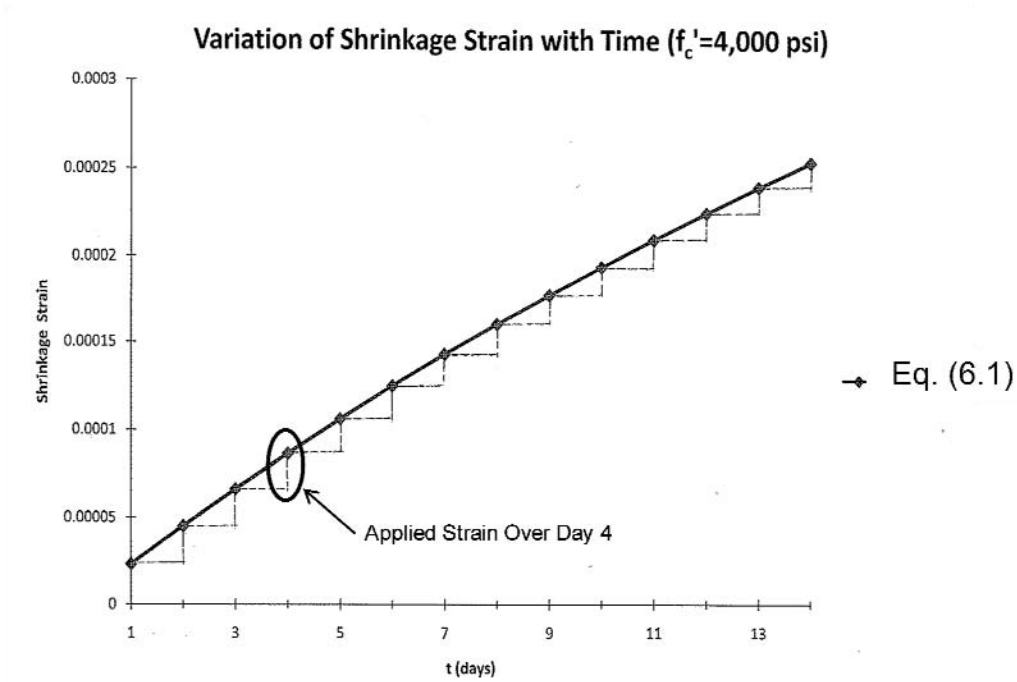


Figure 5.19 Step-Modeling Shrinkage Strain Variation with Time (Komp 2009).

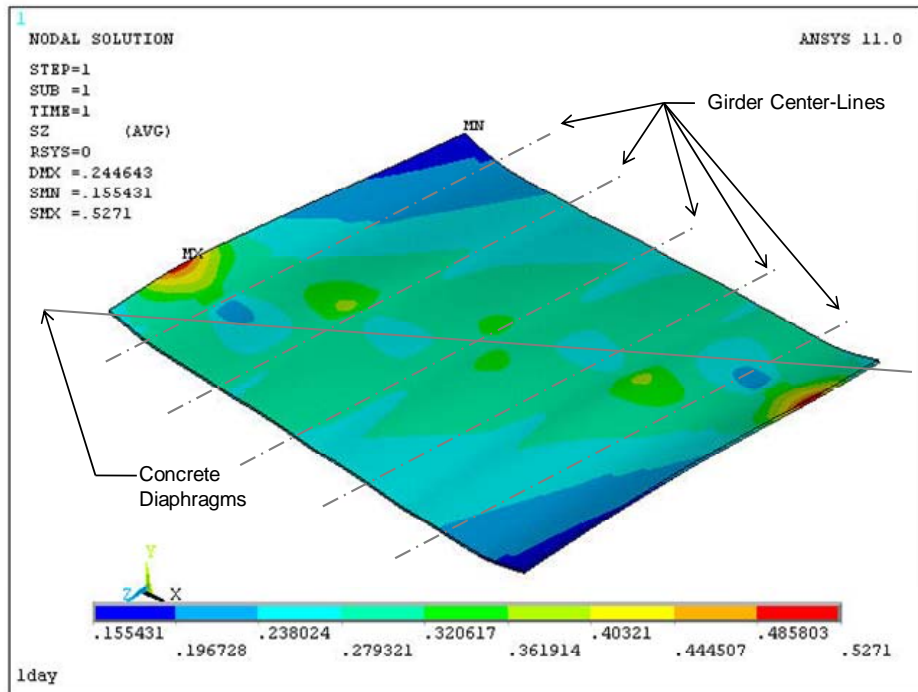


Figure 5.20 Longitudinal Stress Contour at Day 10 in Simulation (Komp 2009).

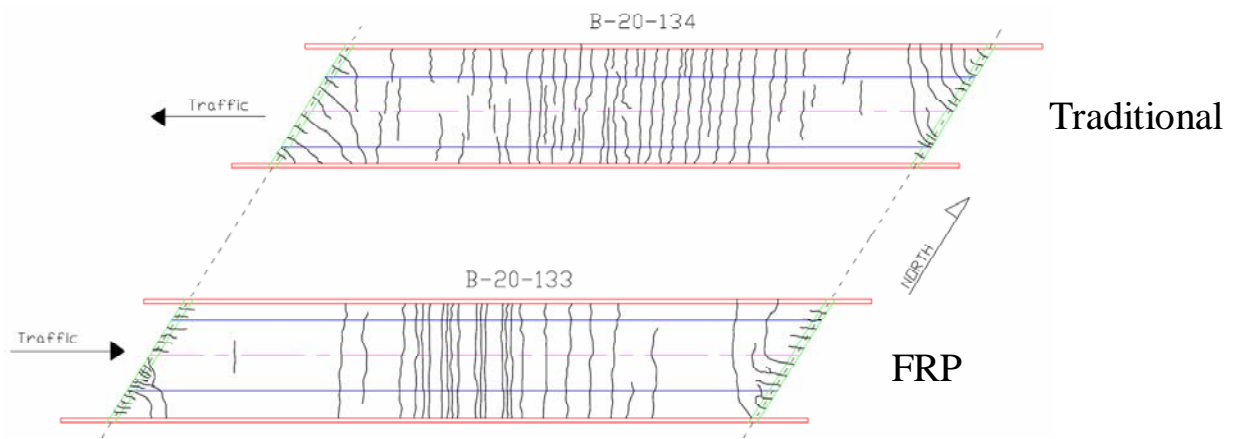


Figure 5.21 Waupun Bridge Crack Mapping (Martin 2006).

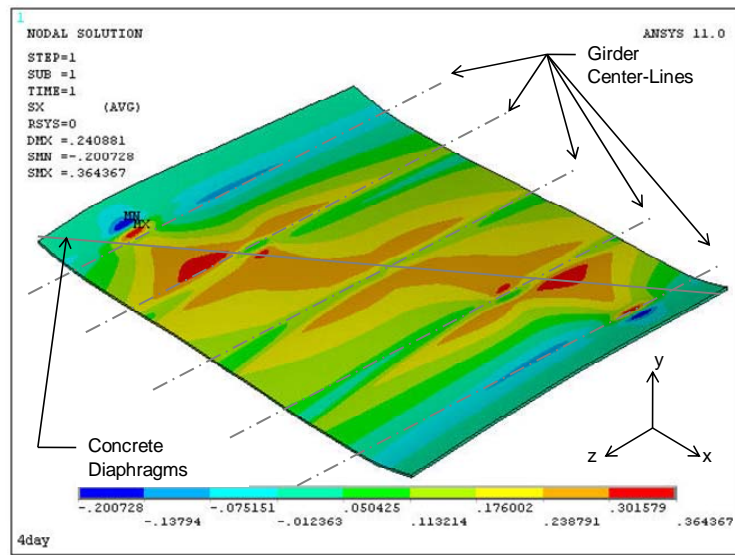


Figure 5.22 Transverse Stress Contour at Day 10 in Simulation (Komp 2009).

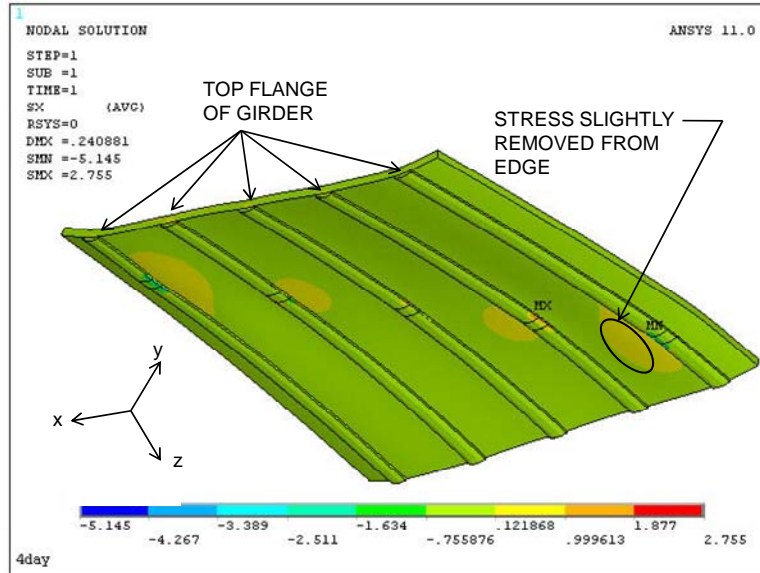


Figure 5.23 Transverse Stresses as the Base of the Bridge Deck (Komp 2009).

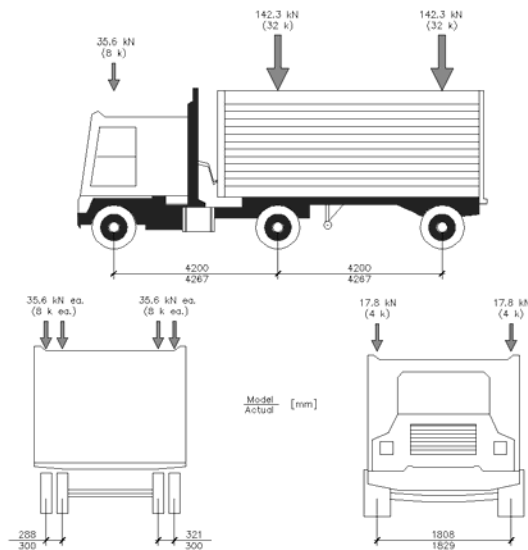


Figure 5.24 HL-93 Truck Loading and Wheel Spacing (Komp 2009).

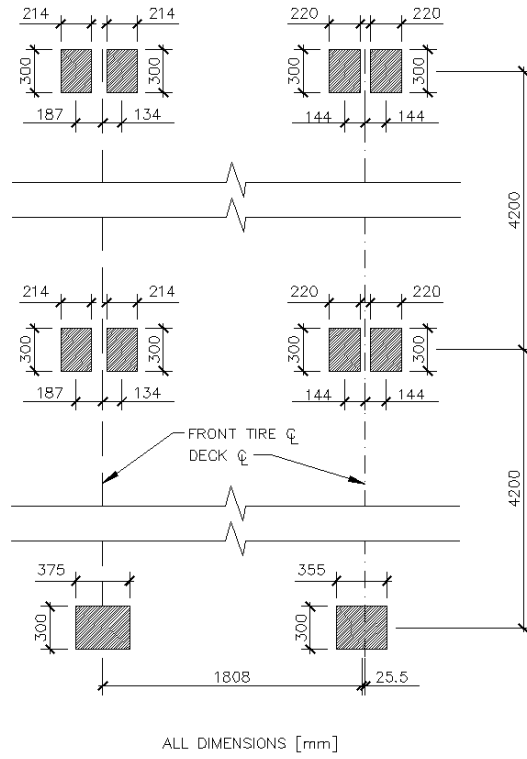


Figure 5.27 Tire Contact Areas and Relative Spacing (Komp 2009).

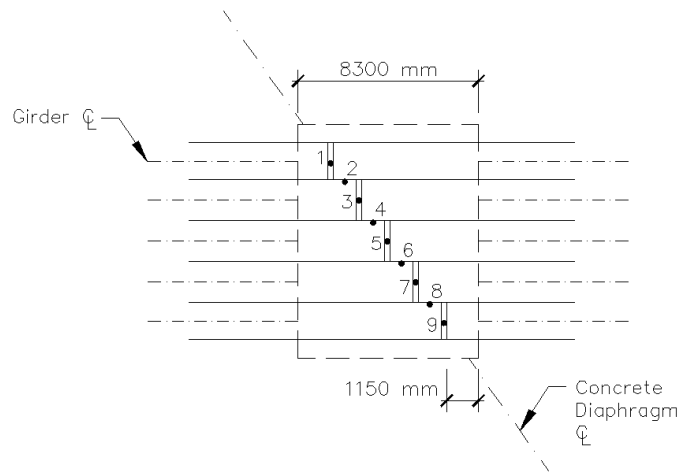


Figure 5.28 Nodal Locations over the Interior Pier (Komp 2009).

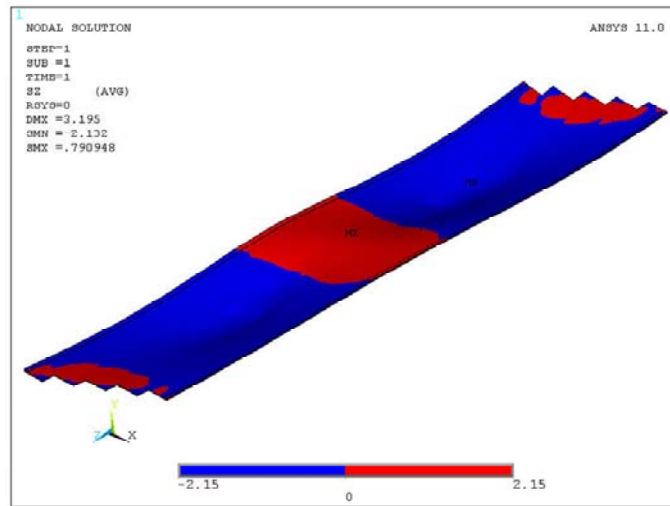


Figure 5.29 Comparison of Tensile and Compressive Stresses at Top Deck Surface (Komp 2009).

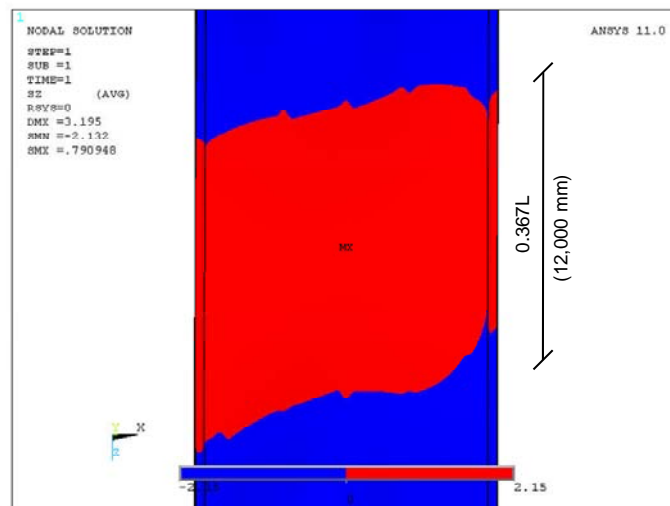


Figure 5.30 Tensile Stresses at Top of Deck over Interior Pier (Komp 2009).

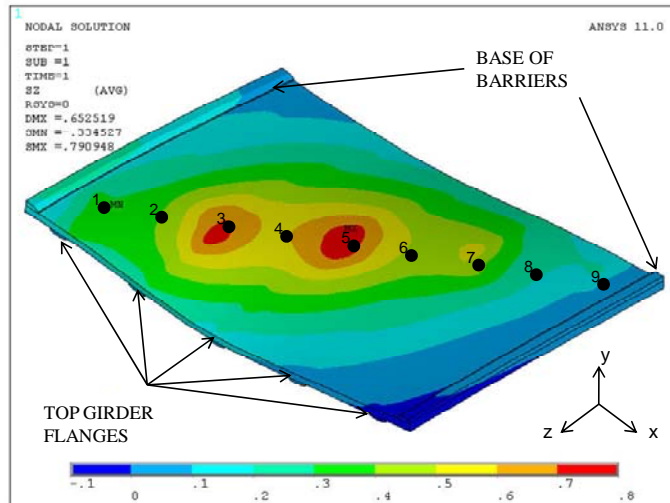


Figure 5.31 Contour Plot of Longitudinal Normal Stresses at the Interior Pier (Komp 2009).

Chapter 6

Summary, Conclusions and Recommendations

6.1 Summary

This report outlines activities undertaken during a five-year monitoring study of Wisconsin's first IBRC bridges. The report provides detailed background on the IBRC program and the bridge superstructures constructed in Waupun, WI and Fond du Lac, WI. A detailed review of literature related to the objectives of the present research effort was provided. A synthesis of the literature was generated to guide the activities undertaken as part of the present effort.

The development of portable strain sensors suitable for use in the proposed research effort was described in detail. Calibration factors for these sensors were also developed. A laboratory-based experimental program designed to evaluate the impact of moisture and freeze-thaw cycling on the shear strength at the interface between the FRP-SIP formwork and concrete was undertaken.

Thorough visual benchmark condition evaluation of the bridges at Waupun and Fond du Lac was conducted. Common NDE methods were reviewed for application in the present research effort. A laboratory-based evaluation of the infrared thermography technique for application in the present research effort was conducted. Finally, the presence of moisture accumulation at the interface between the FRP-SIP formwork and concrete in the Waupun bridge system was assessed using a digital hygrometer.

Two in-situ load tests were conducted. The first occurred in July 2007 and the second occurred in July 2009. Detailed discussion of the data acquisition system and instrumentation was provided. Thorough discussion of all load testing results and insights with regard to degradation of performance with time were given. Finite Element (FE) simulation of shrinkage-induced and vehicle-induced stresses was conducted using commercial-grade FE software.

6.2 Conclusions and Recommendations

The five-year research effort completed several related, yet distinct, studies designed to assess the likely long-term performance of Wisconsin's IBRC structures and also provide direction with regard to further investigation into the performance of these structural systems so that the technologies fostered by them can be introduced in bridge superstructure design going forward. This section of the report outlines conclusions drawn by the research team and makes recommendations regarding further investigation designed to assess long-term performance of these structures and improve the technologies developed.

Impact of Freeze-Thaw Cycling

The research completed indicates that freeze-thaw cycling and the presence of water could be detrimental to the FRP-SIP-formwork-concrete interfacial shear strength. Experimental studies indicated that the mean nominal shear strength at this interface was reduced 13% by water exposure alone and by 16% after 100 freeze-thaw cycles. A design-level shear strength corresponding to 95% confidence after 100 F/T cycles reduced 40% when compared to control specimens. Even specimens exposed to water for 14 days without F/T cycling experienced a 95% confidence-level shear strength reduction of 20%. FE analysis of the deck system using simplified models suggests that shear demands at the concrete FRP-SIP interface are not of sufficient magnitude to cause concerns regarding long-term performance even with the reduction in strength due to moisture presence and freeze-thaw cycling.

NDE Evaluation

After approximately four years of traffic loading, bridges B-20-133/134 showed significant transverse cracking around the central piers and along the abutment joints. Therefore, it is likely that moisture has a direct path to the zone where aggregate interlock between the FRP-SIP formwork and concrete is needed to accomplish the shear transfer needed to ensure that positive tension reinforcement for the bridge deck exists. Without a way to escape, moisture may freeze and thaw as the climate changes during the seasons.

The laboratory freeze-thaw testing indicates that this is likely not of concern, but laboratory testing is limited in its ability to simulate real-world behavior.

Bridges B-20-148/149 are in excellent condition with minor cracking present. At the time of the 2005 visual inspection, these bridges showed virtually no signs of deck cracking other than a few hairline cracks located at the abutments and in the parapet(s). The bridge deck with FRP reinforcement showed no cracks. No cracks were observed to extend through the bridge deck thickness. The lack of cracking present in the simply-supported superstructure when compared to the two-span continuous superstructures found in bridges B-20-133/134 suggests that further study of the continuous superstructure configuration is warranted. Further evaluation of the simply supported bridge superstructures (B-20-148/149) is not warranted.

The NDE techniques of infrared thermography, chain dragging, tap testing, and ultrasonic testing, were reviewed. Tap testing with an impact hammer appears to be the most useful methods for monitoring the bridges studied in the present effort. Infrared thermography is the least likely to yield useful results for monitoring the IBRC bridges. Without an air void at the interface between FRP-SIP form and the concrete deck, there will not be a disruption of the heat transfer and IRT will not show debonding.

Whichever NDE method is chosen to inspect the bridge decks with FRP-SIP, it must be realized that any NDE technique will only be able to look at about half of the FRP area in contact with concrete. The tops of the void spaces that result from the FRP-tubes in the SIP formwork will be impossible to inspect because of the layer of FRP below the openings. This makes it very difficult to get a good idea of how much area is adequately interlocked once a test has been established to determine the quality of the interlock between the aggregate and FRP. It may be that coring the bridge deck and examining the resulting concrete quality and the interface between the concrete and FRP-SIP formwork is the most useful NDE/NDT methodology for the IBRC bridge at Waupun.

No moisture was found when drilling the hygrometer probe holes so there is no concern that moisture is actually accumulating at the interface of the FRP-SIP formwork and the concrete deck as of the date of this report. It should be understood that relative humidity is one measure of the tendency for

the FRP-SIP formwork to inhibit moisture egress from within the deck and may be an indicator for the tendency for moisture to accumulate at the interface. However, the ability of humidity readings to reliably indicate levels of moisture to expect at the interface remains to be definitively proven. It is recommended that further analysis with regard to relative humidity be undertaken in future research efforts as it may be a useful tool for long-term evaluation of bridge decks with FRP-SIP formwork.

In-Situ Load Testing

In-situ load testing of bridges B-20-133 and B-20-148 was conducted to evaluate several critical load transfer mechanisms that could give the research team indication of degradation with time. Two load tests were conducted: July 2007 and July 2009. The load transfer mechanisms evaluated were: (a) wheel load distribution within the bridge deck; (b) composite beam behavior in the superstructure; (c) lane load distribution within the superstructure; and (d) bridge deck deflection relative to the girders.

Bridge deck displacements relative to the girders in both bridges did not change significantly with time. As a result, one can conclude that there has not been a significant change in the bridge deck load transfer mechanism over the two-year period of evaluation and therefore, no degradation in this load transfer mechanism has occurred. The IBRC bridge decks are performing in a manner that is satisfactory and expected.

The wheel load distribution widths present in the FRP-SIP bridge deck system of B-20-133 can be predicted using standard design/analysis procedures found in U.S. design specifications. The in-situ load testing found that this load transfer mechanism did not change significantly (if at all) over the two year evaluation period and thus, the wheel load distribution within this superstructure did not degrade. Although not fully evaluated in the present research report, the in-situ testing illustrates that the wheel load distribution widths in B-20-148 are consistent, but narrower, than that in B-20-133. This is to be expected since common models for strip width found in U.S. design specifications are functions of beam spacing. The spacing of the girders in B-20-133 is wider than the spacing of the girders in B-20-148 and therefore, this narrower strip width is expected. The lack of significant change in strip widths over the

two-year interval suggest that the load transfer mechanisms in the bridge deck have not changed and therefore, there is no reason to suspect degradation and reduced expectations for quality long term performance.

Strain gradients over the height of the girders in the Fond du Lac bridge load tested clearly exhibit composite behavior. Furthermore, the strain gradients did not significantly (if at all) change with time and therefore, one can conclude that there was no change in the composite beam load transfer mechanism within bridge B-20-148 over the two-year monitoring period and therefore, no degradation in this regard.

Lane load distribution factors for wide-flange bulb-tee composite bridge girder systems (e.g. that used in B-20-148) can be computed accurately with standard design/analysis procedures found in modern U.S. bridge design specifications. Furthermore, these lane load distribution factors did not change from the original July 2005 load tests and the July 2007 load test conducted in this research study. As a result, there was no degradation measured in this regard and the long-term performance of this bridge system is expected to be no different than any other traditionally constructed bridge of similar superstructure configuration.

The in-situ load testing conducted was not without difficulty. The portable strain sensors design and fabricated did a terrific job in providing strain readings in a relatively reliable manner. However, there were two glaring difficulties that arose with the instrumentation and the load testing protocols. There were some installation issues that may have lead to elevated strain readings encountered during the July 2009 load test (especially at B-20-148). The low modulus polymer carrier for the strain gauges was bolted in place and this bolting procedure may have resulted in non-straight orientations for the sensors. As a result, the studs and may have introduced significant bending strains into the sensors. As a remedy to this, it is recommended that the washers beneath the sensors be better able to bridge the slight spalling that normally accompanies the installation of the threaded studs.

Positioning the wheel loading was perhaps the most difficult task to accurately complete during the load testing. It may have been better off to space out the wheel load distributions sensors at the

underside of the bridge deck further than the 17.5 inches used. It also may have been prudent to explore more exact (GPS-based) deck marking procedures. This would have helped to ensure that wheels on the bridge deck were positioned as close as possible to locations directly above the bridge deck sensors below.

Numerical Simulation

The finite element simulations conducted indicate that drying shrinkage appears to be capable of causing transverse (and possibly longitudinal) bridge deck cracking at very early stages in the life of a bridge deck. The simulations conducted indicate that cracking may occur as early as 4-8 days after bridge deck placement.

An FE simulation of the tensile strains and stresses induced by HL-93 vehicle-type loading was conducted. The FE model included precast girders, the bridge deck and barriers. Tensile stresses induced by HL-93 vehicle loading were found to be on the order of 20% of the typical magnitudes assumed for the tensile strength of concrete material. When these are superimposed onto the states of stress likely present 10-days after casting the bridge deck, it is likely that the combined effects of vehicle-induced stresses and shrinkage-induced stresses will result in transverse cracking over the interior pier supports in the bridges in Waupun.

The crack maps developed in the benchmark condition assessment of the bridges in Waupun and Fond du Lac indicate that there is no difference between crack patterns developed in the FRP bridges versus the traditionally constructed counterparts. The FE simulations conducted as part of this effort clearly support that there should be no difference in behavior leading to cracking since shrinkage-induced straining and traffic loading are the likely reasons for the transverse cracking. Furthermore, the deck connection detail at the central diaphragms (over the interior piers) in the FRP-SIP formwork bridge at Waupun is expected to neither improve nor detract from the behavior with regard to cracking.

Wisconsin Highway Research Program
University of Wisconsin-Madison
1415 Engineering Drive
Madison, WI 53706
608/262-2013
www.whrp.org